



DELAMINATION OF COMPOSITE SPECIMENS

Ph. D. dissertation

András Szekrényes

Supervisor:

Dr. József Uj

Associate Professor

Department of Applied Mechanics

Budapest University of Technology and Economics

Budapest, Hungary

March, 2005



**BUDAPESTI MŰSZAKI ÉS GAZDASÁGTUDOMÁNYI EGYETEM
GÉPÉSZMÉRNÖKI KAR**

Szerző neve: Szekrényes András

Értekezés címe: Delamination of Composite Specimens

Témavezető neve (ha volt): Dr. Uj József

Értekezés benyújtásának helye (Tanszék, Intézet): Műszaki Mechanikai Tanszék, BME

Dátum: 2005. március 30.

Bírálok:

Javaslat:

1. bíráló neve

nyilvános vitára igen/nem

2. bíráló neve

nyilvános vitára igen/nem

3. bíráló neve (ha van)

nyilvános vitára igen/nem

A bíráló bizottság javaslata:

Dátum:

**(név, aláírás)
a bíráló bizottság elnöke**

NYILATKOZAT

Alulírott Szekrényes András kijelentem, hogy ezt a doktori értekezést magam készítettem és abban csak a megadott forrásokat használtam fel. Minden olyan részt, amelyet szó szerint, vagy azonos tartalomban, de átfogalmazva más forrásokból átvettem, egyértelműen, a forrás megadásával megjelöltem.

Az értekezés bírálatai és a védésről készült jegyzőkönyv a védést követően a Budapesti Műszaki és Gazdaságtudományi Egyetem Gépészmérnöki Kar Dékáni Hivatalában lesznek elérhetőek.

Budapest, 2005. március 30.

Szekrényes András

KOMPOZIT PRÓBATESTEK RÉTEGKÖZI TÖRÉSE

Összefoglaló

A rétegek közötti törés problémája egyaránt vizsgálható analitikusan, véges elem módszerrel és kísérletek segítségével. Az analitikus modellek rúd- és lemezelméleteken alapulnak. A lineárisan rugalmas törésmechanika legfontosabb mennyiségei a rendszer rugóállandója és a repedésfeszítő erő (repedésterjesztő erő, fajlagos energia-fel szabadulási ráta). A repedésfeszítő erő, valamint vegyes (I/II-es) mód esetén I-es és II-es módú komponenseinek és a módok arányának meghatározása fontos gyakorlati feladat.

Az értekezés célja új analitikus és kísérleti eredmények bemutatása kompozit törésmechanikai próbatestek felhasználásával.

A dolgozat első fejezetében ismertetem a kutatási célokat. A második fejezet a kutatómunka során feldolgozott és felhasznált szakirodalom áttekintésével foglalkozik.

A harmadik fejezetben az elsődleges kutatási cél megvalósítása történik. Ebben egy javított analitikus modell kifejlesztését mutatom be lineáris rúd elméletek felhasználásával. Az *Euler-Bernoulli* rúd elmélet mellett a *Winkler-Pasternak*-féle rugalmas ágyazás, a *Timoshenko* rúd elmélet, az ún. *Saint-Venant* féle hatás és a repedés csúcs nyírási deformációjának elvét használok fel egy középsíkban repedéssel ellátott általános terhelésű kompozit rúd rúgóállandójának kiszámításához. A repedésfeszítő erő komponenseit az ún. globális módszer segítségével határozom meg.

A negyedik fejezetben a kifejlesztett modell eredményeit publikált analitikus és numerikus modellek eredményeivel hasonlítom össze. Az eredmények szemléltetése szakirodalomban jól ismert és napjainkban is alkalmazott próbatest típusok felhasználásával történik.

A dolgozat ötödik fejezetében a kifejlesztett modell alkalmazhatóságát kísérletek segítségével igazolom. A kísérleti munkát saját gyártású, egyirányú, üvegszál erősítésű poliészter próbatestek segítségével végzem el. A kísérleti munka során II-es és vegyes I/II-es terhelésű próbatesteket használok fel. A felhasznált vegyes módú próbatestek azonban nem alkalmasak a repedésterjedés vizsgálatára. Az ötödik fejezet végén bemutatom egy meglévő próbatest típus módosított változatát, mely az említett nehézséget kiküszöböli. Az új típusra a kifejlesztett analitikus modell alapján a rugóállandó és a repedésfeszítő erő képleteit is megadom.

A hatodik fejezet az ún. száláthidalási jelenség analitikus-kísérleti vizsgálatát mutatja be, amely során egy olyan módszert ismertetek, amely alkalmas az áthidaló szálak számának és a szálakban ébredő erőnek a becslésére I-es módú próbatest esetén.

Az analitikus és kísérleti eredményeket a hetedik fejezetben foglalom össze, illetve egészítem ki olyan megállapításokkal, amelyek segítik a bemutatott eredmények értelmezését és hasznosítását.

A dolgozat végén hat tézis fogalmazok meg, melyeket az analitikus és kísérleti eredmények alapján állítok össze, az eredmények alkalmazásának lehetőségeit szintén megadom.



DELAMINATION OF COMPOSITE SPECIMENS

András Szekrényes

ABSTRACT

The primary objective of the present thesis is to develop an improved delamination model incorporating linear beam theories. The application of the *Euler-Bernoulli* beam theory is essential. Apart from that the *Winkler-Pasternak* (two-parameter) elastic foundation, *Timoshenko* beam theory, *Saint-Venant* effect and the concept of crack tip shear deformation are adopted in this work. All these theories are used to calculate the total strain energy release rate when a general mixed-mode I/II condition is involved. The mode-mixity analysis is performed by means of WILLIAMS' global method. The beam theory-based solution is compared to existing analytical and numerical solutions. On the other hand existing mode-II and mixed-mode I/II test configurations are used to confirm the applicability of the present solution.

A novel mixed-mode I/II configuration is developed, to which the present analytical solution is applied and experimental results are presented.

Finally, a beam theory-based combined analytical-experimental method is developed to study the fiber-bridging effect in unidirectional double-cantilever beam specimens. The new technique is suitable to estimate the number of bridgings and the bridging force.

The results are completed with comparison of the experimental results with published data and also the fracture envelope of the used material is constructed.

Keywords: *damage, fiber-reinforced composite, delamination, fracture mechanics, experiment, linear beam theory*

ACKNOWLEDGEMENT

This thesis was supported by the Hungarian Scientific Research Fund (OTKA T037324).

I am grateful to my Supervisor Dr. József Uj (Associate Professor) for his valuable helps during the last four years and to Dr. Gábor Stépán (Professor, Head of Department) for his enormous encouragement and support in my Ph.D. education.

Also, I am grateful to my father for his patience in manufacturing the tools for the specimen preparation and the experiments.

NOMENCLATURE

4ENF	- 4-point bend end-notched flexure	I_{y1}^l	- Second order moment of inertia, lower arm, cracked region
a	- Crack length	I_{y2}^u	- Second order moment of inertia, upper beam element, uncracked region
a_0	- Initial crack length	I_{y2}^l	- Second order moment of inertia, lower beam element, uncracked region
a^*	- Measured crack length	J	- J -integral
$a^\#$	- Characteristic length	k	- Shear correction factor
Δa	- Virtual crack extension	K_1	- Shear compliance, upper beam element, uncracked region
a_{55}	- Transverse shear compliance	K_2	- Shear compliance, lower beam element, uncracked region
ADCB	- Asymmetric double-cantilever beam	k_e	- <i>Winkler</i> -type foundation stiffness
b	- Specimen width	k_G	- <i>Pasternak</i> -type foundation stiffness
c	- Length of the uncracked region	$L, 2L$	- Length of the specimen
c^*	- Lever length of the MMB specimen	LEFM	- Linear elastic fracture mechanics
C	- Compliance	MMB	- Mixed-mode bending
CC	- Compliance calibration	MMF	- Mixed-mode flexure
CBT	- Corrected beam theory	ν_{13}	- Poisson ratio
CLS	- Cracked-lap shear	OLB	- Over-leg bending
DBT	- Direct beam theory	ONF	- Over-notched flexure
DCB	- Double-cantilever beam	P	- Applied load
DENF	- Double end-notched flexure	P_C	- Critical load
d_{11}	- Bending compliance	Π	- Potential energy
δ	- Displacement at the load application	s	- Position of the applied load
δ_C	- Critical displacement	SCB	- Single-cantilever beam
δ^*	- Displacement at the initial crack tip	SENF	- Stabilized end-notched flexure
E_{11}	- Flexural modulus	SERR	- Strain energy release rate
E_{33}	- Transverse elastic modulus	SLB	- Single-leg bending
ELS	- End-loaded split	SLFPB	- Single leg four point bend
ENF	- End-notched flexure	TDCB	- Tapered double-cantilever beam
FE	- Finite element	TENF	- Tapered end-notched flexure
FEM	- Finite element method	U	- Strain energy
f_{SH1}, f_{SH2}	- Correction from crack tip deformation	VCCT	- Virtual crack-closure technique
f_{SV}	- Correction from <i>Saint-Venant</i> effect	VMM	- Variable mixed-mode
f_T	- Correction from transverse shear	$w_{u1}(x)$	- Deflection of the upper arm
f_{W1}, f_{W2}	- Correction from <i>Winkler-Pasternak</i> foundation	$w_{l1}(x)$	- Deflection of the lower arm
G_{13}	- Shear modulus	$w_{u2}(x)$	- Deflection of the upper beam element, uncracked region
G_C	- Critical strain energy release rate	$w_{l2}(x)$	- Deflection of the lower beam element, uncracked region
G_{IC}	- Mode-I critical strain energy release rate	$w_2(x)$	- Deflection of the uncracked region
G_{IIC}	- Mode-II critical strain energy release rate	WIF	- Wedge insert fracture
G_{IIIC}	- Mixed-mode I/II critical strain energy release rate	WTDCB	- Width tapered double-cantilever beam
h	- Half of the specimen thickness		
I_{y1}^u	- Second order moment of inertia, upper arm, cracked region		

TABLE OF CONTENTS

1 INTRODUCTION	1
1.1 BACKGROUND	1
1.2 RESEARCH OBJECTIVES	2
2 LITERATURE REVIEW	3
2.1 DELAMINATION SPECIMENS.....	3
2.1.1 Mode-I fracture specimens	3
2.1.2 Mode-II fracture specimens	3
2.1.3 Mixed-mode I/II fracture specimens.....	7
2.2 BEAM MODELS FOR FRACTURE SPECIMENS.....	10
2.2.1 The mode-I DCB specimen	10
2.2.2 Solutions for mode-II specimens	10
2.2.3 Solutions for mixed-mode I/II specimens.....	12
2.3 MODE PARTITIONING.....	12
2.3.1 Analytical methods	12
2.3.2 Numerical methods	13
2.3.3 Agreement and disagreement.....	15
2.4 DIRECT DATA REDUCTION	15
2.4.1 Compliance calibration (CC) method	15
2.4.2 Direct beam theory (DBT).....	16
2.4.3 Corrected beam theory (CBT)	16
2.4.4 Area method.....	16
2.5 FURTHER APPLICATION OF THE FINITE ELEMENT METHOD IN FRACTURE PROBLEMS.....	17
2.5.1 Macromechanical formulation.....	17
2.5.2 Micromechanical formulation.....	18
2.6 THE FIBER-BRIDGING PHENOMENON.....	20
3 IMPROVED SOLUTION FOR DELAMINATION SPECIMENS.....	22
3.1 <i>WINKLER-PASTERNAK</i> FOUNDATION ANALYSIS.....	22
3.2 <i>TIMOSHENKO</i> BEAM THEORY	25
3.3 <i>SAINT-VEENANT</i> EFFECT	27
3.3.1 <i>Saint-Venant</i> effect at the crack tip.....	28
3.3.2 <i>Saint-Venant</i> effect at the clamped end	30
3.4 CRACK TIP SHEAR DEFORMATION ANALYSIS	30
3.5 MODE-MIXITY ANALYSIS - GLOBAL METHOD	33
3.6 COMPLIANCE CALCULATION	35
3.7 DETERMINATION OF THE COEFFICIENT OF THE <i>PASTERNAK</i> FOUNDATION	36
3.8 CONCLUSIONS, SCIENTIFIC SIGNIFICANCE	37
4 COMPARISON WITH OTHER SOLUTIONS	38
4.1 ANALYTICAL SOLUTIONS	38
4.1.1 Beam theory-based solution I.....	38
4.1.2 Beam theory-based solution II.....	40
4.1.3 Solution based on numerical calibration.....	40

4.1.4 Solution based on a refined plate model	41
4.2. FINITE ELEMENT SOLUTION - VCCT METHOD	41
4.3 RESULTS	42
4.3.1 Compliance	43
4.3.2 Strain energy release rate	46
4.4 DISCUSSION	49
4.5 CONCLUSIONS, SCIENTIFIC SIGNIFICANCE	50
5 EXPERIMENTS	51
5.1 MODE-II CONFIGURATIONS	51
5.1.1 Experimental procedure	51
5.1.2 Data reduction	53
5.1.3 Crack stability and frictional effects	54
5.1.4 Results and discussion	55
5.2 MIXED-MODE I/II CONFIGURATIONS	62
5.2.1 Experimental procedure	62
5.2.2 Results and discussion	64
5.3 A NOVEL MIXED-MODE I/II CONFIGURATION: THE OLB TEST	67
5.3.1 Experimental procedure	67
5.3.2 Data reduction	68
5.3.3 Finite element analysis	69
5.3.4 Results and discussion	69
5.4 CONCLUSIONS, SCIENTIFIC SIGNIFICANCE	73
6 FIBER-BRIDGING ANALYSIS IN THE DCB SPECIMEN	74
6.1 BEAM ANALYSIS	74
6.2 EXPERIMENTS	78
6.3 TEST RESULTS	80
6.3.1 Crack initiation tests	80
6.3.2 Crack propagation tests	81
6.4 APPLICATION OF THE DEVELOPED BEAM MODEL	83
6.4.1 Compliance calculation	83
6.4.2 Bridging law computation	83
6.5 RESULTS AND DISCUSSION	84
6.6 APPLICATION GUIDELINE	87
6.7 CONCLUSIONS, SCIENTIFIC SIGNIFICANCE	87
7 SUMMARY OF THE RESULTS	89
7.1 GENERALIZATION OF THE COMPLIANCE OF DELAMINATED COMPOSITE BEAMS	89
7.2 THE CRITICAL LOAD AND DISPLACEMENT	90
7.3 COMPARISON OF THE SERR UNDER DIFFERENT LOADING CONDITIONS	92
7.4 FRACTURE ENVELOPE	94
7.5 CONCLUSIONS, SCIENTIFIC SIGNIFICANCE	96
THESES	97
APPLICATION AND UTILIZATION OF THE RESULTS	100

REFERENCES	i
APPENDICES.....	ix
APPENDIX A	ix
A.1 – Constant parameters, <i>Timoshenko</i> beam theory.....	ix
A.2 – Constant parameters, crack tip shear deformation.....	ix
A.3 – Determination of ω for the <i>Pasternak</i> foundation	ix
APPENDIX B – SPECIMEN PREPARATION.....	x
APPENDIX C – CLAMPING FIXTURE FOR THE ELS AND SCB TESTS.....	xiii
APPENDIX D – CRACK LENGTH CORRECTION	xiii
D.1 ELS specimen	xiii
D.2 SLB and SCB specimens	xiv
APPENDIX E – CRACK STABILITY CHARTS.....	xv
APPENDIX F.....	xvi
F.1 The generalized <i>Krylov</i> -functions	xvi
F.2 Constant parameters	xvi
F.3 Form of the system of equations.....	xvii

LIST OF FIGURES

Fig. 2.1. Three basic types of fracture modes.	4
Fig. 2.2. The mode-I double-cantilever beam specimen (a) and the classical elastic foundation model by KANNINEN (1973) (b).....	5
Fig. 2.3. Mode-II fracture specimens.	6
Fig. 2.4. Mixed-mode I/II test configurations – I.	8
Fig. 2.5. Mixed-mode I/II test configurations – II.	9
Fig. 2.6. Application of the principle of superposition.	11
Fig. 2.7. Parameters for the J -integral.	13
Fig. 2.8. FE mesh for the virtual crack-closure technique (VCCT). Two-dimensional model (a), three-dimensional model (b).	14
Fig. 2.9. Schematic load/displacement curve for the area method.....	16
Fig. 2.10. SHELL/3D modeling technique for delamination in composite specimens.....	18
Fig. 2.11. Macro- and micromechanical FE models for interlaminar fracture investigation...	19
Fig. 2.12. Fiber-bridging in glass/polyester DCB specimen.	20
Fig. 3.1. Two-parameter elastic foundation model.	22
Fig. 3.2. A general loading scheme for <i>Timoshenko</i> beam theory.	26
Fig. 3.3. <i>Saint-Venant</i> effect under pure mode-I (a) and pure mode-II (b). <i>Saint-Venant</i> effect at the clamped end (c).....	28
Fig. 3.4. Deformation of the crack tip due to <i>Saint-Venant</i> effect.	29
Fig. 3.5. Loading scheme for the crack tip deformation analysis.	30
Fig. 3.6. Reduction scheme for mixed-mode partitioning.....	34
Fig. 4.1. Mixed-mode I/II delamination specimens.	38
Fig. 4.2. Details of the FE mesh around the crack tip and boundary conditions.	42
Fig. 4.3. Comparison of the compliance of the SCB (a) and SLB (b) specimens.....	43
Fig. 4.4. Comparison of the compliance of the MMB specimen. Present solution (a), solution by BRUNO and GRECO, 2001 (b), solution by CARLSSON, 1986 – OLSSON, 1992 (c).	44
Fig. 4.5. Comparison of the mode-I (a) and mode-II (b) energy release rate for the SCB specimen.	45
Fig. 4.6. Comparison of the mode-I (a) and mode-II (b) energy release rate for the SLB and MMB specimens.....	46
Fig. 5.1. Mode-II delamination specimens.....	51
Fig. 5.2. End-loaded split (a) and over-notched flexure (b) tests for mode-II interlaminar fracture.....	52
Fig. 5.3. Load/displacement curves up to fracture initiation, ELS test (a), ONF test (b).	56
Fig. 5.4. Measured and calculated compliance from initiation tests, ELS specimen (a), ONF specimen (b).	57
Fig. 5.5. Values of the SERR against the crack length, initiation tests. ELS specimen (a), ONF specimen (b).	58
Fig. 5.6. Load/displacement curves from ONF propagation tests.....	59
Fig. 5.7. Measured and calculated compliance from propagation test of one ONF specimen.	60

Fig. 5.8. SERR against the crack length by different methods, ONF test. Compliance calibration (a), direct beam theory (b), beam theory (c).....	61
Fig. 5.9. The single-leg bending (a) and the single-cantilever beam (b) specimens for mixed-mode I/II interlaminar fracture testing.	62
Fig. 5.10. Load/displacement curves up to fracture initiation, SLB test (a), SCB test (b).....	63
Fig. 5.11. Compliance against the crack length, SLB (a), SCB (b) specimen.	64
Fig. 5.12. Values of the initiation SERR against the crack length, SLB (a), SCB (b) specimen.	65
Fig. 5.13. Free-body diagram of the over-leg bending coupon.	67
Fig. 5.14. Over-leg bending test configuration.	68
Fig. 5.15. Load/displacement traces up to fracture initiation, OLB test.	70
Fig. 5.16. Values of the compliance (a) and the SERR (b) against the crack length, OLB test.	70
Fig. 5.17. Load/displacement traces from the propagation test of six OLB specimens.....	71
Fig. 5.18. SERR under crack propagation from the measurement of two OLB specimens. CC method (a), beam theory (b).	72
Fig. 6.1. For the analysis of the fiber-bridging in the DCB specimen.	74
Fig. 6.2. A general case for asymmetrical fiber-bridging.	76
Fig. 6.3. Experimental setup for DCB testing.	78
Fig. 6.4. Length of the bridged zone at different crack lengths.	79
Fig. 6.5. Load/displacement curves (a), measured and calculated compliance (b) from initiation tests.....	80
Fig. 6.6. Load/displacement (a) curve and compliance curves (a) from propagation tests.....	81
Fig. 6.7. G_I - a data from the propagation test of six specimens (a). Initiation and propagation R-curves, comparison between experiment and analysis (b).	82
Fig. 6.8. Compliance calculated from the present beam model (a). The total bridging force (a) and the total number of bridging fibers (c) against the displacement at the initial crack tip. ..	85
Fig. 6.9. G_I - δ^* curves from experiment and beam analysis (a). Experimental bridging law (b). Analytical bridging law from <i>average stress</i> and <i>J-integral</i> approach (c).	86
Fig. 7.1. The values of the critical load (a) and displacement (b) against the crack length in the case of the DCB, ELS and SCB specimens.	90
Fig. 7.2. The values of the critical load (a) and displacement (b) against the crack length in the case of the ONF, SLB and OLB specimens.	91
Fig. 7.3. Interlaminar fracture envelopes for unidirectional glass/polyester composite under crack initiation (a) and crack propagation (b).	95
Fig. A1. FE model of the DCB specimen for the determination of ω	ix
Fig. B1. Workbench for unidirectional specimen preparation.	xi
Fig. B2. Pressure tool for unidirectional specimens, assembled state (a), front view (b), exploded view (c).	xii
Fig. B3. Unidirectional composite carbon/epoxy (a), glass/epoxy (b), glass/vinylester (c) and glass/polyester (d) specimens.	xii
Fig. C1. Details of the clamping fixture, exploded view (a), assembled state (b).	xiii
Fig. D1. Correction of the ELS system.	xiv
Fig. D2. Correction of the SLB (a) and SCB (b) systems.	xiv
Fig. E1. The crack stability charts of the ELS (a) and ONF (b) specimens.....	xv

LIST OF TABLES

Table 4.1. Mode ratios (G_I/G_{II}) by different methods, SCB specimen.	47
Table 4.2. Mode ratios (G_I/G_{II}) by different methods, SLB specimen.	47
Table 4.3. Mode ratios (G_I/G_{II}) by different methods, MMB specimen.	48
Table 4.4. Comparison of the total SERR ($G_{III}/G_{III,EB}$) by different methods, SLB and SCB specimens.	49
Table 4.5. Comparison of the total SERR ($G_{III}/G_{III,EB}$) by different methods, MMB specimen.	49
.....	
Table 5.1. Comparison of the results by the FE and beam models, ELS specimen.	56
Table 5.2. Comparison of the results by the FE and beam models, ONF specimen.	57
Table 5.3. Compliances and SERRs by beam analysis, SLB specimen.	66
Table 5.4. Compliances and SERRs by beam analysis, SCB specimen.	67
Table 5.5. Comparison of the results by the FE and beam models, OLB specimen.	69
.....	
Table 7.1. Contribution of the various theories and effects to the compliance of delaminated composite beams with midplane crack in explicit form.	89
Table 7.2. Interlaminar fracture energy (G_C -[J/m ²]) values by experimental initiation tests.	93
Table 7.3. Interlaminar fracture energy (G_C -[J/m ²]) values by experimental propagation tests.	93
.....	
Table A1. Corrections for the SERR of the DCB specimen from <i>Winkler-Pasternak</i> elastic foundation if $G_{I3}=100\ 000$ GPa and $\omega=2.5$	x

1 INTRODUCTION

1.1 Background

The composite materials exhibit extremely good strength to weight ratio. Therefore, the composites are being used more and more in the construction of:

- vehicles (helicopters, trucks, racing cars) and equipment for the military
- sport equipments (crash-helmets, pole vault, bicycle frameworks and wheels)
- buildings, roof structures and bridges
- air- and spacecrafts
- fuel tanks and pressure vessels, etc.

The composites are heterogeneous materials, which is an important feature compared for instance to the metals and homogeneous plastics. There are many kinds of failure and damage modes in the composite structures (PHILLIPS, 1989; TSAI, 1992). One of them is the interlaminar fracture (or known as the delamination), which is, at the same time one of the most important failure mode.

The interlaminar fracture of composite materials has been very intensively investigated since the late 1970's. The delamination means degradation between adjacent plies of the material. The composite materials exhibit superior properties only in the fiber direction, hence the delamination of composite structures results in a significant loss of the stiffness and strength. Thus, it is apparent that this failure mode should be identified. There are fracture criterions, which are based on different considerations in order to identify the damage in the material. On the one hand the stress-based criterions may be mentioned, which determine a failure index, of which critical value is equal to unity. At the first stage these types of criterions predicted a general failure index (*Tsai-Wu*, *Tsai-Hill*, (TSAI, 1992)), but the type of the failure mode was not possible to be determined. Later, this void was addressed and several criterions were proposed, which were able to separate certain failure modes (*maximal stress* criterion (WANG et al., 1999), *Hashin-Rotem* criterion (WANG et al., 1999), *Chang-Chang* criterion (HOU et al., 2001; SZEKRÉNYES, 2002b)). In general, the application of these criterions is not apparent in the neighborhood of crack tips where a singular stress field exists. On the other hand the energy-based criterions may be referred to. *Griffith* was the first to make a quantitative connection between strength and crack size (BROEK, 1982; KANNINEN and POPELAR, 1985). Later, *Irwin* and *Rice* (KANNINEN and POPELAR, 1985) made remarkable efforts to contribute to the fracture mechanics. According to the *Griffith-Irwin* linear elastic fracture mechanics (LEFM) approach the cracked body is essentially linear elastic. The crack initiation and propagation is governed by the critical strain energy release rate (SERR) or the stress intensity factor, however there is competing names in the literature to identify this quantity, such as: fracture energy, fracture work, fracture toughness, work of fracture, etc. A remarkable feature is that *Griffith's* criterion is suitable to handle the singularity nature of the problem. According to *Griffith's* formulation (BROEK, 1982; KANNINEN and POPELAR, 1985) the energy release rate is the change in the potential energy Π of the linear elastic system with respect to the crack length a :

$$G_C = -\frac{1}{b} \frac{dII}{da}. \quad (1.1)$$

Crack initiation or propagation may be expected if the energy release rate reaches the critical value, i.e: $G=G_C$. For the determination of G_C some experimentally recorded quantities, such as critical displacement and load is necessary. Eq. (1.1) may be transformed as (BROEK, 1982):

$$G_C = \frac{P^2}{2b} \frac{dC}{da}, \quad (1.2)$$

where P is the external force, b is the width of the delamination, C is the compliance and a is the crack length. Eq. (1.2) is known as the *Irwin-Kies* expression.

1.2 Research objectives

The objective of this thesis is to develop improved solution for delamination modeling of composite beams. The following features are included:

- Calculation of the compliance and strain energy release rate of delaminated composite beams under a general loading condition by using linear beam theories.
- Mode-mixity analysis incorporating the global mode decomposition method.
- Validation of the model by existing numerical and analytical solutions.
- Application of the developed model to few delamination specimens and verification of the developed model by experiments.
- Development of a novel mixed-mode I/II interlaminar fracture test and derivation of the compliance and strain energy release rate incorporating the developed model.
- Development of a combined analytical-experimental method for fiber-bridging modeling.
- Construction of the fracture envelopes for glass/polyester composite

To solve the above-mentioned problems the theory of elasticity, linear beam theories, variational methods, the concepts of linear elastic fracture mechanics and the concepts of differential equations are applied.

The derivation of the formulae is performed by using the code MAPLE. The COSMOS/M 2.0 package is applied to construct finite element models, which were used to validate the analytical expressions.

One of the most important validation techniques is the experimental method, which is essential in the case of composite materials.

2 LITERATURE REVIEW

The increasing application of composite materials in the practice encouraged the researchers to determine the energy release rate with higher and higher accuracy. The problem may be equally investigated analytically, numerically and experimentally. In fact, the delamination problems may be related to crack problems. In the literature three basic forms of the failure in cracks are known (see Fig. 2.1): the mode-I (opening mode), mode-II (in-plane shearing mode) and mode-III (anti-plane shearing or tearing mode) fracture (KANNINEN and POPELAR, 1985). In the practice any combination of these may occur. In the present work our attention is equally focused on mode-I, mode-II and mixed-mode I/II fracture problems, but the investigation of the third mode is outside the scope of this thesis.

2.1 Delamination specimens

For the characterization of the interlaminar fracture the principles of the LEFM have been extended also for composite materials (PHILLIPS, 1989). Similarly to the metals and plastics the failure process in composites is investigated by using different type of specimens. The main feature is that they exhibit an artificial defect, which is called the crack. Some of the fracture specimens were standardized by the American Society for Testing and Materials (ASTM), the International Standards Organization (ISO), the European Structural Integrity Society (ESIS) and the Japanese Industrial Standards Group (JIS).

2.1.1 Mode-I fracture specimens

For mode-I delamination the double-cantilever beam (DCB) specimen (Fig. 2.2) is a useful and well-understood tool (ASTM D5528, ISO/DIS 15024) to measure the mode-I fracture properties of composite materials. Both arms of the coupon are loaded by edge force, causing pure mode-I fracture (see Fig. 2.2a). The DCB specimen is the subject of numerous works. Consequently, a very large amount of theoretical and experimental results are available in the literature (e.g.: HASHEMI, 1990a and 1990b; SCHÖN et al., 2000; MORAIS et al., 2002) as regarding to the DCB specimen. The DCB coupon was modified by some authors, see for example the wedge-insert fracture (WIF) specimen (KUSAKA et al., 1998), the width tapered DCB (WTDCB) test (LEE, 1986) or the (height) tapered DCB (TDCB) specimen (QIAO et al., 2003a).

2.1.2 Mode-II fracture specimens

For mode-II testing six specimens are available for fracture testing, four of them are shown in Fig. 2.3. First, the end-notched flexure (ENF, Fig. 2.3a) specimen (RUSSEL and STREET, 1985; CARLSSON et al., 1986) was developed, however it has a major drawback, namely the crack propagation can not be investigated due to the crack stability problem.

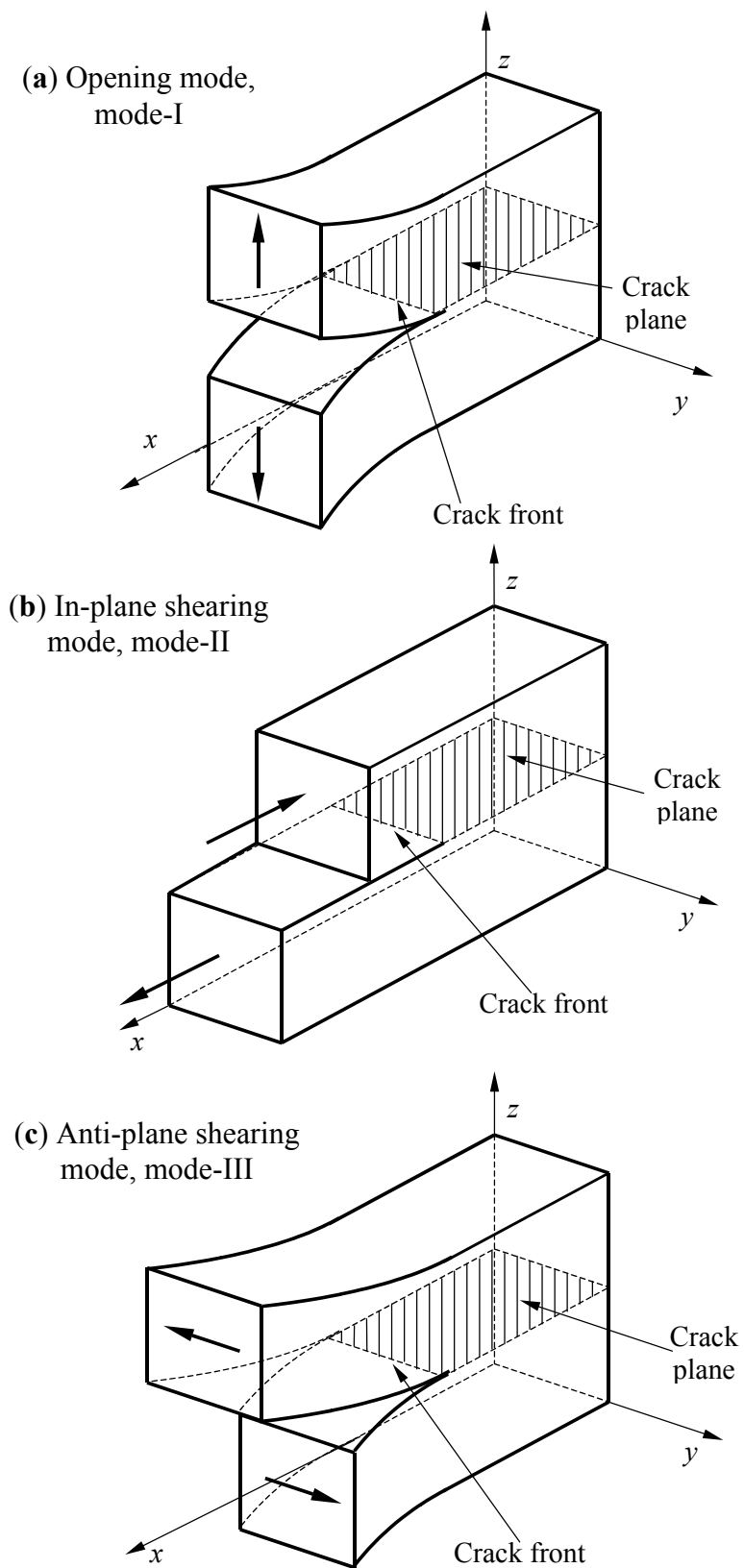


Fig. 2.1.
Three basic types of fracture modes.

Later, to overcome the problem of instability the stabilized end-notched flexure (SENF) test was proposed on a control system of the crack opening displacement (DAVIES et al., 1996). The mode-II end-loaded split (ELS) specimen (Fig. 2.3b) was utilized by other researchers (WANG and WILLIAMS, 1992; WANG et al., 1996). Although it is suitable for crack propagation investigation, the problem of crack stability still remained and apart from that large displacements often occur during testing, which is another disadvantage of this setup. This motivated those researchers, who developed the four-point bend end-notched flexure (4ENF, Fig. 2.3c) configuration (see for example SCHUECKER and DAVIDSON, 2000; DAVIES et al., 2004). The crack propagation is possible to be examined and the large displacements are eliminated. The ENF setup was slightly modified by others and the over-notched flexure (ONF, Fig. 2.3d) test was introduced (TANAKA et al., 1998; WANG et al., 2003). The main advantage of the latter was, in contrast with the 4ENF test, that it may be performed using a simple three-point bending setup. The tapered ENF (TENF) specimen was developed by QIAO et al. (2003b), which is an efficient way for mode-II toughness measurements. The main advantage of this configuration is that in the case of a proper specimen design the compliance rate change (dC/da) is independent of the crack length, and the strain energy release rate is constant during crack propagation. This is important when the crack length is difficult to be measured, for example in carbon-fiber reinforced composites.

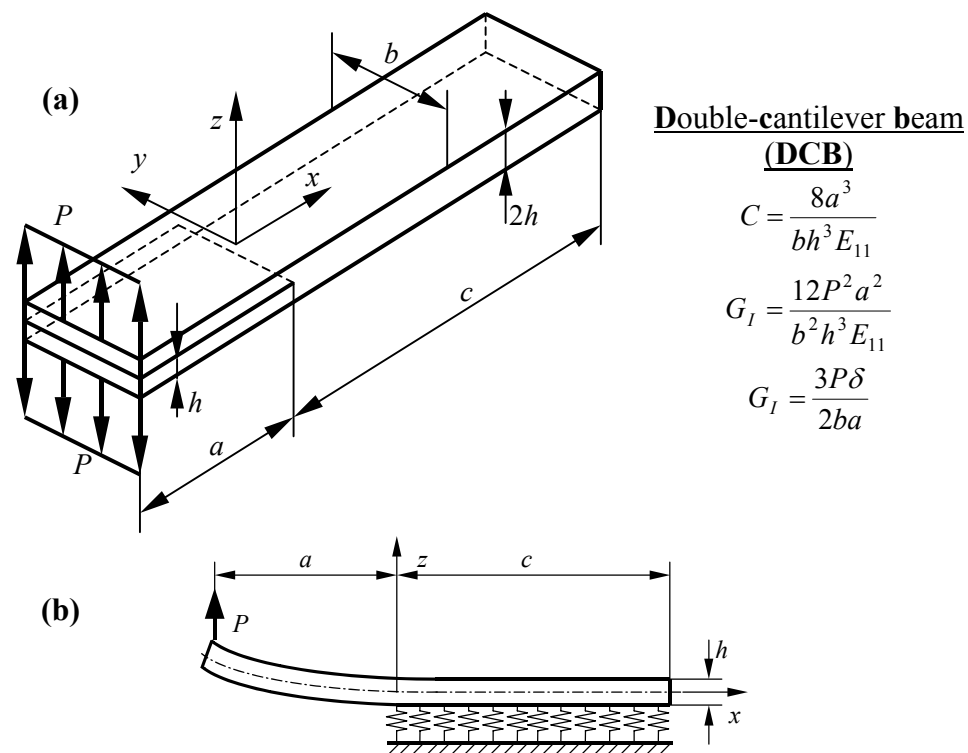
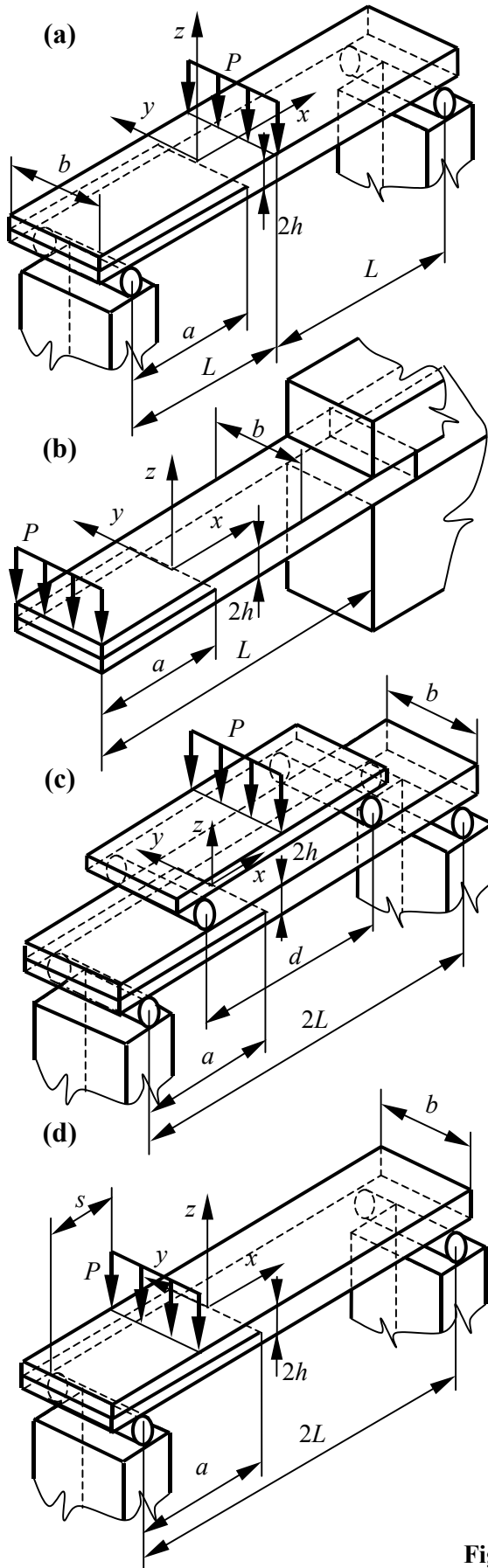


Fig. 2.2.

The mode-I double-cantilever beam specimen (a) and the classical elastic foundation model by KANNINEN (1973) (b).



End-notched flexure (ENF)

$$C = \frac{3a^3 + 2L^3}{8bh^3 E_{11}}, G_{II} = \frac{9P^2 a^2}{16b^2 h^3 E_{11}}$$

$$G_{II} = \frac{9a^2 P \delta}{2b(3a^3 + 2L^3)}$$

advantages: simple fixture, simple coupon geometry, simple closed-form solution

drawbacks: crack stability problem, only initiation toughness, longitudinal sliding

End-loaded split (ELS)

$$C = \frac{3a^3 + L^3}{2bh^3 E_{11}}, G_{II} = \frac{9P^2 a^2}{4b^2 h^3 E_{11}}$$

$$G_{II} = \frac{9a^2 P \delta}{2b(3a^3 + L^3)}$$

advantages: simple coupon geometry, simple closed-form solution, propagation toughness

drawbacks: clamping fixture, crack stability problem, large displacements

4-point end-notched flexure (4ENF)

$$C = \frac{(9a + 6d - 6L)(L - \frac{d}{2})^2}{8bh^3 E_{11}}$$

$$G_{II} = \frac{9(L - d/2)^2 P^2}{16b^2 h^3 E_{11}}$$

$$G_{II} = \frac{9P \delta}{2b(9a + 6d - 6L)}$$

advantages: simple coupon geometry, simple closed-form solution, propagation toughness, pure bending at the crack tip

drawbacks: complex fixture, longitudinal sliding

Over-notched flexure (ONF)

$$C = \frac{s^2 c^3}{8bh^3 E_{11} L^2} \theta, G_{II} = \frac{9P^2 s^2 c^2}{16b^2 h^3 E_{11} L^2}$$

$$G_{II} = \frac{9P \delta}{2b(2L - a) \theta}$$

$$\theta = [1 + 4 \frac{a}{c} + 8 \frac{aL}{c^2} + 16 \frac{aL^2}{c^3} + 8 \frac{Ls(s - 4L)}{c^3}]$$

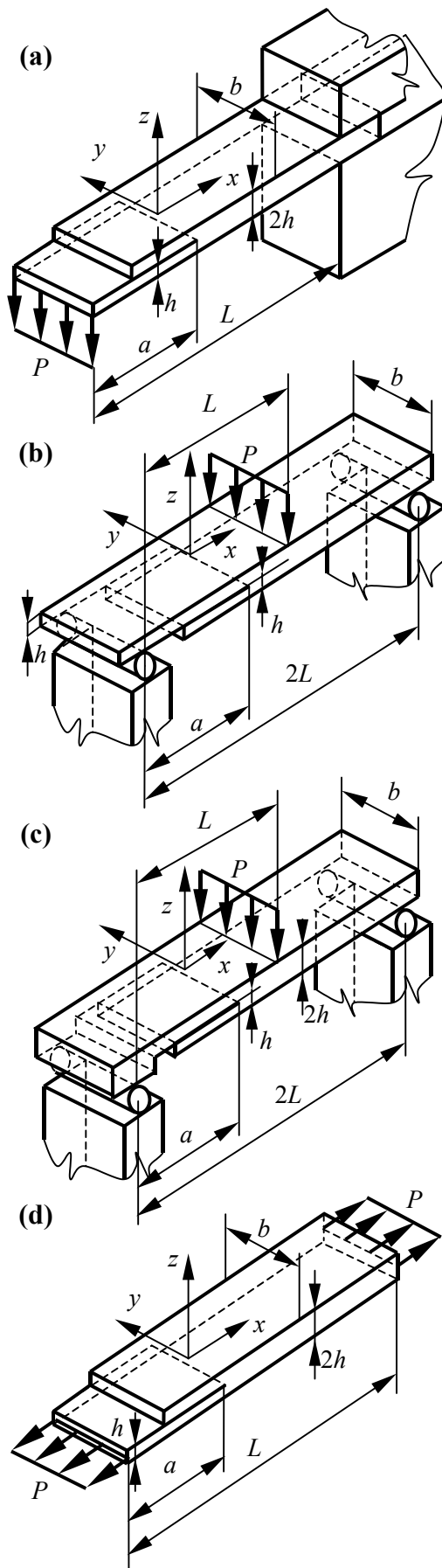
advantages: simple coupon geometry and fixture, simple closed-form solution, stable crack

propagation at any crack length
drawbacks: longitudinal sliding

Fig. 2.3.
Mode-II fracture specimens.

2.1.3 Mixed-mode I/II fracture specimens

The mixed-mode I/II fracture in composite materials has a major role in the development of delamination models. The reason for that is the mixed-mode I/II loading relates to practical conditions. Thus, it is straightforward that many mixed-mode setups were developed in the last three decades. Certain configurations were reviewed by REEDER and CREWS (1990), SUO (1990), TRACY and FERABOLI (2003) and SZEKRÉNYES (2002a). The most popular ones are compiled in Figs. 2.4 and 2.5. The single-cantilever beam (SCB, Fig. 2.4a) specimen allows the investigation of the crack propagation, however large displacements are possible during testing (HASHEMI et al., 1990a and 1990b). The single-leg bending (SLB, Fig. 2.4b) (YOON and HONG, 1990; DAVIDSON et al., 1996) and its twin brother, the mixed-mode flexure (MMF, Fig. 2.4c) (ALBERTSEN et al., 1995; ALLIX et al., 1998; KORJAKIN et al., 1998) setup may be performed in a three-point bending apparatus. Both setups produce linear elastic response, but the mode ratio can be varied only within a limited range. The cracked-lap shear (CLS, Fig. 2.4d) specimen was also an attempt to develop a many-sided configuration (LAI et al., 1996; ALLIX et al., 1998), however it is not too popular nowadays. Also, the double-end notched flexure (DENF, Fig. 2.5a) coupon may be referred to (REYES and CANTWELL, 2000). None of the mentioned configurations became an optimal solution. Thus, many efforts have been made to develop a mixed-mode I/II tool, which enables the variation of the mode-ratio. BRADLEY and COHEN (1985) proposed the asymmetric double-cantilever beam (ADCB, Fig. 2.5b) specimen. This involved loading the arms of the specimen with two different loads, which was possible only by using a complex loading system. HASHEMI and coworkers (1987) developed the variable mixed-mode (VMM) test. Due to the complications and certain disadvantages neither this one became a widely applied test. Then REEDER and CREWS (1990) introduced the mixed-mode bending (MMB, ASTM D6671-01, Fig. 2.5c) specimen, which became the most universal configuration (KENANE et al., 1997; CHEN et al., 1999). The reason for that is it allows the variation of the mode ratio, consequently a complete fracture envelope may be determined. Naturally, this setup has also relative drawbacks, as it is highlighted in Fig. 2.5c. Apart from that only a complex beam theory-based reduction technique can be applied, in contrast with the former setups (SCB, SLB, MMF), where the experimental data may be simply reduced. This leads to some complications in the case of multidirectional laminates due to the discrepancies between the predicted and manufactured bending and shear stiffnesses. Thus, the MMB specimen is mainly accepted for the testing of unidirectional composites. Due to this fact the development of different mixed-mode I/II setups is still in progress nowadays. SUNDARARAMAN and DAVIDSON (1997, 1998) developed the unsymmetric DCB and ENF configurations, both are mixed-mode I/II setups and some improved solutions were presented for these coupons. The single leg four point bend (SLFPB, Fig. 2.5d) test was introduced by TRACY and FERABOLI (2003), while SZEKRÉNYES and UJ (2004f) proposed the over-leg bending (OLB) specimen. A remarkable feature is that these are suitable for crack propagation investigation and the experimental data may be easily reduced.



Single-cantilever beam (SCB)

$$C = \frac{7a^3 + L^3}{2bh^3 E_{11}}, G_{I/II} = \frac{21P^2 a^2}{4b^2 h^3 E_{11}}$$

$$G_{I/II} = \frac{21a^2 P \delta}{2b(7a^3 + L^3)}$$

advantages: simple coupon geometry, simple closed-form solution, propagation toughness
drawbacks: clamping fixture, large displacements, mode ratio changes with crack length, different coupons are needed for different mode ratios

Single-leg bending (SLB)

$$C = \frac{7a^3 + 2L^3}{8bh^3 E_{11}}, G_{I/II} = \frac{21P^2 a^2}{16b^2 h^3 E_{11}}$$

$$G_{I/II} = \frac{21a^2 P \delta}{2b(7a^3 + 2L^3)}$$

advantages: simple coupon geometry and closed-form solution
drawbacks: mode ratio changes with crack length, different coupons are needed for different mode ratios

Mixed-mode flexure (MMF)

$$C = \frac{448a^3 + 121L^3}{64bh^3 E_{11}}, G_{I/II} = \frac{21P^2 a^2}{16b^2 h^3 E_{11}}$$

$$G_{I/II} = \frac{672a^2 P \delta}{b(448a^3 + 121L^3)}$$

advantages: simple coupon geometry and closed-form solution
drawbacks: mode ratio changes with crack length, different coupons are needed for different mode ratios

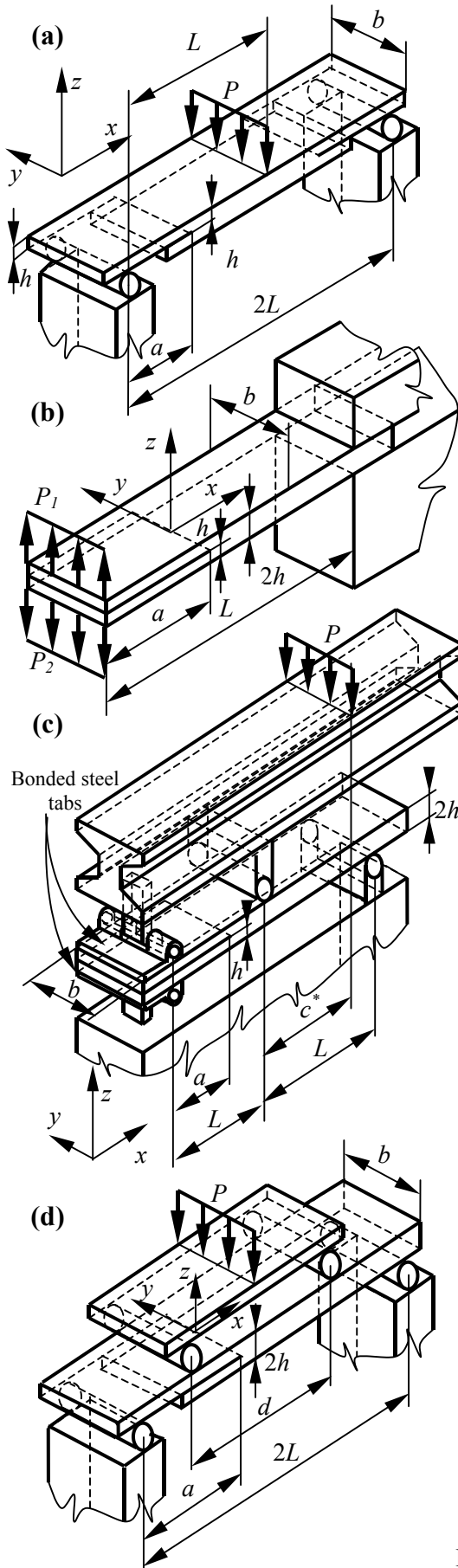
Cracked-lap shear (CLS)

$$C = \frac{a + L}{2bhE_{11}}, G_{I/II} = \frac{P^2}{4b^2 hE_{11}}$$

$$G_{I/II} = \frac{P \delta}{2b(a + L)}$$

advantages: simple coupon geometry, small crack opening displacement, constant mode ratio
drawbacks: nonlinear numerical analysis due to large rotations at the crack tip, different lay-ups are needed for different mode ratios

Fig. 2.4.
Mixed-mode I/II test configurations - I.



Double end-notched flexure (DENF)

$$C = \frac{7a^3 + L^3}{4bh^3 E_{11}}, \quad G_{I/II} = \frac{21P^2 a^2}{8b^2 h^3 E_{11}}$$

$$G_{I/II} = \frac{a^2 P \delta}{2b(7a^3 + L^3)}$$

advantages: simple fixture, simple coupon geometry, simple closed-form solution, propagation toughness

drawbacks: two cracks grow simultaneously at different rates, different coupon geometry needed for different mode ratios

Asymmetric double-cantilever beam (ADCB)

$$C_1 = \frac{7a^3 + L^3}{2bh^3 E_{11}} + \frac{(L^3 - a^3)P_2}{2bh^3 E_{11}P_1}$$

$$C_2 = \frac{7a^3 + L^3}{2bh^3 E_{11}} + \frac{(L^3 - a^3)P_1}{2bh^3 E_{11}P_2}$$

$$G_{I/II} = \frac{6a^2}{b^2 h^3 E_{11}} \left[P_1^2 + P_2^2 - \frac{(P_1 + P_2)^2}{8} \right]$$

advantages: simple coupon geometry, closed-form solution exists

drawbacks: requires complex fixture and bonded steel tabs, complex loading system

Mixed-mode bending (MMB)

$$C = \left(\frac{3c^* - L}{4L} \right)^2 \frac{8a^3}{bh^3 E_{11}} + \left(1 + \frac{c^*}{L} \right)^2 \frac{3a^3 + 2L^3}{8bh^3 E_{11}}$$

$$G_I = \frac{3P^2 a^2 (3c^* - L)^2}{4b^2 h^3 E_{11} L^2}, \quad G_{II} = \frac{9P^2 a^2 (c^* + L)^2}{16b^2 h^3 E_{11} L^2}$$

advantages: simple coupon geometry, variable mode ratio

drawbacks: complex fixture, bonded steel tabs, complex data reduction, questionable in multidirectional laminates

Single leg four point bend (SLFPB)

$$C = \frac{(21a + 10d - 14L)(L - d/2)^2}{8bh^3 E_{11}}$$

$$G_{I/II} = \frac{21(L - d/2)^2 P^2}{16b^2 h^3 E_{11}}$$

$$G_{I/II} = \frac{21P\delta}{2b(21a + 10d - 14L)}$$

advantages: simple coupon geometry, simple closed-form solution, pure bending at the crack tip, propagation toughness

drawbacks: slightly complex fixture, different coupon geometry needed for different mode ratios, longitudinal sliding

Fig. 2.5.

Mixed-mode I/II test configurations - II.

As a final word, we may establish that at present there is not an optimal mixed-mode I/II test. As a result of the many configurations developed by the researchers very large amount of experimental, analytical and numerical investigations were published in the literature.

2.2 Beam models for fracture specimens

Within the scope of the LEFM the interlaminar fracture specimens are treated as slender beams. To characterize the interlaminar fracture two major quantities may be determined: the compliance (C) and the strain energy release rate (G_C). In the early stages the *Euler-Bernoulli* beam theory was applied to derive closed-form solutions for the composite fracture specimens. Later, it was recognized that the result of simple beam theory may be improved in every cases.

2.2.1 The mode-I DCB specimen

The *Winkler*-type elastic foundation (see Fig. 2.2b) was applied first by KANNINEN (1973) to capture the crack tip deformation and rotation in the DCB specimen. The solution was extended by WILLIAMS (1989) for orthotropic materials. The compliance of the DCB specimen has the following form in accordance with WILLIAMS:

$$C_{DCB} = \frac{8a^3}{bh^3E_{11}} \left[1 + 1.92 \left(\frac{h}{a} \right) \left(\frac{E_{11}}{E_{33}} \right)^{\frac{1}{4}} + 1.22 \left(\frac{h}{a} \right)^2 \left(\frac{E_{11}}{E_{33}} \right)^{\frac{1}{2}} + 0.39 \left(\frac{h}{a} \right)^3 \left(\frac{E_{11}}{E_{33}} \right)^{\frac{3}{4}} \right]. \quad (2.1)$$

We may observe that the result of the simple beam theory (refer to the compliance expression in Fig. 2.2a) can be recovered from Eq. (2.1) by considering only the first term in the brackets. The combination of Eqs. (1.2) and (2.1) yields:

$$G_I = \frac{12Pa^2}{b^2h^3E_{11}} \left[1 + 1.28 \left(\frac{h}{a} \right) \left(\frac{E_{11}}{E_{33}} \right)^{\frac{1}{4}} + 0.41 \left(\frac{h}{a} \right)^2 \left(\frac{E_{11}}{E_{33}} \right)^{\frac{1}{2}} \right]. \quad (2.2)$$

Later, the solution became an international standard and numerous authors referred to it (OLSSON, 1992; LI, 1996; SZEKRÉNYES, 2003b). In fact the development of advanced beam and plate models for the DCB specimen did not reach to the end. OLSSON (1992) has made remarkable efforts to develop an improved beam model, namely the solution by WILLIAMS (1989) was completed with transverse shear (*Timoshenko* beam theory) and *Saint-Venant* effects. The compliance expression was obtained by the principle of superposition and it was compared with other analytical and numerical models. The solution by WILLIAMS was extended for angle-ply laminate DCB specimens by OZDIL and CARLSSON (1999a).

2.2.2 Solutions for mode-II specimens

To compose an improved solution for mode-II specimens the first attempt was made by CARLSSON et al. (1986), who applied the *Timoshenko* beam theory to capture shear effects

in the ENF specimen. Based on a singularity approach WHITNEY (1987) introduced another correction. These solutions were not satisfactory and only a small improvement was made. The elegant solution of WILLIAMS for the mode-I DCB specimen encouraged the researchers to develop similar closed-form expressions also in the case of mode-II specimens. CHATTERJE (1991) was the first who considered shear tractions at the crack tip of the ENF coupon. Several solutions were compared in his work. CORLETO and HOGAN (1995) assumed a similar solution to that developed by WILLIAMS in the case of the ENF coupon. Apart from that the work by DING and KORTSCHOT (1999) should be mentioned, in which they applied tangential springs along the uncracked region of the ENF specimen. Their solution resulted in a very complicated expression and, in particular it could not be applied directly. In 2004 WANG and QIAO (2004a) published a novel formulation of the problem of the ENF specimen. They have found that under mode-II condition the problem can not be captured by the same way as it may be in the case of mode-I problems. The reason for that is under mode-II condition there is no relative tangential displacement at the crack tip, consequently a displacement-based variational formulation can not be applied. Therefore, they determined the interlaminar shear stress field and based on beam and strength of materials analysis they obtained a reasonable correction for the ENF coupon. The accuracy of the correction was demonstrated by using models including wide range of composite material properties and was compared with finite element results. The agreement was found to be excellent and, apart from the elegant form, the solution may be easily extended for mixed-mode I/II specimens.

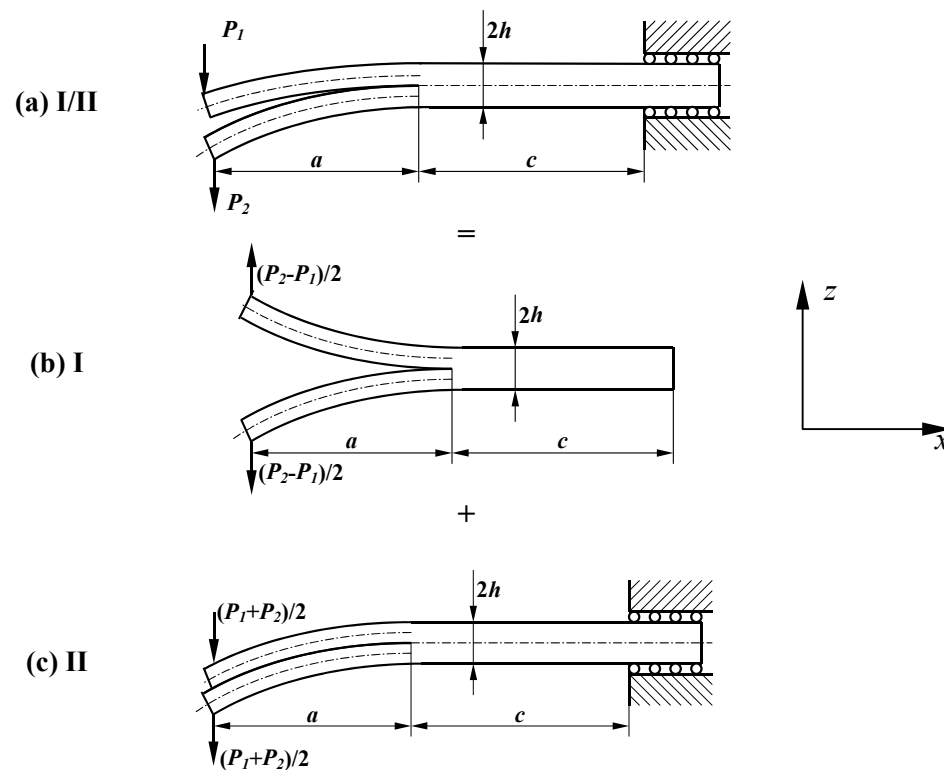


Fig 2.6.
Application of the principle of superposition.

2.2.3 Solutions for mixed-mode I/II specimens

While in the case of mode-I and mode-II specimens large amount of theoretical analyses were performed to develop improved solutions, for mixed-mode I/II coupons significantly less attempts were made to derive similar models. The reason for that is for mixed-mode I/II coupons, in general the principle of superposition is applied. This means that the solution is obtained as the sum of the mode-I and mode-II solutions, for example the mixed-mode SCB specimen is treated as the combination of the mode-I DCB and the mode-II ELS specimens (Fig. 2.6). REEDER and CREWS (1990) adopted the solution of WILLIAMS (1989, DCB specimen) and CARLSSON et al. (1986, ENF specimen) and an improved beam theory-based solution for the MMB specimen has been created. A quite similar analysis was carried out by OZDIL and CARLSSON (1999b) for the MMB specimen. Although the solutions were verified by experiments the extension of these solutions requires further work. This will be one of the major objectives of the current research work.

The application of the classical plate theory (CPT) results in similar equations to those based on *Euler-Bernoulli* beam theory. WHITNEY's (1985) plate solution for the DCB specimen is noteworthy. The plate theory is useful in the case of angle-ply laminate specimens, see for instance the works by DAVIDSON et al. (1995) for the SLB specimen and YANG and SUN (2000) for the ENF specimen.

2.3 Mode partitioning

Under mixed-mode I/II condition the separation of the total SERR (G_{III}) into the individual mode-I (G_I) and mode-II (G_{II}) components is an important issue. In the literature this problem is known as mode partitioning, mode separation, mode decomposition or mode-mixity analysis. Since this problem can not be solved experimentally the researchers are interested in developing analytical and numerical methods.

2.3.1 Analytical methods

The global method was developed by WILLIAMS (1988) based on simple beam theory. Although, this method is very simple and can be applied easily, later several authors showed that the global method is valid only in very particular circumstances (HUTCHINSON and SUO, 1992; BRUNO and GRECO, 2001a), namely when the delamination is symmetrically located in the beam thickness and the upper and lower layers have the same mechanical properties. SUO and HUTCHINSON (1990) proposed the local approach, which is based on a continuum model. The local method is more accurate than the global approach if the delamination is unsymmetrically located in the beam thickness. The local method was generalized for optional stacking sequence by SHEINMAN and KARDOMATEAS (1997). DAVIDSON and coworkers (1995b) proposed the crack tip element (CTE) analysis, but in fact it is equivalent to the local approach. The problem of mode-mixity was also addressed by BRUNO and GRECO

(2001a, 2001b), who applied *Reissner-Mindlin* plates bonded with linear elastic interface. Notable contribution from bending-shear interaction was found and it was shown that this effect (in midplane delaminations) improves only the mode-I component. In their work the mode components were calculated by the J -integral (RICE, 1968) by using the interlaminar stresses and displacements. The J -integral is equivalent to the strain energy release rate undergoing small strains and quasi-static conditions. The J -integral (Fig. 2.7) is defined as:

$$J = \int_{\Gamma} (Udz - \underline{T} \frac{\partial \underline{u}}{\partial x} ds), \quad (2.3)$$

where U is the strain energy, \underline{T} is the traction vector, \underline{u} is the displacement vector, Γ is an arbitrary contour starting from the lower crack face extending counterclockwise around the crack tip to a point on the upper crack face and ds is the differential element of arc Γ . The SERR expressions in Figs. 2.2-2.5 may also be determined by the help of the J -integral. Later, on the base of the works of BRUNO and GRECO (2001a, 2001b) the local method was improved with the effect of bending-shear interaction by WANG and QIAO (2004b) and the method was generalized for 3D problems too (WANG and QIAO, 2004c). Also, WANG and QIAO presented generalized solutions for bimaterial interfaces using the theory of elastic foundation and crack tip deformation (QIAO and WANG, 2004).

As a final word the global method is inaccurate in some cases, but the mode components may be easily evaluated, thus it is still popular in nowadays (DUCEPT et al., 1999; SZEKRÉNYES and UJ, 2004a). In contrast the local method is more complicated, since more equations are necessary for its application, but this method is more reliable in unsymmetrical cases.

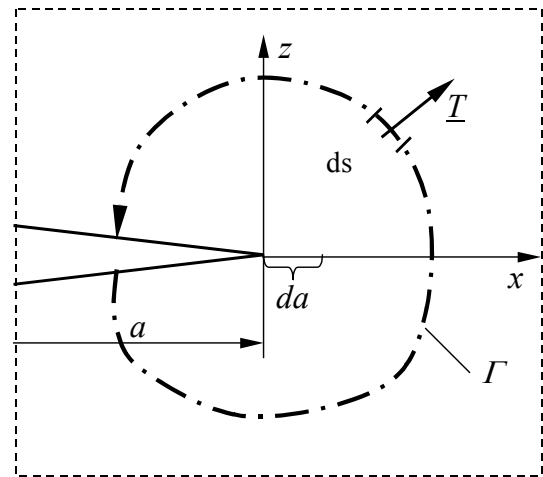


Fig. 2.7.
Parameters for the J -integral.

2.3.2 Numerical methods

The finite element method is also suitable for mode decomposition. The J -integral is usually available in the commercial finite element packages (ABAQUS, ANSYS, COSMOS/M, MARC, etc.). The J -integral may be applied equally using linear elastic and inelastic material models. Another numerical method is the virtual crack-closure technique (VCCT), which was proposed by RYBICKI and KANNINEN (1977). The energy release rate components may be calculated by using the nodal forces and displacements at the crack tip. For a 2D FE model (Fig. 2.8a) the energy release rate components are:

$$G_I = \frac{1}{2b\Delta a} F_{z1}(w_2 - w_3), \quad (2.4)$$

$$G_{II} = \frac{1}{2b\Delta a} F_{x1}(u_2 - u_3), \quad (2.5)$$

where F_z and F_y are nodal forces at the crack tip, w_1 , w_2 , u_1 and u_2 are nodal displacements from Δa distance to the crack tip and b is the specimen width. In the case of the 3D problem in Fig. 2.8b the energy release rate can be computed using the following equations (ZHAO and WANG, 1998):

$$G_I = \frac{1}{2\Delta x\Delta y} F_{z1}(w_2 - w_3), \quad (2.6)$$

$$G_{II} = \frac{1}{2\Delta x\Delta y} F_{y1}(v_2 - v_3), \quad (2.7)$$

$$G_{III} = \frac{1}{2\Delta x\Delta y} F_{x1}(u_2 - u_3), \quad (2.8)$$

where the relevant displacement, force and geometrical parameters are given in Fig. 2.8b. This method has also relative merits and drawbacks. First of all, it is suitable to handle 3D

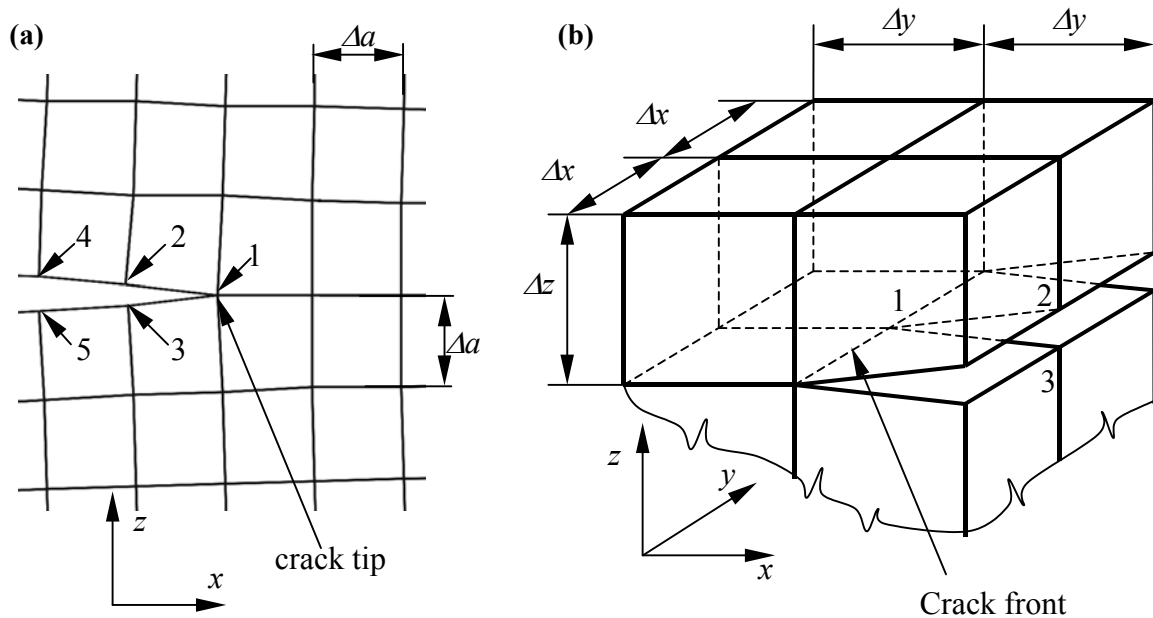


Fig. 2.8.

FE mesh for the virtual crack-closure technique (VCCT). Two-dimensional model (a), three-dimensional model (b).

problems (KRUEGER, 1999; ZHAO and WANG, 1998). Another important feature is that it may be applied for bimaterial interfaces. Although many works reported that the computation is more or less accurate (e.g.: RAJU et al., 1988), others (e.g.: SHEINMANN and KARDOMATEAS, 1997) have shown that the convergence of the solution is not guaranteed, because the results are sensitive to the number and size of the finite elements around the crack tip. Moreover, the mesh refinement in the crack tip neighborhood involves the increase in the mode-II component. Finally, there is not a general consensus considering the size of the virtual crack extension, Δa (refer to Fig. 2.8). Later, the VCCT was slightly modified, consequently other names, such as modified crack-closure integral (MCCI - DUCEPT et al., 1999) and modified

virtual crack-closure technique (MVCCT - YANG and SUN, 2000) are accepted in the literature. Also, the VCCT is applicable in dynamic problems, but only in the case of a linear elastic material model.

2.3.3 Agreement and disagreement

Considering the above-mentioned mode-partitioning methods another issue is the agreement between them under different conditions. A comparative study was performed by DUCEPT et al. (1999) using the UDCB and the unsymmetric MMB specimens. For both configurations the mode ratio was determined by the VCCT, the global method and the local approach. They have found that the local approach and the VCCT give results close to each other, and the global approach is inaccurate in the case of unsymmetrically located crack. However, this should be mentioned that the global approach may be derived by the help of two conditions. The original approach of WILLIAMS (1988) supposes equal curvatures under pure mode-II. This formulation was also applied by DUCEPT et al. (1999) and SZEKRÉNYES and UJ (2004a). On the other hand under pure mode-I the condition of equal axial strains at the crack tip may be considered. This formulation was utilized by BRUNO and GRECO (2001a) and a good agreement was found between the local and the global approaches through asymmetric models loaded by moments and concentrated forces. As regarding to the global method the two different approaches give the same result in the case of midplane delamination and when the upper and lower arms have the same mechanical properties. Later, it has been shown (ZOU et al., 2001, 2002; BRUNO et al., 2003) that when an appropriate kinematical plate model is used for the delaminated laminate and the actual strain state is captured with a good accuracy then, the global and local methods lead to the same results even in the case of asymmetrically located crack along the beam thickness.

2.4 Direct data reduction

Aside from the analytical and numerical solutions (indirect methods) several schemes were developed to reduce directly the experimental data.

2.4.1 Compliance calibration (CC) method

This is the most accurate method, and consequently the most popular one in the literature (DAHLEN et al., 1994; OZDIL and CARLSSON, 1999a). The compliance values are obtained directly from the measured load and displacement values ($C = \delta/P$). The compliance should be determined at each crack length and then it should be expressed as the function of them. This may be achieved by using a curve fitting technique (e.g. least square method). The form of the fitting function may be obtained based on the simple beam theory solution of the specimen. For instance for the DCB specimen the compliance may be fit by a power function:

$$C = \beta a^m, \quad (2.9)$$

which is the generalized form of the solution in Fig. 2.2. The energy release rate may be obtained by the *Irwin-Kies* expression (Eq. (1.2)). A relative drawback of this method is that the accuracy depends on the number of points used for the curve fitting and the extension of the considered crack length range. The method was modified by SHINDO et al. (2001) and the modified compliance calibration (MCC) method was proposed, which is based on similar considerations.

2.4.2 Direct beam theory (DBT)

This approach eliminates the flexural modulus from the beam theory-based solution and only one expression determines the strain energy release rate using the recorded load and displacement values (e.g.: HASHEMI et al., 1990a and b). For the mentioned fracture specimens the relevant equations are compiled in Figs. 2.2, 2.3, 2.4 and 2.5.

2.4.3 Corrected beam theory (CBT)

Similarly to the direct beam theory it also incorporates the measured load and displacement but apart from that it contains a correction for crack tip rotation and deflection (see for example the work by MORAIS et al., 2002).

2.4.4 Area method

In this case the energy release rate is calculated directly from the energy consumed by the crack extension divided by the area of the new crack surface (YANG and SUN, 2000; SHINDO et al., 2001). The area between the loading and unloading curves (see Fig. 2.9) represents the decrease in the stored strain energy caused by the delamination crack extension, i.e.:

$$G_C = \frac{W_i}{A_i} = \frac{(P_i \delta_{i+1} - P_{i+1} \delta_i)}{2b(a_{i+1} - a_i)}, \quad (2.10)$$

where W_i is the increment in the work of the external force, A_i is the new crack surface, P_i is the load at δ_i displacement, P_{i+1} and δ_{i+1} are the load and displacement after the load drop, respectively.

It is recommended to apply more than one of the mentioned techniques for the evaluation of the experimental data. Depending on the combination of the applied method and the definitions of the crack initiation different values may be obtained for the SERR.

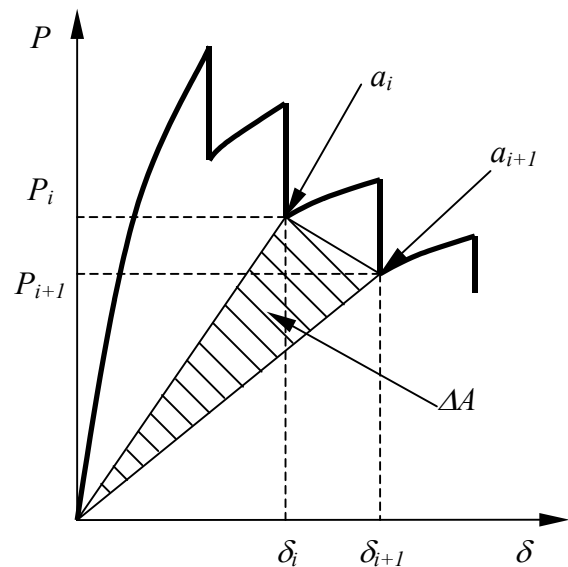


Fig. 2.9.
Schematic load/displacement curve for the area method.

2.5 Further application of the finite element method in fracture problems

The finite element method (FEM) is very intensively applied by the researchers to analyze fracture problems in composite materials. In this points of view the possibilities are quite extended. The FEM allows the macro- and micromechanical investigation of composite structures related to crack problems.

2.5.1 Macromechanical formulation

In the macromechanical scale the composite structures are usually modeled as anisotropic solids with homogenized material properties. It may be assumed that a small plastic zone arises in the vicinity of the crack tip. However, it may be also assumed that due to the small size of the plastic zone it can be neglected. This provides a simple and useful way for the fracture investigation of the composite structures. In general, the FE models of the delamination specimens are constructed by using plane FE elements (TODO and JAR, 1998; YANG and SUN, 2000; SZEKRÉNYES and UJ, 2002). On the one hand these models are suitable to determine the SERR via the VCCT or the J -integral approaches. Other authors used the 2D models in order to investigate further effects. For example TODO et al. (1998, 2000) created the 2D FE models of the DCB and ENF specimens. An experimental observation revealed that in the microscopic scale the crack has an elliptic shape if there is no precrack and the crack initiates directly from the insert. They have found that the crack does not grow along the midplane of the specimen in every case, which may be explained by the former elliptic shape.

The macromechanical models of the fracture specimens may be used to confirm the simple closed-form solutions based on beam theories (TRACY and FERABOLI 2003; SZEKRÉNYES and UJ, 2004a). On the other hand several efforts have been made to obtain improved solutions for composite delamination specimens by using 2D FE models. SUO et al. (1991) provided a correction for the DCB specimen, the solution was combined with the result of the simple beam theory. In comparison with the analytical solutions by OLSSON (1992), SZEKRÉNYES and UJ (2004a, 2005a), the correction by SUO et al. (1991) is the most accurate one. Later, BAO et al. (1992) provided similar solutions also for mode-II and mixed-mode I/II specimens. Independently, WANG and WILLIAMS (1992) performed a similar work for the mode-II ENF and ELS specimens. Although the FE solutions in general are more accurate than the analytical ones, the latter is very important to understand better the different mechanisms and effects at the crack tip. From other perspectives the form of the FE solution is usually built by the result of simple beam theory multiplied by a numerically determined correction.

The FE method is suitable to construct the fully three-dimensional models of the fracture specimens. Very large amount of work was published by the researchers on this subject. Only few and the most important of them are mentioned here.

Considering the DCB specimen an experimental observation showed that the crack front along the width of the DCB specimen is curved. DAVIDSON (1990) created a 3D FE model, and it was shown that the SERR (calculated by the VCCT method) is not uniformly

distributed along the delamination front or along the width of the specimen. Later, many authors investigated the same problem in mode-I, mode-II (ZHENG and SUN, 1995; SUN and ZHENG, 1996), mode-III (ZHAO and WANG, 1998) and mixed-mode I/II cases (DAVIDSON et al., 1995). It is noteworthy that these models were very complicated and the number of elements required to obtain accurate results was very high. In fact the 3D mesh is necessary only in the neighborhood of the crack front. KRUEGER (1999) proposed a SHELL/3D modeling technique to reduce the number of finite elements in those parts where the 3D

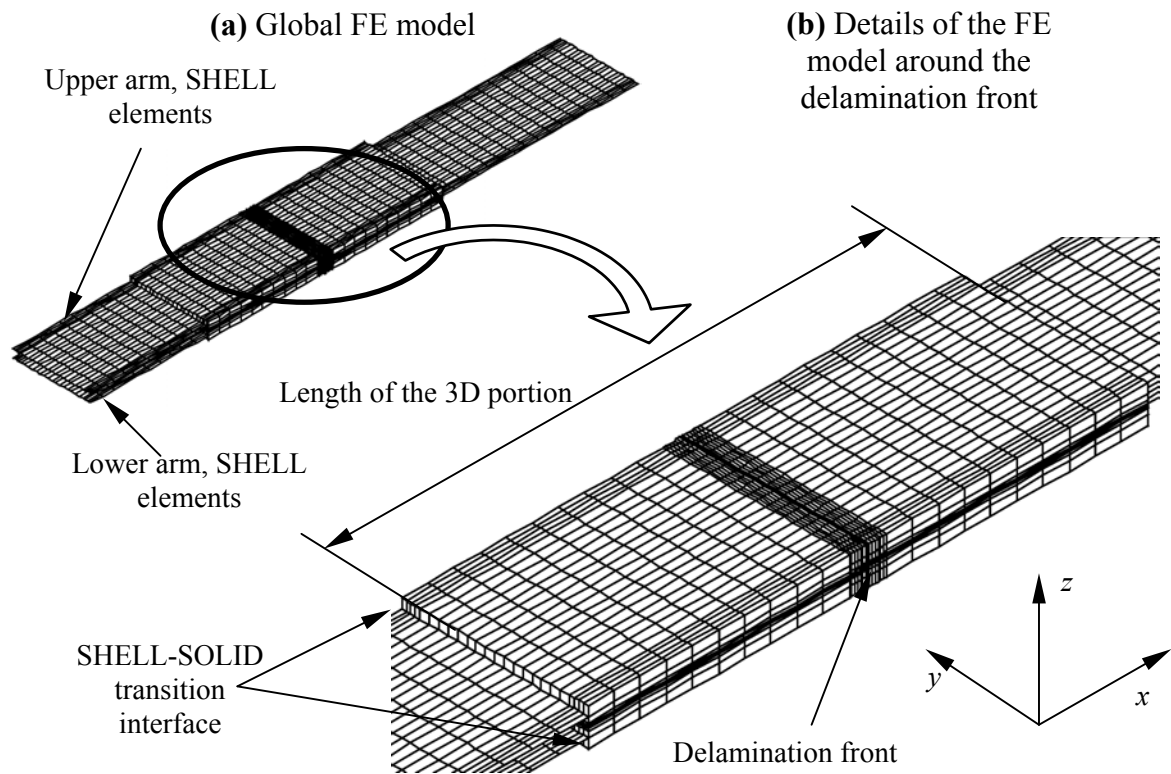


Fig. 2.10.
SHELL/3D modeling technique for delamination in composite specimens.

elements do not play important role. Around the crack tip a fully 3D model was constructed, but far enough from the crack front the remained parts were modeled by SHELL elements. This resulted in a significant saving in the computation time. It was shown that if the size of the 3D region is properly chosen the SHELL/3D model gives the same result as a fully 3D structure. The concept of the SHELL/3D modeling technique is illustrated in Fig. 2.10. The applicability of the technique was demonstrated by the help of DCB, ENF and SLB specimens (KRUEGER, 1999).

2.5.2 Micromechanical formulation

The composites are heterogeneous materials. This fact involved the micromechanical formulation of the crack problems. However, it is apparent that some connection should exist between the macro and micromechanical models of the structure. In the case of the micromechanical formulation the fiber-matrix structure is modeled and interactions between

them may be captured. Many studies were performed to investigate the stress and strain field in the small vicinity of the crack tip of interlaminar fracture specimens.

TODO and JAR (1998, 2000) performed two FE studies, in which they assumed a hypothetic crack shape at the crack tip of the DCB and ENF specimens. Although in their study the 'crack' expression was used, in fact the crack was treated as a notch and an elliptic shape of the 'crack' front was assumed. The concept of the modeling technique by TODO and JAR (1998, 2000) is schematically illustrated in Fig. 2.11. On the other hand they have performed also 2D analysis (as mentioned before), but in the 3D models the displacement

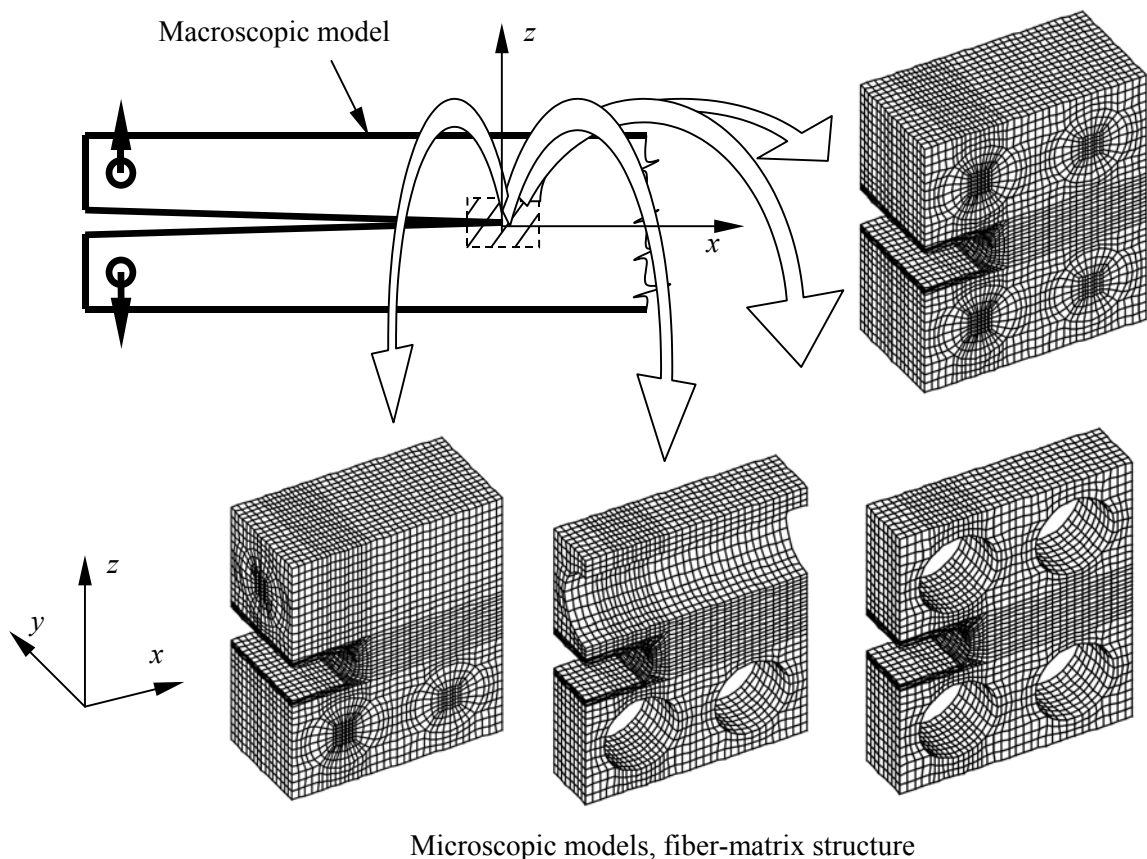


Fig. 2.11.

Macro- and micromechanical FE models for interlaminar fracture investigation.

fields were independent by those of the 2D models and were substantially simplified. The main result of their work was that the crack was found to be susceptible to grow along the fiber/matrix interface. In this case the measured fracture toughness values rather reflect the properties of the fiber/matrix interface than the composite toughness. Later, similar results were obtained by SZEKRÉNYES and UJ (2002c, 2003a) for mixed-mode I/II MMF and CLS specimens. It is remarkable that only linear elastic material model was applied, which is acceptable in the case of the reinforcing fibers, but may give inaccurate results in the case of the matrix material.

DUBOIS and KEUNINGS (1997) performed a combined macro-micromechanical analysis to investigate the effect of the inelastic matrix behavior on the fracture toughness. In

that study the well-known displacement coupling technique (see also SZEKRÉNYES, 2002b) was applied to establish the relation between the macro and micromechanical models. The analysis resulted in a conclusion, whereas the inelasticity of the matrix material decreases the SERR compared to the result of a fully elastic analysis. Nowadays, a quite similar work was carried out by SPEARING and GREGORY (2005) leading to the same conclusions and results as found by DUBOIS and KEUNINGS (1997).

Considering the macro- and micromechanical formulations, it should be mentioned that there also exists the so-called mesomechanical and the multiscale analysis of composites. These are not related strictly to the present work, so they are discussed elsewhere (FEYEL and CHABOCHE, 2000; XIA et al., 2000; MISHNAEVSKY et al., 2001).

2.6 The fiber-bridging phenomenon

The fiber-bridging means that during the delamination process some of the fibers make a 'bridge' between the arms of, for example the DCB specimen (Fig. 2.12). This is an essential feature in unidirectional DCB specimens, as highlighted in many works (KAUTE et al., 1995; TAMUZS et al., 2001). Furthermore, it is observable also in angle-ply laminate DCB

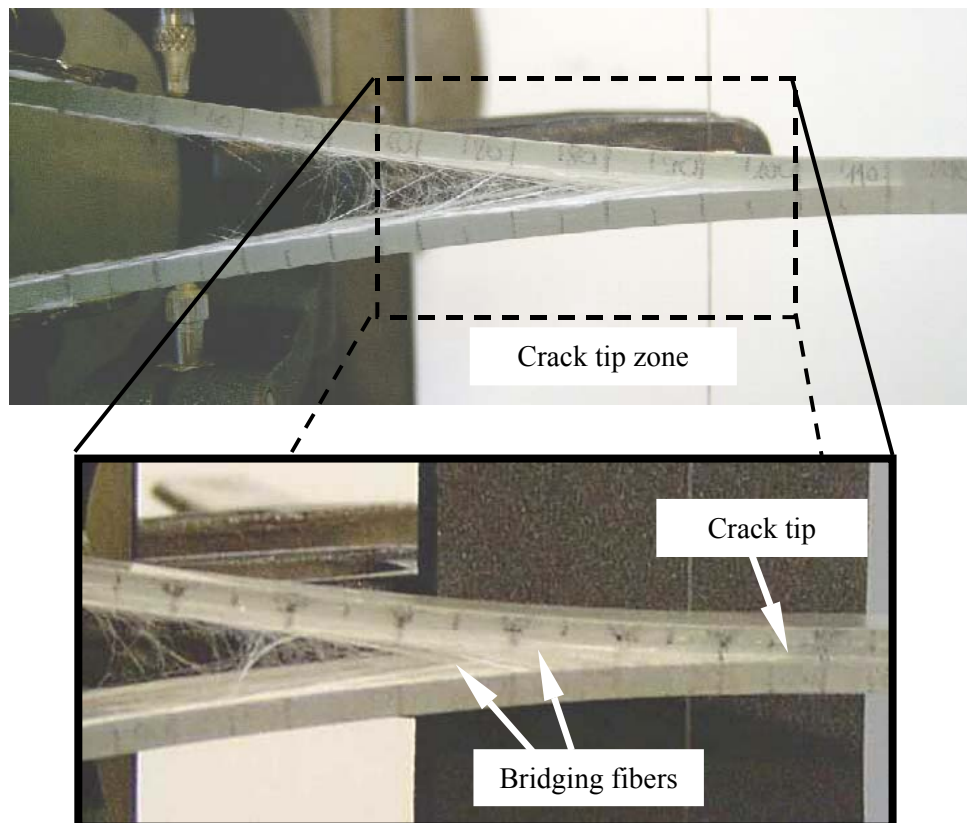


Fig. 2.11.
Fiber-bridging in glass/polyester DCB specimen.

and mixed-mode I/II coupons (OZDIL and CARLSSON, 1999a, 1999b). The beam theory-based (closed-form) solutions do not consider this phenomenon, and in the case of extensive fiber-

bridging these solutions are not suitable to evaluate the experimental data. The bridging fibers enhance the resistance to delamination and usually the energy release rate increases with the crack length. This feature is known as the R-curve (Resistance) effect. To characterize the R-curve behavior and fiber-bridging in composite specimens the bridging law is a useful tool. The bridging law is based on the J -integral and it determines the bridging stress as a function of the displacement at the initial crack tip. SUO et al. (1992) have shown that the R-curve can not be considered as a material property, since it depends on the specimen size and geometry.

Different approximate methods were developed in the literature to handle the fiber-bridging and understand more deeply the phenomenon. KAUTE et al. (1995) introduced a semi-empirical model for fiber-bridging modeling. The bridging law was composed by the product of two terms: the fiber force and the number of bridging fibers per unit area of crack face. The functions of these two parameters were determined based on experiments. Unfortunately, this model required too many parameters to be determined. Since these are, in general not available in the literature and can only be approximately determined the application of KAUTE's model is difficult. The finite element method seemed to be a useful tool to overcome this difficulty. YAN et al. (2001) introduced a numerical model based on an elastic-plastic damage interface between the adjacent plies of the composite laminate. The experiments by HASHEMI et al. (1990a) were utilized to validate their model. Later, TAMUZS et al. (2001) applied also the finite element technique for fiber-bridging modeling in carbon/epoxy DCB specimens. The bridgings were represented by nonlinear spring elements along the bridged zone of the specimen. The behavior of the springs was controlled based on the determined bridging law. Based on their model load/displacement and R-curves were predicted. The results seemed to be very useful, however it should be noted that the load/displacement and R-curves may be experimentally determined, so this model (similarly to the one by YAN et al., 2001) does not provide additional information on the bridgings. SOHN et al. (1997) investigated the fiber-bridging using the bridging stress function in the case of polycrystalline alumina composites. The bridging tractions were estimated based on the measured crack opening displacement. The phenomenon was also studied in short fiber-reinforced composites. An extensive study was carried out by LINDHAGEN and BERGLUND (2000), the fiber-bridging in several type of composite materials was investigated and the bridging laws were determined using the DCB coupon loaded by pure bending moments. Also, FERNBERG and BERGLUND (2001) determined the bridging law for certain short-fiber-reinforced composites. A remarkable feature is that the bridging law was found to be a material parameter in these studies.

3 IMPROVED SOLUTION FOR DELAMINATION SPECIMENS

In this chapter we adopt linear beam theories to obtain refined solution for the compliance and the SERR of midplane delaminated composite beams of which arms have the same mechanical properties. The *Winkler-Pasternak* foundation analysis (ROSA, 1995; SZEKRÉNYES and UJ, 2004c, 2004d, 2005a), *Timoshenko* beam theory (WASHIZU, 1968), *Saint-Venant* effect (OLSSON, 1992) and the concept of crack tip deformation analysis (WANG and QIAO, 2004a; SZEKRÉNYES and UJ, 2004b, 2005b) is utilized in our formulation. The total solution is obtained by the principle of superposition. It should be mentioned that interaction between the former effects is not accounted for. Also, mode-mixity is performed by means of the global approach. Furthermore, we assume that only small displacements arise.

3.1 *Winkler-Pasternak* foundation analysis

Let us consider the problem in Fig. 3.1, where a delaminated beam is subjected to a general loading condition. In the uncracked region the two-parameter elastic foundation model captures the transverse elasticity. The arms of the model are loaded by different loads. A detailed view at the crack tip is also shown at the bottom of Fig. 3.1. The linear springs are connected to the midplane of the upper and lower beam elements. The moment in the torsional springs is proportional with the difference in the angle of rotations of the upper ($w_{u2}(x)$) and lower ($w_{l2}(x)$) beam elements. The potential energy of the system is:

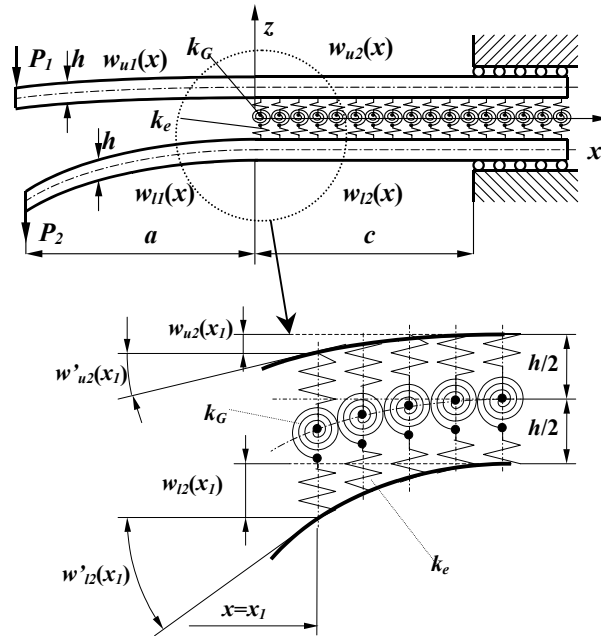


Fig. 3.1.

Two-parameter elastic foundation model.

$$\begin{aligned} \Pi = \frac{1}{2} \int_{(l)} [I_{y2}^u E_{11} w_{u2}''(x)^2 + I_{y2}^l E_{11} w_{l2}''(x)^2 + I_{y1}^u E_{11} w_{u1}''(x)^2 + I_{y1}^l E_{11} w_{l1}''(x)^2 + \\ + k_e (w_{u2}(x) - w_{l2}(x))^2 + k_G (w'_{u2}(x) - w'_{l2}(x))^2] dx + P_1 w_{u1}(-a) + P_2 w_{l1}(-a), \end{aligned} \quad (3.1)$$

where I_{y2}^u , I_{y2}^l , I_{y1}^u and I_{y1}^l are the relevant second order moments of inertia (refer to Fig 3.1), E_{11} is the flexural modulus, k_e is the *Winkler* foundation parameter, k_G is the *Pasternak* foundation parameter and P_1 , P_2 are the external loads. The potential energy in the torsional springs is proportional with the square of the differences in the angle of rotations. Application

of the minimum of the potential energy principle involves the following governing equations for the uncracked region:

$$I_{y2}^l E_{11} \frac{d^4 w_{l2}(x)}{dx^4} - k_G \frac{d^2 w_{l2}(x)}{dx^2} + k_e w_{l2}(x) = -k_G \frac{d^2 w_{u2}(x)}{dx^2} + k_e w_{u2}(x), \quad 0 \leq x \leq c, \quad (3.2)$$

$$I_{y2}^u E_{11} \frac{d^4 w_{u2}(x)}{dx^4} - k_G \frac{d^2 w_{u2}(x)}{dx^2} + k_e w_{u2}(x) = -k_G \frac{d^2 w_{l2}(x)}{dx^2} + k_e w_{l2}(x), \quad 0 \leq x \leq c.$$

Let us define the foundation parameter k_e . The elastic strain (which is assumed not to be disturbed by the torsional springs) in the transverse (z) direction according to Fig. 3.1 is (SZEKRÉNYES and UJ, 2004a):

$$\varepsilon_z = \frac{w_{l2}(x) - w_{u2}(x)}{h}, \quad (3.3)$$

where h is the thickness of one arm. According to OZDIL and CARLSSON (1999a) the definition of the *Winkler* foundation parameter is:

$$k_e = \frac{b \sigma_z(x)}{w_{l2}(x) - w_{u2}(x)}, \quad (3.4)$$

where b is the width of the model. Using the one-dimensional *Hooke's* law we obtain:

$$\sigma_z(x) = E_{33} \varepsilon_z. \quad (3.5)$$

Combining Eqs. (3.3)-(3.5) yields:

$$k_e = \frac{b E_{33}}{h}. \quad (3.6)$$

The rotational foundation parameter can not be so definitely expressed. The relevant literature investigates problems wherein the foundation parameters are varied within a wide range (ROSA, 1995; ALEMDAR et al., 1997; COŞKUN, 2003), or suggestions based on assumptions are given (OMURTAG et al., 1998; KHAZANOVICH, 2003). Some assumptions are required to determine the second foundation stiffness. The rearranged form of the governing equations is:

$$\frac{d^4 w_{l2}(x)}{dx^4} - 2\chi^4 \frac{d^2 w_{l2}(x)}{dx^2} + 4\eta^4 w_{l2}(x) = -2\chi^4 \frac{d^2 w_{u2}(x)}{dx^2} + 4\eta^4 w_{u2}(x), \quad 0 \leq x \leq c, \quad (3.7)$$

$$\frac{d^4 w_{u2}(x)}{dx^4} - 2\chi^4 \frac{d^2 w_{u2}(x)}{dx^2} + 4\eta^4 w_{u2}(x) = -2\chi^4 \frac{d^2 w_{l2}(x)}{dx^2} + 4\eta^4 w_{l2}(x), \quad 0 \leq x \leq c,$$

where η and χ will be defined later. Eq. (3.7) has three distinct solutions depending on which of the conditions $\chi^4 < 2^{1/2} \eta^2$, $\chi^4 = 2^{1/2} \eta^2$ or $\chi^4 > 2^{1/2} \eta^2$, respectively holds (ALEMDAR et al., 1997). It will be shown that in our case the last condition is involved. In this case the characteristic roots of Eq. 3.7 are:

$$m_{41} = \sqrt{\chi^4 - \sqrt{2}\eta^2}, \quad m_{42} = \sqrt{\chi^4 + \sqrt{2}\eta^2}. \quad (3.8)$$

Based on mechanical ground we assume that the effect of rotational springs is similar to the linear springs related to the *Winkler* foundation. We assume the following:

$$\chi^4 = \omega 2^{1/2} \eta^2, \quad (3.9)$$

where $\omega > 1$ and will be determined based on FE calculations. The solution functions of the uncracked part are given by:

$$w_{l2}(x) = c_1 + c_2x + c_3x^2 + c_4x^3 + [c_5 \cosh(m_{41}x) + c_6 \sinh(m_{41}x)] \cosh(m_{42}x) + [c_7 \cosh(m_{41}x) + c_8 \sinh(m_{41}x)] \sinh(m_{42}x), \quad 0 \leq x \leq c, \quad (3.10)$$

$$w_{u2}(x) = c_1 + c_2x + c_3x^2 + c_4x^3 - [c_5 \cosh(m_{41}x) + c_6 \sinh(m_{41}x)] \cosh(m_{42}x) - [c_7 \cosh(m_{41}x) + c_8 \sinh(m_{41}x)] \sinh(m_{42}x), \quad 0 \leq x \leq c.$$

The deflection functions of the upper and lower specimen arms (Fig. 3.1) can be expressed in the usual way (using *Euler-Bernoulli* beam theory):

$$w_{u1}(x) = -\frac{P_1}{I_{y1}^u E_{11}} \left(\frac{x^3}{6} + \frac{ax^2}{2} \right) + c_9x + c_{10}, \quad -a \leq x \leq 0, \quad (3.11)$$

$$w_{l1}(x) = -\frac{P_2}{I_{y1}^l E_{11}} \left(\frac{x^3}{6} + \frac{ax^2}{2} \right) + c_{11}x + c_{12}, \quad -a \leq x \leq 0. \quad (3.12)$$

Using the theorem of parallel axes the second order moments of inertia of the cracked and uncracked portions of the model in Fig. 3.1 are:

$$I_{y1}^u = I_{y1}^l = \frac{h^3b}{12}, \quad I_{y2}^u = I_{y2}^l = \frac{h^3b}{12} + \frac{h^2}{4}bh = \frac{h^3b}{3}, \quad (3.13)$$

where in the calculation of I_{y2}^u and I_{y2}^l the reference plane coincides with the x - y plane of the model depicted in Fig. 3.1. The same manner was applied by DAVIDSON and SUNDARARAMAN (1996) and SUNDARARAMAN and DAVIDSON (1998). This condition assumes strain compatibility along the interface, which is assumed not to be violated by elastic foundation. The coefficients, η and χ may be expressed by using Eqs. (3.2), (3.6), (3.7), (3.9) and (3.13). They have the following form:

$$\eta = \left(\frac{k_e}{4I_{y2}^u E_{11}} \right)^{\frac{1}{4}} = \left(\frac{3}{4} \right)^{\frac{1}{4}} \frac{1}{h} \left(\frac{E_{33}}{E_{11}} \right)^{\frac{1}{4}}, \quad \chi = \left(\frac{k_G}{2I_{y2}^u E_{11}} \right)^{\frac{1}{4}} = \omega^{\frac{1}{4}} \left(\frac{3}{2} \right)^{\frac{1}{8}} \frac{1}{h^{\frac{1}{2}}} \left(\frac{E_{33}}{E_{11}} \right)^{\frac{1}{8}}. \quad (3.14)$$

The constants (c_1 - c_{12}) in Eqs. (3.10), (3.11) and (3.12) can be obtained by using the following boundary and matching conditions considering Eq. (3.13):

$$w_{u2}(c) = 0, \quad w_{l2}(c) = 0, \quad w'_{u2}(c) = 0, \quad w'_{l2}(c) = 0, \quad (3.15)$$

$$w_{u1}(0) = w_{u2}(0), \quad w_{l1}(0) = w_{l2}(0), \quad w'_{u1}(0) = w'_{u2}(0), \quad w'_{l1}(0) = w'_{l2}(0), \quad (3.16)$$

$$w''_{u1}(0) = 4w''_{u2}(0), \quad w''_{l1}(0) = 4w''_{l2}(0), \quad w'''_{u1}(0) = 4w'''_{u2}(0), \quad w'''_{l1}(0) = 4w'''_{l2}(0).$$

It is important to note that Eq. (3.13) should be considered when we match the second and third derivative of the relevant deflection functions in Eq. (3.16). We are interested to find the compliance of each arm, which can be obtained by taking the deflections $w_{u1}(x)$, $w_{l1}(x)$ at the position of $x=-a$ and dividing them by the external loads, P_1 and P_2 , respectively. Meaningful simplifications can be achieved by assuming that the length of the uncracked region c is much larger than half of the specimen thickness h . The simplified compliance expressions are:

$$C_{EB,WP,1} = \frac{1}{I_{y1}^u E_{11}} \left[\frac{7a^3 + L^3}{24} + \frac{(L^3 - a^3)P_2}{24P_1} + \frac{(P_1 - P_2)}{24P_1} \left(\frac{\sqrt{2}\sqrt{\sqrt{2}\eta^2 + \chi^4}}{16\eta^2} a^2 + \frac{\sqrt{2}\eta^2 + \chi^4}{16\eta^4} a + \frac{\sqrt{\sqrt{2}\eta^2 + \chi^4}}{32\eta^4} \right) \right], \quad (3.17)$$

$$C_{EB,WP,2} = \frac{1}{I_{y1} E_{11}} \left[\frac{7a^3 + L^3}{24} + \frac{(L^3 - a^3)P_1}{24P_2} + \frac{(P_2 - P_1)}{24P_2} \left(\frac{\sqrt{2}\sqrt{\sqrt{2}\eta^2 + \chi^4}}{16\eta^2} a^2 + \frac{\sqrt{2}\eta^2 + \chi^4}{16\eta^4} a + \frac{\sqrt{\sqrt{2}\eta^2 + \chi^4}}{32\eta^4} \right) \right], \quad (3.18)$$

where $C_{EB,WP,1}$ and $C_{EB,WP,2}$ are the compliances of the upper and lower arms, respectively, while $L=a+c$ is the full length of the model in Fig. 3.1. Note that the constant parameters, c_{1-12} are extremely complicated, therefore they are not detailed here. Substituting Eq. (3.14) into Eqs. (3.17) and (3.18) the compliances of the upper and lower arms become:

$$C_{EB,WP,1} = \frac{7a^3 + L^3}{2bh^3 E_{11}} + \frac{(L^3 - a^3)P_2}{2bh^3 E_{11}P_1} + \frac{a^3(P_1 - P_2)}{2bh^3 E_{11}P_1} f_{W1}, \quad (3.19)$$

$$C_{EB,WP,2} = \frac{7a^3 + L^3}{2bh^3 E_{11}} + \frac{(L^3 - a^3)P_1}{2bh^3 E_{11}P_2} + \frac{a^3(P_2 - P_1)}{2bh^3 E_{11}P_2} f_{W1}, \quad (3.20)$$

where:

$$f_{W1} = 2.71 \left(\frac{h}{a} \right) \left(\frac{E_{11}}{E_{33}} \right)^{\frac{1}{4}} \phi^{\frac{1}{2}} + 2.45 \left(\frac{h}{a} \right)^2 \left(\frac{E_{11}}{E_{33}} \right)^{\frac{1}{2}} \phi + 1.11 \left(\frac{h}{a} \right)^3 \left(\frac{E_{11}}{E_{33}} \right)^{\frac{3}{4}} \phi^{\frac{1}{2}}, \quad (3.21)$$

where $\phi=1+\omega$. The first two terms in Eqs. (3.19) and (3.20) are the result of the *Euler-Bernoulli* beam theory, while the third one is the correction based on the two-parameter elastic foundation. The energy release rates for the upper and lower arms may be obtained by using Eq. (1.2):

$$G_{EB,WP,1} = \frac{P_1^2}{2b} \frac{dC_{EB,WP,1}}{da}, \quad G_{EB,WP,2} = \frac{P_2^2}{2b} \frac{dC_{EB,WP,2}}{da}. \quad (3.22)$$

Thus, we may obtain:

$$G_{EB,WP,1} = \frac{21P_1^2 a^2}{4bh^3 E_{11}} - \frac{3P_1 P_2 a^2}{4bh^3 E_{11}} + \frac{P_1(P_1 - P_2)a^2}{4bh^3 E_{11}} f_{W2}, \quad (3.23)$$

$$G_{EB,WP,2} = \frac{21P_2^2 a^2}{4bh^3 E_{11}} - \frac{3P_1 P_2 a^2}{4bh^3 E_{11}} + \frac{P_2(P_2 - P_1)a^2}{4bh^3 E_{11}} f_{W2}, \quad (3.24)$$

where:

$$f_{W2} = 5.42 \left(\frac{h}{a} \right) \left(\frac{E_{11}}{E_{33}} \right)^{\frac{1}{4}} \phi^{\frac{1}{2}} + 2.45 \left(\frac{h}{a} \right)^2 \left(\frac{E_{11}}{E_{33}} \right)^{\frac{1}{2}} \phi. \quad (3.25)$$

The SERR of the problem in Fig. 3.1 including the two-parameter elastic foundation may be obtained by summing Eqs. (3.23) and (3.24).

3.2 Timoshenko beam theory

In this section we capture the transverse shear effect using *Timoshenko* beam theory (WASHIZU, 1968). Let us consider the loading scheme in Fig. 3.2. The beam is loaded by different concentrated forces in both arms and has a clamped end. According to the

Timoshenko beam theory the displacement field in slender beams can be described by two parameters:

$$u(x) = u^0(x) + z \cdot \psi(x), \quad (3.26)$$

$$w(x) = w^0(x), \quad (3.27)$$

where $w^0(x)$ and $u^0(x)$ are the displacement components of the mid-surface. The bending moment-curvature relationship is:

$$\frac{M_x(x)}{b} = \frac{\kappa_x}{d_{11}}, \quad (3.28)$$

where d_{11} is the corresponding component of the bending compliance matrix (see later) and b is the specimen width. The curvature is given by:

$$\kappa_x = \frac{d\psi(x)}{dx}. \quad (3.29)$$

The shear strain γ_{xz} can be obtained by differentiating Eqs. (3.26) and (3.27):

$$\gamma_{xz} = \frac{\partial u}{\partial z} + \frac{\partial w}{\partial x} = \psi(x) + \frac{dw}{dx}. \quad (3.30)$$

On the other hand the shear strain can also be expressed in the following way:

$$\gamma_{xz} = \frac{a_{55}}{k} Q_x, \quad (3.31)$$

where a_{55} is the transverse shear compliance of the beam (see later), $k=5/6$ is the shear correction factor and Q_x is the shear force. Since $Q_y=M_y=M_{xy}=0$, we use the following equilibrium equation:

$$\frac{dM_x}{dx} + Q_x = 0, \quad (3.32)$$

where M_x is the bending moment. Combining Eqs. (3.30), (3.31) and (3.32) we obtain the following differential equation:

$$\frac{dw}{dx} = -\psi(x) + \frac{a_{55}}{bk} \frac{dM_x}{dx}. \quad (3.33)$$

The combination of Eq. (3.28) and Eq. (3.29) yields:

$$\psi(x) = \frac{1}{b} \int d_{11} M_x dx. \quad (3.34)$$

Substituting the former expression into Eq. (3.33) and recognizing that there are no normal forces we can write the following governing equation:

$$\frac{dw}{dx} = -\frac{1}{b} \int d_{11} M_x dx + \frac{a_{55}}{bk} \frac{dM_x}{dx}. \quad (3.35)$$

Considering the general loading scheme in Fig. 3.2 the bending moment functions can be written as:

$$M_{u1} = P_1(x+a), \quad M_{l1} = P_2(x+a), \quad -a \leq x \leq 0, \quad (3.36)$$

$$M_2 = (P_1 + P_2)(x+a), \quad 0 \leq x \leq c. \quad (3.37)$$

Substituting these into Eqs. (3.33), (3.34) and (3.35) the components of the displacement field can be expressed. The model has three distinct regions (see Fig. 3.2), the upper (w_{u1}, u_{u1}) and

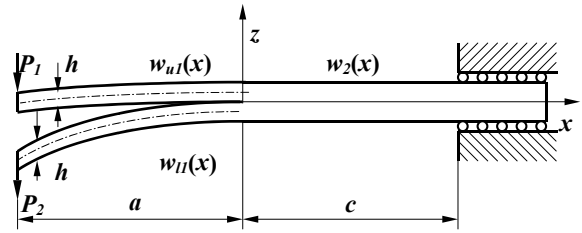


Fig. 3.2.
A general loading scheme for *Timoshenko* beam theory.

lower (w_{II} , u_{II}) arms and the uncracked (w_2 , u_2) region, respectively. The displacement functions for the three distinct parts of the model in Fig. 3.1 are:

$$w_{uI}(x) = -\frac{d_{11,uI}P_1}{b} \left(\frac{x^3}{6} + \frac{ax^2}{2} \right) + \frac{a_{55,uI}P_1x}{bk} + d_1x + d_2, \quad (3.38)$$

$$u_{uI}(x, z) = z \left[\frac{d_{11,uI}P_1}{b} \left(\frac{x^2}{2} + ax \right) - d_1 \right], \quad (3.39)$$

$$w_{II}(x) = -\frac{d_{11,II}P_2}{b} \left(\frac{x^3}{6} + \frac{ax^2}{2} \right) + \frac{a_{55,II}P_2x}{bk} + d_3x + d_4, \quad (3.40)$$

$$u_{II}(x, z) = z \left[\frac{d_{11,II}P_2}{b} \left(\frac{x^2}{2} + ax \right) - d_3 \right], \quad (3.41)$$

$$w_2(x) = -\frac{d_{11,2}(P_1 + P_2)}{b} \left(\frac{x^3}{6} + \frac{ax^2}{2} \right) + \frac{a_{55,2}(P_1 + P_2)x}{bk} + d_5x + d_6, \quad (3.42)$$

$$u_2(x, z) = z \left[\frac{d_{11,2}(P_1 + P_2)}{b} \left(\frac{x^2}{2} + ax \right) - d_5 \right]. \quad (3.43)$$

In order to determine the constant parameters (d_1 - d_6) the following boundary and matching conditions should be used:

$$u_2(c) = 0, \quad w_2(c) = 0, \quad (3.44)$$

$$w_{uI}(0) = w_2(0), \quad u_{uI}(0, z) = u_2(0, z), \quad w_{II}(0) = w_2(0), \quad u_{II}(0, z) = u_2(0, z). \quad (3.45)$$

The bending and shear compliances for the cracked and uncracked portions are:

$$d_{11,uI} = d_{11,II} = \frac{12}{h^3 E_{11}}, \quad a_{55,uI} = a_{55,II} = \frac{1}{hG_{13}}, \quad d_{11,2} = \frac{3}{2h^3 E_{11}}, \quad a_{55,2} = \frac{1}{2hG_{13}}. \quad (3.46)$$

The solution for the compliance of both specimen arms ($C_i = \delta_i/P_i$) can be determined by taking the deflections $w_{uI}(x)$, $w_{II}(x)$ at the position of $x = -a$:

$$C_{EB,TIM,1} = \frac{7a^3 + L^3}{2bh^3 E_{11}} + \frac{(L^3 - a^3)P_2}{2bh^3 E_{11}P_1} + \frac{L(P_1 + P_2) + a(P_1 - P_2)}{2bhkG_{13}P_1}, \quad (3.47)$$

$$C_{EB,TIM,2} = \frac{7a^3 + L^3}{2bh^3 E_{11}} + \frac{(L^3 - a^3)P_1}{2bh^3 E_{11}P_2} + \frac{L(P_1 + P_2) + a(P_2 - P_1)}{2bhkG_{13}P_2}. \quad (3.48)$$

The constants (d_1 - d_6) are given in Appendix A. The SERR can be expressed by differentiating the compliances with respect to crack length (Eq. 3.22). Therefore the SERRs are:

$$G_{EB,TIM,1} = \frac{21P_1^2 a^2}{4b^2 h^3 E_{11}} - \frac{3P_1 P_2 a^2}{4b^2 h^3 E_{11}} + \frac{P_1(P_1 - P_2)}{4b^2 hkG_{13}}, \quad (3.49)$$

$$G_{EB,TIM,2} = \frac{21P_2^2 a^2}{4b^2 h^3 E_{11}} - \frac{3P_1 P_2 a^2}{4b^2 h^3 E_{11}} + \frac{P_2(P_2 - P_1)}{4b^2 hkG_{13}}, \quad (3.50)$$

where in Eqs. (3.49) and (3.50) the first two terms are the results of the classical beam theory, the second one is the effect of transverse shear deformation.

3.3 Saint-Venant effect

OLSSON (1992) considered the problem of *Saint-Venant* effect in the compliance analysis of the mode-I DCB specimen. In this section we adopt the same theory. The

Saint-Venant effect represents a rotational angle at the crack tip or at the clamped end of the model. In Fig. 3.3 three cases are compiled. Fig. 3.3a shows the deformation of the crack tip under pure mode-I condition. In this case the strain compatibility condition is satisfied, hence the *Saint-Venant* effect should be considered. In contrast, focusing our attention on Fig. 3.3b we may observe that the *Saint-Venant* effect must vanish if the pure mode-II condition is involved. In this case the rotational angles would induce opposite axial displacements at the

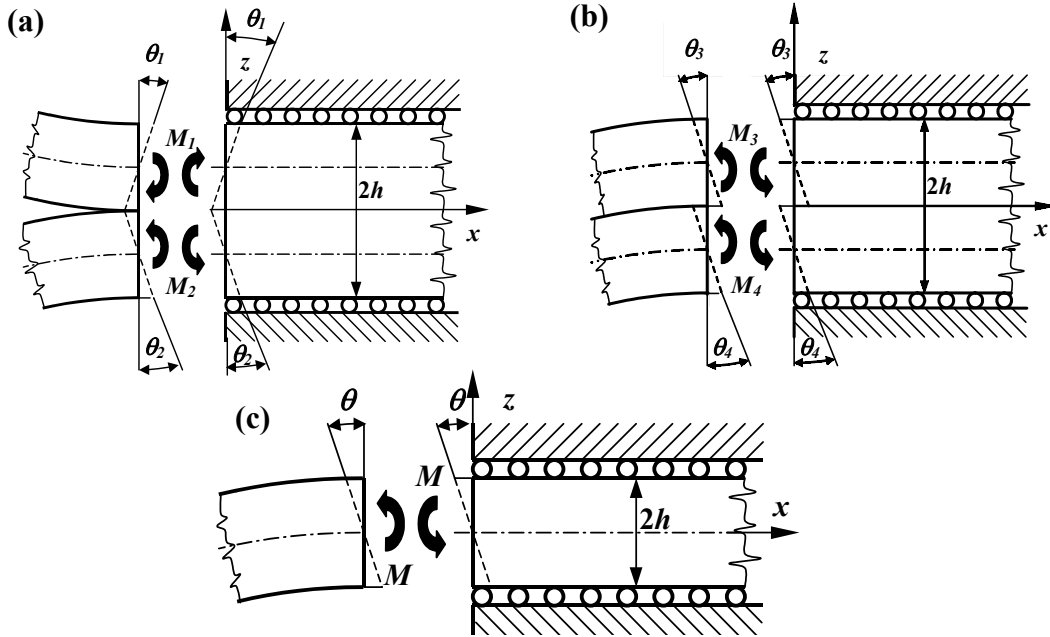


Fig. 3.3.

Saint-Venant effect under pure mode-I (a) and pure mode-II (b). *Saint-Venant* effect at the clamped end (c).

crack tip, which is physically not possible. Finally, Fig. 3.3c shows the clamped end of the uncracked part of the model, where the *Saint-Venant* effect also arises. Therefore, in the sequel we discuss only the pure mode-I condition and the case of the clamped end. We note that in accordance with strength of materials analysis the axial displacements at the clamped end is zero. The present formulation is an attempt to better capture the deformation at the clamped end.

According to OLSSON's analysis the strain energy derivative in the coordinate system in Fig. 3.3 is bounded by the following inequality:

$$\frac{\partial U}{\partial x} \leq 2 \frac{\partial U}{\partial x} \Big|_0 e^{-\frac{2x}{\kappa}}, \quad \kappa = \frac{h}{2\pi} \left(\frac{E_{11}}{G_{13}} \right)^{\frac{1}{2}}, \quad (3.51)$$

where U is the strain energy, κ is the characteristic decay length in the material.

3.3.1 *Saint-Venant* effect at the crack tip

In the followings we investigate the mode-I part of the problem (Fig. 2.6b). In the case of slender beams the derivative of the strain energy per unit length can be calculated as:

$$\left(\frac{\partial U}{\partial x}\right)\Big|_{1_0} = \frac{1}{2} I_{y1}^u E_{11} (w''|_0)^2 = \frac{1}{2} \frac{M_1^2}{I_{y1}^u E_{11}} = \frac{6M_1^2}{bh^3 E_{11}}, \quad (3.52)$$

$$\left(\frac{\partial U}{\partial x}\right)\Big|_{2_0} = \frac{1}{2} I_{y1}^l E_{11} (w''|_0)^2 = \frac{1}{2} \frac{M_2^2}{I_{y1}^l E_{11}} = \frac{6M_2^2}{bh^3 E_{11}}, \quad (3.53)$$

where I_{y1}^u and I_{y1}^l are given by Eq. (3.13). The moments, M_1 and M_2 are (refer to Fig. 2.6b):

$$M_1 = \frac{(P_1 - P_2)a}{2}, \quad M_2 = \frac{(P_2 - P_1)a}{2}. \quad (3.54)$$

For M_3 and M_4 in Fig. 3.3 refer to Fig. 2.6c. From Eqs. (3.51), (3.52) and (3.53) the strain energies ahead of the crack tip are:

$$U_1 \leq \int_0^\infty 2 \left(\frac{\partial U}{\partial x}\right)\Big|_{1_0} e^{-\frac{2x}{\kappa}} dx = \frac{12M_1^2}{bh^3 E_{11}} \int_0^\infty e^{-\frac{2x}{\kappa}} dx \Rightarrow U_1 \leq \frac{6M_1^2 \kappa}{bh^3 E_{11}}, \quad (3.55)$$

$$U_2 \leq \int_0^\infty 2 \left(\frac{\partial U}{\partial x}\right)\Big|_{2_0} e^{-\frac{2x}{\kappa}} dx = \frac{12M_2^2}{bh^3 E_{11}} \int_0^\infty e^{-\frac{2x}{\kappa}} dx \Rightarrow U_2 \leq \frac{6M_2^2 \kappa}{bh^3 E_{11}}. \quad (3.56)$$

Let us consider the lower sign in Eqs. (3.55) and (3.56). Using *Castigliano's* second theorem and adopting the lower sign we obtain the rotational angles at $x=0$:

$$\theta_1 = \frac{\partial U_1}{\partial M_1}, \quad \theta_2 = \frac{\partial U_2}{\partial M_2}. \quad (3.57)$$

The rotational angles by using Eqs. (3.54), (3.55), (3.56) and (3.57) are:

$$\theta_1 = \frac{12M_1 \kappa}{bh^3 E_{11}} = \frac{6(P_1 - P_2)a \kappa}{bh^3 E_{11}}, \quad (3.58)$$

$$\theta_2 = \frac{12M_2 \kappa}{bh^3 E_{11}} = \frac{6(P_2 - P_1)a \kappa}{bh^3 E_{11}}. \quad (3.59)$$

The displacements at the end of the model arms are (see Fig. 3.4):

$$\delta_1 = \theta_1 a = \frac{6(P_1 - P_2)a^2 \kappa}{bh^3 E_{11}}, \quad (3.60)$$

$$\delta_2 = \theta_2 a = \frac{6(P_2 - P_1)a^2 \kappa}{bh^3 E_{11}}. \quad (3.61)$$

Substituting κ (the second in Eq. 3.51) into Eqs. (3.60) and (3.61) we obtain the compliance contributions from the *Saint-Venant* effect for a mixed-mode I/II problem in Fig. 2.6a:

$$C_{SV,1} = \frac{\delta_1}{P_1} = \frac{3}{\pi} \frac{(P_1 - P_2)a^2}{bh^2 E_{11} P_1} \left(\frac{E_{11}}{G_{13}}\right)^{\frac{1}{2}}, \quad (3.62)$$

$$C_{SV,2} = \frac{\delta_2}{P_2} = \frac{3}{\pi} \frac{(P_2 - P_1)a^2}{bh^2 E_{11} P_2} \left(\frac{E_{11}}{G_{13}}\right)^{\frac{1}{2}}. \quad (3.63)$$

The application of Eq. (3.22) results in the SERRs of a mixed-mode I/II problem as:

$$G_{SV,1} = \frac{P_1(P_1 - P_2)a^2}{4b^2 h^3 E_{11}} f_{SV}, \quad (3.64)$$

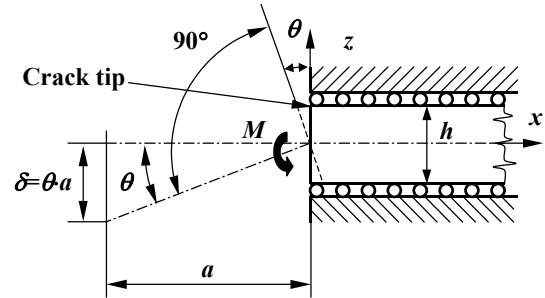


Fig. 3.4.
Deformation of the crack tip due to *Saint-Venant* effect.

$$G_{SV,2} = \frac{P_2(P_2 - P_1)a^2}{4b^2h^3E_{11}} f_{SV}, \quad (3.65)$$

where:

$$f_{SV} = \frac{12}{\pi} \left(\frac{h}{a} \right) \left(\frac{E_{11}}{G_{13}} \right)^{\frac{1}{2}}. \quad (3.66)$$

3.3.2 Saint-Venant effect at the clamped end

A similar analysis at the clamped end of the model (see Fig. 3.3c) results in the following expression:

$$C_{SV} = \frac{3}{\pi} \frac{L^2}{2bh^2E_{11}} \left(\frac{E_{11}}{G_{13}} \right)^{\frac{1}{2}}, \quad (3.67)$$

where $L=a+c$ is the full length of the model. Therefore, the compliance contribution from *Saint-Venant* effect at the clamped end is independent of the crack length. As a consequence, in this case there is no contribution to the strain energy release rate.

3.4 Crack tip shear deformation analysis

WANG and QIAO (2004a) performed an improved beam analysis for the mode-II ENF coupon. Their solution can be easily extended for mixed-mode I/II specimens. Let us consider the problem in Fig. 3.5. Based on strength of materials analysis the shear stresses in the upper and lower arms of the model are:

$$\tau_{01} = \frac{3}{2} \frac{P_1}{bh}, \quad \tau_{02} = \frac{3}{2} \frac{P_2}{bh}. \quad (3.68)$$

We consider the shear stresses in Eq. (3.68) as shear tractions and the effect of the concentrated forces, P_1 and P_2 is not included in the analysis (they have already been considered in Sections 3.1 and 3.2). In contrast with WANG and QIAO in the present analysis we assume that the shear tractions act along the midplane of the upper and lower arms and do not between crack faces. The relationship between the section forces and stresses of the

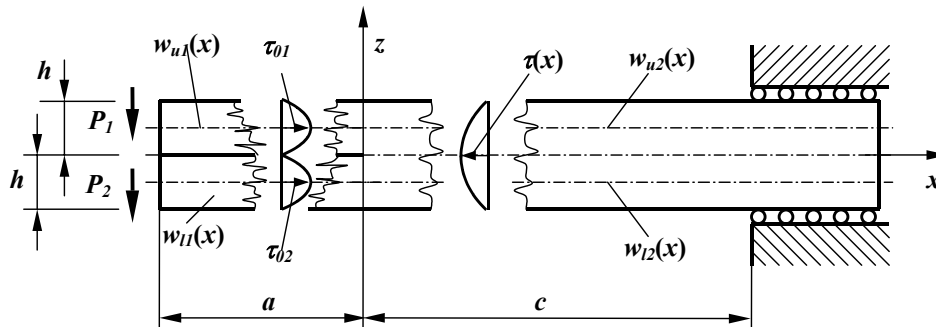


Fig. 3.5. Loading scheme for the crack tip deformation analysis.

uncracked region are:

$$\frac{dN_{u2}}{dx} = b\tau_{u2}, \quad \frac{dN_{l2}}{dx} = b\tau_{l2}, \quad (3.69)$$

$$\frac{dM_{u2}}{dx} = -\frac{h}{2}b\tau_{u2}, \quad \frac{dM_{l2}}{dx} = -\frac{h}{2}b\tau_{l2}, \quad (3.70)$$

where N is the normal force and M is the bending moment. The following constitutive equations are adopted:

$$\frac{d^2w_{u2}}{dx^2} = \frac{-M_{u2}}{I_{y2}^u E_{11}}, \quad \frac{d^2w_{l2}}{dx^2} = \frac{-M_{l2}}{I_{y2}^l E_{11}}, \quad (3.71)$$

where I_{y2}^u and I_{y2}^l are given by Eq. (3.13). The longitudinal displacement at the neutral plane of the uncracked region ($0 \leq x \leq c$) can be written as:

$$u_{u2}(x) = -\int \frac{N_{u2}}{bhE_{11}} dx + K_1\tau_{u2} - \frac{h}{2} \frac{dw_{u2}}{dx}, \quad (3.72)$$

$$u_{l2}(x) = \int \frac{N_{l2}}{bhE_{11}} dx - K_2\tau_{l2} + \frac{h}{2} \frac{dw_{l2}}{dx}, \quad (3.73)$$

where K_1 and K_2 are the shear compliances and will be defined later. Along the interface of the upper and lower beam elements of the uncracked region the axial displacements should be identical, i.e. strain compatibility is required and the relative displacement is zero:

$$u_{u2}(x) - u_{l2}(x) = 0. \quad (3.74)$$

Substituting Eqs. (3.72) and (3.73) into (3.74) and differentiating it twice we have:

$$-\frac{1}{bhE_{11}} \left[\frac{dN_{u2}}{dx} + \frac{dN_{l2}}{dx} \right] + K_1 \frac{d^2\tau_{u2}}{dx^2} + K_2 \frac{d^2\tau_{l2}}{dx^2} - \frac{h}{2} \left[\frac{d^3w_{u2}}{dx^3} + \frac{d^3w_{l2}}{dx^3} \right] = 0. \quad (3.75)$$

In accordance with WANG and QIAO (2004a) the shear compliances may be written as:

$$K_1 = K_2 = \frac{h}{3G_{13}}. \quad (3.76)$$

Combining Eq. (3.69), (3.71) and (3.75) and recognizing that at the interface the shear stresses are equal ($\tau_{u2} = \tau_{l2} = \tau$), the following governing equation can be obtained:

$$\frac{d^2\tau}{dx^2} - \rho^2\tau = 0, \quad \rho = \left(\frac{21G_{13}}{4E_{11}h^2} \right)^{\frac{1}{2}}. \quad (3.77)$$

The solution of Eq. (3.77) is:

$$\tau(x) = f_1 e^{-\rho x} + f_2 e^{\rho x}. \quad (3.78)$$

In most cases of $c \gg h$, the shear stress is small. On the other hand in the case of $x \gg 1/\rho$, f_2 must be a very small constant. Therefore, the second term in Eq. (3.78) can be neglected. On the other hand the longitudinal forces must vanish along the whole length of the model. This condition allows for the determination of f_1 :

$$\int_{-a}^0 (\tau_{01} + \tau_{02}) b h dx - \int_0^c f_1 e^{-\rho x} b \cdot 2h \cdot dx = 0. \quad (3.79)$$

Assuming that $e^{-\rho c} \approx 0$ if $c \gg h$ we obtain from Eqs. (3.68), (3.78) and (3.79) the following:

$$\tau(x) = -\frac{3}{4} \frac{P_1 + P_2}{bh} \rho \cdot ae^{-\rho x}. \quad (3.80)$$

The bending moment functions may be obtained by integrating the shear stress along the uncracked region (Eq. (3.70)):

$$M_{u2}(x) = -\frac{h}{2} \left[\int \frac{3}{4} \frac{P_1 + P_2}{bh} \rho \cdot ae^{-\rho x} b \cdot dx \right] = \frac{3}{8} (P_1 + P_2) ae^{-\rho x}, \quad (3.81)$$

$$M_{l2}(x) = -\frac{h}{2} \left[\int \frac{3}{4} \frac{P_1 + P_2}{bh} \rho \cdot ae^{-\rho x} b \cdot dx \right] = \frac{3}{8} (P_1 + P_2) ae^{-\rho x}. \quad (3.82)$$

Using Eqs. (3.71), (3.81) and (3.82) the deflection functions of the uncracked part become:

$$w_{u2}(x) = -\frac{3}{8} \frac{(P_1 + P_2)a}{I_{y2}^u E_{11} \rho^2} e^{-\rho x} + g_1 x + g_2, \quad (3.83)$$

$$w_{l2}(x) = -\frac{3}{8} \frac{(P_1 + P_2)a}{I_{y2}^l E_{11} \rho^2} e^{-\rho x} + g_3 x + g_4. \quad (3.84)$$

Since the shear stresses act along the neutral plane of the upper and lower specimen arms they do not cause bending moment, consequently we may write:

$$w_{u1}(x) = g_5 x + g_6, \quad (3.85)$$

$$w_{l1}(x) = g_7 x + g_8. \quad (3.86)$$

The boundary and matching conditions for the determination of g_1 - g_8 are (see Fig. 3.5):

$$w_{u2}(c) = 0, \quad w_{l2}(c) = 0, \quad w'_{u2}(c) = 0, \quad w'_{l2}(c) = 0, \quad (3.87)$$

$$w_{u1}(0) = w_{u2}(0), \quad w_{l1}(0) = w_{l2}(0), \quad w'_{u1}(0) = w'_{u2}(0), \quad w'_{l1}(0) = w'_{l2}(0).$$

The constants, g_1 - g_8 are given in Appendix A. The compliance of each arm of the model after simplifications (WANG and QIAO, 2004a) is improved by the following terms:

$$C_{SH,1} = \frac{w_{u1}(-a)}{P_1} = \frac{(P_1 + P_2)a^3}{2P_1 b h^3 E_{11}} f_{SH1}, \quad (3.88)$$

$$C_{SH,2} = \frac{w_{l1}(-a)}{P_2} = \frac{(P_1 + P_2)a^3}{2P_2 b h^3 E_{11}} f_{SH1}, \quad (3.89)$$

where:

$$f_{SH1} = 0.98 \left(\frac{h}{a} \right) \left(\frac{E_{11}}{G_{13}} \right)^{\frac{1}{2}} + 0.43 \left(\frac{h}{a} \right)^2 \left(\frac{E_{11}}{G_{13}} \right). \quad (3.90)$$

The SERR for the upper and lower arms by using Eq. (3.22) are:

$$G_{SH,1} = \frac{P_1(P_1 + P_2)a^3}{2bh^3 E_{11}} f_{SH2}, \quad (3.91)$$

$$G_{SH,2} = \frac{P_2(P_1 + P_2)a^3}{2bh^3 E_{11}} f_{SH2}, \quad (3.92)$$

where:

$$f_{SH2} = 1.96 \left(\frac{h}{a} \right) \left(\frac{E_{11}}{G_{13}} \right)^{\frac{1}{2}} + 0.43 \left(\frac{h}{a} \right)^2 \left(\frac{E_{11}}{G_{13}} \right). \quad (3.93)$$

3.5 Mode-mixity analysis - global method

Here we adopt WILLIAMS' global mode decomposition method (1988). Let us consider the problem in Fig. 3.6a, in which we incorporate the elastic foundation, transverse shear, *Saint-Venant* and crack tip shear deformation effects. The compliance of the upper arm of the model (Fig. 3.6a) by adding Eqs. (3.19), the last term of (3.47), furthermore (3.62) and (3.88) is:

$$C_1 = \frac{7a^3 + L^3}{2bh^3 E_{11}} + \frac{(L^3 - a^3)P_2}{2bh^3 E_{11}P_1} + \frac{L(P_1 + P_2) + a(P_1 - P_2)}{2bhkG_{13}P_1} + \frac{a^3(P_1 - P_2)}{2bh^3 E_{11}P_1} \left(f_{w1} + \frac{f_{SV}}{2} \right) + \frac{a^3(P_1 + P_2)}{2bh^3 E_{11}P_1} f_{SH1}. \quad (3.94)$$

Similarly, the compliance of the lower arm by summing Eqs. (3.20), the last term of (3.48), furthermore (3.63) and (3.89) is:

$$C_2 = \frac{7a^3 + L^3}{2bh^3 E_{11}} + \frac{(L^3 - a^3)P_1}{2bh^3 E_{11}P_2} + \frac{L(P_1 + P_2) + a(P_2 - P_1)}{2bhkG_{13}P_2} + \frac{a^3(P_2 - P_1)}{2bh^3 E_{11}P_2} \left(f_{w1} + \frac{f_{SV}}{2} \right) + \frac{a^3(P_1 + P_2)}{2bh^3 E_{11}P_2} f_{SH1}, \quad (3.95)$$

where f_{w1} is the correction from two-parameter elastic foundation analysis, f_{SV} is the correction from *Saint-Venant* effect and f_{SH1} is from crack tip shear deformation analysis. Note that the *Saint-Venant* effect is considered only at the crack tip. The energy release rates for the upper arm by summing Eqs. (3.23), the last term of (3.49), furthermore (3.64), (3.91) and for the lower arm by summing Eqs. (3.24), the last term of (3.50), furthermore (3.65) and (3.92) are:

$$G_1 = \frac{21P_1^2 a^2}{4bh^3 E_{11}} - \frac{3P_1 P_2 a^2}{4bh^3 E_{11}} + \frac{P_1(P_1 - P_2)a^2}{4bh^3 E_{11}} (f_{w2} + f_T + f_{SV}) + \frac{P_1(P_1 + P_2)a^2}{4bh^3 E_{11}} f_{SH2}, \quad (3.96)$$

$$G_2 = \frac{21P_2^2 a^2}{4bh^3 E_{11}} - \frac{3P_1 P_2 a^2}{4bh^3 E_{11}} + \frac{P_2(P_2 - P_1)a^2}{4bh^3 E_{11}} (f_{w2} + f_T + f_{SV}) + \frac{P_2(P_1 + P_2)a^2}{4bh^3 E_{11}} f_{SH2}, \quad (3.97)$$

where f_T is defined as:

$$f_T = \frac{1}{k} \left(\frac{h}{a} \right)^2 \left(\frac{E_{11}}{G_{13}} \right). \quad (3.98)$$

According to Fig. 3.6 we reduce problem (a) into problem (b), where $M_I = P_1 a$, $M_2 = P_2 a$, and $M_3 = M_I + M_2$ are bending moments at the crack tip. The sum of Eqs. (3.96) and (3.97) (i.e. the total SERR) can be transformed as:

$$G_T = \frac{21(M_1^2 + M_2^2) - 6M_1 M_2 + (M_1 - M_2)^2 (f_{w2} + f_T + f_{SV}) + (M_1 + M_2)^2 f_{SH2}}{4b^2 h^3 E_{11}} = G_I + G_{II} + G_{I/II}^*. \quad (3.99)$$

We assume that the equivalent bending moments can be decomposed as follows (WILLIAMS, 1988; DUCEPT et al., 1999):

$$M_I = M_I + M_{II}, \quad (3.100)$$

$$M_2 = \alpha M_I + \varphi M_{II}.$$

WILLIAMS (1988) supposes that in the case of pure mode-II the upper and lower specimen arms have the same curvature:

$$\frac{12M_{II}}{bh^3E_{11}} = \frac{12\varphi M_{II}}{bh^3E_{11}}. \quad (3.101)$$

From this beam kinematics assumption it follows that $\varphi=1$. Substituting Eq. (3.100) into Eq. (3.99) we can separate the term containing the product of $M_I \cdot M_{II}$:

$$G_{I/II}^* = \frac{(9 + f_{SH2})M_I M_{II}(1 + \alpha)}{b^2 h^3 E_{11}}. \quad (3.102)$$

In order to cancel Eq. (3.102) we choose

$\alpha=-1$. From Eqs. (3.99) and (3.100) the mode-I and mode-II components become:

$$G_I = \frac{M_I^2(12 + f_{W2} + f_T + f_{SV})}{b^2 h^3 E_{11}}, \quad (3.103)$$

$$G_{II} = \frac{M_{II}^2(9 + f_{SH2})}{b^2 h^3 E_{11}}. \quad (3.104)$$

Rearranging Eq. (3.100) we may obtain the mode-I and mode-II bending moments as follows:

$$M_I = (M_1 - M_2)/2, \quad M_{II} = (M_1 + M_2)/2. \quad (3.105)$$

The functions in Eqs. (3.103) and (3.104) are:

$$f_{W2} = 5.42 \left(\frac{h}{a} \right) \left(\frac{E_{11}}{E_{33}} \right)^{\frac{1}{4}} \phi^{\frac{1}{2}} + 2.45 \left(\frac{h}{a} \right)^2 \left(\frac{E_{11}}{E_{33}} \right)^{\frac{1}{2}} \phi, \quad (3.106)$$

$$f_T = \frac{1}{k} \left(\frac{h}{a} \right)^2 \left(\frac{E_{11}}{G_{13}} \right), \quad (3.107)$$

$$f_{SV} = \frac{12}{\pi} \left(\frac{h}{a} \right) \left(\frac{E_{11}}{G_{13}} \right)^{\frac{1}{2}}, \quad (3.108)$$

$$f_{SH2} = 1.96 \left(\frac{h}{a} \right) \left(\frac{E_{11}}{G_{13}} \right)^{\frac{1}{2}} + 0.43 \left(\frac{h}{a} \right)^2 \left(\frac{E_{11}}{G_{13}} \right). \quad (3.109)$$

According to Eq. (3.103) the *Winkler-Pasternak* foundation, transverse shear and the *Saint-Venant* effect contributes only to the mode-I component. The first is obvious, since the two-parameter elastic foundation incorporates the differences between the lateral displacements and the angle of rotations of the upper and lower beam elements. Under mode-II these are equal to zero. As regarding to the transverse shear effect the conclusion

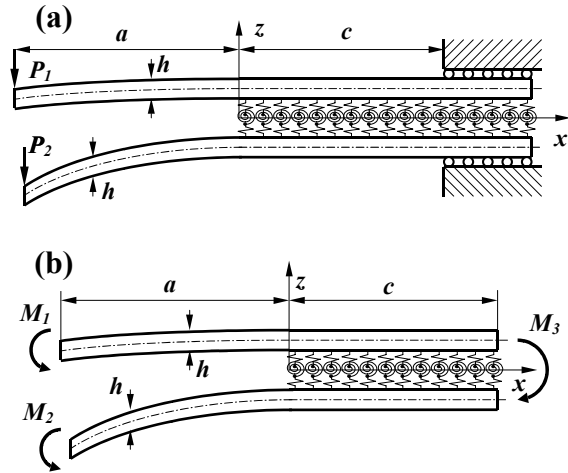


Fig. 3.6.
Reduction scheme for mixed-mode partitioning.

may be explained by the fact that under pure mode-II the cracked and uncracked regions exhibit the same shear compliance. This was supported also by OZDIL and CARLSSON (1999a) and WANG and QIAO (2004a). It has already been discussed why the *Saint-Venant* effect contributes only to the mode-I component. On the other hand the crack tip deformation improves only the mode-II component according to Eq. (3.104).

3.6 Compliance calculation

We give a general expression based on a superposition analysis, which can be used to calculate the compliance for a delaminated beam under general loading condition. The method is the generalization of that presented by OZDIL and CARLSSON (1999b). In a general form the mode-I and mode-II bending moments in Eq. (3.100) may be written as:

$$M_I = P \cdot f_I \cdot a^\#, \quad M_{II} = P \cdot f_{II} \cdot a^\#, \quad (3.110)$$

where P is the external load, f_I and f_{II} are related to geometrical parameters of the system and $a^\#$ is the characteristic length (in each case may be related to the crack length). However, this time it is helpful to use concentrated forces instead of the moments:

$$P_I = P \cdot f_I, \quad P_{II} = P \cdot f_{II}, \quad (3.111)$$

i.e.: $M_I = P_I a^\#$ and $M_{II} = P_{II} a^\#$. We note that Eqs. (3.94) and (3.95) is applicable only in particular circumstances, namely when the external loads act at the end of the specimen arms. Although the extension of the model (Eqs. (3.94) and (3.95)), for example to the ELS, SCB and DCB specimens is relatively simple, the application, for instance to the SLB and MMB specimens is not so trivial. Hence, we utilize the results obtained in Section 3.5. Based on the present chapter the compliance of composite beams with midplane delamination may be written as:

$$C = C_{EB} + C_{TIM} + C_{W1} + C_{SV1} + C_{SH1} + C_{SV}, \quad (3.112)$$

where C_{EB} is the result of *Euler-Bernoulli* beam theory, C_{TIM} is the contribution of transverse shear deformation, C_{W1} is the effect of the *Winkler-Pasternak* foundation, C_{SV1} is from the *Saint-Venant* effect at the crack tip, C_{SH1} accounts for the crack tip shear deformation and C_{SV} considers the *Saint-Venant* effect at the clamped end. The determination of the first two terms requires a unique analysis. Usually, these two terms may be determined by following the way in Section 3.2. On the other hand C_{SV} (Eq. (3.67)) is a simple additive term. Considering the other three terms it has been shown that the *Winkler-Pasternak* foundation and the *Saint-Venant* effect at the crack tip contributes to the mode-I, while the crack tip deformation improves the mode-II component. We assume that the deflection at the point of load application is equal to the sum of the displacements related to the mode-I and mode-II effects:

$$\delta = f_I \delta_I + f_{II} \delta_{II}, \quad (3.113)$$

where f_I and f_{II} are the same as those mentioned in Eq. (3.110). The compliance corrections related to the mode-I and mode-II effects may be expressed as:

$$C_I = \frac{\delta_I}{P_I} = C_{W1} + C_{SV1}, \quad C_{II} = \frac{\delta_{II}}{P_{II}} = C_{SH1}. \quad (3.114)$$

The combination of Eqs. (3.111) and (3.114) with Eq. (3.113) leads to the following:

$$\delta = C_I f_I^2 P + C_{II} f_{II}^2 P. \quad (3.115)$$

The compliance of the system is defined as $C=\delta/P$, hence we obtain:

$$C = C_I f_I^2 + C_{II} f_{II}^2. \quad (3.116)$$

It should be mentioned that the moments M_I and M_{II} (and so even P_I and P_{II}) are calculated by using the loads at the end of the specimen arms, on the other hand the effect of the external load is incorporated in Eq. (3.111). Therefore, the terms C_{WI} , C_{SVI} and C_{SHI} may be calculated by eliminating P_I and P_2 in the last two terms of Eqs. (3.94) and (3.95), i.e.:

$$C_{WI} = \frac{a^3}{2bh^3 E_{11}} f_{WI}, \quad C_{SVI} = \frac{a^3}{2bh^3 E_{11}} \frac{f_{SV}}{2}, \quad C_{SHI} = \frac{a^3}{2bh^3 E_{11}} f_{SHI}. \quad (3.117)$$

Combining Eqs. (3.114), (3.116) and (3.117) the following expression is obtained:

$$C = C_{EB} + C_{TIM} + \frac{f_I^2 a^3}{2bh^3 E_{11}} (f_{WI} + \frac{f_{SV}}{2}) + \frac{f_{II}^2 a^3}{2bh^3 E_{11}} f_{SHI} + C_{SV}, \quad (3.118)$$

where f_{WI} is given by Eq. (3.21), f_{SV} is given by Eq. (3.66), f_{SHI} is defined by Eq. (3.90) and C_{SV} is given by Eq. (3.67). Finally, there is now only one unknown parameter, ω , of which determination is detailed in the following.

3.7 Determination of the coefficient of the *Pasternak* foundation

We assumed that the torsional springs in the two-parameter elastic foundation (see Fig. 3.1) are related to the through-thickness (E_{33}) modulus of the specimen. Let us consider a spring with stiffness of infinity, this is equivalent to the case, when $E_{33}=\infty$. If this is the case there are no relative lateral displacement between the upper and lower beam elements of the uncracked region. Moreover, in this case the relative angle of rotation of the upper and lower beam elements is also equal to zero, and consequently the potential energy in the torsional springs becomes zero (Eq. (3.1)). This indicates that the initial assumption is right. In order to determine the unknown parameter of ω the FE method is used. However, some modifications in comparison with the traditional analyses should be made. First of all the effect of two-parameter elastic foundation should be separated within the model. In other words the transverse shear, *Saint-Venant* and crack tip shear deformation effects, which are related to the shear modulus of the model should be eliminated. This may be achieved if we construct a model, wherein the shear modulus tends to infinity, i.e.: $G_{13}\rightarrow\infty$. If this is the case the terms in Eq. (3.112), which are related to the shear modulus G_{13} vanish, since the related corrections (C_{TIM} , f_{SV} , f_{SHI} , C_{SV}) become zero. It may be assumed that the remained correction arises from the *Winkler-Pasternak* foundation (f_{WI}).

To determine ω the simplest way is to consider the FE model of a special DCB specimen (see Fig. 2.6b), which exhibits shear modulus of $G_{13}=100\ 000$ GPa. The compliance of the FE model of the DCB specimen may be written as (WANG and WILLIAMS, 1992):

$$C_{FE}^{DCB} = \frac{8(a + \xi h)^3}{bh^3 E_{11}}, \quad (3.119)$$

where ξ is the correction from the FE analysis if $G_{13}=100\ 000$ GPa. Rearranging Eq. (3.119) ξ is equal to:

$$\xi = \sqrt[3]{\frac{C_{FE}^{DCB} b E_{11}}{8} - \frac{a}{h}}. \quad (3.120)$$

The corrected SERR by using Eqs. (1.2) and (3.119) is:

$$G_{I,FE}^{DCB} = \frac{12P^2(a + \xi h)^2}{b^2 h^3 E_{11}}, \quad (3.121)$$

where it was assumed that the correction ξ does not depend on the crack length, it depends only on material properties.

For the application of the analytical model (Eqs. (3.103) and (3.104)) we need the bending moments at the crack tip of the DCB specimen, which are: $M_I = -M_{II} = Pa$. Furthermore, Eq. (3.105) yields that $M_I = Pa$ and $M_{II} = 0$ and from Eq. (3.110) that $f_I = 1$ and $f_{II} = 0$. Incorporating Eqs. (3.103) and (3.106) the strain energy release rate of the DCB specimen including only the effect of the two-parameter elastic foundation is:

$$G_{I,WP}^{DCB} = \frac{12P^2 a^3}{b^2 h^3 E_{11}} + \frac{P^2 a^2}{b^2 h^3 E_{11}} \left[5.42 \left(\frac{h}{a} \right) \left(\frac{E_{11}}{E_{33}} \right)^{\frac{1}{4}} \phi^{\frac{1}{2}} + 2.45 \left(\frac{h}{a} \right)^2 \left(\frac{E_{11}}{E_{33}} \right)^{\frac{1}{2}} \phi \right], \quad (3.122)$$

where $\phi = 1 + \omega$. The FE analysis was performed by using the COSMOS/M 2.0 package. The DCB specimen was meshed with linear elastic PLANE2D elements under plane stress state. The upper and lower arms of the model were subjected to a concentrated force equal to unity (see Fig. A1 in Appendix A). The displacements of the arms were used to calculate the compliance of the model, the value of ξ was determined from Eq. (3.120). The next step is to compare Eq. (3.121) with Eq. (3.122). In Eq. (3.122) ω should be chosen in order to reach the best agreement with Eq. (3.121), i.e. with the FE solution, where G_{I3} is equal to 100 000 GPa. A large amount of FE analysis on models of the DCB specimen with different geometry and material properties were performed in the crack length range of $a=30$ to 100mm. The results are summarized in Table A1 (Appendix A). In all the cases it was found that if we choose $\omega=2.5$ then the agreement between the FE and analytical solution is excellent. Also, this result ($\omega > 1$) give reason for why Eq. (3.10) was chosen as the solution of Eq. (3.7).

3.8 Conclusions, scientific significance

The global mode decomposition method was improved with the *Winkler-Pasternak* foundation, transverse shear, *Saint-Venant* effect and shear deformation of the crack tip. It was shown that the first three of these effects contribute only to the mode-I strain energy release rate, while the crack tip shear deformation improves only the mode-II component. Also, a general expression for the compliance of unidirectional composite beams with midplane delamination was developed, however the determination of the terms related to the *Euler-Bernoulli* and *Timoshenko* beam theory - depending on the geometry of the problem - requires a unique analysis. Finally, the coefficient of the *Pasternak* foundation parameter, ω was determined using the developed model and the finite element method and was found to be a constant value ($\omega=2.5$).

4 COMPARISON WITH OTHER SOLUTIONS

In this section the models of the SCB, SLB and MMB delamination specimens are examined. Four different solutions are extended for these fracture specimens including mode-mixity analysis: beam theory-based solution I, which was developed in Chapter 3, beam theory-based solution II. (CARLSSON et al., 1986; WILLIAMS, 1989; OLSSON, 1992), a solution based on refined plate theory (BRUNO and GRECO, 2001a, 2001b) and a numerical (FE) solution by BAO et al. (1992). Furthermore, mode decomposition based on the VCCT was achieved in all the three mixed-mode specimens. The delamination coupons are illustrated in Fig. 4.1.

4.1 Analytical solutions

4.1.1 Beam theory-based solution I.

Comparing Fig. 3.6a with Fig. 4.1a we may write: $M_I=0$, $M_2=Pa$. From Eq. (3.105) it follows that $M_I=M_{II}=Pa/2$. Comparing the latter to Eq. (3.110) we may write that $f_I=f_{II}=1/2$ and $a^\# = a$. The compliance of the SCB specimen based on Eq. (3.118) (where the terms C_{EB} and C_{TIM} were determined by following the way in Section 3.2) becomes ($\omega=2.5$):

$$C^{SCB} = \frac{7a^3 + L^3}{2bh^3 E_{11}} + \frac{3(2a^2 + L^2)}{\pi 2bh^2 E_{11}} \left(\frac{E_{11}}{G_{13}} \right)^{\frac{1}{2}} + \frac{a^3}{2bh^3 E_{11}} \left[0.98 \left(\frac{h}{a} \right) \left(\frac{E_{11}}{G_{13}} \right)^{\frac{1}{2}} + 0.43 \left(\frac{h}{a} \right)^2 \left(\frac{E_{11}}{G_{13}} \right) \right] + \frac{a+L}{2bhkG_{13}} + \frac{a^3}{2bh^3 E_{11}} \left[5.07 \left(\frac{h}{a} \right) \left(\frac{E_{11}}{E_{33}} \right)^{\frac{1}{4}} + 8.58 \left(\frac{h}{a} \right)^2 \left(\frac{E_{11}}{E_{33}} \right)^{\frac{1}{2}} + 2.08 \left(\frac{h}{a} \right)^3 \left(\frac{E_{11}}{E_{33}} \right)^{\frac{3}{4}} \right]. \quad (4.1)$$

Also, the *Saint-Venant* effect at the clamped end should be considered, i.e. Eq. (3.67) is also included in the second term of Eq. (4.1). The SERR of the SCB coupon in Fig. 4.1a may be obtained from Eqs. (3.103)-(3.109):

$$G_I^{SCB} = \frac{12P^2 a^2}{4b^2 h^3 E_{11}} \left[1 + 0.85 \left(\frac{h}{a} \right) \left(\frac{E_{11}}{E_{33}} \right)^{\frac{1}{4}} + 0.71 \left(\frac{h}{a} \right)^2 \left(\frac{E_{11}}{E_{33}} \right)^{\frac{1}{2}} + 0.32 \left(\frac{h}{a} \right) \left(\frac{E_{11}}{G_{13}} \right)^{\frac{1}{2}} + 0.1 \left(\frac{h}{a} \right)^2 \left(\frac{E_{11}}{G_{13}} \right) \right], \quad (4.2)$$

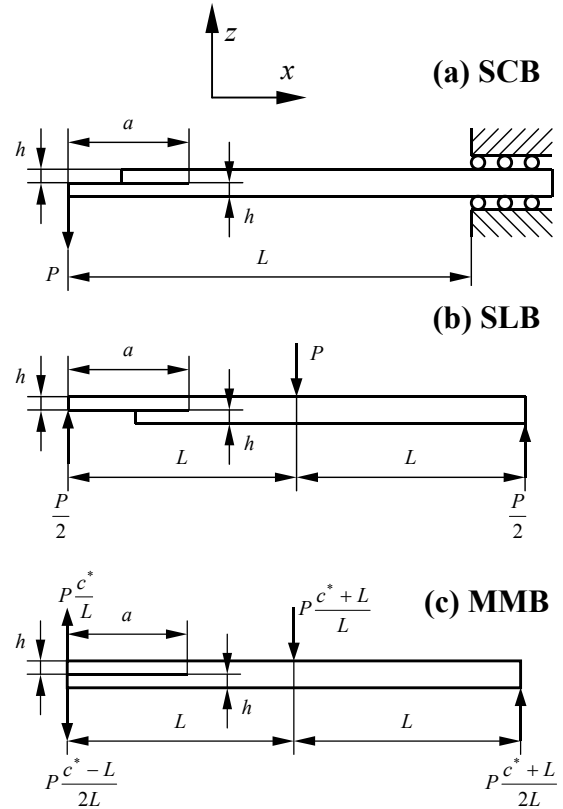


Fig. 4.1. Mixed-mode I/II delamination specimens.

$$G_{II}^{SCB} = \frac{9P^2 a^2}{4b^2 h^3 E_{11}} \left[1 + 0.22 \left(\frac{h}{a} \right) \left(\frac{E_{11}}{G_{13}} \right)^{\frac{1}{2}} + 0.048 \left(\frac{h}{a} \right)^2 \left(\frac{E_{11}}{G_{13}} \right) \right]. \quad (4.3)$$

In a similar fashion it may be shown (SZEKRÉNYES and UJ, 2004a) that the compliances, C_{EB} and C_{TIM} of the SLB specimen (Fig. 4.1b) may be obtained by replacing $2L^3$ with L^3 in the first term and $2L$ with L in the fourth term of Eq. (4.1). Furthermore, we may write that $M_I = Pa/2$, $M_2 = 0$. From Eq. (3.105) it follows that $M_I = M_{II} = Pa/4$. Comparing the latter to Eq. (3.110) we obtain that $f_I = f_{II} = 1/4$ and $a^\# = a$. The compliance of the SLB specimen by using Eq. (3.118) is (note that there is not a clamped end, i.e. C_{SV} in Eq. (3.118) is not included):

$$\begin{aligned} C^{SLB} = & \frac{7a^3 + 2L^3}{8bh^3 E_{11}} + \frac{1}{\pi} \frac{3a^2}{4bh^2 E_{11}} \left(\frac{E_{11}}{G_{13}} \right)^{\frac{1}{2}} + \frac{a^3}{8bh^3 E_{11}} \left[0.98 \left(\frac{h}{a} \right) \left(\frac{E_{11}}{G_{13}} \right)^{\frac{1}{2}} + 0.43 \left(\frac{h}{a} \right)^2 \left(\frac{E_{11}}{G_{13}} \right) \right] + \\ & + \frac{a + 2L}{8bhkG_{13}} + \frac{a^3}{8bh^3 E_{11}} \left[5.07 \left(\frac{h}{a} \right) \left(\frac{E_{11}}{E_{33}} \right)^{\frac{1}{4}} + 8.58 \left(\frac{h}{a} \right)^2 \left(\frac{E_{11}}{E_{33}} \right)^{\frac{1}{2}} + 2.08 \left(\frac{h}{a} \right)^3 \left(\frac{E_{11}}{E_{33}} \right)^{\frac{3}{4}} \right]. \end{aligned} \quad (4.4)$$

Using the same mode-I and mode-II bending moments we obtain from Eqs. (3.103)-(3.109):

$$\begin{aligned} G_I^{SLB} = & \frac{12P^2 a^2}{16b^2 h^3 E_{11}} \left[1 + 0.85 \left(\frac{h}{a} \right) \left(\frac{E_{11}}{E_{33}} \right)^{\frac{1}{4}} + 0.71 \left(\frac{h}{a} \right)^2 \left(\frac{E_{11}}{E_{33}} \right)^{\frac{1}{2}} + \right. \\ & \left. + 0.32 \left(\frac{h}{a} \right) \left(\frac{E_{11}}{G_{13}} \right)^{\frac{1}{2}} + 0.1 \left(\frac{h}{a} \right)^2 \left(\frac{E_{11}}{G_{13}} \right) \right], \end{aligned} \quad (4.5)$$

$$G_{II}^{SLB} = \frac{9P^2 a^2}{16b^2 h^3 E_{11}} \left[1 + 0.22 \left(\frac{h}{a} \right) \left(\frac{E_{11}}{G_{13}} \right)^{\frac{1}{2}} + 0.048 \left(\frac{h}{a} \right)^2 \left(\frac{E_{11}}{G_{13}} \right) \right]. \quad (4.6)$$

The simplest way to obtain the compliance of the MMB specimen (Fig. 4.1c) is to refer to the work of OZDIL and CARLSSON (1999b):

$$C^{MMB} = \left(\frac{3c^* - L}{4L} \right)^2 C^{DCB} + \left(1 + \frac{c^*}{L} \right)^2 C^{ENF}, \quad (4.7)$$

i.e. the solution for the MMB specimen (Fig. 2.5c) may be obtained by combining the unique solutions for the mode-I DCB (Fig. 2.2a) and the mode-II ENF (Fig. 2.3a) specimens. For the former case $P_I = P$, $P_2 = -P$, while for the latter case $P_1 = P_2 = -P/4$. Following the way suggested before the compliance of the MMB specimen becomes:

$$\begin{aligned} C^{MMB} = & \left(\frac{3c^* - L}{4L} \right)^2 \left[\frac{8a^3}{bh^3 E_{11}} + \frac{2a^3}{bh^3 E_{11}} \left[\frac{6}{\pi} \left(\frac{h}{a} \right) \left(\frac{E_{11}}{G_{13}} \right)^{\frac{1}{2}} + \frac{1}{k} \left(\frac{h}{a} \right)^2 \left(\frac{E_{11}}{G_{13}} \right) \right] + \right. \\ & \left. + \frac{2a^3}{bh^3 E_{11}} \left[5.07 \left(\frac{h}{a} \right) \left(\frac{E_{11}}{E_{33}} \right)^{\frac{1}{4}} + 8.58 \left(\frac{h}{a} \right)^2 \left(\frac{E_{11}}{E_{33}} \right)^{\frac{1}{2}} + 2.08 \left(\frac{h}{a} \right)^3 \left(\frac{E_{11}}{E_{33}} \right)^{\frac{3}{4}} \right] \right] + \\ & + \left(1 + \frac{c^*}{L} \right)^2 \left[\frac{3a^3 + 2L^3}{8bh^3 E_{11}} + \frac{L}{4bhkG_{13}} + \frac{a^3}{8bh^3 E_{11}} \left[0.98 \left(\frac{h}{a} \right) \left(\frac{E_{11}}{G_{13}} \right)^{\frac{1}{2}} + 0.43 \left(\frac{h}{a} \right)^2 \left(\frac{E_{11}}{G_{13}} \right) \right] \right]. \end{aligned} \quad (4.8)$$

Note that Eq. (4.8) may also be obtained by using Eq. (3.118). For the MMB specimen (Fig. 4.1c): $M_1 = Pc^*a/L$, $M_2 = P(c^* - L)a/2L$, thus we have from Eqs. (3.103)-(3.109):

$$G_I^{MMB} = \frac{12P^2a^2(3c^* - L)^2}{16b^2h^3E_{11}L^2} \left[1 + 0.85 \left(\frac{h}{a} \right) \left(\frac{E_{11}}{E_{33}} \right)^{\frac{1}{4}} + 0.71 \left(\frac{h}{a} \right)^2 \left(\frac{E_{11}}{E_{33}} \right)^{\frac{1}{2}} + 0.32 \left(\frac{h}{a} \right) \left(\frac{E_{11}}{G_{13}} \right)^{\frac{1}{2}} + 0.1 \left(\frac{h}{a} \right)^2 \left(\frac{E_{11}}{G_{13}} \right) \right], \quad (4.9)$$

$$G_{II}^{MMB} = \frac{9P^2a^2(c^* + L)^2}{16b^2h^3E_{11}L^2} \left[1 + 0.22 \left(\frac{h}{a} \right) \left(\frac{E_{11}}{G_{13}} \right)^{\frac{1}{2}} + 0.048 \left(\frac{h}{a} \right)^2 \left(\frac{E_{11}}{G_{13}} \right) \right]. \quad (4.10)$$

The mode ratio (G_I/G_{II}) in each case may be obtained by combining the equations above.

4.1.2 Beam theory-based solution II.

The classical solution of WILLIAMS (1989) for the mode-I DCB specimen was improved with transverse shear and *Saint-Venant* effect by OLSSON (1992). On the other hand CARLSSON et al. (1986) performed an improved analysis for the mode-II ENF specimen based on *Timoshenko* beam theory. Later, REEDER and CREWS (1990) obtained a solution for the MMB specimen based on the solutions by WILLIAMS (1989) and CARLSSON et al. (1986). The MMB specimen was treated as the superposition (refer to Fig. 2.6) of the DCB and ENF specimens. Combining the results of these works (by summing the proper corrections) the following expressions may be derived for the energy release rate components:

$$G_I = \frac{M_I^2(12 + f_W + f_T + f_{SV})}{b^2h^3E_{11}}, \quad (4.11)$$

$$G_{II} = \frac{M_{II}^2(9 + f_{SH})}{b^2h^3E_{11}}, \quad (4.12)$$

where f_W is the correction from WILLIAMS classical elastic foundation model (Fig. 2.2b):

$$f_W = 15.36 \left(\frac{h}{a} \right) \left(\frac{E_{11}}{E_{33}} \right)^{\frac{1}{4}} + 4.92 \left(\frac{h}{a} \right)^2 \left(\frac{E_{11}}{E_{33}} \right)^{\frac{1}{2}}, \quad (4.13)$$

$$f_{SH} = 1.8 \left(\frac{h}{a} \right)^2 \left(\frac{E_{11}}{G_{13}} \right), \quad (4.14)$$

where f_T and f_{SV} is defined by Eqs. (3.107 and (3.108). The equations above will be referred to as the solution by CARLSSON and OLSSON. The bending moments at the crack tip in the case of the SCB, SLB and MMB specimens are the same as those mentioned in Section 4.1.1.

4.1.3 Solution based on numerical calibration

BAO et al. (1992) derived the energy release rate components based on FE calculation for certain composite specimens. The following generalized expressions can be obtained based on their formulation:

$$G_I = \frac{12M_I^2 Y_I^2}{b^2 h^3 E_{11}}, \quad (4.15)$$

$$G_{II} = \frac{9M_{II}^2 Y_{II}^2}{b^2 h^3 E_{11}}, \quad (4.16)$$

where:

$$Y_I = 1 + (0.677 + 0.146\beta - 0.0178\beta^2 + 0.00242\beta^3)\psi^{-\frac{1}{4}}\left(\frac{h}{a}\right), \quad (4.17)$$

$$Y_{II} = 1 + (0.206 + 0.0761\beta - 0.00978\beta^2 + 0.00112\beta^3)\psi^{-\frac{1}{4}}\left(\frac{h}{a}\right), \quad (4.18)$$

$$\psi = \frac{E_{33}}{E_{11}}, \quad \beta = \frac{(E_{11}E_{33})^{\frac{1}{2}}}{2G_{13}} - (\nu_{13}\nu_{31})^{\frac{1}{2}} - 1. \quad (4.19)$$

The above solution is based on the principle of superposition, for instance the solution for the mixed-mode SCB specimen was obtained as the sum of the mode-I DCB and the mode-II ELS specimens (refer to Fig. 2.6). Moreover it is assumed that $\nu_{13} = \nu_{31}$.

4.1.4 Solution based on a refined plate model

BRUNO and GRECO (2001a, 2001b) utilized a linear elastic interface model between two *Reissner-Mindlin* plates. Their solution can be simply extended for the mixed-mode I/II coupons in Fig. 4.1. The solution after some transformations can be written as:

$$G_I = \frac{M_I^2 (12 + f_{BS} + f_T)}{b^2 h^3 E_{11}}, \quad (4.20)$$

$$G_{II} = \frac{9M_{II}^2}{b^2 h^3 E_{11}}, \quad (4.21)$$

$$f_{BS} = 7.59 \left(\frac{h}{a}\right) \left(\frac{E_{11}}{G_{13}}\right)^{\frac{1}{2}}, \quad (4.22)$$

where f_T is given by Eq. (3.107). It should be noted that this formulation gives equivalent result to the simple beam theory as regarding to the mode-II component (see Eq. (4.21)).

4.2 Finite element solution - VCCT method

For the mixed-mode I/II specimens a series of FE models were constructed to obtain the mode ratios within reasonable crack length ranges. For the SCB and SLB specimens the compliance was also computed in order to give some comparison with the analytical solutions. The models were developed in the commercial code COSMOS/M 2.0 using PLANE2D elements under plane stress state, which is consistent with the beam formulation of the problems. The FE models of the SCB and SLB specimens were subjected to a concentrated force equal to unity. In the case of the MMB specimen the concentrated forces at

the upper arm and the center point of the specimen were calculated based on Fig. 4.1, in this case $P=1$ N was used. Otherwise, the end point of the lower arm and the point below the left support was constrained in direction x and $x-z$, respectively (see Fig. 2.5c). The details of the FE model for the SCB specimen, together with the boundary conditions are demonstrated in Fig. 4.2. The models for the SLB and MMB specimens were quite similar ones. The specimens were 150 mm long, $b=20$ mm wide and $2h=6.1$ mm thick. The material properties are given for glass/polyester composite specimens, which were manufactured in our laboratory. The flexural modulus of the specimens were determined through a non-standard three-point bending test with the following dimensions: span length of $2L=151$ mm, width of $b=20$ mm and thickness of $2h=6.1$ mm. The experiment resulted in $E_{11}=33$ GPa. Additional material properties were predicted by means of *Niederstadt's* (THAMM, 1985) approximate rule of mixture, this way $E_{33}=7.2$ GPa, $G_{13}=3$ GPa and $\nu_{13}=\nu_{31}=0.27$ were obtained. The

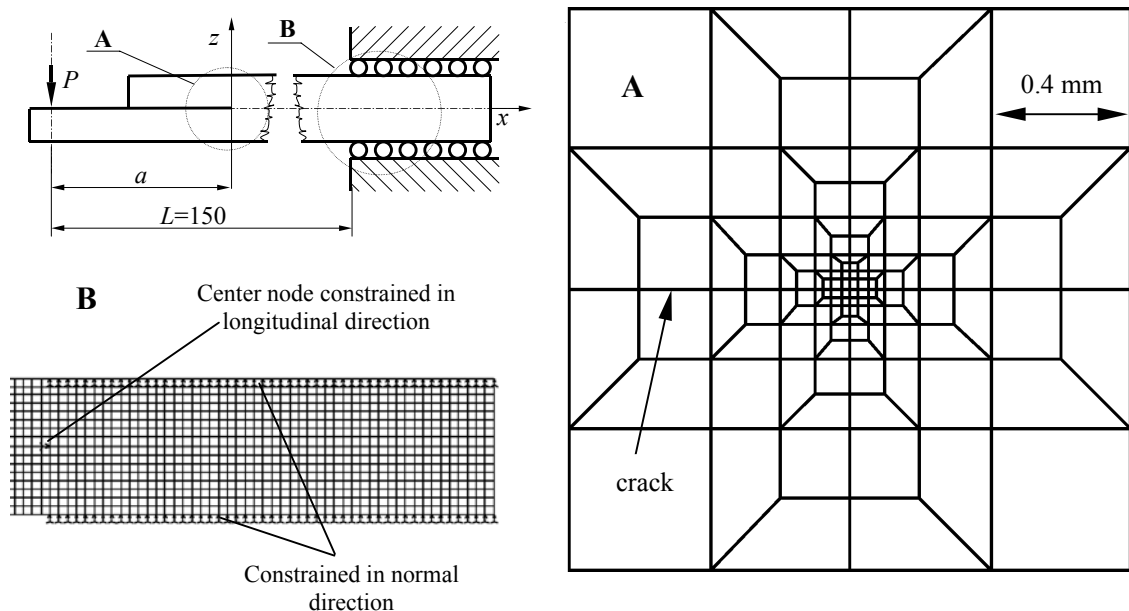


Fig. 4.2.
Details of the FE mesh around the crack tip and boundary conditions.

equations of the VCCT method are given in Chapter 2 (see Eqs (2.4) and (2.5)). A finite element mesh around the crack tip, as suggested by DAVIDSON et al. (1996) was constructed, as it is shown in Fig. 4.2. The *Saint-Venant* effect at the clamped end of the SCB specimen was also accounted for, as it is illustrated also in Fig. 4.2. Also, the case of the traditional clamped end was studied in this case. Crack tip elements with finite crack extension of $\Delta a=0.025$ mm were constructed.

4.3 Results

In the following the compliance and SERR expressions from different solutions are compared to each other (SZEKRÉNYES, 2004a; SZEKRÉNYES and UJ, 2005a). It should be mentioned that only those compliance expressions are given above, which are based on our

solution. In the work of BAO et al. (1992) expressions for the compliance are not given, and so, this void was addressed by our FE models, except in the case of the MMB specimen, where due to the complex fixture the compliance calculation is difficult. The other two solutions for the compliance of the specimens are detailed in relevant papers (CARLSSON et al., 1986; WILLIAMS, 1989; OLSSON, 1992; BRUNO and GRECO, 2001a, 2001b). All the equations were normalized with the results of the *Euler-Bernoulli* (C_{EB}) beam theory. These are the first terms in Eqs. (4.1)-(4.10). The normalized compliance and SERR expressions are plotted against the normalized crack length.

4.3.1 Compliance

The normalized compliance expressions for the SCB coupon are shown in Fig. 4.3a. Without the *Saint-Venant* effect the solutions agree well. The FE solution provides somewhat different values compared to the analytically obtained curves if the *Saint-Venant* effect is

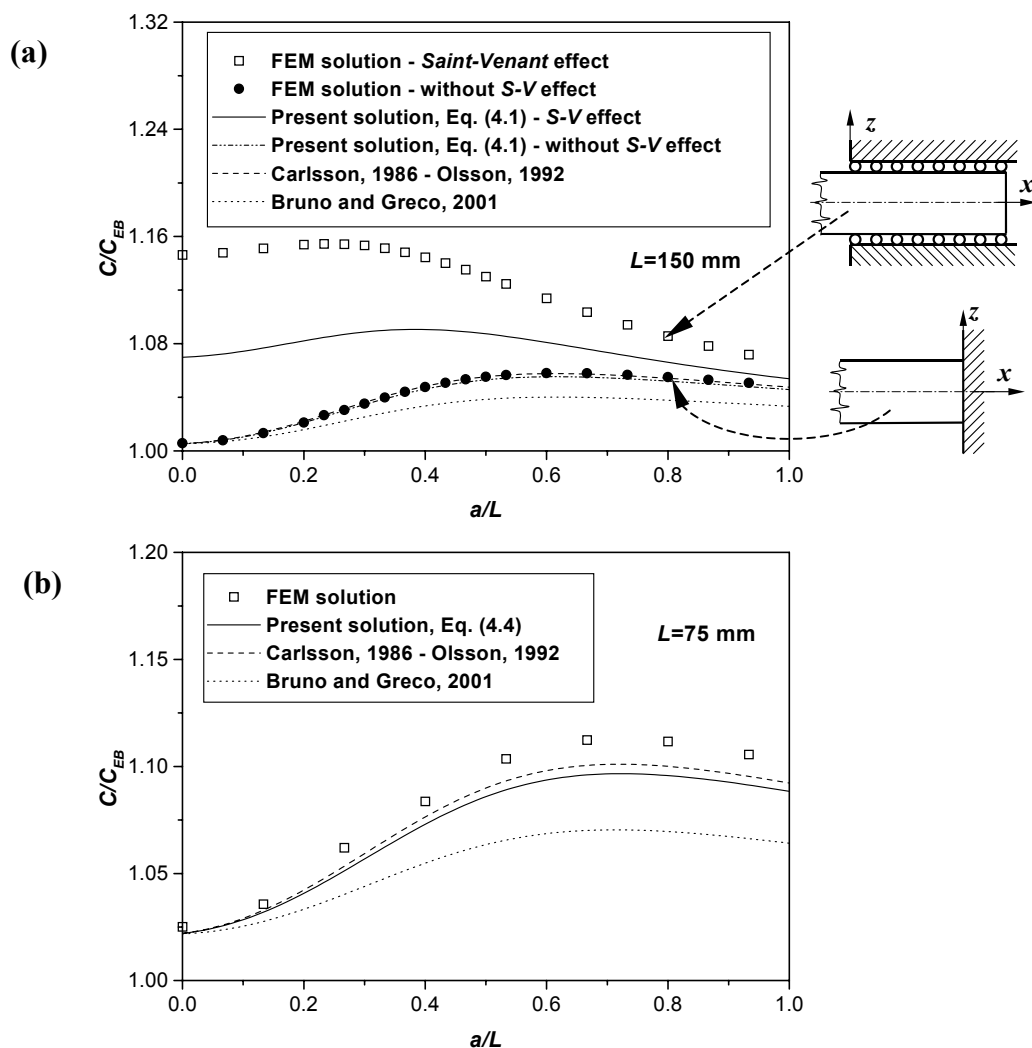


Fig. 4.3. Comparison of the compliance of the SCB (a) and SLB (b) specimens.

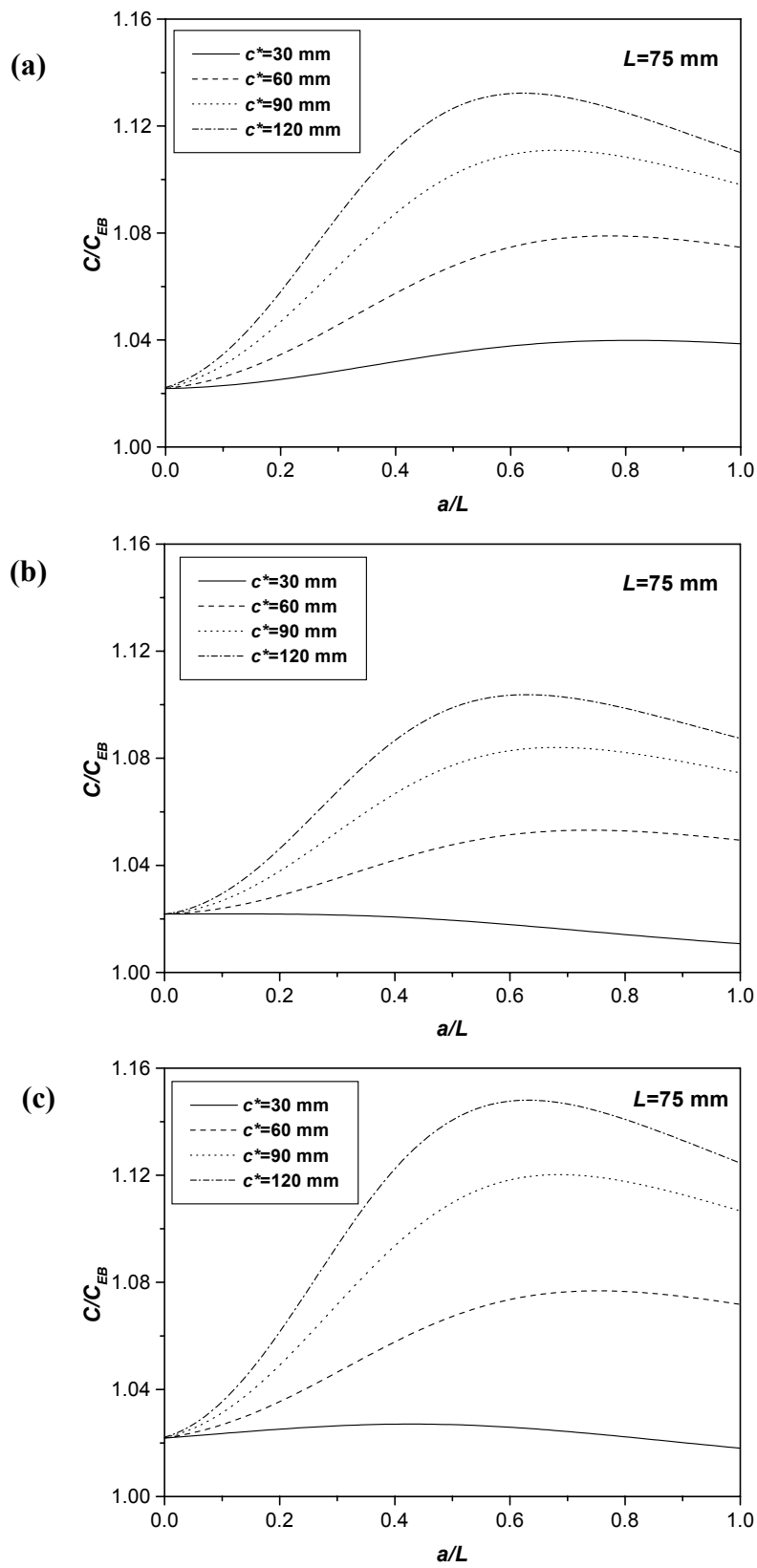


Fig. 4.4.

Comparison of the compliance of the MMB specimen. Present solution (a), solution by BRUNO and GRECO, 2001 (b), solution by CARLSSON, 1986 – OLSSON, 1992 (c).

included. It should be mentioned that the contribution from the *Saint-Venant* effect (the second term in Eq. (4.1)) at the clamped end of the SCB specimen is about half time of that predicted by the FE model. In fact all the analytical curves follow the same trend. Quite similar curves were obtained in the case of the SLB specimen, as it is shown in Fig. 4.3b. For the MMB specimen the normalized compliance was displayed at four different lever lengths c^* by three different solutions (refer to Fig. 4.4). In the case of $c^*=30$ mm the present solution

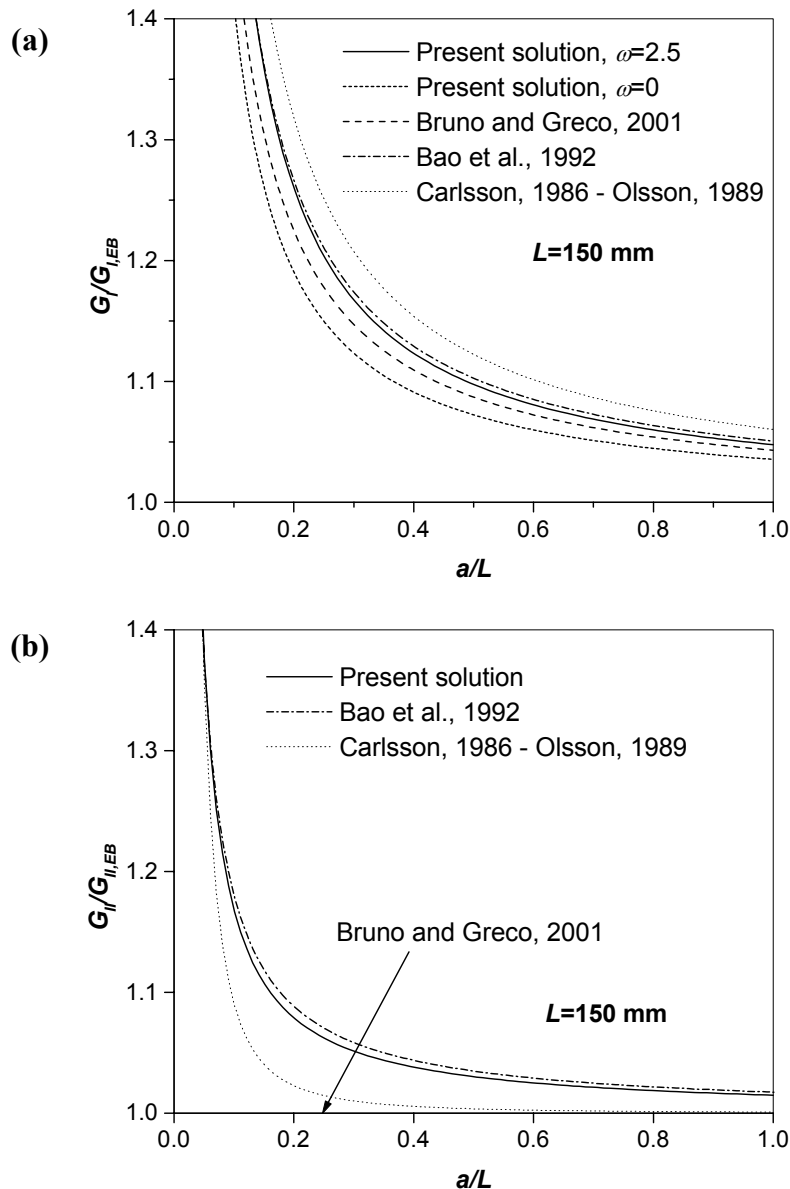


Fig. 4.5.

Comparison of the mode-I (a) and mode-II (b) energy release rate for the SCB specimen.

provides the largest improvement. If $c^*=60$ mm the present and CARLSSON-OLSSON's solution show similar tendencies. At the other lever length values the solution by CARLSSON-OLSSON gives the largest improvement.

In fact, in most of the cases demonstrated in Figs. 4.3 and 4.4 the solution by OLSSON and CARLSSON provides the largest enhancement, however it should be mentioned, that the

SERR - which is more important than the compliance - incorporates the derivative of the compliance with respect to the crack length (refer to Eq. (1.2)).

4.3.2 Strain energy release rate

G_I and G_{II}

The results for the SERR of the SCB specimen are illustrated in Fig. 4.5. For the glass/polyester specimens (Fig. 4.5a) our solution gives the best correlation compared to the numerical solution. The overprediction by OLSSON and CARLSSON in comparison with BAO's solution is somewhat surprising. Fig 4.5a also contains the result of the present solution if

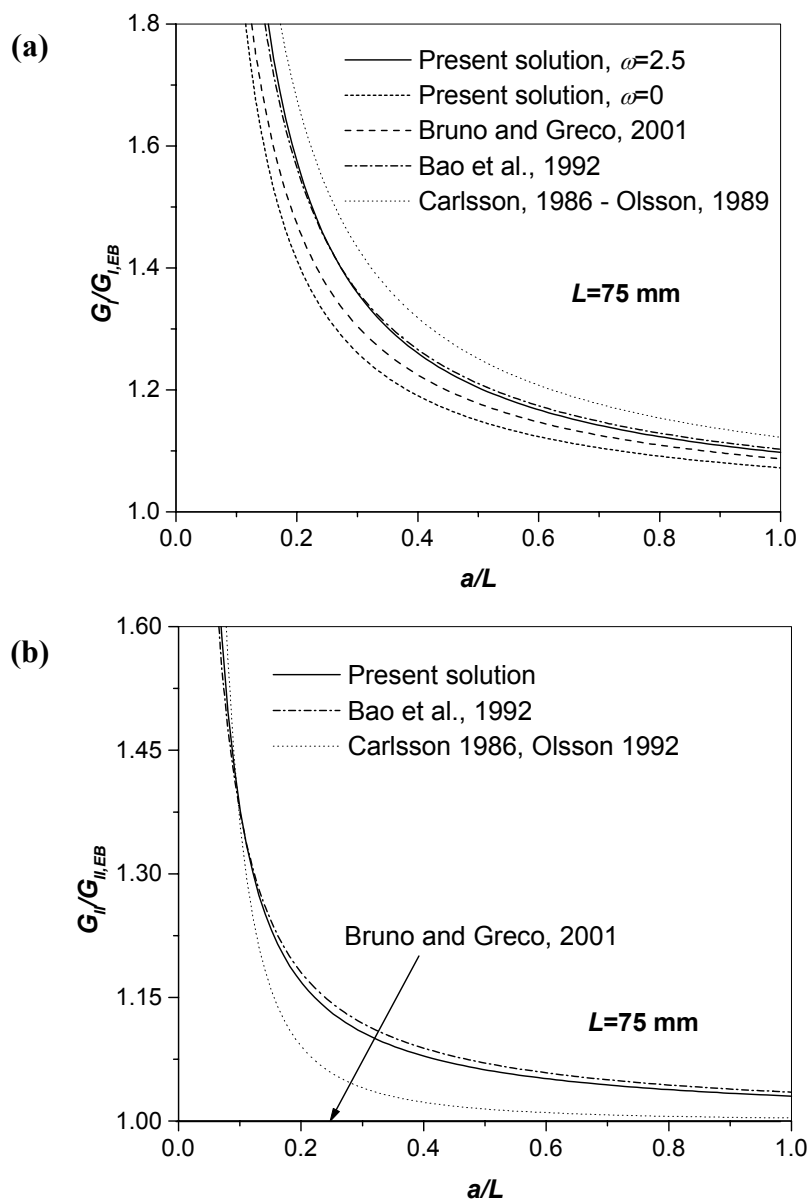


Fig. 4.6.

Comparison of the mode-I (a) and mode-II (b) energy release rate for the SLB and MMB specimens.

$\omega=0$. In this case the difference between the present solution and the one by CARLSSON-OLSSON is proportional to the difference between Eqs. (4.13) and (3.106). Figs. 4.6a and 4.6b present the same results for the SLB and MMB coupons. For both specimens essentially the same trends were obtained.

The normalized mode-II component is plotted in Figs. 4.5b-4.6b. In each case, the agreement was excellent between our model and the one by BAO et al. In contrast, the mode-II component is equivalent to the formula of *Euler-Bernoulli* beam model in accordance with the formulation of BRUNO and GRECO (Fig. 4.6b). Although the model by CARLSSON provides some correction for the mode-II component, it is clear, that our solution (which is based on the work by WANG and QIAO (2004a)) seems to be more reasonable.

The mode ratio

The mode ratios for the SCB specimen by five different approximations are compiled in Table 4.1. Slightly distinct results were obtained even in this case. The models by BRUNO and GRECO and CARLSSON-OLSSON show larger mode-I dominance compared to the other solutions. BAO's numerical formulation shows good agreement with our results. Finally, the plane stress FE model also shows some crack length dependence of the mode ratio but the mode-I dominance is not as significant here as in any of the former cases.

Table 4.2 presents the results for the SLB specimen. In this respect our solution matches well with BAO's solution and the result of the VCCT. Notice that the mode ratios by the closed-form solutions are the same as they are in the case of the SCB specimen.

Table 4.1.
Mode ratios (G_I/G_{II}) by different methods, SCB specimen.

a [mm]	20	30	40	50	60	70	80	90	100
	1.676	1.557	1.500	1.465	1.443	1.427	1.415	1.406	1.398 *
	1.764	1.633	1.555	1.509	1.479	1.458	1.442	1.430	1.420 **
	1.665	1.555	1.500	1.467	1.445	1.429	1.417	1.408	1.400 ***
	1.893	1.719	1.626	1.569	1.530	1.502	1.481	1.465	1.452 ****
	1.250	1.176	1.144	1.120	1.105	1.093	1.085	1.078	1.073 *****

* present, ** BRUNO and GRECO, 2001, *** BAO et al., 1992, **** CARLSSON 1986, OLSSON 1992, ***** VCCT

Table 4.2.
Mode ratios (G_I/G_{II}) by different methods, SLB specimen.

a [mm]	20	30	40	50	60	70
	1.676	1.557	1.500	1.465	1.443	1.427 *
	1.764	1.633	1.555	1.509	1.479	1.458 **
	1.665	1.555	1.500	1.467	1.445	1.429 ***
	1.893	1.719	1.626	1.569	1.530	1.502 ****
	1.658	1.572	1.529	1.502	1.493	1.483 *****

* present, ** BRUNO and GRECO, 2001, *** BAO et al., 1992, **** CARLSSON 1986, OLSSON 1992, ***** VCCT

In Table 4.3 the mode ratios are collected at four different lever length values for the MMB specimen. At $c^*=30$ mm some discrepancies were recognized between the closed-form solutions and the results of the VCCT method, maybe the lever length is not long

enough in this case to open the crack in a sufficient degree. Our and BAO's solution closely agree at each lever length, not only in the case of the numerical values, but also in the case of the dependence of the mode ratio on the crack length. At $c^*=60$ mm the VCCT agrees well with the values by CARLSSON and OLSSON's model, in contrast if $c^*=90$ mm the VCCT shows the best agreement with BAO's and the present solution. Finally if $c^*=120$ mm the results of the VCCT show significant differences in comparison with the closed-form solutions.

The summary of these results indicates that the mode ratio depends on the method applied for calculation.

Table 4.3.

Mode ratios (G_I/G_{II}) by different methods, MMB specimen.

a [mm]	25	30	40	50	60	70	
$c^*=30$ mm	0.033	0.032	0.031	0.030	0.029	0.029	*
	0.035	0.033	0.032	0.031	0.030	0.030	**
	0.033	0.032	0.031	0.030	0.029	0.029	***
	0.037	0.035	0.033	0.032	0.031	0.031	****
	0.179	0.175	0.173	0.175	0.175	0.177	*****
$c^*=60$ mm	0.971	0.942	0.907	0.887	0.873	0.863	*
	1.025	0.987	0.940	0.913	0.895	0.882	**
	0.965	0.938	0.906	0.886	0.873	0.863	***
	1.083	1.040	0.983	0.949	0.925	0.909	****
	1.102	1.066	1.038	1.025	1.015	1.018	*****
$c^*=90$ mm	2.242	2.176	2.095	2.047	2.016	1.993	*
	2.367	2.279	2.171	2.107	2.065	2.036	**
	2.227	2.166	2.091	2.045	2.015	1.993	***
	2.500	2.400	2.270	2.191	2.137	2.098	****
	2.078	2.015	1.962	1.929	1.914	1.914	*****
$c^*=120$ mm	3.428	3.328	3.204	3.131	3.083	3.048	*
	3.621	3.486	3.320	3.223	3.159	3.113	**
	3.406	3.313	3.197	3.128	3.081	3.048	***
	3.469	3.372	3.246	3.169	3.116	3.078	****
	2.843	2.759	2.686	2.637	2.620	2.616	*****

* present, ** BRUNO and GRECO, 2001, *** BAO et al., 1992, **** CARLSSON 1986, OLSSON 1992, ***** VCCT

The total strain energy release rate

Finally we investigate the total SERR (G_I+G_{II}) by the four improved solutions in comparison with the simple beam theory. The results for the SLB and the SCB specimens are collected in Table 4.4. The solution for the SLB specimen is given at the crack lengths of $a=20$ to 70 mm, while for the SCB specimen the whole range ($a=20$ to 100 mm) is valid. The differences are not significant, but it may be observed that in this respect the solution by BRUNO and GRECO exhibits the smallest enhancing effect. Further consequences may be drawn by focusing our attention on Table 4.5, where the results are listed for the MMB specimen at four different lever length values. If $c^*=30$ and 60 mm then our and BAO's solution seems to be the best. The other two solutions provide poor results, which may be explained by the fact that in this case there exists a mode-II dominated condition. Increasing

the lever length the mode-I component becomes more and more dominant, therefore the difference between the other solutions and the one by BAO et al. subsequently decays.

Table 4.4.

Comparison of the total SERR ($G_{III}/G_{III,EB}$) by different methods, SLB and SCB specimens.

a [mm]	20	30	40	50	60	70	80	90	100
	1.287	1.183	1.134	1.105	1.087	1.074	1.064	1.057	1.051 *
	1.197	1.128	1.095	1.075	1.063	1.053	1.047	1.041	1.037 **
	1.301	1.196	1.145	1.115	1.095	1.081	1.071	1.063	1.057 ***
	1.303	1.192	1.140	1.110	1.090	1.077	1.067	1.059	1.053 ****

* present, ** BRUNO and GRECO, 2001, *** BAO et al., 1992, **** CARLSSON 1986, OLSSON 1992

Table 4.5.

Comparison of the total SERR ($G_{III}/G_{III,EB}$) by different methods, MMB specimen.

a [mm]	25	30	40	50	60	70	
$c^*=30$ mm	1.102	1.084	1.062	1.049	1.040	1.034	*
	1.007	1.006	1.004	1.003	1.003	1.002	**
	1.116	1.097	1.072	1.057	1.048	1.041	***
	1.042	1.031	1.019	1.013	1.010	1.008	****
$c^*=60$ mm	1.196	1.160	1.117	1.092	1.076	1.065	*
	1.121	1.100	1.074	1.059	1.049	1.042	**
	1.203	1.168	1.124	1.099	1.082	1.070	***
	1.191	1.155	1.112	1.088	1.072	1.061	****
$c^*=90$ mm	1.241	1.197	1.144	1.114	1.094	1.080	*
	1.177	1.146	1.108	1.086	1.071	1.061	**
	1.247	1.204	1.151	1.120	1.099	1.085	***
	1.263	1.215	1.157	1.124	1.102	1.087	****
$c^*=120$ mm	1.261	1.214	1.156	1.123	1.101	1.086	*
	1.201	1.166	1.123	1.097	1.081	1.069	**
	1.267	1.220	1.163	1.129	1.107	1.091	***
	1.295	1.241	1.177	1.140	1.115	1.098	****

* present, ** BRUNO and GRECO, 2001, *** BAO et al., 1992, **** CARLSSON 1986, OLSSON 1992

4.4 Discussion

As a consequence, the different solutions give distinct results, which should be clarified. According to the present formulation the total SERR was obtained by a superposition scheme, which incorporates the influence of *Winkler-Pasternak* foundation, *Saint-Venant* effect, transverse shear and crack tip shear deformation. Interaction between them was not considered, but the mode-I and mode-II components are equally supported by reasonable values. Moreover, the comparison showed that the relationship of our solution to the one by BAO et al. is similar in all the presented cases.

We may assume that BAO's numerical model provides the more accurate result. Their model incorporates all the former effects and the possible interaction between them. We can also state that the form of the formulae is the most difficult in this case. For example the

analytical solution showed that the transverse elastic modulus, E_{33} has not any influence on the mode-II SERR (refer to Eq. (4.3)), in contrast it is included in BAO et al.'s solution (refer to Eq. (4.18)).

The refined plate model by BRUNO and GRECO affirms the significance of bending–shear interaction. Their model does not provide improved solution for the mode-II component, whereas the present and BAO's solutions show that the mode-II component should be contributed apart from simple beam theory. Thus, the overestimated mode ratios may be explained by the lack of correction for the mode-II component. Furthermore the solution does not depend on the through-thickness modulus (E_{33}) of the specimens, it depends only on the shear modulus (G_{13}). Therefore, this solution seems to be a little bit simplified.

The combined solution by CARLSSON and OLSSON is based on similar considerations to those of the present beam model. In Chapter 3 the elastic foundation was captured based on a general loading scheme under mixed-mode I/II condition, where the theorem of parallel axes (Eqs. (3.13) and (3.16)) was considered. Consequently, this effect was ignored in OLSSON's (WILLIAMS') solution, the model does not account for the theorem of parallel axes in the case of the elastic foundation and so it causes the discrepancy between Eq. (4.13) and Eq. (3.106) (if $\omega=0$). Consequently, the generalization of WILLIAMS' solution (Eqs. (2.1)-(2.2)), which was applied by numerous authors (REEDER and CREWS, 1990; OZDIL and CARLSSON, 1999b, CHEN et al., 1999) for mixed-mode I/II coupons is not straightforward. Apart from that, the mode-II component by CARLSSON is only slightly contributed in comparison with the present (WANG and QIAO, 2004a) and BAO's solution. This may cause again overprediction in the mode ratio.

It should be kept in mind that in the case of the VCCT method there is also some uncertainty, which was already highlighted in Section 2.3.2.

4.5 Conclusions, scientific significance

Based on the improved solution developed in the former chapter it was shown that in the case of mixed-mode I/II coupons the elastic foundation effect has a different form (Eq. (3.106)) compared to the classical solution by WILLIAMS (Eq. (4.13)). The source of the discrepancy between the present and WILLIAMS' solution is that in the former the second order moment of inertia with a reference plane located at the midplane of the uncracked region was calculated (theorem of parallel axes). In contrast, WILLIAMS (1989) computed the second order moment of inertia with beam height h only. This resulted in a four times higher second order moment of inertia of the uncracked region in our solution. The improved solution was extended for the models of several mixed-mode I/II delamination coupons, such as the SLB, SCB and MMB specimens. The results were compared with previously developed beam, plate and FE solutions, respectively. It was found that the present solution gives the reasonably good description of both the compliance and the strain energy release rate and in every cases shows similar relationship to the FE solution by BAO et al. (1992).

5 EXPERIMENTS

Through the experimental measurements the attention was focused on two important things. First, apart from the analytical and numerical models the experimental method is essential in order to verify the developed solutions for delamination specimens. Second, the experiments provide some structural information on the composite material, such as stiffness, strength and mainly, the resistance to delamination. In light of these conclusions the experiments play an important role in the design and development of composite structures. Thus, in the sequel some configurations previously developed in the literature will be used to confirm the application of the current analytical solution. These configurations were selected by keeping the simplicity in view. In the last subsection a novel mixed-mode configuration is presented. The details of the specimen preparation are given in Appendix B. Four kind of composite materials were manufactured in our laboratory, as it is shown by Fig. B1. For the experimental measurements only glass/polyester specimens were used. The flexural properties of the specimens were mentioned in Section 4.2.

5.1 Mode-II configurations

In the present section we analyze the mode-II ELS and ONF specimens (SZEKRÉNYES 2004b; SZEKRÉNYES and UJ, 2005b). The mode-II fracture specimens are illustrated in Fig. 5.1. Our choice can be explained by the fact that these specimens are suitable for crack propagation tests and require simpler experimental equipment than the 4ENF test (refer to Fig. 2.3c). The location of load introduction and constraints of the ELS and ONF configurations are essentially different (Fig. 2.3). Comparison between their results may be useful. Moreover, relatively small amount of experimental result was found by us as regarding to the glass fiber-reinforced ELS and, especially the ONF specimens. The test coupons are analyzed by using linear beam theories, the finite element method and experiments. Comparison between the results of the analysis, numerical solution and experiment is made.

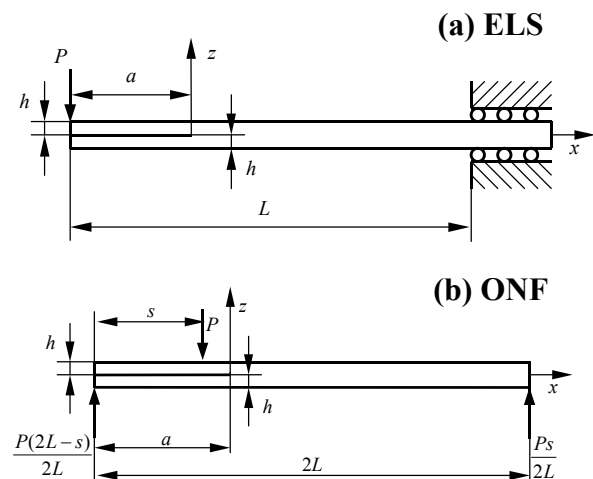


Fig. 5.1.
Mode-II delamination specimens.

5.1.1 Experimental procedure

The fixtures for the ELS and ONF tests are illustrated in Fig. 5.2. The tests were carried out using an *Amsler* testing machine under displacement control. The load-deflection

data was measured, the former was read from the scale of the testing machine, the latter was monitored by the dial gauge, shown in Figs. 5.2a and 5.2b. The distance between the load and the clamped cross section was $L=150$ mm in the case of the ELS geometry. The full span length was $2L=151$ mm for the ONF test, the position of the external load was $s=47.5$ mm (refer to Fig. 5.1). The special clamping fixture detailed in Fig. C4 (see Appendix C) was used for the ELS test. The contact regions above the supports were slightly roughened in order to prevent longitudinal sliding during the ONF test.

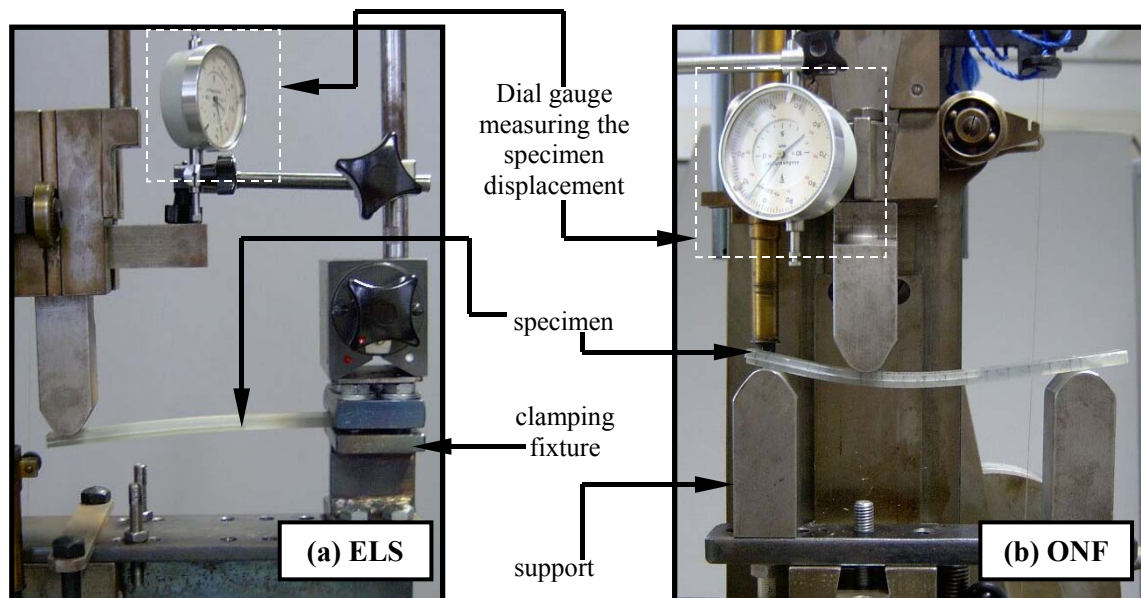


Fig. 5.2.

End-loaded split (a) and over-notched flexure (b) tests for mode-II interlaminar fracture.

Two kinds of measurements were carried out. At the first stage crack initiation tests were performed on both configurations. In the case of the ELS test the specimens with the following initial crack length values were prepared: 35, 40, 45, 50, 55, 60, 65, 70, 75, 80, 90, 100, 110, 120, 130 and 140 mm. This allowed the determination of the fracture properties at crack initiation in a quite extended ($0.23L \leq a \leq 0.93L$) crack length range. For the ONF test the crack length range from 50 to 105 mm ($0.33 \cdot 2L \leq a \leq 0.69 \cdot 2L$) with 5 mm increment was investigated. If the initial crack length was higher than 105 mm (ONF test) we were not able to facilitate crack initiation and large displacement of the specimens occurred. The specimens were tested to failure at the crack length of interest and the critical load and deflection were recorded.

At the second stage crack propagation tests using six ONF specimens with $a_0=50$ mm initial crack length were performed. A millimeter scale was traced on the lateral sides of the specimens, the crack length was measured visually by following the crack front on the upper surface of the specimens and the position of the crack tip was marked. The compliance of the specimens was determined at each crack length. The reason for using only the ONF test for crack propagation is that in the case of the ELS configuration the crack initiation was followed by large displacements. We were not able to control the crack propagation even in those crack lengths, where the stable crack propagation would have been expected.

5.1.2 Data reduction

Four methods were used for data reduction: the beam theory-based approach developed in Chapter 3, the compliance calibration (CC) (e.g.: OZDIL and CARLSSON, 1999a), the direct beam theory approach (e.g.: HASHEMI et al., 1990b) and the VCCT. In the case the ELS geometry due to the large radius of the loading head the system was corrected. This is strictly related to our non-standard fixture, thus it is detailed in Appendix D. The ONF system was not corrected, which may be explained by the fact that the correction gives misleading result in this case.

Using the developed beam model (see Chapter 3) the compliance of the ELS specimen may be obtained based on similar concepts as it was done in the case of Eqs. (4.1) and (4.4). With the aid of Fig. 5.1a we may write: $M_I=M_2=Pa/2$. From Eq. (3.105) it follows that $M_I=0$ and $M_{II}=Pa/2$. Comparing the latter to Eq. (3.110) we may write that $f_I=0$, $f_{II}=1/2$ and $a^\# = a$. The terms C_{EB} and C_{TIM} were determined by following the way in Section 3.2. The compliance based on Eq. (3.118) is:

$$C^{ELS} = \frac{3a^3 + L^3}{2bh^3 E_{11}} + \frac{L}{2bhkG_{13}} + \frac{3}{\pi} \frac{L^2}{2bh^2 E_{11}} \left(\frac{E_{11}}{G_{13}} \right)^{\frac{1}{2}} + \frac{a^3}{2bh^3 E_{11}} \left[0.98 \left(\frac{h}{a} \right) \left(\frac{E_{11}}{G_{13}} \right)^{\frac{1}{2}} + 0.43 \left(\frac{h}{a} \right)^2 \left(\frac{E_{11}}{G_{13}} \right) \right]. \quad (5.1)$$

Note that the *Saint-Venant* effect at the clamped end (Eq. (3.67)) is considered. The SERR by using Eq. (1.2) is given by the following expression:

$$G_{II}^{ELS} = \frac{9P^2 a^2}{4b^2 h^3 E_{11}} \left[1 + 0.22 \left(\frac{h}{a} \right) \left(\frac{E_{11}}{G_{13}} \right)^{\frac{1}{2}} + 0.048 \left(\frac{h}{a} \right)^2 \left(\frac{E_{11}}{G_{13}} \right) \right]. \quad (5.2)$$

Based on Chapter 3 similar equations may be derived also for the ONF specimen. The required parameters based on Fig. 5.1a are: $M_I=M_2=Ps(2L-a)/2L$, therefore from Eq. (3.105): $M_I=0$, $M_{II}=Ps(2L-a)/4L$, furthermore from Eq. (3.110) it follows that $f_I=0$, $f_{II}=s/4L$ and $a^\# = 2L-a$. This means that the crack length a in Eq. (3.118) should be replaced with $2L-a$. Substituting $2L-a$ with c and determining the relevant terms, C_{EB} and C_{TIM} in Eq. (3.118) the compliance of the ONF specimen becomes:

$$C^{ONF} = \frac{s^2 c^3}{8bh^3 E_{11} L^2} \left[1 + 4 \frac{a}{c} + 8 \frac{aL}{c^2} + 16 \frac{aL^2}{c^3} + 8 \frac{Ls(s-4L)}{c^3} \right] + \frac{s(2L-s)}{4bhkG_{13}L} + \frac{s^2 c^3}{8bh^3 E_{11} L^2} \left[0.98 \left(\frac{h}{c} \right) \left(\frac{E_{11}}{G_{13}} \right)^{\frac{1}{2}} + 0.43 \left(\frac{h}{c} \right)^2 \left(\frac{E_{11}}{G_{13}} \right) \right], \quad (5.3)$$

where c is the length of the uncracked region ($2L-a$). The first term is from *Euler-Bernoulli* beam theory, the second one is from *Timoshenko* beam theory and the last term is from crack tip deformation analysis. The SERR by using Eq. (1.2) becomes:

$$G_{II}^{ONF} = \frac{9P^2 s^2 c^2}{16b^2 h^3 E_{11} L^2} \left[1 + 0.22 \left(\frac{h}{c} \right) \left(\frac{E_{11}}{G_{13}} \right)^{\frac{1}{2}} + 0.048 \left(\frac{h}{c} \right)^2 \left(\frac{E_{11}}{G_{13}} \right) \right]. \quad (5.4)$$

To the best of our knowledge these equations are not yet published in the literature. In the followings we verify the derived equations by numerical models and experiments.

In the case of the ELS test for the application of the CC method the experimental compliance values were fit by the following polynomial of the form (HASHEMI et al., 1990a):

$$C^{ELS} = C_{01} + ma^3, \quad (5.5)$$

where C_{01} and m were found by using least square fitting. The compliance of the ONF specimen may be written as (WANG et al., 2003):

$$C^{ONF} = C_{02} + n(2L - a)^3. \quad (5.6)$$

The coefficients C_{02} and n were determined by using least square fitting. The SERR may be calculated by Eq. (1.2).

In the case of the DBT the flexural modulus of the specimens is eliminated. The relevant equations based on direct beam theory are:

$$G_{II}^{ELS} = \frac{9P\delta a^2}{2b(3a^3 - L^3)}, \quad (5.7)$$

$$G_{II}^{ONF} = \frac{9P\delta}{2b(2L - a)} \frac{1}{\theta}, \quad (5.8)$$

where:

$$\theta = 1 + \frac{4a}{2L - a} + \frac{8aL}{(2L - a)^2} + \frac{16L^2a}{(2L - a)^3} + \frac{8Ls(s - 4L)}{(2L - a)^3}, \quad (5.9)$$

where P is the load, δ is the experimentally determined specimen displacement at the point of load application, respectively.

Finally, we describe the details of the numerical analysis. The FE analysis was performed under plane stress condition to validate the beam theory-based expressions. The specimens were meshed with linear PLANE2D elements using the commercial code COSMOS/M 2.0. In order to prevent the penetration between the nodes along the crack faces the same vertical displacements were imposed by using the command CPDOF. The boundary conditions were the same as those mentioned in Section 4.2. The compliance of the models was used to validate the beam theory-based solution. The mode-II energy release rate (G_{II}) was calculated using the virtual crack-closure technique (VCCT). At the crack tip the same mesh was applied as it was shown in Fig. 4.2. The finite crack extension was $\Delta a = 0.025$ mm.

5.1.3 Crack stability and frictional effects

The problem of crack stability was investigated by CARLSSON et al. (1986) for the ENF specimen and DAVIES et al. (1992) for the ELS specimen. For the commonly assumed fixed grip condition the SERR may be expressed as (CARLSSON et al., 1986):

$$G_{II} = \frac{\delta^2}{2bC^2} \frac{dC}{da}. \quad (5.10)$$

Stable crack propagation can be expected if dG_{II}/da is zero or negative. Differentiating Eq. (5.10) with respect to the crack length yields:

$$\frac{dG_{II}}{da} = \frac{\delta^2}{2bC^2} \left(\frac{d^2C}{da^2} - \frac{2}{C} \left(\frac{dC}{da} \right)^2 \right). \quad (5.11)$$

We consider only the first term in Eq. (5.1). Substituting it into Eq. (5.11) we obtain:

$$a/L \geq 0.55, \quad (5.12)$$

i.e. stable crack propagation in the ELS specimen may be expected if Eq. (5.12) is satisfied. If we suppose to perform only crack initiation tests, then Eq. (5.12) can be ignored, since in this case we need the critical load and the deflection only at the point of fracture initiation. These may be determined experimentally also at those crack lengths ($a < 0.55L$), which do not satisfy Eq. (5.12). The stability chart for the ELS specimen is illustrated in Appendix E (Fig. E1a).

For the ONF specimen the result of the simple beam theory is the first term in Eq. (5.3). Substituting it into Eq. (5.11), and assuming that the right hand of Eq. (5.11) is equal to zero we obtain a fourth order polynomial as a function of the crack length. The polynomial has four roots, of which two are real:

$$(a)_1 = 2L, \quad (a)_2 = \frac{1}{3}(144L^3 - 144sL^2 + 36Ls^2)^{\frac{1}{3}} + 2L. \quad (5.13)$$

Since s is always less than L it appears that we should consider only the first root. If $a \leq (a)_1$ then dG_{II}/da is zero or negative. On the other hand it is obvious, that a always should be higher than s but (as Eq. (5.13) shows) should be less than $2L$. Thus, the requirement is:

$$s < a < 2L, \quad (5.14)$$

i.e. stable crack propagation may be expected at any crack length. The stability chart for certain s values is plotted in Appendix E. (Fig. E1b).

The effect of friction in mode-II fracture specimens was investigated by WANG et al. (2003). The *Coulomb*-type friction model including frictional coefficients within $\mu=0.25$ and 0.5 was adopted in their work. The developed beam and FE models indicated negligible effects induced by friction. In the case of $\mu=0.25$ the energy release rate of the ONF specimen changes by only 3% due to friction between crack faces. Since this is close to a practical value (e.g.: SCHÖN, 2000) the effect of friction in both specimens was neglected in the current investigations. The frictional effect was found to be insignificant also by PEREIRA and MORAIS (2004).

5.1.4 Results and discussion

Crack initiation tests

The recorded load/displacement curves up to fracture initiation are illustrated in Fig. 5.3. The response was essentially linear elastic, which confirms the application of LEFM. It is apparent that the critical load decreases with the initial crack length in the case of the ELS specimen. On the contrary, the ONF specimen requires higher load values for fracture initiation as the crack length increases. The range of the applied load is approximately three times higher in the ONF than in the ELS case. In spite of this the ELS specimens suffered from large displacements, especially in the ranges of $a=35-60$ mm, and $110-140$ mm, as it can

be seen from Fig. 4.3a. During the ONF test no large displacements were experienced, which is one of the great advantages of this setup.

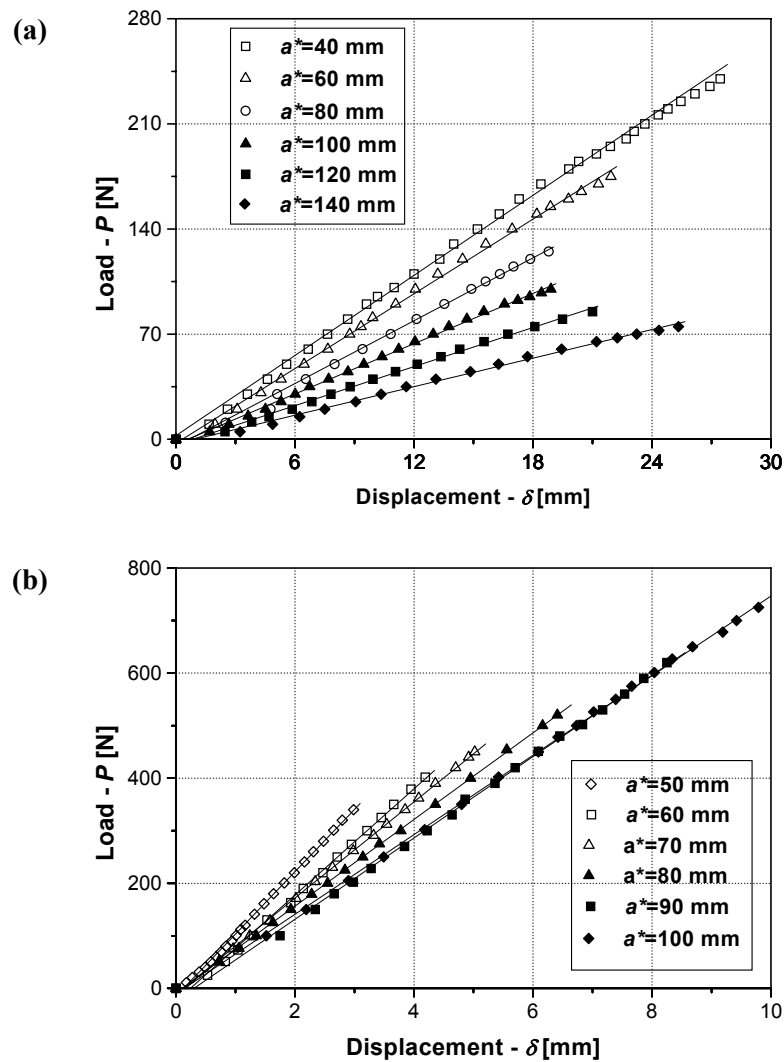


Fig. 5.3. Load/displacement curves up to fracture initiation, ELS test (a), ONF test (b).

The compliance values calculated from the beam theory-based solution (Eq. (5.1)) were compared with the results of the FE analysis. Tables 5.1 and 5.2 show the ratio between the results of the two solutions for both configurations. The agreement between them was found to be excellent, which confirms the applicability of the analytical solution.

Table 5.1. Comparison of the results by the FE and beam models, ELS specimen.

a [mm]	35	40	45	50	55	60	65	70	75	80	90	100	110	120	130	140
C_{FE}/C_{Beam}	1.069	1.069	1.067	1.066	1.064	1.063	1.060	1.058	1.056	1.053	1.048	1.043	1.039	1.034	1.030	1.027

a - crack length, C_{FE} - compliance, plane stress FE model, C_{Beam} - compliance, beam model, Eq. (5.1)

Table 5.2.

Comparison of the results by the FE and beam models, ONF specimen.

a [mm]	50	55	60	65	70	75	80	85	90	95	100	105
C_{FE}/C_{Beam}	1.074	1.071	1.070	1.068	1.066	1.066	1.065	1.065	1.064	1.063	1.063	1.063

a - crack length, C_{FE} - compliance, plane stress FE model, C_{Beam} - compliance, beam model, Eq. (5.3)

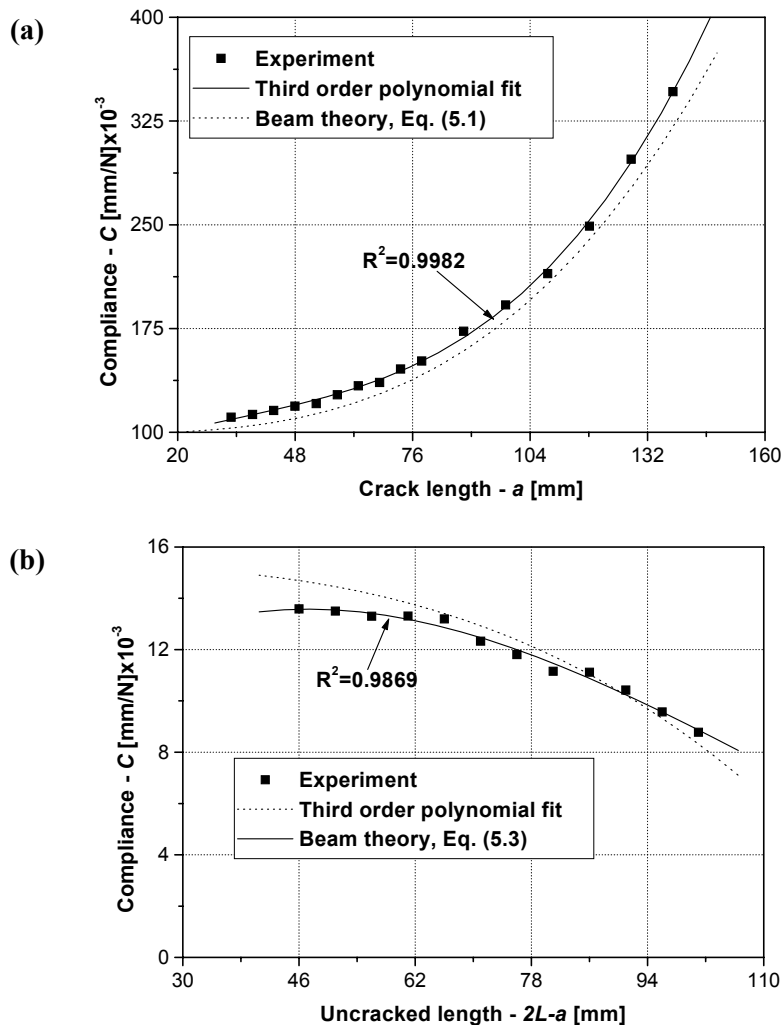


Fig. 5.4.

Measured and calculated compliance from initiation tests, ELS specimen (a), ONF specimen (b).

The compliance curves determined based on crack initiation tests are plotted in Fig. 5.4. For the ELS specimen the advanced beam model (Eq. (5.1)) shows very good agreement with the experimental points. The ONF test produces a somewhat unusual compliance curve. It is important to note that in this case the characteristic distance is the length of the uncracked region. Eq. (5.3) does not agree closely with the experimental compliance values. It was mentioned before that the ONF specimens require relatively high load values for crack initiation, on the other hand the values of the displacements are relatively small (in comparison with the ELS test, Fig. 5.3a). Hence, a little difference in the

measured and calculated displacement values causes comparatively large differences in the compliance, as it was shown in Fig. 5.4b.

Four methods were used to calculate the SERR. Its values versus the crack length are illustrated in Fig. 5.5. Each set of data points was fit with a third order polynomial. For the ELS test the CC method indicates a $G_{II,ss,init}=713 \text{ J/m}^2$ approximate plateau value, while the direct beam theory gives a $G_{II,ss,init}=765 \text{ J/m}^2$ for the same quantity. This means 7%

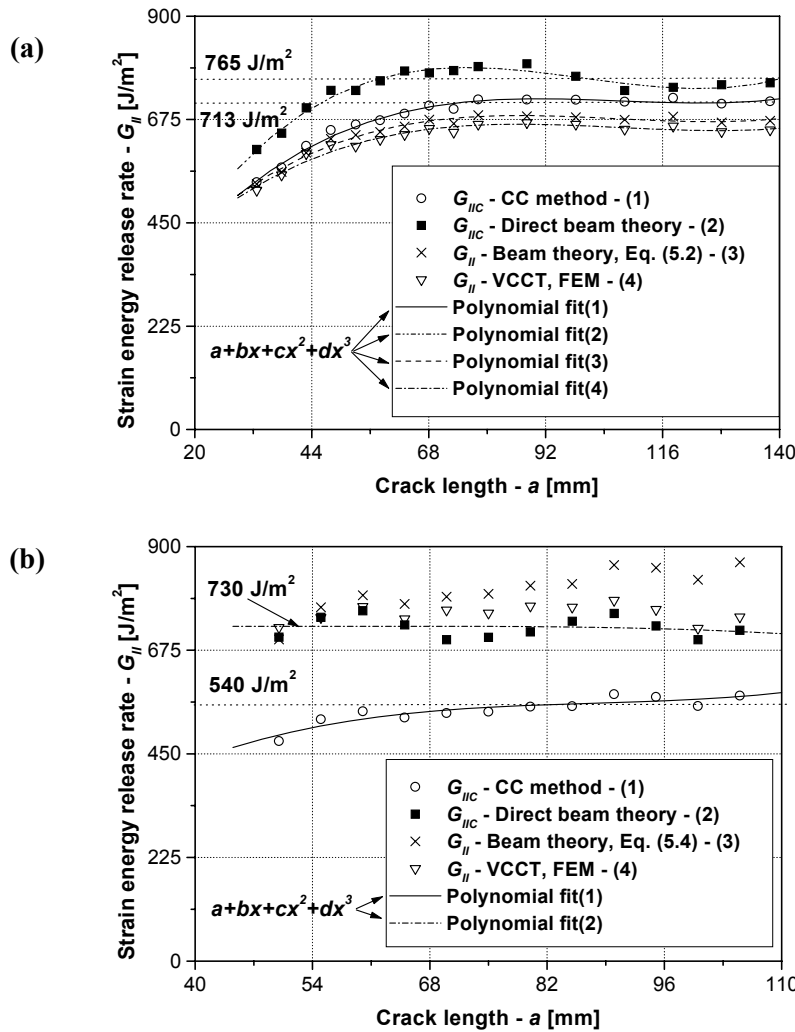


Fig. 5.5.

Values of the SERR against the crack length, initiation tests. ELS specimen (a), ONF specimen (b).

difference between them. The analytical solution (Eq. (5.2)) agrees well with the results of the CC and the VCCT methods, however the latter provides slightly lower values. As a consequence, the four reduction schemes more or less show good correlation in the case of the ELS coupon. From other perspectives it is clear from Fig. 5.5a, that the SERR values depend on the crack length, but this dependence is not serious. Fig. 5.5b presents the SERR values from the ONF test as obtained by the various methods of data reduction. It seems that in this case the CC method gives somewhat surprising results. The direct beam theory indicates a $G_{II,ss,init}=730 \text{ J/m}^2$ steady-state value (which correlates well with the results of the ELS test),

while the value of 540 J/m^2 was obtained by means of the CC method (26% difference compared to the result of DBT). Both the analytical (Eq. (5.2)) and numerical (VCCT) solutions show values, which are closer to the results of the direct beam theory. The reason for the CC method does not agree with the other methods is the same as it was mentioned in the discussion of Fig. 5.4b. It seems that in this case the CC method is very sensitive to the accuracy of the measuring instrument.

Crack propagation tests

We have found that the ELS geometry was not suitable to investigate crack propagation in the current material. The reason for that may be explained by the followings. The specimens suffered from relatively large displacements in order to reach the point of fracture initiation. For the crack propagation much larger displacements were required. After

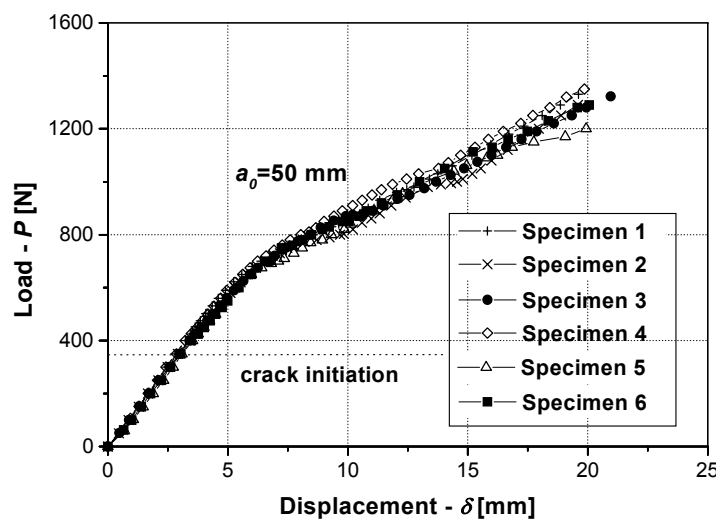


Fig. 5.6.

Load/displacement curves from ONF propagation tests.

crack initiation the crack seemed to be beyond control, i.e. the crack has reached the clamped end in a flash. This indicates that the stiffness of the system was not large enough for the ELS testing. This may be supported by the large amount of experimental works, performed, in general, only on those composite materials, which exhibit high flexural modulus (HASHEMI et al., 1990a and 1990b; WANG et al., 1996; WANG et al., 2003). Thus, in the sequel the attention is focused on the ONF test to measure the propagation toughness.

The recorded load/displacement curves from six ONF specimens are shown in Fig. 5.6. It is noteworthy, that the range of the applied load is about twice higher in comparison with that of the crack initiation tests (refer to Fig. 5.3b). Crack initiation was observed always around 350-400 N.

The measured compliance values and the calculated curves are plotted in Fig. 5.7 as obtained by the crack propagation test data of one ONF specimen. A remarkable feature is that the experimentally measured compliance values somewhat differ from those, which were recorded through the crack initiation tests (refer to Fig. 5.4b). In spite of this the beam theory-

based solution (Eq. (5.3)) matches better with the experimental values than in the case of the crack initiation tests. However, there is also some discrepancy between the measured and calculated curves. The fiber-bridging is one possible source of the mentioned discrepancy. During crack propagation some of the fibers were pulled out, these caused the extensive fiber-bridging between the crack faces. This feature increased the resistance to delamination, and consequently, a higher load value was required for the crack advance. Therefore, further work is required to clarify these results.

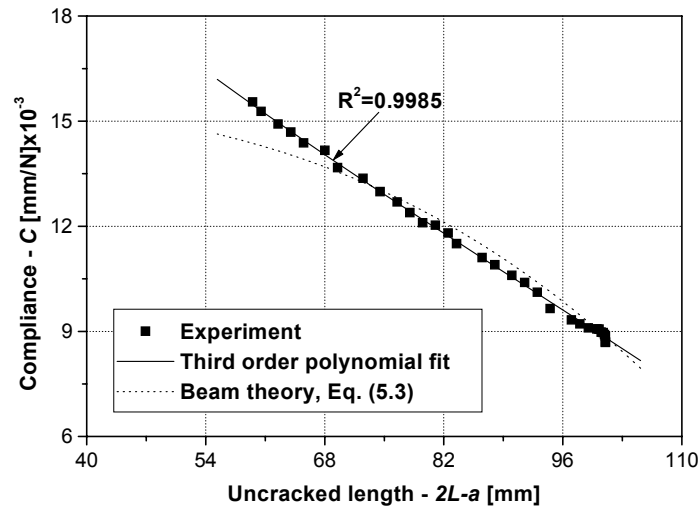


Fig. 5.7.

Measured and calculated compliance from the propagation test of one ONF specimen.

Three reduction schemes were used to calculate the SERR. The results for two specimens are presented in Figs. 5.8a, 5.8b and 5.8c. The CC method shows that the value at which steady-state crack propagation occurred is 2693 and 2442 J/m², respectively. Considering the data of six specimens the mean value of 2787 J/m² was obtained for the critical SERR. The plateau values were determined by using the asymptotic values of the fits in Fig. 5.8. The relevant steady-state values are 2584 J/m² and 2234 J/m² (2637 J/m² mean value from six specimens) from the DBT and 2911 J/m² and 2534 J/m² (2817 J/m² average value from six coupons) from the beam theory-based solution, respectively. It should be kept in mind that the CC method is the only data reduction technique, which considers the effect of fiber-bridging. We have found that the CC technique is sensitive to the accuracy of the displacement measurement. It is important to note that in the case of propagation tests the CC method showed good agreement with the analytical and the direct beam theory approaches. In spite of this the result of the CC method is slightly dubious. An experimental reduction scheme, which gives reliable results for crack initiation test and is able to account for the effect of fiber-bridging would be useful. Further work is required to clarify these results.

For comparison we provide some experimental results, which were previously published on similar systems. OZDIL et al. (1998) investigated unidirectional glass/polyester ENF specimens with $a=32$ mm, $2L=100$ mm and $V_f=45\%$. The value of $G_{IIC}=496\pm135$ J/m² was obtained for the SERR at crack initiation by using the simple beam theory solution. This

is significantly less than those obtained by us (713 J/m² from ELS test and 730 J/m² from the ONF test), however that value was obtained at a definite crack length, while in our experiments the extended range of crack length was investigated. DAVIES et al. (1996) presented slightly higher G_{IIc} values for glass/epoxy ELS and ENF specimens as obtained by

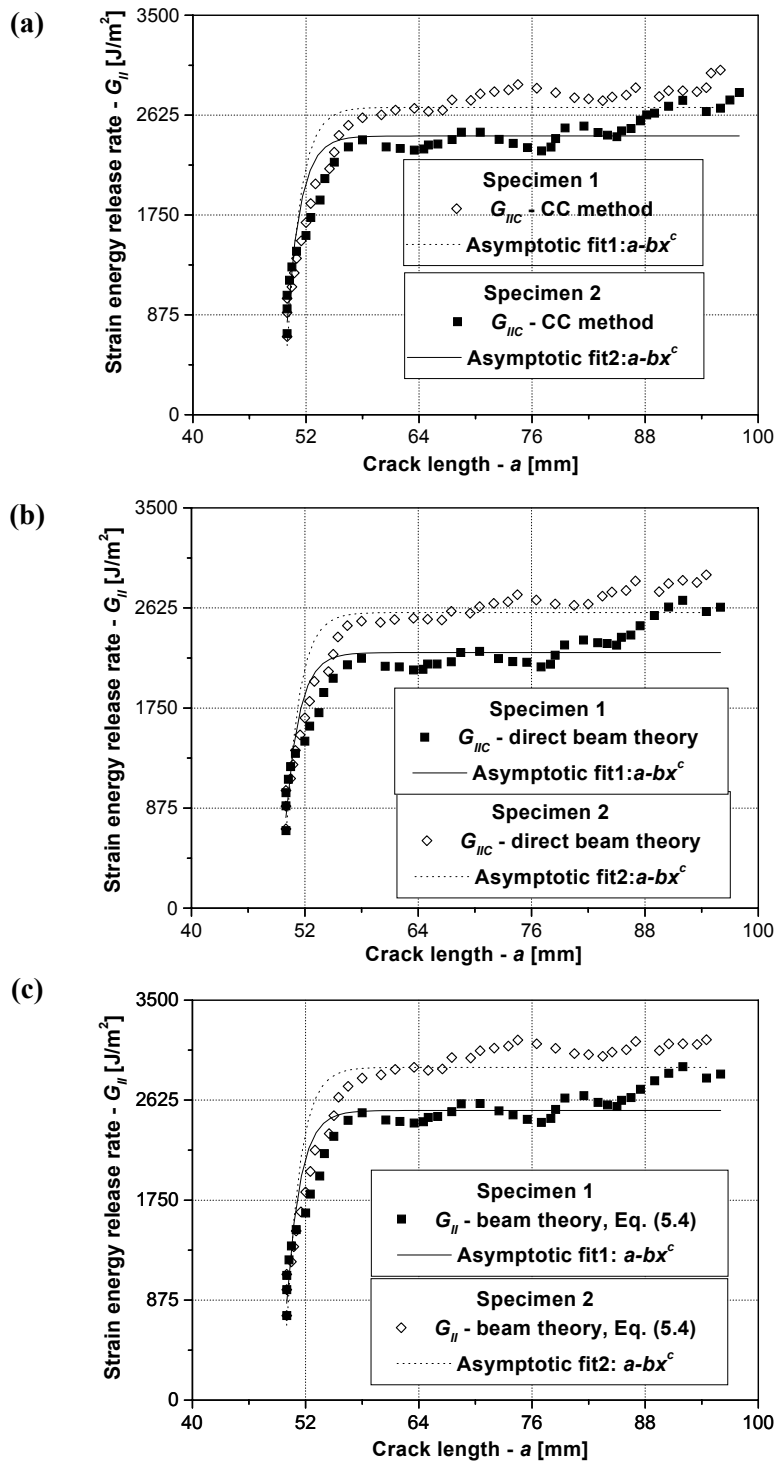


Fig. 5.8.

SERR against the crack length by different methods, ONF test. Compliance calibration (a), direct beam theory (b), beam theory (c).

three different reduction techniques. For the ELS coupon the critical SERRs (at crack initiation) were within $1500\text{--}2000\text{ J/m}^2$. In the case of the ENF test they were around $1400\text{--}1500\text{ J/m}^2$. The significance of the employed data reduction was highlighted in the former work. Considering the propagation tests the work of DAVIES et al. (2004) may be referred to, wherein they tested unidirectional glass/epoxy 4ENF specimens. For specimens with similar fiber-volume fraction (52%) to that of our coupons and with $2L=100\text{ mm}$, they measured $2013\pm 135\text{ J/m}^2$ toughness value at crack initiation and $3040\pm 450\text{ J/m}^2$ propagation toughness in the range of $a=47\text{--}76\text{ mm}$. These values are higher in comparison with our results, however the R-curve followed a similar trend to that found by us in Figs. 5.8a, 5.8b and 5.8c.

5.2 Mixed-mode I/II configurations

In the following sections we investigate unidirectional mixed-mode I/II SLB and SCB specimens. Apart from the analytical solution (refer to Chapter 4) we further analyze them by the help of experiments (SZEKRÉNYES and UJ, 2003c, 2004a, 2004c). Although these tests are not as universal as the MMB, they require simpler experimental equipment, as it has been highlighted in the literature review. The SLB and SCB tests produce linear load-deflection curve up to fracture and simple reduction techniques can be applied. The mixed-mode I/II specimens have been demonstrated in Fig. 4.1.

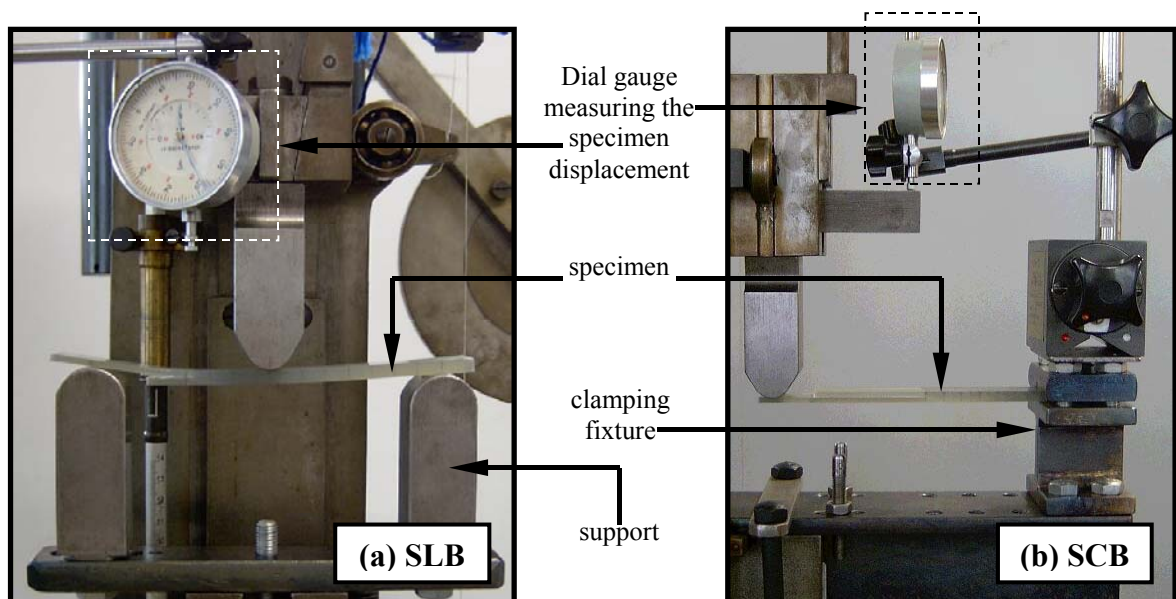


Fig. 5.9.

The single-leg bending (a) and the single-cantilever beam (b) specimens for mixed-mode I/II interlaminar fracture testing.

5.2.1 Experimental procedure

The fixtures for the SLB and SCB specimens are illustrated in Fig. 5.9. The SLB test was performed in a three-point bending fixture (see Fig. 5.9a) with span length of $2L=151$

mm. The special fixture depicted in Fig. 5.9b was used to carry out the SCB test with full length of $L=150$ mm. In order to avoid the effects of fiber-bridgings (which arises due to the mixed-mode I/II condition), specimens with different crack lengths were prepared and only crack initiation tests were performed. The SLB coupons with crack lengths from $a=20$ to 75 mm ($0.13 \cdot 2L \leq a \leq 0.5 \cdot 2L$) with 5 mm increment were used. For the ELS specimen the former crack length range was improved from $a=80$ to 140 mm ($0.13L \leq a \leq 0.93L$) with 10 mm increment. The tests were conducted under displacement control using an *Amsler* testing machine. The load-deflection data was recorded, the deflection was monitored by the dial gauge, shown in Figs. 5.9a-b.

Two methods were used in this case to calculate the fracture properties of the specimens. The correction of the SLB and SCB systems is detailed in Appendix D.

The relevant equations based on the proposed model are given by Eqs. (4.1)-(4.3) for the SCB specimen and by Eqs. (4.4)-(4.6) for the SLB specimen.

For both specimens we apply also the compliance calibration (CC) method. The

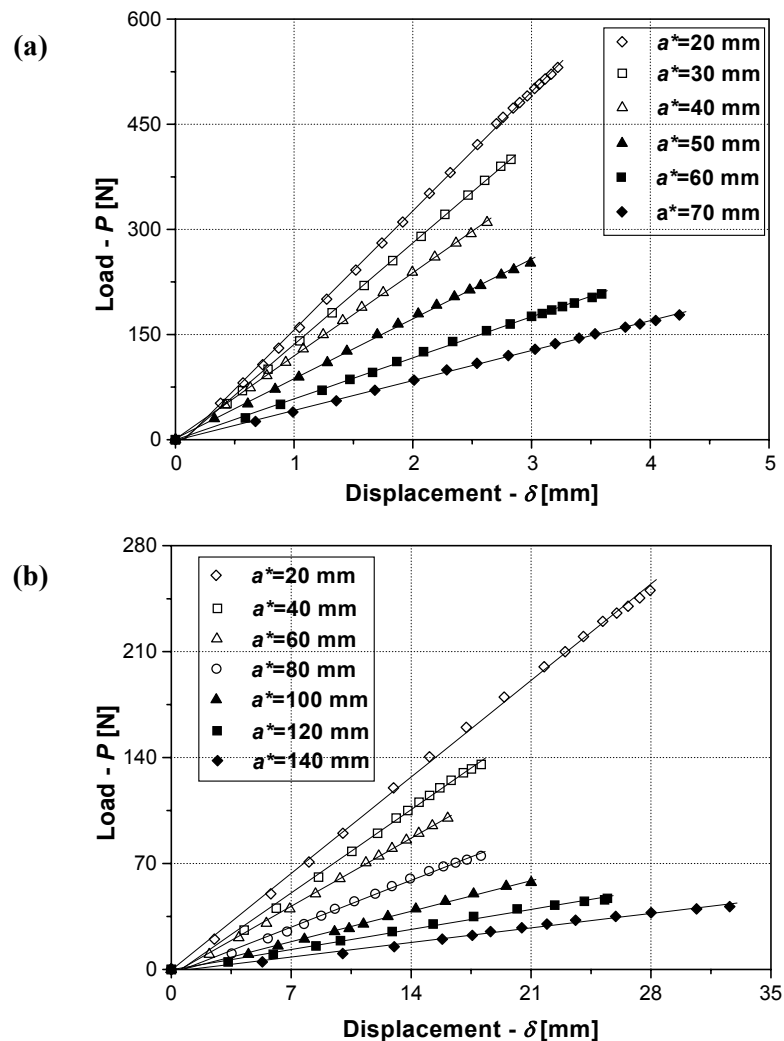


Fig. 5.10.

Load/displacement curves up to fracture initiation, SLB test (a), SCB test (b).

compliance was calculated by means of the same polynomial function, as it is given by Eq. (5.5), while the SERR was computed by using Eq. (1.2).

5.2.2 Results and discussion

For both tests linear load/deflection curves were recorded up to fracture initiation, as it is shown by Figs. 5.10a and 5.10b. These results are quite similar to those, reported in Section 5.1.4 for mode-II crack initiation tests (refer to Fig. 5.3). On the base of these results

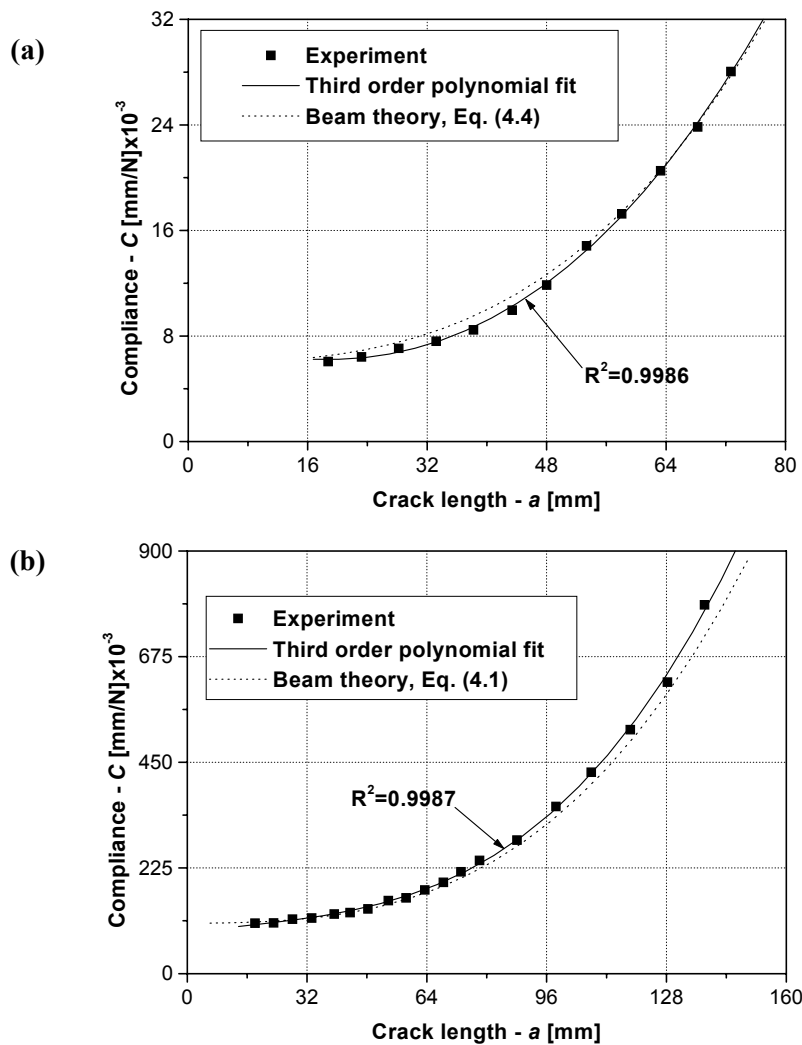


Fig. 5.11. Compliance against the crack length, SLB (a), SCB (b) specimen.

the application of the LEFM is again justified. An immediate observation is that the critical load values are approximately twice higher in the case of the SLB test, than those for the SCB test. From other perspectives, we may draw that the large displacements arise only in the case of the SCB test. In this respect the critical range of the crack length is: $a=20-30$ and $a=110-140$ mm. During the SLB test the small displacements are always ensured.

The compliance curves are illustrated in Fig. 5.11 for the SLB and SCB specimens. In both cases the correlation between the results of the model (Eq. (4.4), Eq. (4.1)) and experiment was found to be quite good, but it should be noted that Eq. (4.4) slightly overestimates the experimental points, however this is not significant. The SERR values by the CC method and beam theory can be seen in Figs. 5.12a and 5.12b. The agreement between

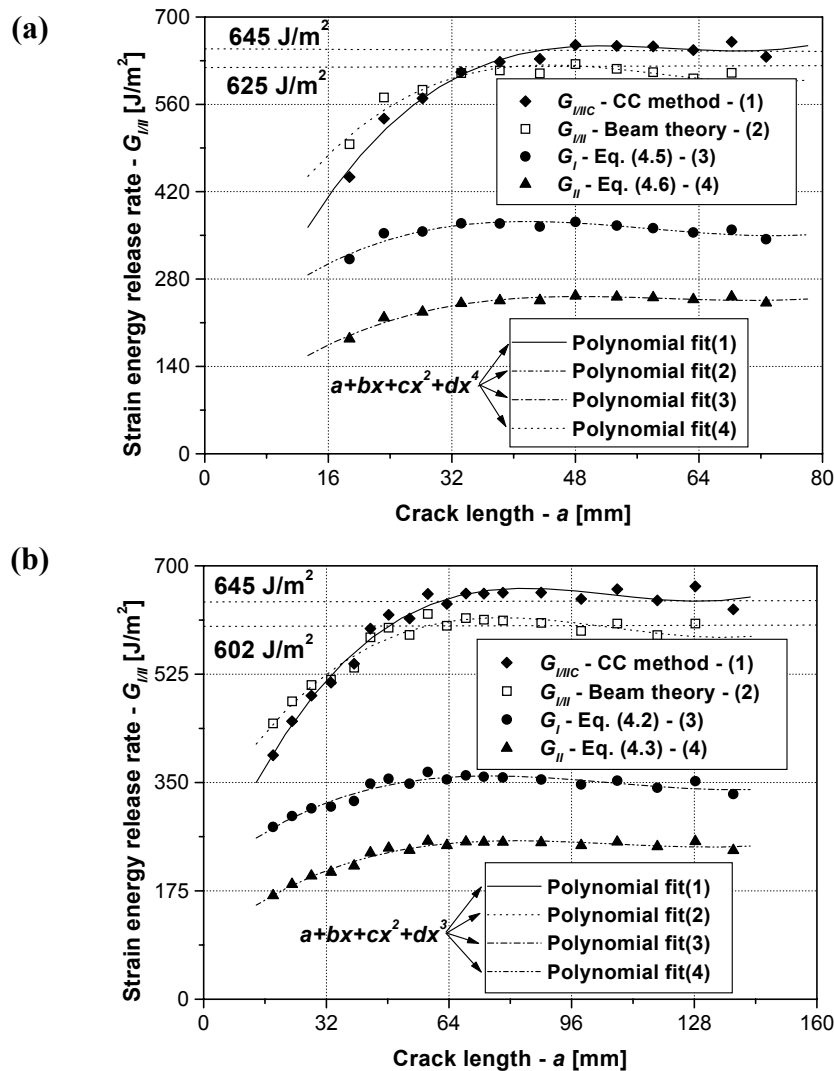


Fig. 5.12.

Values of the initiation SERR against the crack length, SLB (a), SCB (b) specimen.

the model (Eq. (4.5) and (4.6) for the SLB, Eqs. (4.2) and (4.3) for the SCB specimen) and experiment is also very good. The CC method indicates an average steady-state value of $G_{I/II,ss,init}=645$ J/m² for both tests, which is an excellent correspondence. The advanced beam model gives a $G_{I/II,ss,init}=625$ J/m² plateau value for the SLB and a $G_{I/II,ss,init}=602$ J/m² for the SCB specimen (refer to Figs. 5.12a and 5.12b). The mode-I and mode-II energy release rate components are also plotted in Fig. 5.12, the relevant mode ratios can be found in Tables 4.1 and 4.2.

Since the MMF specimen is quite similar to the SLB coupon and both produce the same mode ratio ($G_I/G_{II}=4/3$) based on simple beam theory we provide comparison between our experimental work and those by ALBERTSEN et al. (1995) and KORJAKIN et al. (1998). The former work reported $G_{III,init}=145 \text{ J/m}^2$ value at crack initiation and $G_{III,ss}=330 \text{ J/m}^2$ mean values at crack propagation for carbon-fiber reinforced MMF specimens. In the latter work the relevant quantities were $G_{III,init}=456 \text{ J/m}^2$ and $G_{III,ss}=525 \text{ J/m}^2$ for glass/epoxy MMF specimens. Similar R-curves were obtained by HASHEMI et al. (1990b) for the SCB specimen, who determined (based on crack propagation tests) $G_{III,init}=1200 \text{ J/m}^2$ initiation toughness and $G_{III,ss}=1480 \text{ J/m}^2$ plateau value using PES SCB specimens (1990b). The same authors reported $G_{III,init}=1510 \text{ J/m}^2$ and $G_{III,ss}=1810 \text{ J/m}^2$ values for carbon/PEEK SCB specimens (1990a). Although the current study presents only values at crack initiation, the behavior is similar to results previously published on similar systems.

The contributions of the various effects to the compliance and the SERR of the SLB specimen are listed in Table 5.3. Overall, all these effects provide only a small improvement. The SERR values are summarized also in Table 5.3. In this point of view the *Timoshenko* beam model supports the strain energy release rate with very small values. The contribution of elastic foundation, *Saint-Venant* effect and crack tip shear deformation decays subsequently, but provides reasonable values at small crack length. Table 5.4 presents the compliances and SERRs obtained from the SCB test. As expected, the *Saint-Venant* effect is the most significant one, the other effects are negligible in the case of the compliance. The SERR calculated by beam analysis are also presented in Table 5.4 for the SCB specimen. The effect of transverse shear can be neglected, as demonstrated in Table 5.4. The two-parameter elastic foundation, *Saint-Venant* and crack tip shear deformation effects show meaningful values at the beginning phase ($a=20$ to 50 mm) as shown by the last four columns in Table 5.4.

Table 5.3.

Compliances and SERRs by beam analysis, SLB specimen.

a [mm]	C_{EB}	C_{WP}	C_{TIM} [mm/N]·10 ⁻³	C_{SV}	C_{CTS}	$G_{III,EB}$	$G_{III,WP}$	$G_{III,TIM}$ [J/m ²]	$G_{III,SV}$	$G_{III,CTS}$
20	6.20	0.08	0.14	0.05	0.03	396.51	52.74	6.21	37.70	21.58
25	6.49	0.11	0.15	0.07	0.04	480.43	49.97	4.91	36.87	20.69
30	7.00	0.16	0.15	0.11	0.06	509.79	42.56	3.53	32.18	17.79
35	7.72	0.21	0.15	0.15	0.09	547.74	38.14	2.74	29.35	16.05
40	8.68	0.27	0.16	0.20	0.11	562.47	33.59	2.12	26.19	14.20
45	9.98	0.34	0.16	0.26	0.14	566.89	29.49	1.66	23.23	12.52
50	11.42	0.41	0.17	0.31	0.18	587.17	27.39	1.40	21.74	11.66
55	13.47	0.50	0.17	0.39	0.21	586.08	24.42	1.13	19.52	10.43
60	15.67	0.59	0.18	0.46	0.25	585.37	22.29	0.96	17.92	9.54
65	18.56	0.69	0.18	0.54	0.30	579.88	20.17	0.80	16.29	8.65
70	21.79	0.80	0.18	0.63	0.35	591.73	19.01	0.70	15.42	8.17
75	25.12	0.90	0.19	0.72	0.39	570.03	17.14	0.59	13.94	7.37

a - crack length

C_{EB} - Euler-Bernoulli beam model

C_{WP} - Winkler-Pasternak foundation model

C_{TIM} - Timoshenko beam model

C_{SV} - Saint-Venant effect

C_{CTS} - Crack tip shear deformation

$G_{III,EB}$ - Euler-Bernoulli beam model

$G_{III,WP}$ - Winkler-Pasternak foundation model

$G_{III,TIM}$ - Timoshenko beam model

$G_{III,SV}$ - Saint-Venant effect

$G_{III,CTS}$ - Crack tip shear deformation

Table 5.4.
Compliances and SERRs by beam analysis, SCB specimen.

a [mm]	C_{EB}	C_{WP}	C_{TIM} [mm/N]·10 ⁻³	C_{SV}	C_{CTS}	$G_{I/II,EB}$	$G_{I/II,WP}$	$G_{I/II,TIM}$ [J/m ²]	$G_{I/II,SV}$	$G_{I/II,CTS}$
20	102.71	0.32	0.58	6.51	0.12	345.79	47.07	5.61	33.54	19.24
30	106.80	0.68	0.62	6.80	0.27	430.21	35.50	2.90	26.88	14.84
40	115.51	1.24	0.66	7.25	0.51	475.50	27.19	1.64	21.27	11.51
50	126.90	1.82	0.69	7.71	0.75	544.90	24.95	1.25	19.83	10.63
60	146.03	2.61	0.72	8.33	1.09	574.48	21.44	0.89	17.26	9.18
70	172.37	3.51	0.76	9.06	1.47	575.06	18.19	0.65	14.76	7.81
80	206.33	4.51	0.79	9.87	1.91	576.17	15.87	0.50	12.96	6.84
90	251.77	6.69	0.83	10.83	2.41	576.30	14.00	0.40	11.49	6.04
100	311.37	7.05	0.86	11.94	3.00	567.34	12.28	0.31	10.12	5.31
110	377.31	8.41	0.90	13.06	3.59	581.11	11.44	0.27	9.46	4.95
120	465.54	10.07	0.93	14.43	4.31	565.29	10.12	0.21	8.39	4.38
130	564.79	11.77	0.97	15.84	5.04	585.18	9.64	0.19	8.01	4.18
140	680.33	13.61	1.00	17.35	5.84	552.59	8.44	0.15	7.02	3.66

- a - crack length
- C_{EB} - Euler-Bernoulli beam model
- C_{WP} - Winkler-Pasternak foundation model
- C_{TIM} - Timoshenko beam model
- C_{SV} - Saint-Venant effect
- C_{CTS} - Crack tip shear deformation
- $G_{I/II,EB}$ - Euler-Bernoulli beam model
- $G_{I/II,WP}$ - Winkler-Pasternak foundation model
- $G_{I/II,TIM}$ - Timoshenko beam model
- $G_{I/II,SV}$ - Saint-Venant effect
- $G_{I/II,CTS}$ - Crack tip shear deformation

5.3 A novel mixed-mode I/II configuration: the OLB test

In the current section we develop another alternative for the mixed-mode I/II fracture investigation in composites: the over-leg bending (OLB) specimen (SZEKRÉNYES and UJ, 2004f, 2005c). The original idea is based on the mode-II over-notched flexure test (ONF, Fig. 2.3d) (WANG et al., 2003), which is the modification of the ENF (Fig. 2.3a) specimen. The only difference between them is that in the ONF setup the load is introduced eccentrically between the two supports. We apply the developed beam model to the novel configuration (see Fig. 5.13), moreover FE analysis and experiments are also performed. Some comparison is made between the OLB and the traditional SLB configurations.

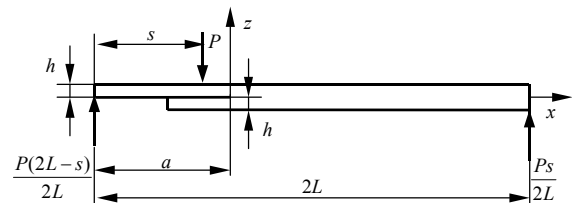


Fig. 5.13.
Free-body diagram of the over-leg bending coupon.

5.3.1 Experimental procedure

Crack initiation and propagation tests were performed using unidirectional glass/polyester specimens. In the case of the initiation tests the crack length range from $a=55$ to 115 mm with 5 mm increment was investigated, while the crack propagation tests using six specimens with $a=50$ mm initial crack length were performed. The OLB configuration is

illustrated in Fig. 5.14. The tests were carried out in a similar fashion to that mentioned in Section 5.1.1 (ONF test) with the same dimensions ($2L=151$ mm, $s=47.5$ mm).

5.3.2 Data reduction

Two methods were used for data reduction: beam theory-based approach described in Chapter 3 and the CC method. The finite element analysis was performed in order to confirm the analytical solution. It is remarkable that although the fixture is the same as before, this time the radii of the supports is not considered in the data reduction. The reason for that is the correction gives misleading results.

For the analytical compliance expression of the OLB specimen (Fig. 5.13) the required parameters are: $M_I=Ps(2L-a)/2L$, $M_2=0$ therefore from Eq. (3.105): $M_I=M_{II}=Ps(2L-a)/4L$, furthermore from Eq. (3.110) it follows that $f=f_{II}=s/4L$ and $a^\# = 2L-a$. Thus, the crack length a in Eq. (3.118) should be replaced with $2L-a$. Calculating the relevant terms, C_{EB} and C_{TIM} in Eq. (3.118) (Chapter 3) the compliance of the OLB specimen has the following form:

$$\begin{aligned}
 C^{OLB} = & \frac{s^2 c^3}{8bh^3 E_{11} L^2} \left[1 + 8 \frac{a}{c} + 16 \frac{aL}{c^2} + 32 \frac{aL^2}{c^3} + 16 \frac{Ls(s-4L)}{c^3} \right] + \frac{s[4L(2L-s) - sc]}{8bhkG_{13}L^2} + \\
 & + \frac{s^2 c^3}{8bh^3 E_{11} L^2} \left[5.07 \left(\frac{h}{c} \right) \left(\frac{E_{11}}{E_{33}} \right)^{\frac{1}{4}} + 8.58 \left(\frac{h}{c} \right)^2 \left(\frac{E_{11}}{E_{33}} \right)^{\frac{1}{2}} + 2.08 \left(\frac{h}{c} \right)^3 \left(\frac{E_{11}}{E_{33}} \right)^{\frac{3}{4}} \right] + \\
 & + \frac{s^2 c^3}{8bh^3 E_{11} L^2} \left[0.98 \left(\frac{h}{c} \right) \left(\frac{E_{11}}{G_{13}} \right)^{\frac{1}{2}} + 0.43 \left(\frac{h}{c} \right)^2 \left(\frac{E_{11}}{G_{13}} \right) \right] + \frac{1}{\pi} \frac{3s^2 c^2}{4bh^2 E_{11} L^2} \left(\frac{E_{11}}{G_{13}} \right)^{\frac{1}{2}}.
 \end{aligned} \tag{5.15}$$

The SERR components by the help of Eqs. (3.103)-(3.109) are:

$$\begin{aligned}
 G_I^{OLB} = & \frac{12P^2 s^2 c^2}{16b^2 h^3 E_{11} L^2} \left[1 + 0.85 \left(\frac{h}{c} \right) \left(\frac{E_{11}}{E_{33}} \right)^{\frac{1}{4}} + 0.71 \left(\frac{h}{c} \right)^2 \left(\frac{E_{11}}{E_{33}} \right)^{\frac{1}{2}} \right. \\
 & \left. + 0.32 \left(\frac{h}{c} \right) \left(\frac{E_{11}}{G_{13}} \right)^{\frac{1}{2}} + 0.1 \left(\frac{h}{c} \right)^2 \left(\frac{E_{11}}{G_{13}} \right) \right],
 \end{aligned} \tag{5.16}$$

$$G_{II}^{OLB} = \frac{9P^2 s^2 c^2}{16b^2 h^3 E_{11} L^2} \left[1 + 0.22 \left(\frac{h}{c} \right) \left(\frac{E_{11}}{G_{13}} \right)^{\frac{1}{2}} + 0.048 \left(\frac{h}{c} \right)^2 \left(\frac{E_{11}}{G_{13}} \right) \right], \tag{5.17}$$

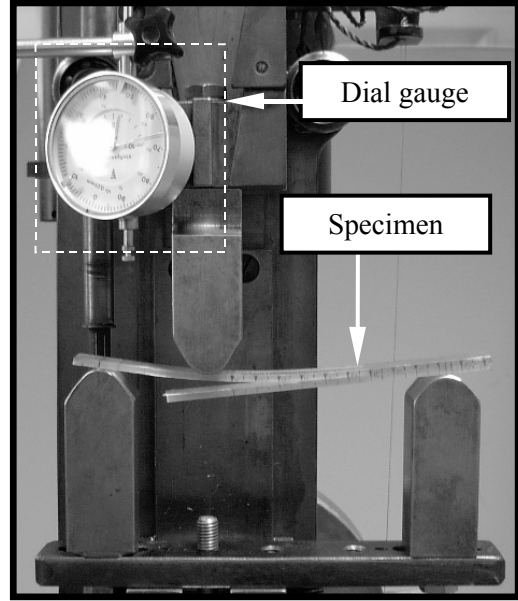


Fig. 5.14.
Over-leg bending test configuration.

where s is the position of the applied load from the left side of the specimen and $c=2L-a$ is the length of the uncracked part. The total fracture energy ($G_{III}=G_I+G_{II}$) can be calculated by summing the equations above. The mixed mode-ratio (G_I/G_{II}) can be also computed.

In accordance with the CC method the compliance of the OLB specimen may be written as (WANG et al., 2003):

$$C^{OLB} = C_{02} + n(2L - a)^3. \quad (5.18)$$

The coefficients C_{02} and n were determined by least square fitting. The form of Eq. (5.18) may be explained by focusing our attention on Eq. (5.5), which was also applied in the case of the mixed-mode I/II SLB and SCB coupons. The difference between Eq. (5.5) and Eq. (5.18) is only the characteristic length. The SERR was calculated from Eq. (1.2).

5.3.3 Finite element analysis

The FE analysis was performed under plane stress condition only to validate the beam theory-based formulae. The specimens were meshed with PLANE2D elements using the commercial code COSMOS/M 2.0. The boundary conditions were the followings. At the end of the upper specimen arm the displacements in the directions x and z were constrained, while at the end of the uncracked part the displacement in the direction z was constrained (Fig. 5.13). The mode mix ratio (G_I/G_{II}) was calculated using the virtual crack-closure technique (VCCT). At the crack tip the usual FE mesh with finite crack extension of $\Delta a=0.025$ mm was used (refer to Fig. 5.2).

5.3.4 Results and discussion

Crack initiation tests

The compliances calculated from the beam model were compared with the results of the FE analysis. Table 5.5 shows the ratio of the results of the two solutions. Eq. (5.15) shows very good agreement with the FE results, which confirms the application of the analytical solution. The mode-mix ratio is also collected in Table 5.5. The ratio by FE analysis changes within 1.31 to 1.24 in the case of the OLB specimen. For comparison the relevant mode ratios changes within 1.66 to 1.48 in the case of the SLB specimen by FE analysis (refer to Table 4.2). The beam model predicts values between 1.68 and 1.43 for the SLB test and, in accordance with Table 5.5 G_I/G_{II} changes within 1.4 to 1.52 for the OLB

Table 5.5.

Comparison of the results by the FE and beam models, OLB specimen.

a [mm]	55	60	65	70	75	80	85	90	95	100	105	110	115
C_{FE}/C_{Beam}	1.016	1.013	1.010	1.009	1.007	1.006	1.005	1.004	1.003	1.002	1.002	1.001	1.001
$(G_I/G_{II})_{Beam}$	1.402	1.406	1.410	1.415	1.420	1.427	1.434	1.443	1.453	1.465	1.480	1.499	1.524
$(G_I/G_{II})_{FE}$	1.314	1.319	1.308	1.304	1.299	1.294	1.298	1.280	1.272	1.275	1.249	1.250	1.236

a - crack length, C_{FE} - compliance, plane stress FE model, C_{Beam} - compliance, beam model, Eq. (5.15), $(G_I/G_{II})_{Beam}$ - mode mix ratio, beam model, $(G_I/G_{II})_{FE}$ - mode mix ratio, FE model

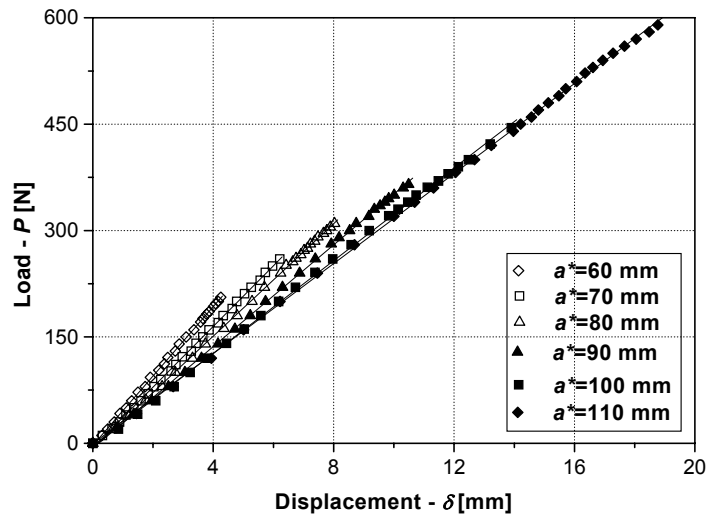


Fig. 5.15.

Load/displacement traces up to fracture initiation, OLB test.

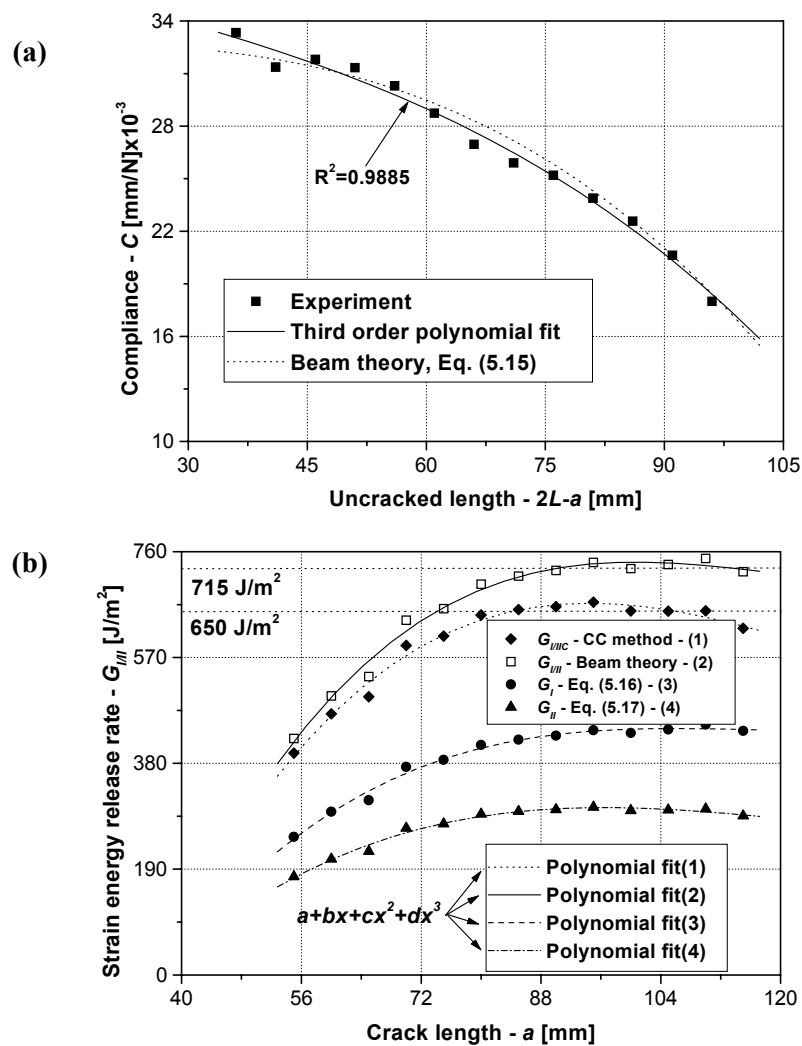


Fig. 5.16.

Values of the compliance (a) and the SERR (b) against the crack length, OLB test.

specimen. Based on the VCCT method the crack length dependence of the mode mix ratio is somewhat stronger in the case of the SLB coupon (compare Table 5.5 with Table 4.2).

Fig. 5.15 shows the load/displacement curves recorded up to fracture initiation. Each curve is typically linear. During the OLB test both the critical force and displacement increases with the crack length. In addition reaching the crack length of $a=100$ mm it seems that the specimens suffer from large displacements. In comparison with the SLB test (refer to Fig. 5.10a) the ranges of the applied load are essentially the same in both tests, but it should be kept in mind that the crack length ranges are different. The SLB test indicates the critical load reaches the highest value if the smallest crack length is considered (Fig. 5.10a). The results of the OLB test in Fig. 5.15 are in sharp contrast with these facts.

The compliances and SERR values are illustrated in Fig. 5.16. In the case of the compliance curve, similarly to the ONF specimen, the characteristic distance is the length of the uncracked region c . Overall, the beam model (Eq. (5.15)) correlates very well with the measured points. The values of the SERR at crack initiation are plotted in Fig. 5.16b. In the case of the OLB specimens the CC method results in a 650 J/m^2 plateau value, while the beam model predicts a 715 J/m^2 for the same quantity (9% difference). These results show the opposite trends, which were found in the case of the SLB specimen. In other words the beam model overpredicts the experiments. The nature of the curves are eventually the same as determined from the SLB and SCB tests (refer to Figs. 5.12a and 5.12b).

Crack propagation tests

It has been shown in the previous sections that neither the SLB nor the SCB specimen was suitable to perform propagation tests under the current geometrical and material parameters. In the case of the SLB test at short crack lengths ($a=20\text{-}45$ mm) sudden jumps (15-30 mm) in the crack advance frequently occurred. The remaining interval (until the point

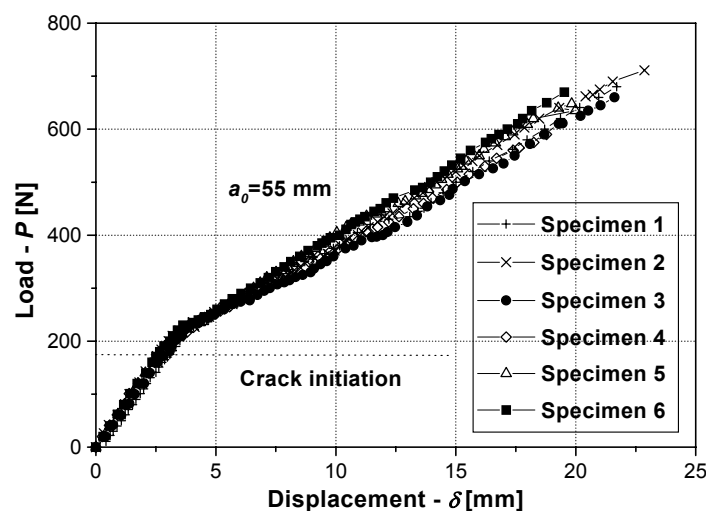


Fig. 5.17.
Load/displacement traces from the propagation test of six OLB specimens.

of load introduction) was insufficient for studying crack propagation. On the other hand the large displacements were great obstacles, when we tried to use the SCB specimen for crack propagation investigations. Hence, the OLB test was used as a candidate to measure the mixed-mode I/II crack propagation.

The load/displacement curves of six specimens are depicted in Fig. 5.17. The range of the applied load is eventually the same as those recorded during crack initiation tests (refer to Fig. 5.15). Crack initiation always occurred at $P=170-180$ N.

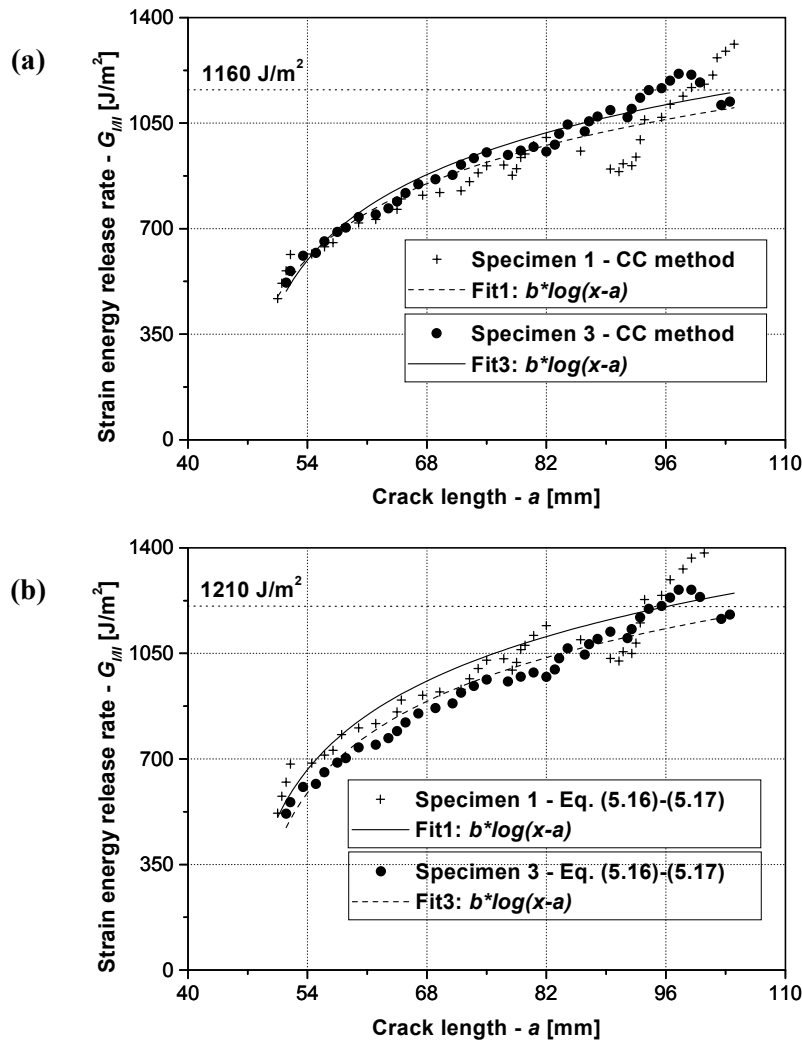


Fig. 5.18.

SERR under crack propagation from the measurement of two OLB specimens. CC method (a), beam theory (b).

The compliance curves of each specimen were essentially the same as those determined through crack initiation test (refer to Fig. 5.16a). The R-curves at crack propagation are plotted in Fig. 5.18. Although six specimens were tested, we display the results obtained by only two of them. The curves show the R-curve behavior, i.e. there is not a clear plateau value (as it was for instance in the ONF test in Fig. 5.8) and the SERR grows up to 1160 J/m² in accordance with the CC method and about 1210 J/m² according to beam

theory. This involves less than 5% difference between the results of the applied reduction techniques. Note that fiber-bridging was observed during testing, however this effect was not considered here. Furthermore, due to the relatively small displacements before the crack tip region the influence of the fiber-bridging was estimated to be small. Although the fiber-bridging is absolutely accidental, its extension was only mild in each case.

For comparison TRACY et al. (2003) determined similar propagation R-curves with 1500 J/m² and 1750 J/m² plateau values using the proposed SFPLB configuration (see Fig. 2.5d) with carbon/epoxy coupons to those, shown in Fig. 5.18. Also, beam theory-based formulae were used for data reduction in their study. The small difference between our and TRACY et al.'s results may be explained by the different materials applied for testing.

5.4 Conclusions, scientific significance

The mode-II and the mixed-mode I/II interlaminar fracture in unidirectional glass/polyester ELS, ONF, SLB and SCB specimens were investigated from the theoretical and experimental points of view, respectively. Closed-form solutions were obtained for the compliance and the strain energy release rate of the mentioned delamination coupons. The experiments and the developed finite element models verified the analytical solution. This indicates that linear beam theories can be applied for analysis.

Considering the ELS, SLB and SCB configurations the results of the present beam model agreed closely with the results of the experiments and the other applied reduction techniques. From other perspectives, it was found that the CC method is very sensitive to the accuracy of the measuring instrument in the case of the ONF specimen. Therefore, misleading results were obtained when we evaluated the data by crack initiation test using this technique. Consequently, the application of the CC method is not recommended in this case.

Under the current geometry and material the traditional SLB and SCB configurations were suitable only to investigate crack initiation events, as it was discussed in Section 5.3. Therefore, a novel mixed-mode I/II configuration was proposed, here called the over-leg bending (OLB) specimen. Also, the compliance and the strain energy release rate were derived using the developed model for delamination coupons in Chapter 3. The closed-form solution showed – similarly to the SLB and SCB specimens – quite good agreement with the reduced experimental data. A remarkable advantage of the test is that the large displacements (which play a dominant role in composites with low flexural modulus) do not influence the crack propagation and the propagation can be easily controlled. The test gives essentially a linear elastic response and simple reduction techniques can be applied for data evaluation. A relative drawback of the test (similarly to the SLB and SCB coupons) is that the mode ratio may be changed only in a small degree.

6 FIBER-BRIDGING ANALYSIS IN THE DCB SPECIMEN

The aim of this chapter is to develop a beam theory-based solution for fiber-bridging modeling (SZEKRÉNYES 2003a, 2003b; SZEKRÉNYES and UJ, 2004e, 2005d). The main objective is to provide information on the number of bridgings and the bridging force. The approximate character of these quantities would be useful in order to understand the phenomenon more deeply. Traditional DCB test (see Fig. 2.2) on unidirectional glass/polyester specimens is performed providing input data for the analysis.

6.1 Beam analysis

In this section a closed-form expression is developed for the compliance of unidirectional DCB specimens. The model incorporates the *Winkler*-type elastic foundation (classical solution of WILLIAMS (1989) and considers the effect of fiber-bridging. The bridgings are represented by elastic beam elements, of which extensional stiffness and initial length is utilized. Let us consider the model of the DCB specimen loaded by edge forces in Fig. 6.1. The governing equations of the deflections are:

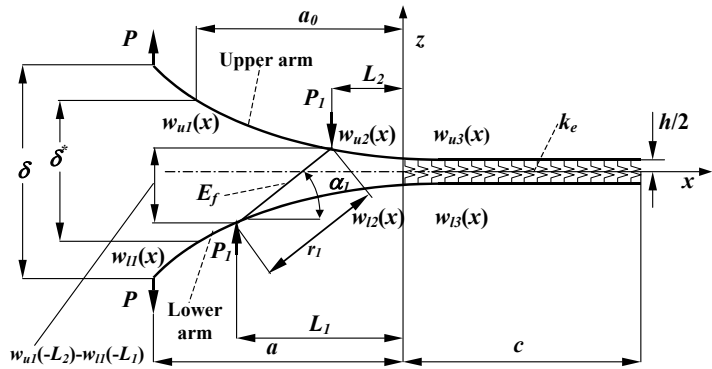


Fig. 6.1.

For the analysis of the fiber-bridging in the DCB specimen.

The governing equations of the deflections are:

$$\frac{d^2 w(x)}{dx^2} = \frac{-M(x)}{I_y E_{11}}, \quad -a \leq x \leq 0, \quad (6.1)$$

$$\frac{d^4 w(x)}{dx^4} + 4\lambda^4 w(x) = 0, \quad 0 \leq x \leq c. \quad (6.2)$$

The deflection functions of the lower arm can be expressed by solving Eq. (6.1), thus we have:

$$w_{l1}(x) = -\frac{P}{I_y E_{11}} \left[\frac{1}{2} ax^2 + \frac{1}{6} x^3 \right] + h_1 x + h_2, \quad -a \leq x \leq -L_1, \quad (6.3)$$

$$w_{l2}(x) = -\frac{P}{I_y E_{11}} \left[\frac{1}{2} ax^2 + \frac{1}{6} x^3 \right] + \frac{P_1}{I_y E_{11}} \left[\frac{1}{2} L_1 x^2 + \frac{1}{6} x^3 \right] + h_3 x + h_4, \quad -L_1 \leq x \leq 0, \quad (6.4)$$

where $I_y = bh^3/12$ is the second order moment of inertia and E_{11} is the flexural modulus. The subscript l refers to the lower arm. In the uncracked region the solution may be obtained by

combining the generalized *Krylov*-functions (PONOMARJOV, 1968), which are compiled in Appendix F. Based on Fig. 6.1 the boundary and matching conditions are:

$$\begin{aligned} w_{I3}''(c) &= 0, & w_{I3}'''(c) &= 0, \\ w_{I1}(-L_1) &= w_{I2}(-L_1), & w_{I1}'(-L_1) &= w_{I2}'(-L_1), \\ w_{I2}(0) &= w_{I3}(0), & w_{I2}'(0) &= w_{I3}'(0), \\ w_{I2}''(0) &= w_{I3}''(0), & w_{I2}'''(0) &= w_{I3}'''(0). \end{aligned} \quad (6.5)$$

Eq. (6.5) is necessary for the determination of the constant parameters (h_1 - h_8) in Eqs. (6.3), (6.4) and (F.2) (see Appendix F). For the upper half of the model the same boundary value problem may be established. We assume a joint-like connection between the bridging and the specimen arms. Thus, the elongation in the bridging is (refer to Fig. 6.1):

$$\Delta r_1 = r_1 - L_{01} = \sqrt{[w_{u1}(-L_2) - w_{I1}(-L_1)]^2 + L_{01}^2} - L_{01}, \quad (6.6)$$

where $L_{01} = |L_2 - L_1|$ is the initial length of the bridging. The displacements in Eq. (6.6) can be expressed by taking the deflections at the positions of $x = -L_1$ and $x = -L_2$, thus we obtain:

$$\begin{aligned} w_{u1}(-L_2) &= (\lambda^3 [PL_2^2(3a - L_2) - 2P_1L_2^3] + 6L_2\lambda^2(Pa - P_1L_2) + \\ &+ 3\lambda[P(L_2 + a) - 2P_1L_2] + 3(P - P_1)) / (6\lambda^3 I_y E_{I1}), \end{aligned} \quad (6.7)$$

$$\begin{aligned} w_{I1}(-L_1) &= -(\lambda^3 [PL_1^2(3a - L_1) - 2P_1L_1^3] + 6L_1\lambda^2(Pa - P_1L_1) + \\ &+ 3\lambda[P(L_1 + a) - 2P_1L_1] + 3(P - P_1)) / (6\lambda^3 I_y E_{I1}). \end{aligned} \quad (6.8)$$

Eqs. (6.7) and (6.8) were substantially simplified based on the work of OZDIL and CARLSSON (1999a). The tensile force in the bridging can be obtained by using the following equations:

$$F_1 = s_1 \Delta r_1, \quad s_1 = \frac{A_1 E_f}{L_{01}}, \quad A_1 = n_f \frac{d_f^2 \pi}{4}, \quad (6.9)$$

where s_1 is the extensional stiffness, A_1 is the cross-section of the bridging, E_f is the elastic modulus of the fiber, n_f is the number of fibers per bridging and d_f is the fiber diameter. The offaxis angle between the bridging and the axis x by the help of Fig. 6.1 becomes:

$$\alpha_1 = \arctan \left[\frac{w_{u1}(-L_2) - w_{I1}(-L_1)}{|L_2 - L_1|} \right]. \quad (6.10)$$

Let us denote the vertical component of the force F_1 as P_1 . According to Fig. 6.1 P_1 may be obtained as:

$$P_1 = F_1 \sin \alpha_1. \quad (6.11)$$

Substituting Eqs. (6.6), (6.7) and (6.8) into Eq. (6.11) and substituting Eqs. (6.7) and (6.8) into Eq. (6.10) and combining it again with Eq. (6.11) a transcendental equation may be obtained, of which solution is the force P_1 . The compliance of the lower arm becomes:

$$\begin{aligned} C_l &= \frac{w_{I1}(-a)}{P} = [2a^3\lambda^3 + 6a^2\lambda^2 + 6a\lambda + 3 + \\ &- \frac{P_1}{P} ((3aL_1^2 - L_1^3)\lambda^3 + 6aL_1\lambda^2 B + 3\lambda(L_1 + a) + 3)] / (6\lambda^3 I_y E_{I1}). \end{aligned} \quad (6.12)$$

The compliance of the DCB specimen ($C_{DCB} = \delta/P$) may be obtained by summing the compliances of the upper and lower arms, consequently we have:

$$C_{DCB} = C_l + C_u = \frac{2a^3\lambda^3 + 6a^2\lambda^2 + 6a\lambda + 3}{3\lambda^3 I_y E_{11}} \quad (6.13)$$

$$- \frac{P_1 [(3a(L_1^2 + L_2^2) - (L_1^3 + L_2^3))\lambda^3 + 6a(L_1 + L_2)\lambda^2 + 3\lambda(L_1 + L_2 + 2a) + 6]}{P \cdot 6\lambda^3 I_y E_{11}}$$

Incorporating the value of λ (see Appendix F) into Eq. (6.13) yields:

$$C_{DCB} = C_{DCB}^0 - C_{DCB}^{FB}, \quad (6.14)$$

where:

$$C_{DCB}^{FB} = \frac{P_1 [(3a(L_1^2 + L_2^2) - (L_1^3 + L_2^3))\lambda^3 + 6a(L_1 + L_2)\lambda^2 + 3\lambda(L_1 + L_2 + 2a) + 6]}{P \cdot 6\lambda^3 I_y E_{11}}, \quad (6.15)$$

where the term C_{DCB}^0 in Eq. (6.14) is given by Eq. (2.1), which is the specimen compliance based on the classical elastic foundation model (WILLIAMS, 1989). The effect of fiber-bridging is incorporated in the term C_{DCB}^{FB} . The SERR may be obtained by using Eq. (1.2). Combining it with Eq. (2.1) the energy release rate may be easily obtained without the bridging effect, the relevant expression (WILLIAMS, 1989; OLSSON, 1992; OZDIL and CARLSSON, 1999) is given by Eq. (2.2). Considering Eq. (6.15) we must differentiate all those parameters which depend on the crack length. Although the location of the bridgings, $L_1(a)$ and $L_2(a)$ are linear functions of the crack length a , the force $P_1(a)$ as a function of the crack length is difficult to obtain (see Eqs. (6.10) and (6.11)). Hence, a closed-form solution is not available for the SERR and furthermore, the dependence of L_1 and L_2 on the crack length is not considered.

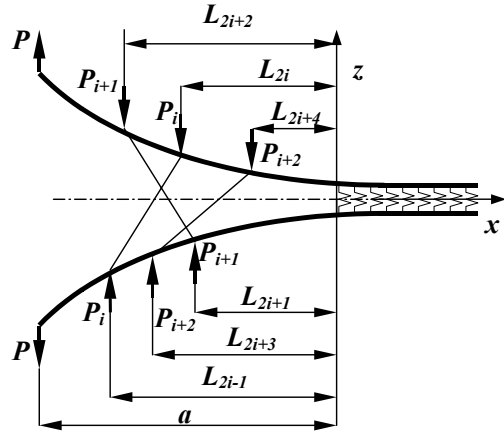


Fig. 6.2.
A general case for asymmetrical fiber-bridging.

It is evident that the equations above should be generalized in order to model any amount (n) of bridging fibers. In the followings the model introduced before is modified for ' n ' number of bridgings. In Fig. 6.2 a general asymmetric arrangement can be seen. The elongation in the ' j '-th bridging is (where ' j ' is a number between 1 and ' n ')

$$\Delta r_j = r_j - L_{0j} = \sqrt{[w_u(-L_{2j}) - w_l(-L_{2j-1})]^2 + L_{0j}^2} - L_{0j}, \quad (6.16)$$

where $L_{0j} = |L_{2j} - L_{2j-1}|$ is the initial length of the ' j '-th bridging. The value of the deflection at $x = -L_{2j}$ in the upper arm is:

$$w_u(-L_{2j}) = \sum_{i=1}^n (\lambda^3 [PL_{2j}^2(3a - L_{2j}) + P_i \phi_{2i}] + 6L_{2j} \lambda^2 (Pa - P_i L_{2i}) + 3\lambda [P(L_{2j} + a) - P_i(L_{2i} + L_{2j})] + 3(P - P_i)) / (6\lambda^3 I_y E_{11}), \quad (6.17)$$

where:

$$\begin{aligned}\phi_{2i} &= L_{2i}^2(L_{2i} - 3L_{2j}) & ,\text{if: } & |L_{2j}| \geq |L_{2i}|, \\ \phi_{2i} &= L_{2j}^2(L_{2j} - 3L_{2i}) & ,\text{if: } & |L_{2j}| < |L_{2i}|, \quad j=1,2,3,\dots,n.\end{aligned}\quad (6.18)$$

The deflection at the position of $x=-L_{2j-1}$ in the lower arm becomes:

$$\begin{aligned}w_i(-L_{2j-1}) &= -\sum_{i=1}^n (\lambda^3 [PL_{2j-1}^2(3a - L_{2j-1}) + P_i\phi_{2i-1}] + 6L_{2j-1}\lambda^2(Pa - P_iL_{2i-1}) + \\ &+ 3\lambda[P(L_{2j-1} + a) - P_i(L_{2i-1} + L_{2j-1})] + 3(P - P_i)) / (6\lambda^3 I_y E_{11}),\end{aligned}\quad (6.19)$$

where:

$$\begin{aligned}\phi_{2i-1} &= L_{2i-1}^2(L_{2i-1} - 3L_{2j-1}) & ,\text{if: } & |L_{2j-1}| \geq |L_{2i-1}|, \\ \phi_{2i-1} &= L_{2j-1}^2(L_{2j-1} - 3L_{2i-1}) & ,\text{if: } & |L_{2j-1}| < |L_{2i-1}|, \quad j=1,2,3,\dots,n.\end{aligned}\quad (6.20)$$

It is obvious that the distances, L_{2j} and L_{2j-1} should strictly determine the location of the ‘ j ’-th bridging. The tensile force in the ‘ j ’-th bridging is:

$$F_j = s_j \Delta r_j, \quad s_j = \frac{A_j E_f}{L_{0j}}, \quad A_j = n_f \frac{d_f^2 \pi}{4}, \quad (6.21)$$

where s_j is the extensional stiffness of the ‘ j ’-th bridging. The offaxis angle between the ‘ j ’-th bridging and the axis x may be obtained as:

$$\alpha_j = \arctan\left[\frac{w_u(-L_{2j}) - w_l(-L_{2j-1})}{|L_{2j} - L_{2j-1}|}\right]. \quad (6.22)$$

The ‘ j ’-th force P_j , according to Fig. 6.2 is:

$$P_j = F_j \sin \alpha_j. \quad (6.23)$$

Combining Eqs. (6.16)-(6.23) the system of equations may be built, from which the solutions for the forces ($P_i, i=1\dots n$) may be obtained. The mathematical form of the equation system is detailed in Appendix F. The compliance of the bridged DCB specimen becomes:

$$\begin{aligned}C_{DCB} &= \sum_{i=1}^n \{ \lambda^3 [4Pa^3 + P_i(L_{2i}^2(L_{2i} - 3a) + L_{2i-1}^2(L_{2i-1} - 3a))] + 6\lambda^2 [a(2Pa - P_i(L_{2i} + L_{2i-1}))] + \\ &+ 3\lambda [4Pa - P_i(L_{2i} + L_{2i-1} + 2a)] + 6(P - P_i) \} / (6P\lambda^3 I_y E_{11}).\end{aligned}\quad (6.24)$$

The number of unknown forces, as well as the number of bridgings is equal to n . Note that interaction between elastic foundation and the bridgings is included in Eqs. (6.17), (6.19) and (6.24). It should be kept in mind that the upper and lower deflection functions are forced to depend on each other in the case of asymmetrically arranged bridgings. This effect was assumed to be very small in the case of sufficient number of bridgings, and consequently, it is neglected in the above formulation. Also, the horizontal component of the tensile force in Eq. (6.21) was ignored. As we mentioned before the SERR can not be expressed in closed-form. In the following we use only the compliance expression.

The J -integral results in the following expression for the energy release rate including the bridged zone (SUO et al., 1992; LINDHAGEN et al., 2000):

$$J = G_I = \int_0^{\delta^*} \sigma(\delta) d\delta + G_{I0}, \quad (6.25)$$

where G_{I0} is the energy release rate from matrix cracking (and it is assumed to be a constant value), the first term is the contribution of the fiber-bridging to the steady-state fracture toughness. Differentiating Eq. (6.25) with respect to δ the bridging stress becomes:

$$\sigma(\delta) = \frac{\partial G_I}{\partial \delta^*}, \quad (6.26)$$

where δ^* is the crack opening displacement at the initial crack tip (see Fig. 6.1.). Eq. (6.26) is called the bridging law. An exact expression for the displacement at the initial tip ($\delta^* = \delta_u^* - \delta_l^*$) may be obtained by replacing L_{2j} and L_{2j-1} with $a - a_0$ in Eqs. (6.17-6.20).

It should be noted that the present model does not account for those bridgings, of which initial length changes (i.e. fiber peels away from matrix) as the crack propagates. Further local effects, such as fiber debonding, failure, pull-out and sliding are also ignored. All these mechanisms are demonstrated in the work by KAUTE et al. (1995). As a consequence, the developed model is suitable only for approximate computations. Due to the complexity of our model a simple numerical solver was developed in the code MAPLE (HECK, 1993).

6.2 Experiments

The flexural and other material properties are consistent with those, mentioned in Section 4.2. For the sake of completeness they are: $E_{11}=33$ GPa, $E_{33}=7.2$ GPa, $h=3.05$ mm, $b=20$ mm. The fiber diameter and the fiber modulus are: $d_f=12$ μm and $E_f=70$ GPa, respectively (PHILLIPS, 1989).

The DCB test setup is depicted in Fig. 6.3. Steel hinges were bonded to the upper and lower specimen arms. The tests were conducted under displacement control using an *Amsler* testing machine, illustrated in Fig. 6.3. Load/deflection data was recorded, the deflection was

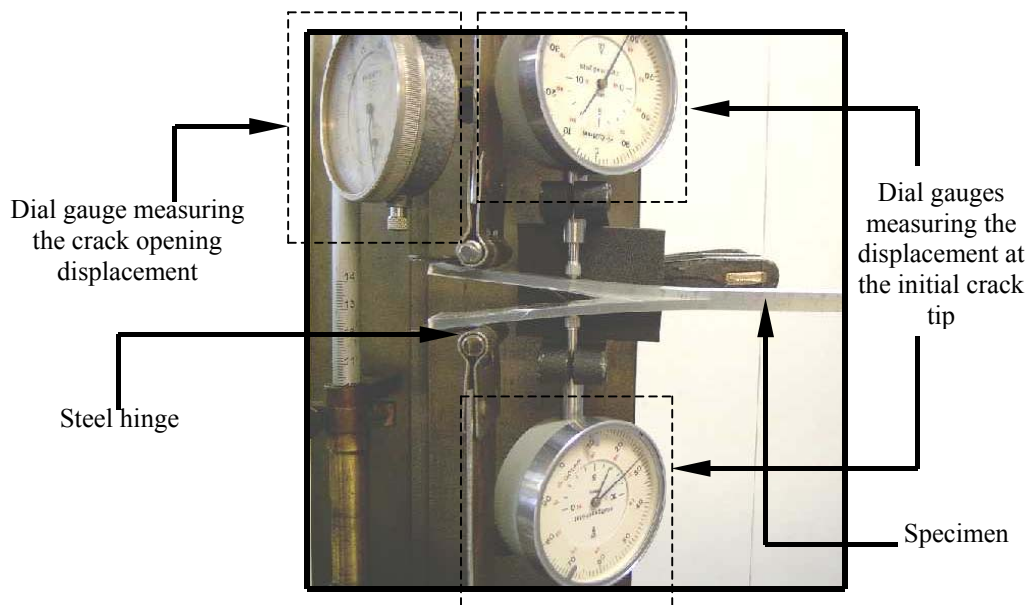


Fig. 6.3.
Experimental setup for DCB testing.

monitored by the dial gauge, shown at the upper left of Fig. 6.3. Crack initiation/propagation was followed visually, the curved crack front was easily observable through the upper and lower specimen surfaces.

Two kinds of measurements were performed. At the first stage we eliminated the effect of fiber-bridging by using 18 specimens with the following crack lengths: 30, 35, 40, 45, 50, 55, 60, 65, 70, 75, 80, 90, 100, 110, 120, 130, 140 and 150 mm. The specimens were loaded only up to fracture initiation and the compliance was determined for each specimen at the same point. This procedure was suitable to determine the fracture properties at crack initiation without the fiber-bridging effect in the mentioned ($a=30-150$ mm) crack length range.

At the second stage six specimens with an initial crack length of $a_0=30$ mm were investigated in the same test configuration, as shown in Fig. 6.3. In this case the complete R-curve including the bridging effect was determined within the same crack length interval ($a=30-150$ mm). The displacement at the initial crack tip was recorded by using the two dial gauges depicted in Fig. 6.3. It was necessary for the determination of the bridging law. The data reduction was the same as in the case of the crack initiation tests. Some specimens with extensive fiber-bridging are shown in Fig. 6.4.

The compliance calibration method was used to reduce the experimental data. The compliance of the DCB specimen is given by Eq. (2.9), where β and m may be found by using a fitting technique. Furthermore, the crack length was corrected in accordance with THAMM et al. (1985), who suggested a correction for large displacements:

$$a = Na^*, \quad N = 1 - \frac{1}{6} \left(\frac{\delta}{a^*} \right)^2, \quad (6.27)$$

where a^* is the measured, a is the corrected crack length and δ is the experimentally measured displacement at the point of load application. The length of the initial crack was similarly corrected. Thus, the relevant equations are:

$$a_0 = Na^* - N^*(a^* - a_0^*), \quad N^* = 1 - \frac{1}{6} \left(\frac{\delta^*}{a^* - a_0^*} \right)^2, \quad (6.28)$$

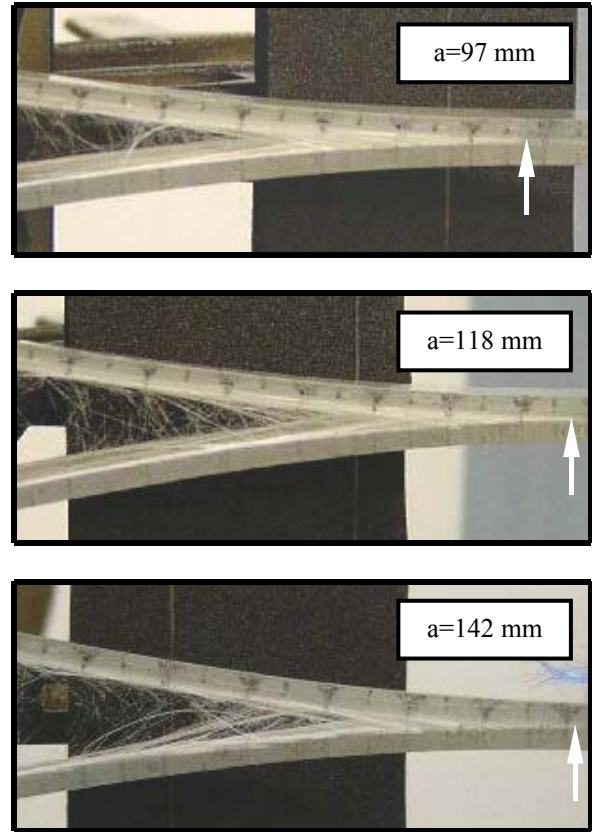


Fig. 6.4.
Length of the bridged zone at different crack lengths.

where a_0^* is the measured, a_0 is the corrected value of the initial crack length and δ^* is the experimentally measured displacement at the initial crack tip (refer to Fig. 6.1).

6.3 Test results

6.3.1 Crack initiation tests

Linear load/displacement curves were recorded through crack initiation tests, as shown by Fig. 6.5a. The compliance versus the crack length is plotted in Fig. 6.5b, only Eq. (2.1) was used for data evaluation. The correlation was found to be excellent between the *Winkler* foundation model and the experimental points. It is noteworthy, that the exponent (m) in

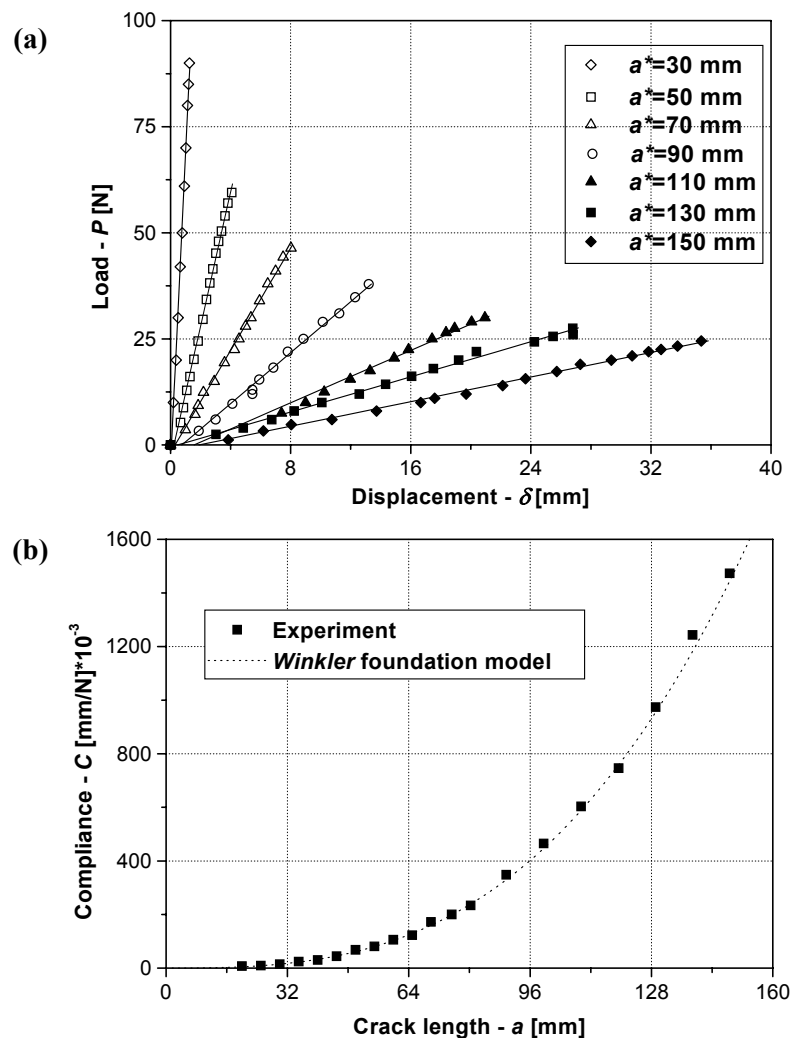


Fig. 6.5.

Load/displacement curves (a), measured and calculated compliance (b) from initiation tests.

Eq. (2.9) was less than 3. The fracture resistance curve at crack initiation can be seen in Fig. 6.7b. The steady-state value is about 412 J/m^2 . Also, the points by the analysis and

experiments almost coincide. The closed-form solution was obtained by combining Eqs. (2.1) and (1.2), of which result (Eq. (2.2)) compared to the experimentally determined values agrees quite closely in the entire crack length interval. As a consequence, in this case the classical elastic foundation model provides the reasonably accurate description of both the compliance and the energy release rate.

6.3.2 Crack propagation tests

A typical load/displacement curve is plotted in Fig. 6.6a. The crack initiation was observed at $P=86-90$ N, while the peak value of the load was always about 117-122 N. During testing extensive fiber-bridging was observed as it is shown by the photographs in Fig. 6.4, the bridgings appeared under a shallow angle. The crack always propagated along the

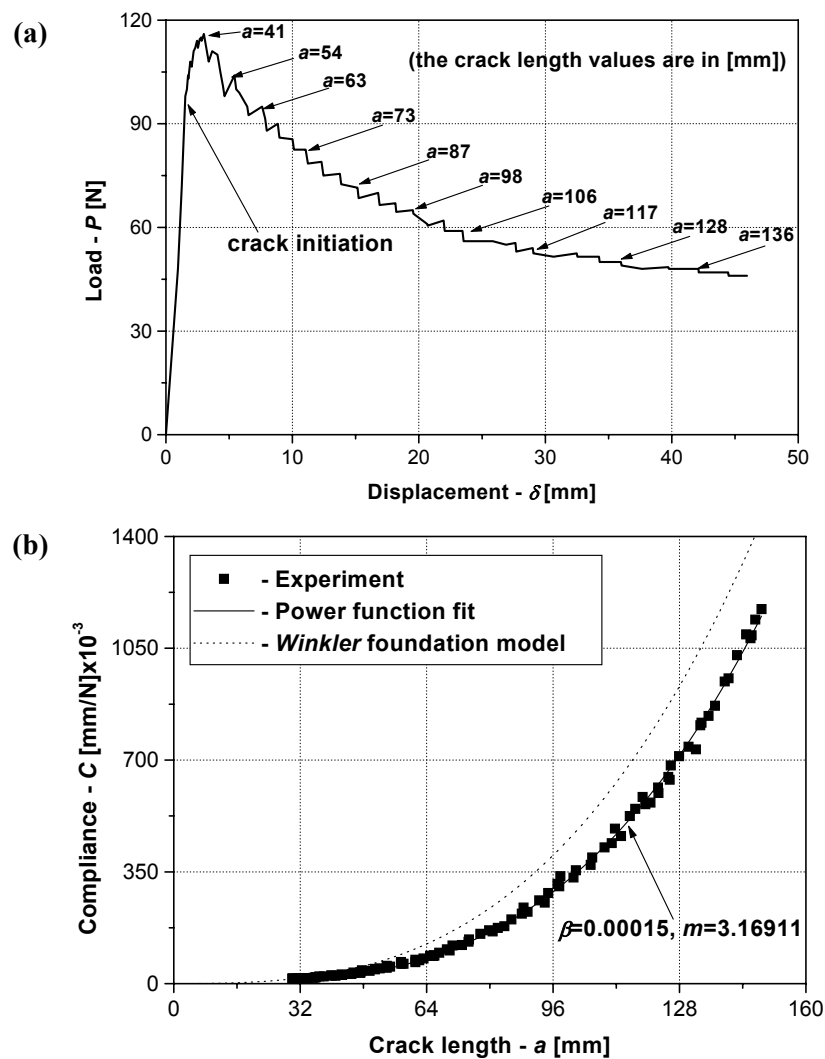


Fig. 6.6.

Load/displacement curve (a) and compliance curves (b) from propagation tests.

midplane of the specimens. In Fig. 6.6b the experimental compliance values and the analytical curve (Eq. (2.1)) are illustrated. The exponent (m) in Eq. (2.9) was higher than 3 for all the six specimens. An immediate observation is that the model (Eq. (2.1)) significantly overpredicts the experimental compliance values. The values of the energy release rate and the averaged G_I - a data is plotted in Figs. 6.7a and b. Again, the closed-form solution is given by Eq. (2.2). The difference was found to be particularly significant between the analytically and experimentally determined SERR values (Fig. 6.7b).

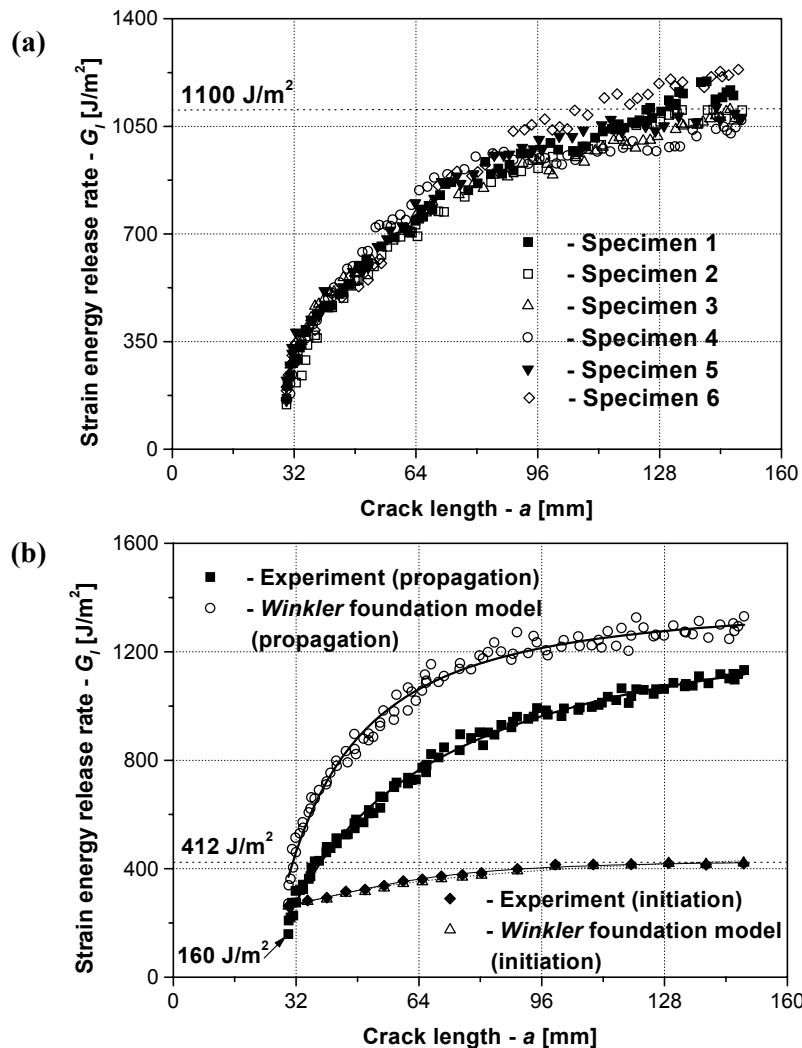


Fig. 6.7.

G_I - a data from the propagation test of six specimens (a). Initiation and propagation R-curves, comparison between experiment and analysis (b).

As shown by Fig. 6.7b distinct values were obtained for the strain energy release rate from the crack initiation and crack propagation tests at the crack length value of $a=30$ mm. For both tests the force at crack initiation was the same (86-90 N) at this point. The difference may be explained by the fact that the derivative of the compliance was higher in the case of crack initiation than in the case of propagation tests (refer to Figs. 6.5b and 6.6b).

6.4 Application of the developed beam model

The accuracy of the classical elastic foundation model (Eq. (2.1)) was demonstrated through the crack initiation tests. Thus, we may assume that the overpredictions experienced in the crack propagation tests arise due to the fiber-bridging phenomenon. In order to estimate the number of bridging fibers and the bridging force the experimental data was evaluated by using the model developed in Section 6.1.

6.4.1 Compliance calculation

The computation was performed according to the following procedure. Based on the crack propagation test data the applied load P , the displacements, δ and δ^* measured from the tests of six specimens were averaged with respect to the crack length. The experimental compliance was calculated based on the averaged P and δ values, then the compliance values were fit by using a third order polynomial of the form:

$$C = C_0 + C_1 a + C_2 a^2 + C_3 a^3. \quad (6.29)$$

The reason for that is the analytical compliance expression (Eq. (6.24)) can be written in the form of a third order polynomial. On the other hand Eq. (2.9) and Eq. (6.29) gives somewhat distinct result as regarding to the number of bridgings, especially in the range of $a=30$ to 50 mm. The application of Eq. (2.9) is reasonable if we calculate the SERR, but at this stage Eq. (6.29) is more reasonable. The analytical compliance value (Eq. (6.24)) was computed for the actual crack length by an iterative technique. In each step the crack increment was 3-5 mm, while the number and location of the bridgings were chosen in order to hold the difference between the analytical and experimental compliance values (Fig. 6.6b) within $\pm 2-3\%$. Also, the displacement at the initial crack tip (δ^*) was considered and the difference between the analytical and experimental values was held within $\pm 2-3\%$. Only symmetrically arranged bridgings were applied with the same fiber content. Finally, it was assumed that the average bridging stress calculated from the beam model (see Eq. (6.30)) is equal to that obtained by Eq. (6.26). If these criteria are satisfied it was believed to be a possible solution of the problem.

6.4.2 Bridging law computation

Two approaches were used to calculate the nonlinear bridging law. The first method (denoted as the *average stress* method) is based on the average bridging stress:

$$\sigma(\delta^*) = \frac{n \cdot n_f \sum_{i=1}^n P_i}{A(a)}, \quad (6.30)$$

where n is the number of bridgings, n_f is the number of fibers per bridging, P_i are the forces in the bridgings and $A(a)$ is the area of the bridged zone at the actual crack length. The length of the bridged zone is illustrated in Fig. 6.4 at certain crack lengths, where the white arrows

show the position of the crack tip. At the beginning of the delamination process the bridged zone extended over the initial crack tip with several millimeters, but it reached an approximately constant value (45 mm) during crack propagation. The area of the bridged zone yields by multiplying the bridged length with the specimen width b . It should be mentioned, that the bridging law (Eq. (6.26)) assumes a uniform stress distribution. Similarly, in Eq. (6.30) the average stress is considered. It is evident that the bridging force is not uniformly distributed. Thus, the result of Eq. (6.30) is only approximate.

For the second approach Eq. (6.25) is used. Although it is based on the experimentally determined quantities, these may be calculated also by the present beam model. The compliance values calculated from Eq. (6.24) may be fit by Eq. (2.9). The SERR may be obtained by using Eq. (1.2), then the bridging law is determined by the help of Eq. (6.26) incorporating a curve fit of the $G_I\text{-}\delta^*$ data. This method was denoted as the J -integral method. Comparison of the two analytical and the experimental bridging laws is made.

6.5 Results and discussion

The compliance values calculated by the present beam model are illustrated in Fig. 6.8a. The comparison with the experimental values in Fig. 6.6b shows a good agreement. The coefficient (β) and the exponent (m) of the fit curve (Eq. (2.9)) are essentially the same in Fig. 6.6b as in Fig. 6.8a. As a consequence, the same energy release rate values may be determined from the calculated compliance curve in Fig. 6.8a, as those plotted in Fig. 6.7b.

The total bridging force and the number of bridging fibers are illustrated in Figs. 6.8b and 6.8c as a function of the displacement at the initial tip. The force reaches a peak value of about 176 N and then it slightly decreases until the value of 120 N. At the beginning of the delamination the number of bridging fibers reaches a maximum value and then it decreases significantly as the crack opens (Fig. 6.8c). KAUTE et al. (1995) presented quite similar results using a semi-empirical model. In their work the fiber force was assumed to be constant after crack initiation, while the number of bridgings decreased in accordance with an exponential function.

Fig. 6.9a shows the $G_I\text{-}\delta^*$ curves determined from experiment and analysis. As expected, the correlation was found to be excellent, despite the beam model shows a little overestimation. Figs. 6.9b and 6.9c demonstrate the bridging laws. The result of the *average stress* method (Eq. (6.30)) is depicted in Fig. 6.9c, in comparison with the J -integral approach the agreement seems to be very good. According to the *average stress* method the stress is equal to zero at crack initiation, it reaches a peak value (0.32 MPa, refer to Fig. 6.9c) and finally decays notably. At the crack initiation the J -integral method indicates 4.92 MPa (Fig. 6.9c) value based on beam analysis and 3.94 MPa from experiment (Fig. 6.9b). For comparison the work by TAMUZS et al. (2001) may be referred to, wherein the presented bridging law follows the same trend as it was found by us.

According to Eq. (6.25) the term G_{I0} from matrix cracking is assumed to be a constant value. The first term in Eq. (6.25) is defined by the integral over the total crack opening. Consequently, the term, G_{I0} may be determined by subtracting the first term from the total

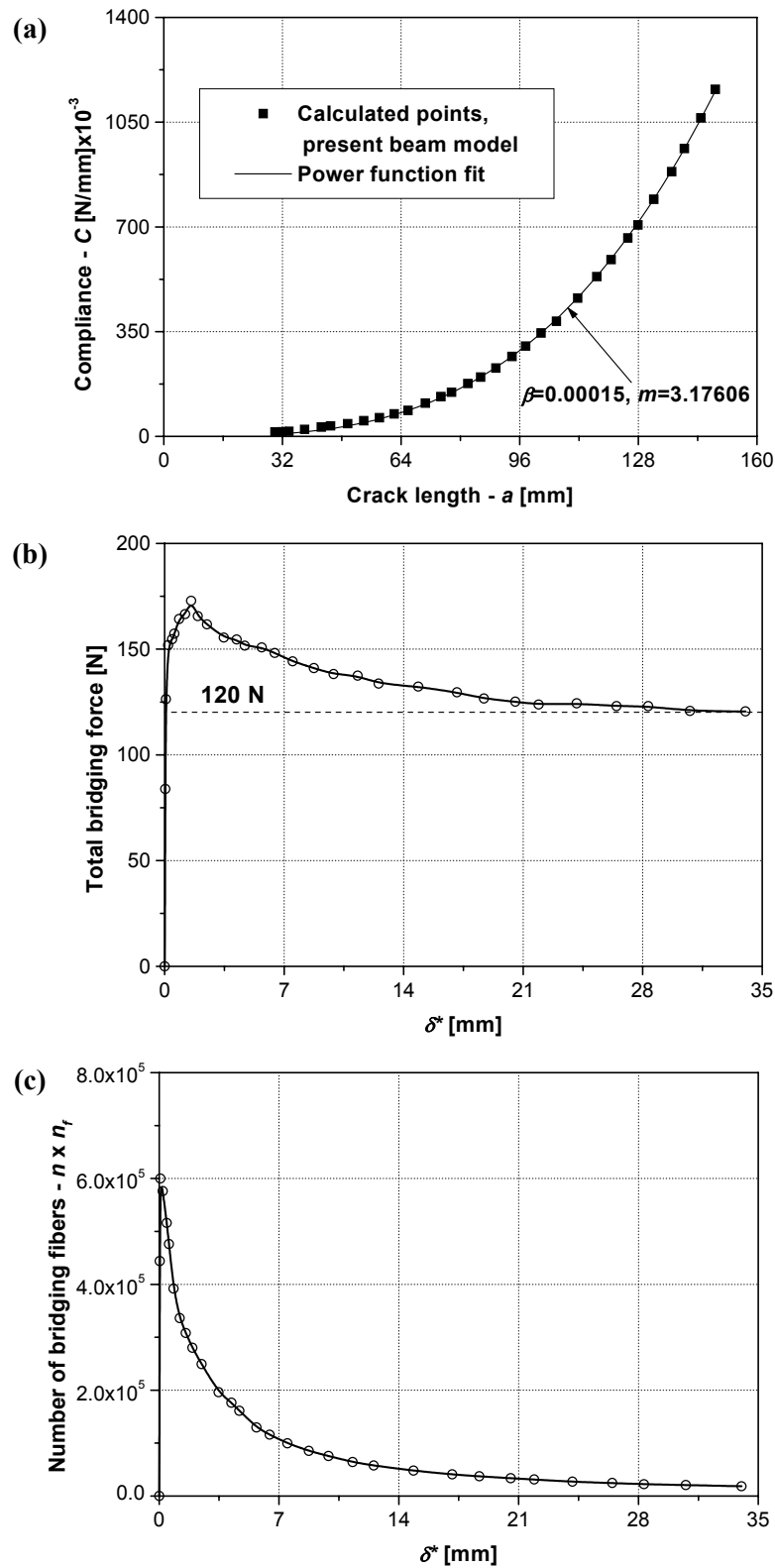


Fig. 6.8. Compliance calculated from the present beam model (a). The total bridging force (b) and the total number of bridging fibers (c) against the displacement at the initial crack tip.

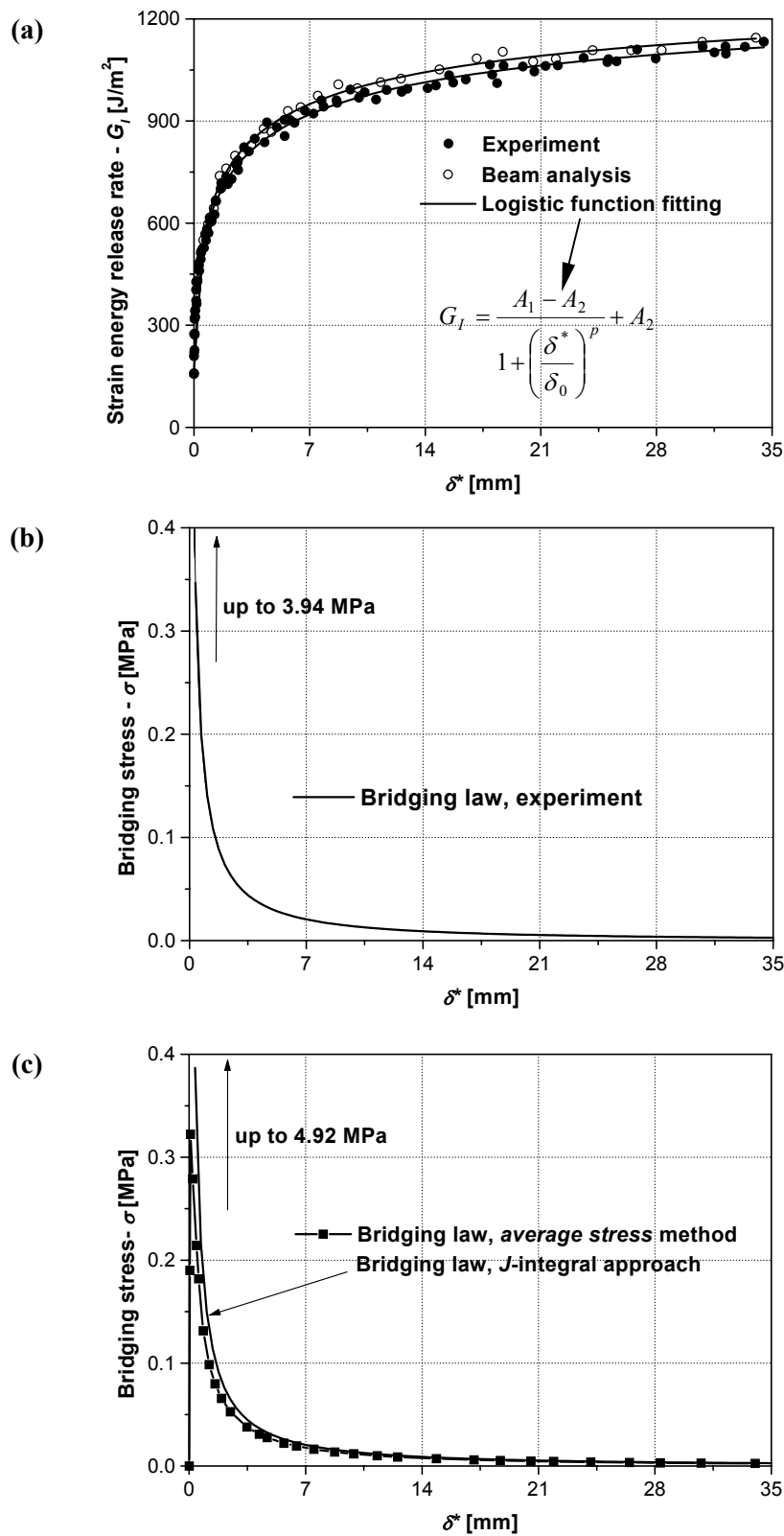


Fig. 6.9. G_I - δ^* curves from experiment and beam analysis (a). Experimental bridging law (b). Analytical bridging law from *average stress* and *J-integral* approach (c).

strain energy release rate. Based on the experimentally determined bridging law this term is approximately equal to 160 J/m^2 , which is identical to the initiation value in Fig. 6.7b (square symbols). A reasonable assumption is that during crack initiation tests the total energy release rate comes from matrix cracking and it is a constant value at any crack length. In spite of this, the initiation toughness increases (from 280 to 415 J/m^2) with the crack length in accordance with Fig. 6.7b. HASHEMI et al. (1990b) experienced similar behavior to that found by us. In fact, the dependence of the initiation SERR on the initial crack length is not serious in Fig. 6.7b and we assumed that for the current material Eq. (6.25) is valid.

It was mentioned by LINDHAGEN and BERGLUND (2000) that as the crack advances the steady-state toughness is equal to the area under the curve of the bridging law. Note that the length of the specimen was not large enough to reach a plateau value, in other words some fiber-bridging was observed at the end of the delamination process (refer to Fig. 6.7b). LINDHAGEN and BERGLUND investigated short-fiber-reinforced composite specimens and they have found that in some cases the SERR from matrix cracking may be neglected. On the base of our experiments the SERR increases up to 1100 J/m^2 . At this point the matrix cracking (160 J/m^2) contributes to the total energy release rate with about 15%, which is not negligible.

6.6 Application guideline

The following guideline may be given for the application of the newly developed approach:

- Perform experimental crack propagation tests on proper number of DCB specimens, record the load/crack opening displacement data and the corresponding crack length values and measure the displacement at the initial crack tip at each crack length. Determine approximately the length of the bridged zone at each crack length.
- Evaluate the experimental data by means of the compliance calibration method using Eq. (2.9) and determine the bridging law by the help of Eq. (6.26).
- Calculate the analytical compliance values (Eq. (6.24)) including the effect of the fiber-bridgings at the crack length of interest. Fit the experimental compliance values by Eq. (6.29). The number and the location of the bridgings may be estimated by holding the difference between the experimental (Eq. (6.29)) and analytical displacements (δ and δ^*) within $\pm 2\text{-}3\%$. Furthermore, the average bridging stress may be equated to that calculated by the J -integral. Record the number of bridgings and calculate the total bridging force.

6.7 Conclusions, scientific significance

The fiber-bridging phenomenon was investigated using linear beam theory and experiments in unidirectional glass/polyester DCB coupons. Extensive fiber-bridging was observed during the crack propagation tests. The objective of the present chapter was to determine approximately the number of bridging fibers and the bridging force. Based on linear beam theory the compliance of the bridged DCB specimen was derived. The bridging

mechanism was simulated by elastic beam elements. A numerical solver was written using the MAPLE package. The location and the number of fibers were determined by an iterative technique.

A hyperbolic character was found in the case of the number of bridging fibers as a function of the displacement at the initial crack tip. The bridging force reaches a peak value first, and then it tends to a plateau value of about 120 N as the crack advances. The bridging law was calculated based on experiments and analysis. Comparison between them showed good agreement, but it should be kept in mind that in one of the analytical approaches the average bridging stress was considered.

The obtained results were compared with other ones, previously published on similar systems. Similar behavior was found, which partly confirms the analytical solution. From other perspectives the present formulation involves several approximations. For instance, local effects (fiber pull-out, fiber breakage, etc.) were not taken into account.

Although the application of the model is slightly time-consuming, the calculation may be performed (in contrast with the previously developed numerical and semi-empirical approaches) by the help of some essential material properties, namely the fiber diameter d_f and the elastic modulus of the fibers E_f .

7 SUMMARY OF THE RESULTS

In the final chapter we summarize the results of the analysis and the experimental interlaminar fracture tests.

7.1 Generalization of the compliance of delaminated composite beams

Based on Chapters 3 and 6 the compliance of midplane delaminated composite beams, of which arms exhibit the same mechanical properties may be written in the form of a full third order polynomial as the function of the crack length:

$$C = C_0 a^0 + C_1 a^1 + C_2 a^2 + C_3 a^3, \quad (7.1)$$

where the terms C_0 , C_1 , C_2 and C_3 may be related to the different theories and effects in accordance with Table 7.1.

Table 7.1.

Contribution of the various theories and effects to the compliance of delaminated composite beams with midplane crack in explicit form.

	C - compliance			
	C_0	C_1	C_2	C_3
Application of the <i>Euler-Bernoulli</i> beam theory	+	+	+	+
Application of the <i>Timoshenko</i> beam theory	+	+	-	-
Application of the <i>Winkler-Pasternak</i> foundation	+	+	+	-
<i>Saint-Venant</i> effect at the crack tip	+	+	+	-
<i>Saint-Venant</i> effect at the clamped end	+	-	-	-
Crack tip shear deformation	+	+	+	-
Fiber-bridging phenomenon	+	+	-	-

Notation:

- + the corresponding coefficient in the compliance is influenced
- the corresponding coefficient in the compliance is not influenced

It should be mentioned that the *Euler-Bernoulli* beam theory results in a full third order polynomial for the compliance of the ONF (Eq. (5.3)) and OLB specimens (Eq. (5.15)). This is the reason for that why all the terms (C_0 , C_1 , C_2 and C_3) are influenced by the *Euler-Bernoulli* beam theory. Also, the crack tip shear deformation (third term in Eq. (5.3) and fourth term in Eq. (5.15)) affects the terms related to a^0 , a^1 and a^2 in Eq. (7.1) because $c=2L-a$. The same conclusion may be drawn if we investigate the *Saint-Venant* effect at the crack tip in the case of the OLB specimen. The developed beam model in Chapter 6 showed that the fiber-bridging influences only the terms C_0 and C_1 (refer to Eq. (6.24)). It is remarkable that this effect was analyzed only in a mode-I problem and the dependence of some parameters on the crack length was not taken into account. Consequently the effect of the bridgings is incorporated only in an explicit form.

Table 7.1 also explains why we used a full third order polynomial for the compliance calculation in Chapter 6 (see Eq. (6.29)). Although in the case of a bridged DCB specimen the

Euler-Bernoulli beam model affects only the term C_3 , the consideration of the other effects - especially the fiber-bridging - requires a full third order polynomial.

7.2 The critical load and displacement

The critical load is denoted here as the value, which is necessary to induce crack initiation. Also, the critical displacement is the value at the same point. Figs. 7.1a and 7.1b

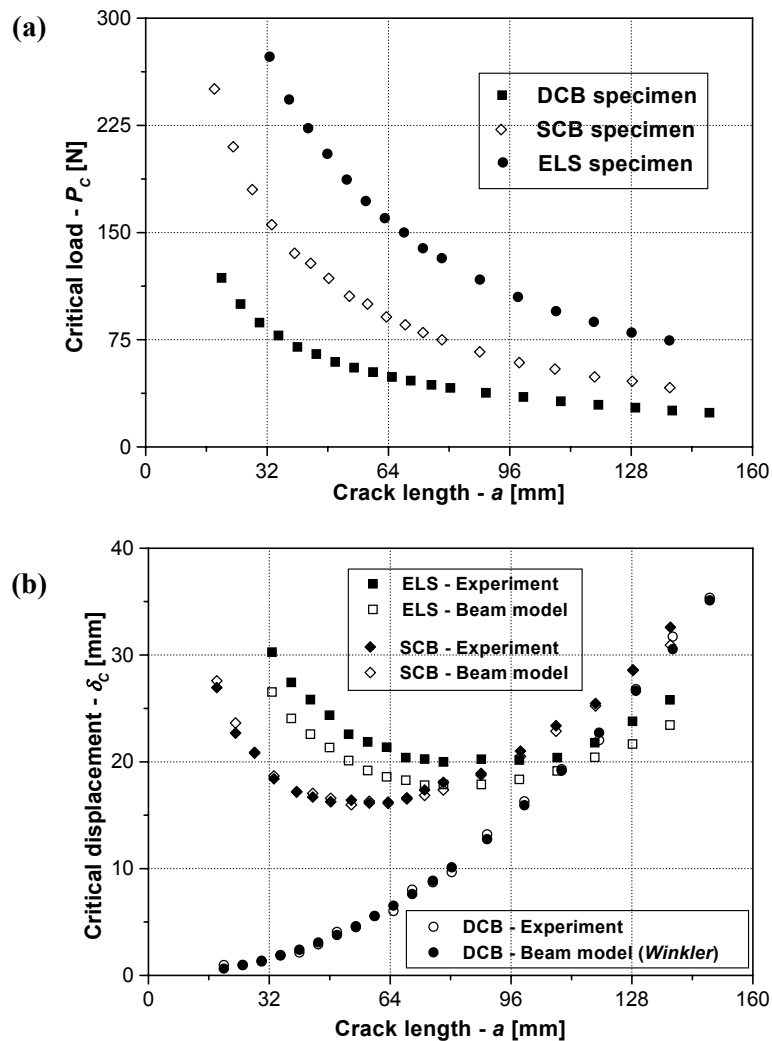


Fig. 7.1.

The values of the critical load (a) and displacement (b) against the crack length in the case of the DCB, ELS and SCB specimens.

illustrate the critical load and the critical displacement at crack initiation against the crack length in the case of the DCB, ELS and SCB specimens. The critical load shows hyperbolic, while the displacement has parabolic relation for all the three specimens. It is shown in Fig. 7.1 that in each case large displacements occur, however it does not matter in the case of the DCB specimen. The reason for this is that the crack length can be easily corrected if large

displacement occurs and the crack propagation is always stable without any significant crack jumps. On the other hand the presence of the large displacements is a serious problem in the case of the ELS and SCB specimens. In fact it was reason for that we were not able to perform crack propagation tests in these cases. The large displacements caused sudden jumps in the crack advance.

The mode-II ELS specimen was studied by HASHEMI et al. (1990a). In their tests the crack length range of $0.5L < a < 0.81L$ was investigated for carbon/PEEK specimens. Also, in another study the relevant range of the crack length was $0.58L < a < 0.92L$ for PES-fiber composite specimens (HASHEMI et al., 1990b). It is important to note that in these papers

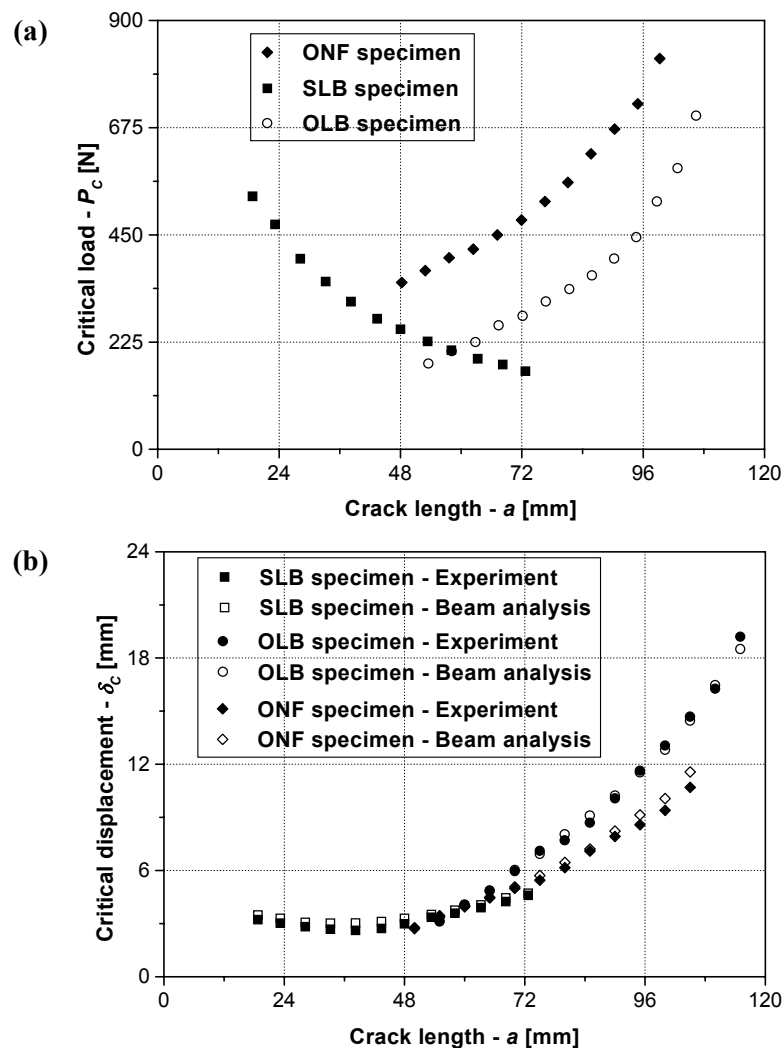


Fig. 7.2.

The values of the critical load (a) and displacement (b) against the crack length in the case of the ONF, SLB and OLB specimens.

propagation tests were also performed. The flexural modulus of the specimens in HASHEMI et al.'s works were $E_{II}=124$ GPa and $E_{II}=132$ GPa, respectively, i.e. the flexural modulus of the specimens used by them were about 3.8-4 times higher than that of our specimens. This

indicates that the stiffness of the ELS system in our experiments was not large enough, and consequently it was not possible to conduct crack propagation tests. However, to minimize the large displacements in crack initiation tests the recommended crack length range is (see Fig. 7.1): $55 \text{ mm} < a < 130 \text{ mm}$, i.e. $0.37L < a < 0.87L$. It is also interesting that the critical displacement in Fig. 7.1 reaches the lowest value at $a=80 \text{ mm}$, i.e. $a/L=0.53$, which is eventually the limit of the stable crack propagation (refer to Eq. (5.12)).

Quite similar conclusions may be drawn in the case of the SCB specimen. It is clear from Fig. 7.1a that large displacements occur again. For a useful crack length interval the lower bound is $a=35 \text{ mm}$, the upper one is $a=120 \text{ mm}$, writing simply: $0.23L < a < 0.8L$. HASHEMI et al. performed experiments on mixed-mode carbon/PEEK (HASHEMI et al., 1990a) and PES-fiber (HASHEMI et al., 1990b) SCB specimens with $L=135 \text{ mm}$ and $L=120 \text{ mm}$, respectively. The relevant crack length ranges were $0.5L < a < 0.8L$ and $0.2L < a < 0.7L$, respectively, which agrees well with the ranges used in the present experiments.

In Fig. 7.2 the results of the three other configurations, namely the ONF, SLB and the newly designed OLB specimens are summarized. A remarkable feature is that all these are three-point bending setups, however the load is eccentrically introduced in the ONF and OLB setups. In accordance with Fig. 7.2a we may observe that the critical load follows a parabolic trend in the case of the ONF and OLB specimens. As regarding to the results of the SLB test, similarly to the results in Fig. 7.1b, the load shows a hyperbolic nature as a function of the crack length. Furthermore, comparing the ONF to OLB results in Fig. 7.2a shows that at each crack length a higher load value is required under mode-II condition. Fig. 7.2b presents the values of the displacements at crack initiation as obtained by the three types of tests. No large displacements were experienced through the SLB test, which indicates that the chosen crack interval ($0.13 \cdot 2L < a < 0.49 \cdot 2L$) is reasonable for fracture investigation using linear beam theories. For comparison KORJAKIN et al. (1998) used glass/epoxy MMF specimens within the crack length range of $0.25 \cdot 2L < a < 0.45 \cdot 2L$ ($2L=76 \text{ mm}$). The displacements are somewhat higher for the OLB and ONF tests, however the result of the beam analysis gives values close to the measured points. Hence, we may state that the ONF and OLB specimens are efficient tools for crack initiation and propagation tests without the presence of large displacements and without the necessity of considering stability range in the case of the ONF test.

7.3 Comparison of the SERR under different loading conditions

It is also an important issue to compare the steady-state values of the critical strain energy release rate under different loading conditions. In this section we consider the result of the CC method, except in the case of the ONF test, where we refer to results of the direct beam theory. In Table 7.2 a review on those interlaminar fracture toughness values is given, which were measured by other authors and those determined within the scope of this work.

Running through the fracture toughness results at crack initiation presented in Table 7.2, we may establish the following relation: $G_{IC} < G_{I/II} < G_{IIC}$, i.e. the initiation fracture toughness exhibits the lower value under pure mode-I, while it reaches the highest value under pure mode-II condition. This trend was found considering also the results by the other

Table 7.2.Interlaminar fracture energy (G_C -[J/m²]) values by experimental initiation tests.

Author - material	DCB mode-I	ENF	ELS mode-II	ONF	SLB (MMF)	SCB	OLB	MMB
						mixed-mode I/II		
Present – glass/polyester	412	-	713	730	645	645	650	-
HASHEMI et al. – carbon/PEEK	1800	-	1730	-	-	1530	-	-
HASHEMI et al. – PES-fiber	800	-	1250	-	-	1180	-	-
OZDIL et al. – glass/polyester	282	496	-	-	-	-	-	311
KORJAKIN et al. – glass/epoxy	223	2115	-	-	456	-	-	-
ALBERTSEN et al. – C/HG9106	120	335	565	-	145	-	-	-
DAHLEN et al. – T300/976	135	450	-	-	-	196	-	-
DAHLEN et al. – IM7/977-2	333	994	-	-	-	497	-	-
DAVIDSON et al. – IM7/977-2	360	910	-	-	370	-	-	-
POLAHA et al. – graphite/epoxy	265	875	-	-	335	-	-	-

authors, except those by HASHEMI et al. (1990a) for carbon/PEEK composite specimens, whose results are compiled in Table 7.2. In this respect the results of our experimental test are absolutely reasonable.

Let us consider the results listed in Table 7.3, where the values of the propagation toughness are demonstrated for different type of composite materials by few authors. This time we can not observe an explicit trend, since the relative values of the fracture toughness are quite different ones. The source of this fact can only be that the different materials behave differently under mode-I, mode-II and mixed-mode I/II conditions. However, looking at Table 7.3 an immediate observation is that the mode-II critical SERR measured by our test is

Table 7.3.Interlaminar fracture energy (G_C -[J/m²]) values by experimental propagation tests.

Author - material	DCB mode-I	ENF	ELS mode-II	ONF	MMF	SCB	OLB	MMB
						mixed-mode I/II		
Present – glass/polyester	1100	-	-	2787	-	-	1160	-
HASHEMI et al. – carbon/PEEK	2290	-	2890	-	-	2080	-	-
HASHEMI et al. – PES-fiber	2000	-	1850	-	-	1480	-	-
KORJAKIN et al. – glass/epoxy	552	-	-	-	525	-	-	-
ALBERTSEN et al. – C/HG9106	490	-	800	-	330	-	-	-
REYES et al. – glass/polyprop.	2450	3800	-	-	-	-	-	4750

significantly higher compared to those measured under pure mode-I and mixed-mode I/II conditions. As a final word our results for the propagation toughness are reasonable and enrich the referable values in the composite literature.

It is noteworthy that in this study only specimens with mode-I precrack were used. The effect of precracking mode on the initiation toughness was investigated by POLAHA et al. (1996), DAVIDSON et al. (1999) and MORAIS et al. (2004). All these authors have found that in the case of mode-I precracking the toughness may be expected to be lower in comparison with the mode-II precracking. Also, the toughness has a higher value when the crack is initiated directly from the insert, as it is shown by MORAIS et al. (2004). Thus, the presented results should be considered in the light of these establishments.

7.4 Fracture envelope

The fracture envelope for the present composite material was composed by using two criterions. In accordance with the traditional criterion the following relation may be established between the mode-I and mode-II strain energy release rates (HASHEMI et al., 1990a, 1990b):

$$\left(\frac{G_I}{G_{IC}}\right)^{p_1} + \left(\frac{G_{II}}{G_{IIC}}\right)^{p_2} = 1, \quad (7.2)$$

where G_{IC} is the critical strain energy release rate under pure mode-I, G_{IIC} is the mode-II critical strain energy release rate and can be equated to the steady-state values collected in the first row of Tables 7.2 and 7.3. To construct the fracture envelope we need at least three points. The pure mode-I and mode-II toughnesses are known. The mixed-mode I/II toughness in Tables 7.2 and 7.3 should be decomposed into mode-I and mode-II parts. Although in Chapter 4 it was shown that the mode-ratio (G_I/G_{II}) has different values at each crack length, we utilize the result of the *Euler-Bernoulli* beam theory. In this case the mode ratio of the OLB specimen is equal to 1.33, so a third point is known for Eq. (7.2). WILLIAMS' criterion (HASHEMI et al., 1990a, 1990b) recommends the following expression:

$$\left(\frac{G_I}{G_{IC}} - 1\right)\left(\frac{G_{II}}{G_{IIC}} - 1\right) - I_i \left(\frac{G_I}{G_{IC}}\right)\left(\frac{G_{II}}{G_{IIC}}\right) = 0, \quad (7.3)$$

where I_i is the interaction parameter between the mode-I and mode-II strain energy release rates. If $I_i=0$ then there is no interaction. Also, if $I_i=1$ then Eq. (7.3) states a simple addition. The power parameters (p_1, p_2) in Eq. (7.2) and the interaction parameter (I_i) in Eq. (7.3) may be determined by a curve fitting technique.

The fracture envelopes at crack initiation and crack propagation are depicted in Fig. 7.3. In fact the difference between the traditional and WILLIAMS' criterion is negligible, both criteria describe the same failure locus. Overall, the fit curves report that there is a notable interaction between the mode-I and mode-II loading.

For comparison several works may be referred to. Quite similar fracture envelope was determined by RIKARDS et al. (1998) for glass/epoxy composite, only initiation toughness values were measured with the compact tension shear (CTS) specimen. HASHEMI et al.

determined fracture envelopes for crack initiation and propagation by using the DCB, ELS and SCB specimens for carbon/PEEK (1990a) and polyether sulphone-fiber (1990b) composites. The determined envelopes followed the same trend as it was found by us in Figs. 7.3a and 7.3b.

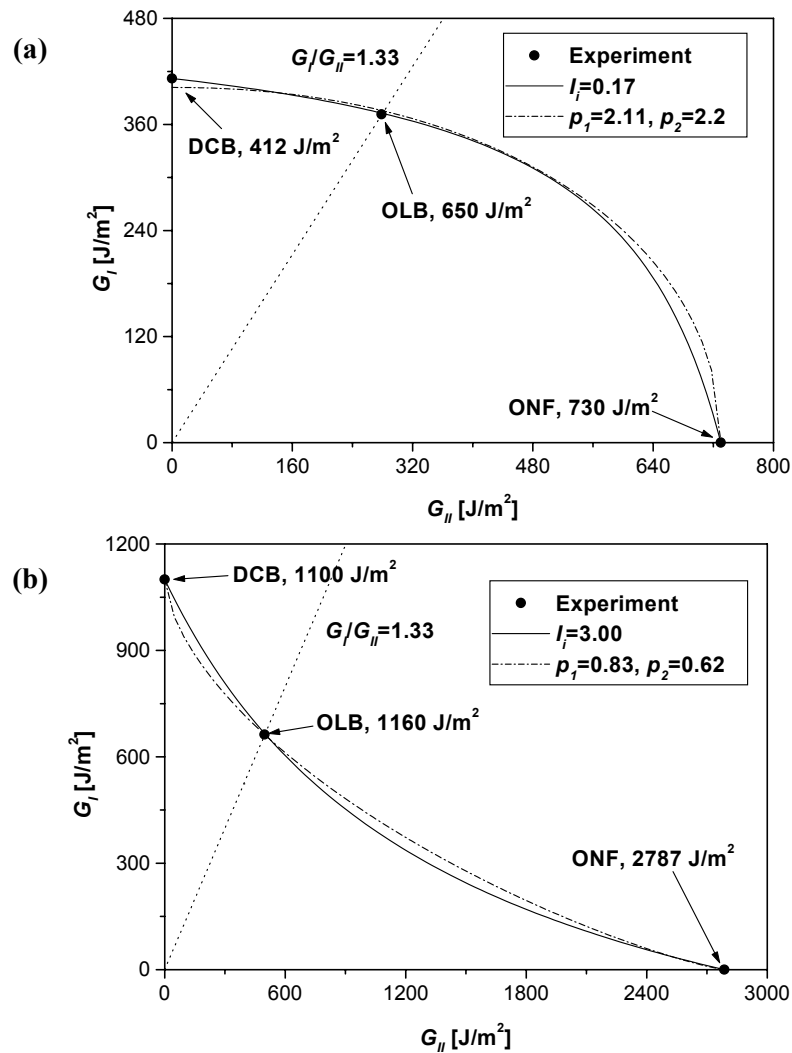


Fig. 7.3.

Interlaminar fracture envelopes for unidirectional glass/polyester composite under crack initiation (a) and crack propagation (b).

Since the strain energy release rate is an interface property the presented envelopes may also be used to predict failure locus in practical composite structures, which are manufactured by using the same constituents and exhibit the same fiber-volume fraction as the present glass/polyester material. However, to evaluate the mode-I and mode-II SERRs and the mode-ratio in a real structure, which can not be considered as a slender beam a numerical (FE) model incorporating the VCCT method is required.

7.5 Conclusions, scientific significance

The compliance of delaminated composite beams with midplane crack was generalized in the form of a third order polynomial, where the coefficients were related to the different theories and effects. The results of Table 7.1 were applied in the fiber-bridging analysis of the DCB specimen (Chapter 6).

The fracture behavior of the DCB, ELS and SCB specimens was studied in a quite extended range of crack length. In some points of view (considering the critical load and critical displacement) comparison between them was made. It was shown that the critical load follows a hyperbolicly decreasing trend in the function of the crack length in the case of crack initiation. The critical displacements were also investigated and in each case a parabolic nature was established. The large displacements are significant in the case of the ELS and SCB specimens, which may cause the crack to be uncontrollable. As a consequence, crack propagation tests were not possible to be performed. In the case of the DCB specimen large displacement have also been observed, however these do not influence the crack propagation and the geometry of the system may be simply corrected.

In the case of the ONF, SLB and OLB specimens comparison was also made. The results of ONF and OLB tests were found to be slightly unusual as regarding to the critical displacement and the critical load against the crack length. The traditional SLB test provided similar results to that of the SCB specimen. In contrast, the critical load showed a parabolic relation with the crack length in the case of the ONF and OLB setups. An important feature is that the large displacements were not experienced in these cases. In particular, the ONF and OLB configurations are efficient tools to measure the propagation toughness.

Using the results of the interlaminar fracture tests the approximate fracture envelope of the present glass/polyester composite was constructed including crack initiation and crack propagation conditions. Two criterions were adopted, both predicted a strong interaction between the mode-I and mode-II strain energy release rates.

THESES

1. Thesis

It was shown that the correction function derived by using the Winkler-type elastic foundation for the strain energy release rate of composite beams with midplane delamination and when the upper and lower arms exhibit the same mechanical properties under mixed-mode I/II condition may be written as:

$$f_{W2} = 5.42 \left(\frac{h}{a} \right) \left(\frac{E_{11}}{E_{33}} \right)^{\frac{1}{4}} + 2.45 \left(\frac{h}{a} \right)^2 \left(\frac{E_{11}}{E_{33}} \right)^{\frac{1}{2}}. \quad (8.1)$$

The classical solution of WILLIAMS for the mode-I double-cantilever beam specimen including the Winkler-type elastic foundation resulted in the following term:

$$f_W = 15.36 \left(\frac{h}{a} \right) \left(\frac{E_{11}}{E_{33}} \right)^{\frac{1}{4}} + 4.92 \left(\frac{h}{a} \right)^2 \left(\frac{E_{11}}{E_{33}} \right)^{\frac{1}{2}}. \quad (8.2)$$

The difference between Eqs. (8.1) and (8.2) may be explained by the theorem of parallel axes. The present formulation considers that the reference plane with respect to bending coincides with the midplane of the model. This fact resulted in a four times higher second order moment of inertia of the uncracked region of the model in comparison with WILLIAMS' formulation. This indicates that the generalization of WILLIAMS' solution for mixed-mode I/II problems is unjustified. The difference between the two solutions was demonstrated by using the models of SCB, SLB and MMB specimens.

2. Thesis

The global mode decomposition method was completed with the Winkler-Pasternak foundation, transverse shear, Saint-Venant and crack tip shear deformation effects in that case when the upper and lower arms of the model exhibit the same mechanical properties and the delamination is symmetrically located along the beam thickness. The individual components of the strain energy release rate are:

$$G_I = \frac{M_I^2 (12 + f_{W2} + f_T + f_{SV})}{b^2 h^3 E_{11}}, \quad (8.3)$$

$$G_{II} = \frac{M_{II}^2 (9 + f_{SH2})}{b^2 h^3 E_{11}}. \quad (8.4)$$

2.1 *It was shown that the Winkler-Pasternak elastic foundation (f_{W2}), transverse shear (f_T) and the Saint-Venant (f_{SV}) effect improves only the mode-I, while the crack tip shear deformation (f_{SH2}) contributes only to the mode-II strain energy release rate.*

2.2 *Using the developed strain energy release rate expressions (Eqs. (8.3) and (8.4)) and the finite element method the coefficient of the Pasternak foundation parameter was determined. It was found to be a constant value ($\omega=2.5$).*

2.3 The results of the solution were compared with existing beam, plate and finite element solutions, respectively. It was found that the present solution gives the reasonably good description of both the compliance and the strain energy release rate and in each case shows similar relationship to the finite element solution.

2.4 Mode-II (ELS, ONF) and mixed-mode I/II (SLB, SCB) experimental tests were performed on unidirectional glass/polyester composite specimens with midplane delamination to demonstrate the applicability of the developed beam model, which was found to be suitable to reduce the experimental data.

3. Thesis

An improved expression was derived for the compliance of composite beams, which accounts for the Winkler-Pasternak foundation (f_{W1}), transverse shear (C_{TIM}), Saint-Venant (f_{SV} , C_{SV}) and crack tip shear deformation (f_{SH1}) effects, in that case when the arms of the model exhibit the same mechanical properties and the delamination is symmetrically located along the beam thickness:

$$C = C_{EB} + C_{TIM} + \frac{f_I^2 a^3}{2bh^3 E_{11}} \left(f_{W1} + \frac{f_{SV}}{2} \right) + \frac{f_{II}^2 a^3}{2bh^3 E_{11}} f_{SH1} + C_{SV}. \quad (8.5)$$

3.1 The application of Eq. (8.5) was demonstrated through models of unidirectional SCB, SLB and MMB specimens. The obtained results were compared with results by finite element calculations and existing analytical models. It was shown that the developed compliance expression ensures the desired accuracy.

3.2 The applicability of Eq. (8.5) was demonstrated through experiments performed on unidirectional glass/polyester composite ELS, ONF, SCB and SLB specimens. In each case the result of Eq. (8.5) was in good agreement with the measured compliance values.

4. Thesis

A novel mixed-mode I/II test configuration was developed, which is called the over-leg bending (OLB) specimen. The OLB specimen is the modified version of the traditional single-leg bending (SLB) coupon.

4.1 The applicability of the test was demonstrated by using unidirectional glass/polyester specimens with midplane delamination. The compliance and the individual strain energy release rate components of the novel configuration were derived by the help of the developed beam model.

4.2 A remarkable advantage of the test is that the large displacements (which play a dominant role in composites with low flexural modulus) can be avoided and the crack propagation can be easily controlled (in contrast with the SLB and SCB coupons). The test gives essentially a linear elastic response and simple reduction techniques can be applied for data evaluation. A relative drawback of the test is that the mode-ratio may be varied only with a small degree.

5. Thesis

A combined analytical-experimental approach was developed to investigate the fiber-bridging effect in unidirectional mode-I double-cantilever beam specimens with midplane delamination.

5.1 The beam theory-based solution is suitable to predict the number of bridging fibers and the bridging force. The application of the model is slightly time-consuming, however the calculation may be performed (in contrast with the previously developed numerical and semi-empirical approaches) by the help of some essential material properties, such as the fiber diameter d_f and elastic modulus of the fibers E_f .

5.2 A numerical solver for the application of the model was developed in the code MAPLE. The applicability of the model was demonstrated by using unidirectional glass/polyester double-cantilever beam specimens. It was shown that the number of bridging fibers follows a hyperbolicly decreasing trend as the crack advances, while the bridging force reaches a peak value and then it tends to a steady-state value. In comparison with the results of a semi-empirical solution the obtained results are quite similar.

6. Thesis

6.1 It was established that in the case of the DCB, ELS, SCB and SLB specimens the critical load at crack initiation approximately exhibits a hyperbolic behavior against the crack length. In contrast, the critical force has approximately a parabolic nature in the case of the ONF and OLB coupons. The latter may be explained by the eccentricity introduced load between the two supports and that the characteristic distance is the length of the uncracked region instead of the crack length.

6.2 The critical displacement at crack initiation showed approximately a parabolic dependence on the crack length in each specimen type (DCB, ELS, ONF, SCB, SLB and OLB). In the case of the ELS and SCB specimens the limitation of the large displacements was established and the reasonable range of the crack length was indicated.

6.3 It was shown that the smallest critical displacement occurs in the ELS coupon if $a=0.53L$, which is eventually the limit of crack stability ($a \geq 0.55L$).

APPLICATION AND UTILIZATION OF THE RESULTS

The presented results may be equally utilized in the field of the theoretical and experimental fracture mechanics in accordance with the followings:

- The derived and verified formulae may be applied for indirect evaluation of data by interlaminar fracture tests. Closed-form solutions with high accuracy may be derived for the compliance and strain energy release rate of midplane delaminated composite specimens of which arms have the same mechanical properties. The mode ratio can also be calculated.
 - The formula of the compliance can show what type of function should be used for the curve fitting of the experimental compliance values, since in some cases the *Euler-Bernoulli* beam theory results in an incomplete third order polynomial.
 - The novel OLB configuration is an efficient tool for interlaminar fracture testing in composites with low flexural modulus.
 - The combined experimental-analytical fiber-bridging modeling technique is suitable to estimate the number of bridging fibers and the bridging force.
 - Based on the measured critical load/crack length diagrams - assuming similar behavior in other type of composite materials - it is possible to estimate how the displacement changes with the crack length.
 - Using the critical load/crack length diagrams of the ELS, SCB and OLB specimens - assuming similar behavior in other type of composite materials - the ranges of the large displacements may be established and the efficiency of propagation tests can be facilitated.
 - The presented strain energy release rate values at crack initiation and propagation may be used as reference results.
 - The determined interlaminar fracture envelopes may be used for the design of composite structures manufactured from glass/polyester composite material with the same fiber-volume fraction.
-

REFERENCES

- ALBERTSEN H. - IVENS J. - PETERS P. - WEVERS M. - VERPOEST I. (1995) Interlaminar fracture toughness of CFRP influenced by fiber surface treatment: Part 1. Experimental results, *Composites Science and Technology* **54**, 133-145. – [1]
- ALEMDAR B.N. - GÜLKAN P. (1997) Beams on generalized foundations: supplementary element matrices, *Engineering Structures* **19**, 910-920. – [2]
- ALLIX O. - LÉVÉQUE D. - PERRET L. (1998) Identification and forecast of delamination in composite laminates by an interface model, *Composites Science and Technology* **58**, 671-678. – [3]
- BAO G. - HO S. - SUO Z. - FAN B. (1992) The role of material orthotropy in fracture specimens for composites, *International Journal of Solids and Structures* **29**, 1105-1116. – [4]
- BRADLEY W.L. - COHEN R.N. (1985) Matrix deformation and fracture in graphite-reinforced epoxies, *Delamination and Debonding of Materials*, American Society for Testing and Materials, Philadelphia, ASTM STP **876**, 389-410. – [5]
- BROEK D. (1982) Elementary engineering fracture mechanics, *Martinus Nijhoff Publishers*, The Hague. – [6]
- BRUNO D. - GRECO F. (2001a) Mixed mode delamination in plates: a refined approach, *International Journal of Solids and Structures* **38**, 9149-9177. – [7]
- BRUNO D. - GRECO F. (2001b) Delamination in composite plates: influence of shear deformability on interfacial debonding, *Cement & Concrete Composites* **23**, 33-45. – [8]
- BRUNO D. - GRECO F. - LONETTI P. (2003) A coupled interface-multilayer approach for mixed mode delamination and contact analysis in laminated composites, *International Journal of Solids and Structures* **40**, 7245-7268. – [9]
- CARLSSON L.A. - GILLESPIE J.W. - PIPES R.B. (1986) On the analysis and design of the end notched flexure (ENF) specimen for mode II testing, *Journal of Composite Materials* **20**, 594-604. – [10]
- CHATTERJE S.N. (1991) Analysis of test specimens for interlaminar mode II fracture toughness, Part 1. Elastic laminates, *Journal of Composite Materials* **25**, 470-493. – [11]
- CHEN J.H. - SERNOW R. - SCHULZ G. - HINRICHSSEN G. (1999) A modification of the mixed-mode bending test apparatus, *Composites Part A: Applied Science and Manufacturing* **30**, 871-877. – [12]
- CORLETO C.R. - HOGAN H.A. (1995) Energy release rates for the ENF specimen using a beam on an elastic foundation, *Journal of Composite Materials* **29**, 1420-1436. – [13]
- COŞKUN İ. (2003) The response of a finite beam on a tensionless Pasternak foundation subjected to a harmonic load, *European Journal of Mechanics* **22**, 151-161. – [14]
- DAHLEN C. - SPRINGER G.S. (1994) Delamination growth in composites under cyclic loads, *Journal of Composite Materials* **28**, 732-781. – [15]
- DAVIDSON B.D. (1990) An analytical investigation of delamination front curvature in double cantilever beam specimens, *Journal of Composite Materials* **24**, 1124-1137. – [16]
- DAVIDSON B.D. - KRÜGER R. - KÖNIG M. (1995a) Three-dimensional analysis of center-delaminated unidirectional and multidirectional single-leg bending specimens, *Composites Science and Technology* **54**, 385-394. – [17]
- DAVIDSON B.D. - HU H. - SCHAPERLY R.A. (1995b) An analytical crack tip element for layered elastic structures, *Journal of Applied Mechanics* **62**, 294-305. – [18]
- DAVIDSON B.D. - SUNDARARAMAN V. (1996) A single leg bending test for interfacial fracture toughness determination, *International Journal of Fracture* **78**, 193-210. – [19]

- DAVIDSON B.D. - KOUDELA K.L. (1999) Influence of the mode mix of precracking on the delamination toughness of laminated composites, *Journal of Reinforced Plastics and Composites* **18**, 408-414. – [20]
- DAVIES P. - KAUSCH H.H. - WILLIAMS J.G. - KINLOCH A.J. - CHARALAMBIDES M.N. - PAVAN A. - MOORE D.R. - PREDIGER R. - ROBINSON I. - BURGOYNE N. - FRIEDRICH K. - WITTICH H. - REBELO C.A. - TORRES MARQUES A. - RAMSTEINER F. - MELVE B. - FISCHER M. - ROUX N. - MARTIN D. - CZARNOCKI P. - NEVILLE D. - VEPOEST I. - GOFFAUX B. - LEE R. - WALLS K. - TRIGWELL N. - PARTRIDGE I.K. - JAUSSAUD J. - ANDERSEN S. - GIRAUD Y. - HALE G. - MCGRATH G. (1992) Round-robin interlaminar fracture testing of carbon-fibre-reinforced epoxy and PEEK composites, *Composites Science and Technology* **43**, 129-136. – [21]
- DAVIES P. - DUCEPT F. - BRUNNER A.J. - BLACKMAN B.R.K. - MORAIS DE A.B. (1996) Development of a standard mode II shear fracture test procedure, In: *Proceedings of the 7th European Conference on Composite Materials (ECCM-7) Vol. 2*, pp 9-15, London, May. – [22]
- DAVIES P. - CASARI P. - CARLSSON L.A. (2005) Influence of fiber volume fraction on the interlaminar fracture toughness of glass/epoxy using the 4ENF specimen, *Composites Science and Technology* **65**, 295-300. – [23]
- DING W. - KORTSCHOT M.T. (1999) A simplified beam analysis of the end notched flexure mode II delamination specimen, *Composite Structures* **45**, 271-278. – [24]
- DUBOIS F. - KEUNINGS R. (1997) DCB testing of thermoplastic composites: a non-linear micro-macro numerical analysis, *Composites Science and Technology* **57**, 437-450. – [25]
- DUCEPT F. - GAMBY D. - DAVIES P. (1999) A mixed-mode failure criterion derived from tests of symmetric and asymmetric specimens, *Composites Science and Technology* **59**, 609-619. – [26]
- FERNBERG S.O. - BERGLUND L.A. (2001) Bridging law and toughness characterization of CSM and SMC composites, *Composites Science and Technology* **61**, 2445-2454. – [27]
- FEYEL F. - CHABOCHE J.-L. (2000) FE² multiscale approach for modelling the elastoviscoplastic behaviour of long fibre SiC/Ti composite materials, *Computer Methods in Applied Mechanics and Engineering* **183**, 309-330. – [28]
- FILIPICH C.P. - ROSALES M.B. (2002) A further study about the behaviour of foundation plies and beams in a Winkler-Pasternak soil, *International Journal of Mechanical Sciences* **44**, 21-36. – [29]
- HASHEMI S. - KINLOCH J. - WILLIAMS J.G. (1987) Interlaminar fracture of composite materials. In: *Proceedings of the 6th ICCM and ECCM Conference*, Elsevier Applied Science, London, **Vol.3**, 3.254-3.264. – [30]
- HASHEMI S. - KINLOCH J. - WILLIAMS J.G. (1990a) The effects of geometry, rate and temperature on mode I, mode II and mixed-mode I/II interlaminar fracture toughness of carbon-fibre/poly(ether-ether ketone) composites, *Journal of Composite Materials* **24**, 918-956. – [31]
- HASHEMI S. - KINLOCH J. - WILLIAMS J.G. (1990b) Mechanics and mechanisms of delamination in a poly(ether sulphone)-fibre composite, *Composites Science and Technology* **37**, 429-462. – [32]
- HECK A. (1993) Introduction to Maple, *Springer-Verlag*, New York. – [33]
- HOU J.P. - PETRINIC N. - RUIZ C. - HALLETT S.R. (2001) Prediction of impact damage in composite plates, *Composite Science and Technology* **60**, 273-281. – [34]
- HUTCHINSON J.W. - SUO Z. (1992) Mixed mode cracking in layered materials. In: *Advances in Applied Mechanics*, Academic Press, New York, 63-191. – [35]
-

- KANNINEN M.F. (1973) An augmented double cantilever beam model for studying crack propagation and arrest, *International Journal of Fracture* **9**, 83-92. – [36]
- KANNINEN M.F. - POPELAR C.H. (1985) *Advanced Fracture Mechanics*, Oxford University Press, New York. – [37]
- KAUTE D.A.W. - SHERCLIFF H.R. - ASHBY M.F. (1995) Modelling of fibre bridging and toughness of ceramic matrix composites, *Scripta Metallurgica et Materialia* **32**, 1055-1060. – [38]
- KENANE M. - BENZEGGAGH M.L. (1997) Mixed-mode delamination fracture toughness of unidirectional glass/epoxy composites under fatigue loading, *Composites Science and Technology* **57**, 597-605. – [39]
- KHAZANOVICH L. (2003) Finite element analysis of curling of slabs on Pasternak foundation. In: *16th ASCE Engineering Mechanics Conference*, July 16-18, University of Washington, Seattle. – [40]
- KORJAKIN A. - RIKARDS R. - BUCHHOLZ F.-G. - WANG H. - BLEDZKI A.K. - KESSLER A. (1998) Comparative study of interlaminar fracture toughness of GFRP with different fiber surface treatments, *Polymer Composites* **19**, 793-806. – [41]
- KRUEGER R. (1999) A SHELL/3D modeling technique for delaminations in composite laminates. In: *Proceedings of the American Society for Composites, 14th Technical Conference*, Dayton, Ohio, Technomic Publishing, 843-852. – [42]
- KUSAKA T. - HOJO M. - MAI Y.-W. - KUROKAWA T. - NOJIMA T. - OCHIAI S. (1998) Rate dependence of mode I fracture behaviour in carbon-fibre/epoxy composite laminates, *Composites Science and Technology* **58**, 591-602. – [43]
- LAI Y.- H. - RAKESTRAW M.D. - DILLARD D.A. (1996) The cracked lap shear specimen revisited – a closed form solution, *International Journal of Solids and Structures* **33**, 1725-1743. – [44]
- LEE S.H. (1986) A comparison of fracture toughness of matrix controlled failure modes: delamination and transverse cracking, *Journal of Composite Materials* **20**, 185-196. – [45]
- LI Z. (1996) A new technique for determining fracture toughness K_{Ic} and its confidence with single DCB specimen, *Engineering Fracture Mechanics* **55**, 133-137. – [46]
- LINDHAGEN J.E. - BERGLUND L.A. (2000) Application of bridging-law concepts to short-fibre composites Part 1: DCB test procedures for bridging law and fracture energy, *Composites Science and Technology* **60**, 871-883. – [47]
- MISHNAEVSKY L.L., JR - SCHMAUDER S. (2001) Continuum mesomechanical finite element modeling in materials development: A state-of-the-art review, *Applied Mechanics Reviews* **54**, 49-74. – [48]
- MORAIS DE A.B. - MOURA DE M.F. - MARQUES A.T. - CASTRO DE P.T. (2002) Mode-I interlaminar fracture of carbon/epoxy cross-ply composites, *Composites Science and Technology* **62**, 679-686. – [49]
- MORAIS DE A.B. - REBELO C.C. - DE CASTRO P.M.S.T. - MARQUES T. - DAVIES P. (2004) Interlaminar fracture studies in Portugal: past, present and future, *Fatigue and Fracture of Engineering Materials and Structures* **27**, 767-773. – [50]
- OLSSON R. (1992) A simplified improved beam analysis of the DCB specimen, *Composites Science and Technology* **43**, 329-338. – [51]
- OMURTAG M.H. - KADIOĞLU F. (1998) Free vibration analysis of orthotropic plates resting on Pasternak foundation by mixed finite element formulation, *Computers and Structures* **67**, 253-265. – [52]
- OZDIL F. - CARLSSON L.A. - DAVIES P. (1998) Beam analysis of angle-ply laminate end-notched flexure specimens, *Composites Science and Technology* **58**, 1929-1938. – [53]
-

- OZDIL F. - CARLSSON L.A. (1999a) Beam analysis of angle-ply laminate DCB specimens, *Composites Science and Technology* **59**, 305-315. – [54]
- OZDIL F. - CARLSSON L.A. (1999b) Beam analysis of angle-ply laminate mixed-mode bending specimens, *Composites Science and Technology* **59**, 937-945. – [55]
- PEREIRA A.B. - MORAIS DE A.B. (2004) Mode II interlaminar fracture of glass/epoxy multidirectional laminates, *Composites Part A: Applied Science and Manufacturing* **35**, 265-272. – [56]
- PHILLIPS L.N. (1989) Design with advanced composite materials, *The Design Council, Springer-Verlag*, London. – [57]
- POLAHA J.J. - DAVIDSON B.D. - HUDSON R.C. - PIERACCI A. (1996) Effects of mode ratio, ply orientation and precracking on the delamination toughness of a laminated composite, *Journal of Reinforced Plastics and Composites* **15**, 141-173. – [58]
- PONOMARJOV S. D. (1968) Strength calculations in mechanical engineering, **Vol.2: Beams and springs**, *Technical Book Publisher*, Budapest.
{Szilárdsági számítások a gépészetben, **2. Kötet**. Rudak, rugók, *Műszaki Könyvkiadó*, Budapest.} – [59]
- QIAO P. - WANG J. - DAVALOS J.F. (2003a) Tapered beam on elastic foundation model for compliance rate change of TDCB specimen, *Engineering Fracture Mechanics* **70**, 339-353. – [60]
- QIAO P. - WANG J. - DAVALOS J.F. (2003b) Analysis of tapered ENF specimen and characterization of bonded interface fracture under mode-II loading, *International Journal of Solids and Structures* **40**, 1865-1884. Corrigendum **40**, 4091. – [61]
- QIAO P. - WANG J. (2004) Mechanics and fracture of crack-tip deformable bimaterial interface, *International Journal of Solids and Structures* **41**, 7423-7444. – [62]
- RAJU I.S. - CREWS JR. J.H. - AMINPOUR M.A. (1988) Convergence of strain energy release rate components for edge-delaminated composite laminates, *Engineering Fracture Mechanics* **30**, 383-396. – [63]
- REEDER J.R. - CREWS J.R. (1990) Mixed-mode bending method for delamination testing, *AIAA Journal* **28**, 1270-1276. – [64]
- REYES G. - CANTWELL W.J. (2000) The mechanical properties of fibre-metal laminates based on glass fibre reinforced polypropylene, *Composites Science and Technology* **60**, 1085-1094. – [65]
- RICE J.R. (1968) Mathematical analysis in the mechanics of fracture. *Fracture - An Advanced treatise*, **Vol II**, Academic Press, New York, 191-308. – [66]
- RIKARDS R. – BUCHHOLZ F.G. – WANG H. – BLEDZKI A.K. – KORJAKIN A. - RICHARD H.-A. (1998) Investigation of mixed mode I/II interlaminar fracture toughness of laminated composites by using a CTS type specimen, *Engineering Fracture Mechanics* **61**, 325-342. – [67]
- ROSA, DE M.A. (1995) Free vibrations of Timoshenko beams on two-parameter elastic foundation, *Computers & Structures* **57**, 151-156. – [68]
- RUSSEL A.J. - STREET K.N. (1985) Moisture and temperature effects on the mixed-mode delamination fracture of unidirectional graphite/epoxy, *Delamination and Debonding of Materials*, American Society for Testing and Materials, Philadelphia, ASTM STP **876**, 349-370. – [69]
- RYBICKI E.F. - KANNINEN M.F. (1977) A finite element calculation of stress intensity factors by a modified crack closure integral, *Engineering Fracture Mechanics* **9**, 931-938. – [70]
- SCHÖN J. - NYMAN T. - BLOM A. - ANSELL H. (2000) A numerical and experimental investigation of delamination behaviour in the DCB specimen, *Composites Science and Technology* **60**, 173-184. – [71]
-

- SCHÖN J. (2000) Coefficient of friction of composite delamination surfaces, *Wear* **237**, 77-89. – [72]
- SCHUECKER C. - DAVIDSON B.D. (2000) Evaluation of the accuracy of the four-point bend end-notched flexure test for mode II delamination toughness determination, *Composites Science and Technology* **60**, 2137-2146. – [73]
- SHEINMAN I. - KARDOMATEAS G.A. (1997) Energy release rate and stress intensity factors for delaminated composite laminates, *International Journal of Solids and Structures* **34**, 451-459. – [74]
- SHINDO Y. - HORIGUCHI K. - WANG R. - KUDO H. (2001) Double cantilever beam measurement and finite element analysis of cryogenic mode I interlaminar fracture toughness of glass-cloth/epoxy laminates, *Journal of Engineering Materials and Technology* **123**, 191-197. – [75]
- SOHN K.-S. - LEE S. - BAIK S. (1997) Analysis of bridging stress effect of polycrystalline alumina using double cantilever beam method, *Acta Materialia* **45**, 3445-3457. – [76]
- SPEARING S.M. - GREGORY J.R. (2005) Modeling inelastic matrix crack tip deformation in a double cantilever beam specimen, *Journal of Composite Materials* (to appear). – [77]
- SUN C.T. - ZHENG S. (1996) Delamination characteristics of double-cantilever beam and end-notched flexure composite specimens, *Composites Science and Technology* **56**, 451-459. – [78]
- SUNDARARAMAN V. - DAVIDSON B.D. (1997) An unsymmetric double cantilever beam test for interfacial fracture toughness determination, *International Journal of Solids and Structures* **34**, 799-817. – [79]
- SUNDARARAMAN V. - DAVIDSON B.D. (1998) An unsymmetric end-notched flexure test for interfacial fracture toughness determination, *Engineering Fracture Mechanics* **60**, 361-377. – [80]
- SUO Z. (1990) Delamination specimens for orthotropic materials, *Journal of Applied Mechanics* **57**, 627-634. – [81]
- SUO Z. - BAO G. - FAN B. - WANG T.C. (1991) Orthotropy rescaling and implications in fracture of composites, *International Journal of Solids and Structures* **28**, 235-248. – [82]
- SUO Z. - BAO G. - FAN B. (1992) Delamination R-curve phenomena due to damage, *Journal of the Mechanics and Physics of Solids* **40**, 1-16. – [83]
- SUO Z. - HUTCHINSON J.W. (1990) Interface crack between two elastic layers, *International Journal of Fracture* **43**, 1-18. – [84]
- SZEKRÉNYES A. - UJ J. (2002) Finite element modelling of the damage and failure in fiber reinforced composites (Overview), *Periodica Polytechnica Mechanical Engineering* **46/2**, 139-158. – [85]
- SZEKRÉNYES A. (2002a) Overview on the experimental investigations of the fracture toughness in composite materials. *HEJ - Mechanical Engineering and Transport Section* (<http://heja.szif.hu/MET/MET-020507-A/met020507.pdf>). – [86]
- SZEKRÉNYES A. (2002b) Finite element analysis of a layered cylinder using the connection between the macro- and microstructure. In: *Proceedings of the Third Conference on Mechanical Engineering*, Springer Hungarica, Budapest, Vol I., 269-273. – [87]
- SZEKRÉNYES A. (2002c) Finite element investigation of the interlaminar crack initiation in composite fracture specimens, *Euro Conference on Numerical methods and Computational Mechanics - NMCM2002*, University of Miskolc, July 15-19, Miskolc. – [88]
- SZEKRÉNYES A. (2003a) Beam and finite element models for fiber-bridgings in unidirectional DCB specimens. In: *Proceedings of the MicroCAD 2003 International Scientific*
-

- Conference, Section F: Applied Mechanics, Modern Numerical Methods*, University of Miskolc, March 6-7, Miskolc, 31-36. – [89]
- SZEKRÉNYES A. (2003b) Modelling of the delamination and fiber-bridging in unidirectional composites under mode-I loading conditions, *Journal on Composite Mechanics and Design* **9;2**, 167-180. – [90]
- SZEKRÉNYES A. - UJ J. (2003a) Analysis of the interlaminar crack initiation in mixed-mode I+II composite fracture specimens, *Periodica Polytechnica Mechanical Engineering* **47/2**, 103-118. – [91]
- SZEKRÉNYES A. - UJ J. (2003b) Fracture mechanical analysis of the mixed-mode ELS and SLB specimens, *IXth Hungarian Conference on Mechanics*, University of Miskolc, August 27-29, Miskolc.
{Kévert módú törésmechanikai vizsgálatok az ELS és SLB típusú kompozit próbatestek felhasználásával, *IX. Magyar Mechanikai Konferencia*, Miskolci Egyetem, 2003, augusztus 27-29, Miskolc.} – [92]
- SZEKRÉNYES A. (2004a) Comparison of some data reduction schemes for composite delamination specimens, *Periodica Polytechnica Mechanical Engineering* **48/1**, 151-161. – [93]
- SZEKRÉNYES A. (2004b) Analysis and measurement of the crack propagation and interlaminar fracture under mode-II condition, *Jubilee Program Series, Mechanics of Reinforced Materials and Structures*, Technical College of Budapest, Bánki Donát Faculty of Mechanical Engineering, November 11-12, Budapest.
{Repedésterjedés és rétegeközi szilárdság analitikus és kísérleti vizsgálata párhuzamos elcsúszás esetén. *Jubileumi rendezvénysorozat, Erősített anyagok és szerkezetek mechanikája*, Budapesti Műszaki Főiskola, Bánki Donát Gépészmérnöki Főiskolai Kar, 2004. november 11-12, Budapest.} – [94]
- SZEKRÉNYES A. - UJ J. (2004a) Beam and finite element analysis of quasi-unidirectional SLB and ELS specimens, *Composites Science and Technology* **64**, 2393-2406. – [95]
- SZEKRÉNYES A. - UJ J. (2004b) Interlaminar fracture investigation in glass/polyester ELS specimens, *Plastics and Rubber* (to appear).
{Rétegeközi szilárdság vizsgálata ELS típusú üveg/poliészter próbatesteken, *Műanyag és Gumi* (megjelenés alatt).} – [96]
- SZEKRÉNYES A. - UJ J. (2004c) Application of elastic foundation beams in composite fracture mechanics - Analysis of the ELS specimen. In: *Proceedings of the Fourth Conference on Mechanical Engineering*, Springer Hungarica, Budapest, Vol I., 191-195. – [97]
- SZEKRÉNYES A. - UJ J. (2004d) Experimental investigations of slender glass/polyester coupons, *Mechanoplast First National Conference for Ph.D. students*, Headquarter of the Scientific Society for Engineering, June 10, Budapest.
{Rúdszerű üveg/poliészter próbatestek kísérleti vizsgálata. *Mechanoplast, első országos doktorandusz konferencia*, Gépipari Tudományos Egyesület Székháza, 2004. június 10, Budapest.} – [98]
- SZEKRÉNYES A. - UJ J. (2004e) Advanced beam model for fiber-bridging in unidirectional composite double-cantilever beam specimens, *21st International Congress of Theoretical and Applied Mechanics - ICTAM*, August 15-21, Warsaw, Poland. – [99]
- SZEKRÉNYES A. - UJ J. (2004f) Modified single-leg bending test for mixed-mode I/II interlaminar fracture in composites, *21st Danubia-Adria Symposium on Experimental Methods in Solid Mechanics*, September 29-October 2, Brijuni/Pula, Croatia. – [100]
- SZEKRÉNYES A. - UJ J. (2005a) Comparison of some improved solutions for mixed-mode composite delamination coupons, *Composite Structures* (to appear). – [101]
-

- SZEKRÉNYES A. - UJ J. (2005b) Mode-II fracture analysis in unidirectional E-glass/polyester composite, *Journal of Composite Materials* (to appear). – [102]
- SZEKRÉNYES, A. - Uj J. (2005c) Approximate interlaminar fracture envelopes for unidirectional E-glass/polyester composite, *Periodica Polytechnica Mechanical Engineering* **49/1**, (to appear). – [103]
- SZEKRÉNYES A. - UJ J. (2005d) Advanced beam model for fiber-bridging in unidirectional composite double-cantilever beam specimens, *Engineering Fracture Mechanics* (to appear) – [104]
- TAMUZS V. - TARASOV S. - VILKS U. (2001) Progressive delamination and fiber bridging modelling in double cantilever beam composite specimen, *Engineering Fracture Mechanics* **68**, 513-525. – [105]
- TANAKA K. - YUASA T. - KATSURA K. (1998) Continuous mode II interlaminar fracture toughness measurement by over notched flexure test. In: *Proceedings of the 4th European Conference on Composites: Testing and Standardization*, 171-179. – [106]
- THAMM F. - BORBÁS L. - GÁTI R. - GÁL J. (1996) Interlaminar fracture toughness of native composite laminates, Part I., *Plastics and Rubber* **33**, 246-250.
{Hazai laminátok rétegeközi szilárdságának vizsgálata I., *Műanyag és Gumi* **33**, 246-250.} – [107]
- THAMM F. (1985) Strength of Plastic Materials II. *Technical Book Publisher*, Budapest.
{Műanyagok szilárdságtana II. *Műszaki Könyvkiadó*, Budapest.} – [108]
- TODO M. - JAR P.-Y.B. (1998) Study of mode-I interlaminar crack growth in DCB specimens of fibre-reinforced composites, *Composites Science and Technology* **58**, 105-118. – [109]
- TODO M. - JAR P.-Y.B. - Takahashi K. (2000) Initiation of a mode-II interlaminar crack from an insert film in end-notched flexure composite specimen, *Composites Science and Technology* **60**, 263-272. – [110]
- TRACY G.D. - FERABOLI P. - KEDWARD K.T. (2003) A new mixed mode test for carbon/epoxy composite systems, *Composites Part A: Applied Science and Manufacturing* **34**, 1125-1131. – [111]
- TSAI S. W. (1992) Theory of composites design, *Think Composites*, Dayton, Ohio. – [112]
- WANG H. - VU-KHANH T. (1996) Use of end-loaded-split (ELS) test to study stable fracture behaviour of composites under mode-II loading, *Composite Structures* **36**, 71-79. – [113]
- WANG J.T. - LOTT C.G. - SLEIGHT D.W. (1999) Analysis of discrete-source damage progression in a tensile stiffened composite panel, *AIAA Paper 99-1336*, 1-14. – [114]
- WANG J. - QIAO P. (2004a) Novel beam analysis of the end notched flexure specimen for mode-II fracture, *Engineering Fracture Mechanics* **71**, 219-231. – [115]
- WANG J. - QIAO P. (2004b) On the energy release rate and mode mix of delaminated shear deformable composite plates, *International Journal of Solids and Structures* **41**, 2757-2779. – [116]
- WANG J. - QIAO P. (2004c) Interface crack between two shear deformable elastic layers, *Journal of the Mechanics and Physics of Solids* **52**, 891-905. – [117]
- WANG W.-X. - TAKAO Y. - NAKATA M. (2003) Effects of friction on the measurement of the mode II interlaminar fracture toughness of composite laminates. In: *Proceedings of the 14th International Conference on Composite Materials* (CD-ROM), Manuscript No.:1429, July 14-18, San Diego, California, USA. – [118]
- WANG. Y. - WILLIAMS J.G. (1992) Corrections for mode II fracture toughness specimens of composite materials, *Composites Science and Technology* **43**, 251-256. – [119]
-

- WASHIZU K. (1968) Variational methods in elasticity and plasticity, *Pergamon Press*, Headington Hill Hall, Oxford, London. – [120]
- WHITNEY J.M. (1985) Stress Analysis of the double cantilever beam specimen, *Composites Science and Technology* **23**, 201-219. – [121]
- WHITNEY J.M. (1987) Singularity approach to the analysis of the end notched flexure specimen. In: *Proceedings of the Second Conference on Composite Materials*, American Society for Composites, Lancaster, PA, Technomic Publishing, 391-398. – [122]
- WILLIAMS J.G. (1988) On the calculation of energy release rates for cracked laminates, *International Journal of Fracture* **36**, 101-119. – [123]
- WILLIAMS J.G. (1989) End corrections for orthotropic DCB specimens, *Composites Science and Technology* **35**, 367-376. – [124]
- XIA Z. - CHEN Y. - ELLYIN F. (2000) A meso/micro-mechanical model for damage progression in glass-fiber/epoxy cross-ply laminates by finite-element analysis, *Composites Science and Technology* **60**, 1171-1179. – [125]
- YAN A.-M. - MARECHAL E. - NGUYEN-DANG H.A. (2001) Finite element model of mixed-mode delamination in laminated composites with an R-curve effect, *Composites Science and Technology* **61**, 1413-1427. – [126]
- YANG Z. - SUN C.T. (2000) Interlaminar fracture toughness of a graphite/epoxy multidirectional composite, *Journal of Engineering Materials and Technology* **122**, 428-433. – [127]
- YOON S.H. - HONG C.S. (1990) Modified end notched flexure specimen for mixed mode interlaminar fracture in laminated composites, *International Journal of Fracture* **43**, R3-R9. – [128]
- ZHAO D. - WANG Y. (1998) Mode III fracture behavior of laminated composite with edge crack in torsion, *Theoretical and Applied Fracture Mechanics* **28**, 109-123. – [129]
- ZHENG S. - SUN C.T. (1995) A double-plate finite element model for the impact-induced delamination problem, *Composites Science and Technology* **53**, 111-118. – [130]
- ZOU Z. - REID S.R. - SODEN P.D. - LI S. (2001) Mode separation of energy release rate for delamination in composite laminates using sublaminates, *International Journal of Solids and Structures* **38**, 2597-2613. – [131]
- ZOU Z. - REID S.R. - LI S. - SODEN P.D. (2002) Application of a delamination model to laminated composites structures, *Composites Structures* **56**, 375-389. – [132]
-

APPENDIX A

A.1 – Constant parameters, *Timoshenko* beam theory

The constant parameters in Eqs. (3.38)-(3.43) are:

$$d_1 = d_3 = d_5 = \frac{d_{11,2}(P_1 + P_2)(L^2 - a^2)}{2b}, \quad (\text{A.1})$$

$$d_2 = d_4 = d_6 = -(P_1 + P_2) \left(\frac{d_{11,2}(2L^3 + a^3 - 3aL^2)}{6b} + \frac{a_{55,2}(a - L)}{bk} \right).$$

A.2 – Constant parameters, crack tip shear deformation

The constant parameters in Eqs. (3.83)-(3.86)

$$g_1 = g_3 = -\frac{9(P_1 + P_2)ae^{-\rho c}}{8b^2h^3\rho}, \quad (\text{A.2})$$

$$g_2 = g_4 = \frac{9(P_1 + P_2)a(1 + \rho c)e^{-\rho c}}{8b^2h^3\rho},$$

$$g_5 = g_7 = \frac{9(P_1 + P_2)a(1 - \rho c)e^{-\rho c}}{8b^2h^3\rho},$$

$$g_6 = g_8 = \frac{9(P_1 + P_2)a[(1 + \rho c)e^{-\rho c} - 1]}{8b^2h^3\rho}.$$

A.3 – Determination of ω for the *Pasternak* foundation

The FE model of the DCB specimen is depicted in Fig. A1. The results of the analysis described in Section 3.7 are listed in Table A1.

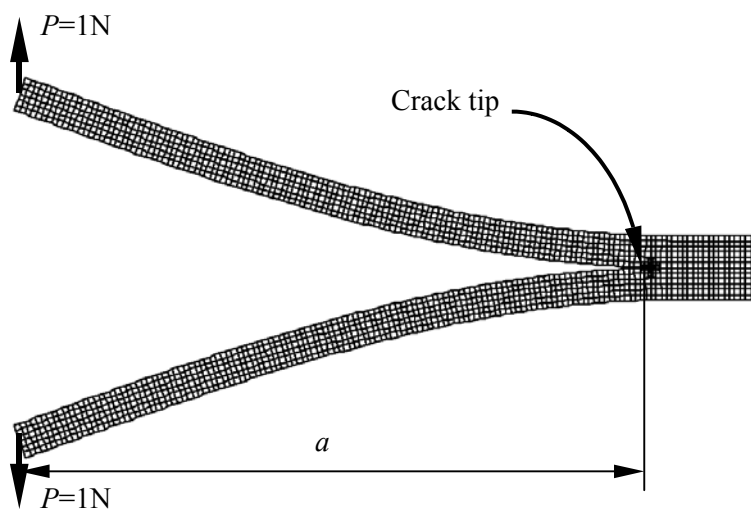


Fig. A1.

FE model of the DCB specimen for the determination of ω .

Table A1.

Corrections for the SERR of the DCB specimen from *Winkler-Pasternak* elastic foundation if $G_{13}=100\ 000$ GPa and $\omega=2.5$.

	a [mm]	30	40	50	60	70	80	90	100
E-glass/polyester specimen: $E_{11}=33$ GPa, $E_{33}=7.2$ GPa, $\nu_{13}=0.27$ (present)									
$h=2$ mm	$G_{I,FEM}/G_{I,EB}$	1.090	1.067	1.053	1.047	1.041	1.035	1.031	1.028
	$G_{I,WP}/G_{I,EB}$	1.089	1.066	1.052	1.043	1.037	1.032	1.028	1.025
	Difference [%]	0.092	0.094	0.095	0.382	0.384	0.289	0.291	0.292
$h=3.05$ mm	$G_{I,FEM}/G_{I,EB}$	1.143	1.106	1.084	1.070	1.060	1.052	1.046	1.042
	$G_{I,WP}/G_{I,EB}$	1.142	1.103	1.081	1.067	1.057	1.049	1.043	1.039
	Difference [%]	0.087	0.271	0.276	0.280	0.283	0.285	0.287	0.288
$h=4.5$ mm	$G_{I,FEM}/G_{I,EB}$	1.218	1.161	1.128	1.106	1.090	1.079	1.070	1.063
	$G_{I,WP}/G_{I,EB}$	1.219	1.158	1.123	1.101	1.086	1.074	1.066	1.059
	Difference [%]	-0.082	0.258	0.443	0.452	0.357	0.463	0.373	0.376
Carbon/epoxy specimen: $E_{11}=124$ GPa, $E_{33}=10$ GPa, $\nu_{13}=0.25$ (HASHEMI et al. (1990a))									
$h=2$ mm	$G_{I,FEM}/G_{I,EB}$	1.124	1.092	1.073	1.066	1.057	1.050	1.044	1.040
	$G_{I,WP}/G_{I,EB}$	1.117	1.086	1.067	1.056	1.047	1.041	1.036	1.033
	Difference [%]	0.062	0.549	0.559	0.938	0.946	0.854	0.766	0.673
$h=3.05$ mm	$G_{I,FEM}/G_{I,EB}$	1.192	1.142	1.113	1.094	1.080	1.070	1.062	1.056
	$G_{I,WP}/G_{I,EB}$	1.187	1.135	1.106	1.087	1.074	1.064	1.057	1.051
	Difference [%]	0.419	0.613	0.628	0.640	0.574	0.561	0.471	0.473
$h=4.5$ mm	$G_{I,FEM}/G_{I,EB}$	1.291	1.213	1.169	1.140	1.119	1.104	1.092	1.083
	$G_{I,WP}/G_{I,EB}$	1.294	1.210	1.163	1.133	1.112	1.097	1.086	1.076
	Difference [%]	-0.232	0.247	0.513	0.614	0.656	0.634	0.549	0.646
Isotropic specimen: $E_{11}=33$ GPa, $E_{33}=33$ GPa, $\nu_{13}=0.27$									
$h=2$ mm	$G_{I,FEM}/G_{I,EB}$	1.058	1.044	1.035	1.030	1.026	1.023	1.020	1.018
	$G_{I,WP}/G_{I,EB}$	1.059	1.044	1.035	1.029	1.025	1.022	1.019	1.017
	Difference [%]	-0.095	0.000	0.000	0.097	0.097	0.098	0.098	0.098
$h=3.05$ mm	$G_{I,FEM}/G_{I,EB}$	1.091	1.068	1.054	1.045	1.038	1.034	1.030	1.027
	$G_{I,WP}/G_{I,EB}$	1.093	1.068	1.054	1.045	1.038	1.033	1.029	1.026
	Difference [%]	-0.183	0.000	0.000	0.000	0.000	0.097	0.097	0.097
$h=4.5$ mm	$G_{I,FEM}/G_{I,EB}$	1.137	1.102	1.081	1.067	1.057	1.050	1.045	1.040
	$G_{I,WP}/G_{I,EB}$	1.143	1.104	1.082	1.067	1.057	1.050	1.044	1.039
	Difference [%]	-0.528	-0.181	-0.093	0.000	0.000	0.000	0.096	0.096

$G_{I,FEM}$ – plane stress FE model, Eq. (3.121), $G_{I,WP}$ – analytical solution, Eq. (3.122)

$G_{I,EB}$ – solution based on *Euler-Bernoulli* beam theory

APPENDIX B – Specimen preparation

The constituent materials were procured by native companies (Novia Ltd, Alvin-Plast Ltd). The unidirectional coupons were manufactured by using the workbench in Fig. B1. The pure glass-fiber roving (EC 13 2520 907) was run through the resin bath full of unsaturated

polyester (styrol: 42.7%; R 10-20-36/38; S 24-26-51; CAS No.:100-42-5; EU No.:202-851-5) and was rolled up to a steel frame (see Fig. B1). The latter ensured the thickness of the bundles by means of those notches, highlighted in Fig. B1. A polyamide (PA) insert with thickness of 0.04 mm was placed at the midplane of each bundle to make an artificial starting defect. After the sufficient amount of roving was rolled up, then the frame was put to the special pressure block tool depicted in Fig. B2. With the aid this tool two pieces of specimens can be manufactured simultaneously. The thickness of the coupons, and so even the fiber-

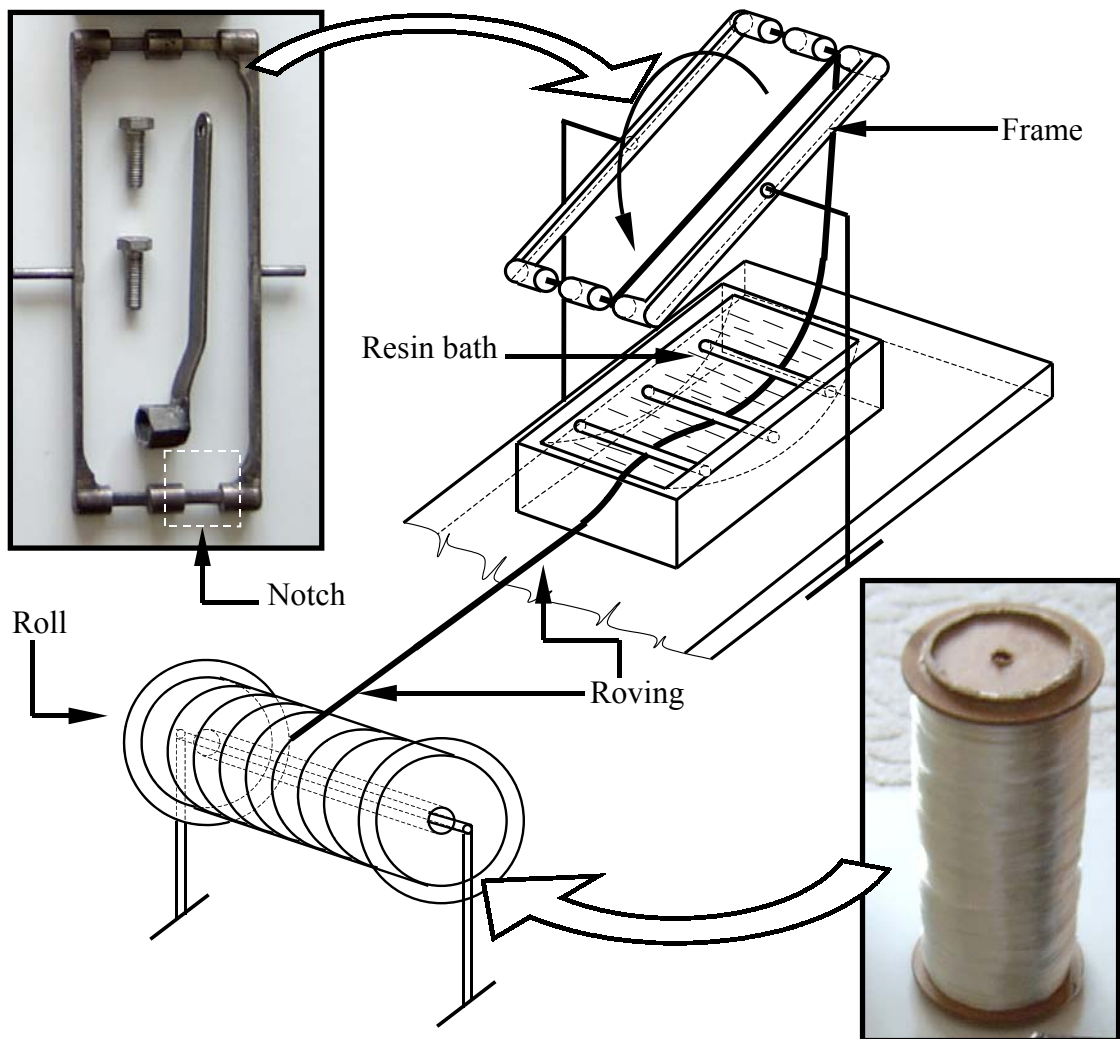


Fig. B1.

Workbench for unidirectional specimen preparation.

volume fraction may be controlled by the screws, shown in Fig. B2b. The tool was left on room temperature until the bundles became dry (6-8 hours).

Then the specimens were removed from the tool and were further left on room temperature until 4-6 hours. Finally, they were cut to the desired length and were precracked in opening mode of about 4-5 mm by using a sharp blade. This involved an area full of pulled-out fibers before the crack tip, but this effect was assumed to be negligible. The manufactured specimens have nominal width of $b=20$ mm, thickness of $2h=6.1$ mm, full length of about 180 mm and fiber-volume fraction of $V_f=43\%$. A millimeter scale was traced

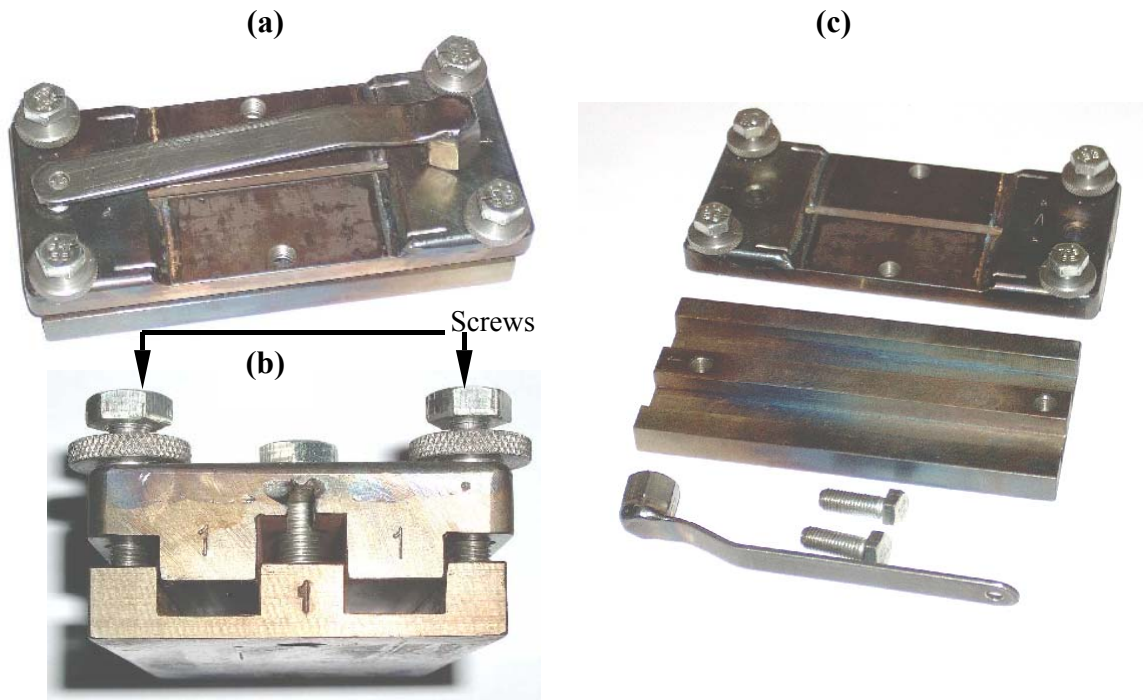


Fig. B2.
Pressure tool for unidirectional specimens, assembled state (a), front view (b), exploded view (c).

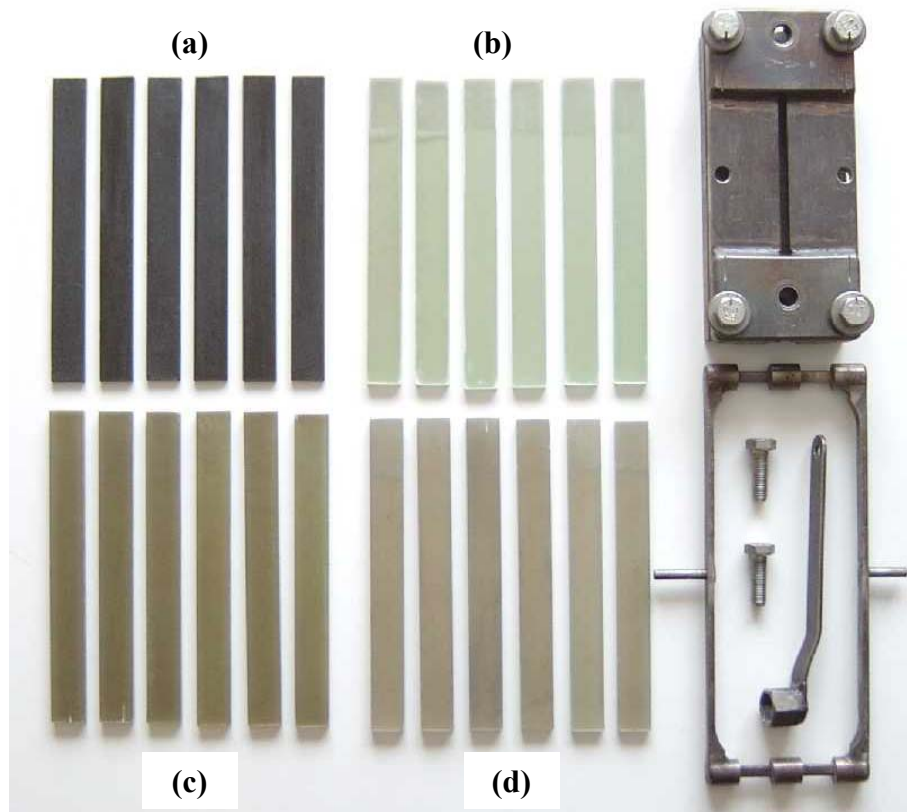


Fig. B3.
Unidirectional composite carbon/epoxy (a), glass/epoxy (b), glass/vinylester (c) and glass/polyester (d) specimens.

on the lateral sides of the coupons in order to facilitate the visual measurement of the crack length. Four types of composite material can be manufactured in our laboratory, as it is shown in Fig. B3. In the present work only $[0^\circ]_{14}$ E-glass/polyester specimens were tested. In this point of view the transparency is a great advantage of the glass/polyester material. The properties of the E-glass-fiber are $E=70$ GPa and $\nu=0.27$, while for the unsaturated polyester resin they are $E=3.5$ GPa and $\nu=0.35$ (PHILLIPS, 1989). Both were considered as isotropic.

APPENDIX C – Clamping fixture for the ELS and SCB tests

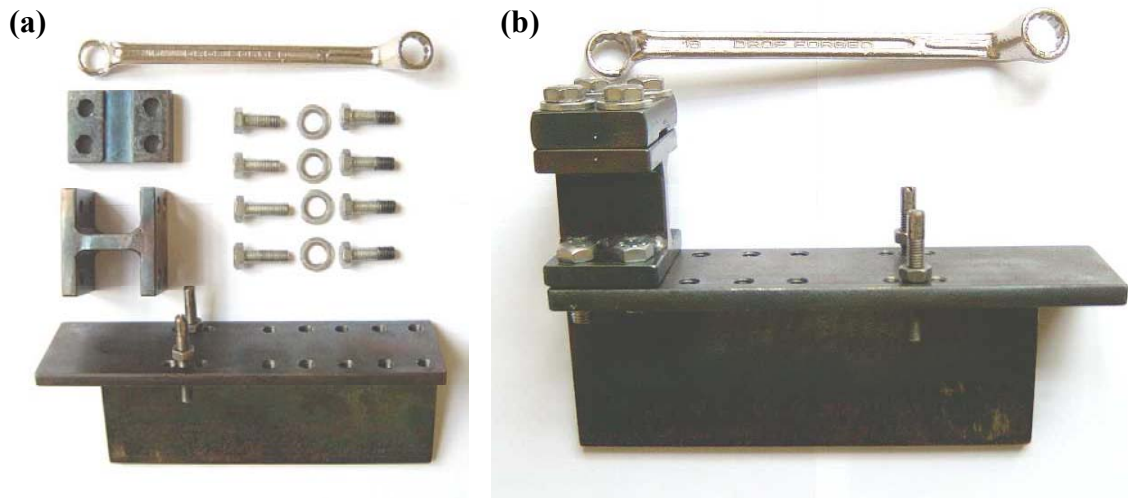


Fig. C1.

Details of the clamping fixture, exploded view (a), assembled state (b).

APPENDIX D – Crack length correction

D.1 ELS specimen

The loading head of our (non-standard) test fixture have relatively large radii (refer to Figs. 5.2a and b). Figure D1a shows how the contact line between the loading head and the specimen changes as the load increases, and so, for example the crack length becomes shorter. This fact should be considered in the data reduction. The corrections are calculated based on simple beam theory and the experimentally measured displacement at the point of load application.

For the ELS coupon the end displacement and the derivative of the deflection based on simple beam theory are:

$$\delta = \frac{P(3a^{*3} + L^{*3})}{2bh^3 E_{11}}, \quad \phi = \frac{3P(3a^{*2} + L^{*2})}{4bh^3 E_{11}}. \quad (D.1)$$

On the base of Fig. D1a the corrected crack length and the specimen length are:

$$a = a^* - R \sin \phi \cong a^* - R\left(\phi - \frac{\phi^3}{3!} + \dots\right), \quad L = L^* - R \sin \phi \cong L^* - R\left(\phi - \frac{\phi^3}{3!} + \dots\right). \quad (D.2)$$

Combining the first and second expressions in Eq. (D.1) one may obtain:

$$\phi = \chi\delta, \chi = \frac{3(3a^{*2} + L^{*2})}{2(3a^{*3} + L^{*3})}. \quad (D.3)$$

Eq. (D.2) can be rewritten as:

$$a \cong a^* - R_1(\chi\delta - \frac{(\chi\delta)^3}{6}), \quad (D.4)$$

$$L \cong L^* - R_1(\chi\delta - \frac{(\chi\delta)^3}{6}).$$

Note that in all the equations a is the corrected, a^* is the measured crack length, L is the corrected, L^* is the measured specimen length and δ is the experimentally measured specimen displacement. The radius of the loading head is: $R_l=6$ mm.

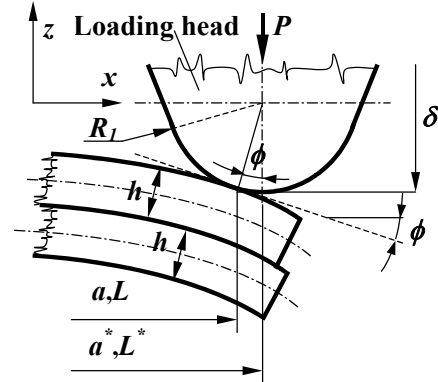


Fig. D1.
Correction of the ELS system.

D.2 SLB and SCB specimens

The corrections for the crack length and other geometrical parameters are calculated in the same fashion as it was shown before. Let us consider the schematic illustration in Fig. D2a. The corrected parameters of the SLB specimen are:

$$a \cong a^* - R_1(\chi_3\delta - \frac{(\chi_3\delta)^3}{6}), \quad (D.5)$$

$$2L \cong 2L^* - R_1([\chi_3 + \chi_4]\delta - \frac{([\chi_3 + \chi_4]\delta)^3}{6}), \quad (D.6)$$

where:

$$\chi_3 = \frac{7a^{*3} - 3L^{*3} - 21L^*a^{*2}}{7a^{*3}L^* + 2L^{*4}}, \quad (D.7)$$

$$\chi_4 = \frac{7a^{*3} + 3L^{*3}}{7a^{*3}L^* + 2L^{*4}}. \quad (D.8)$$

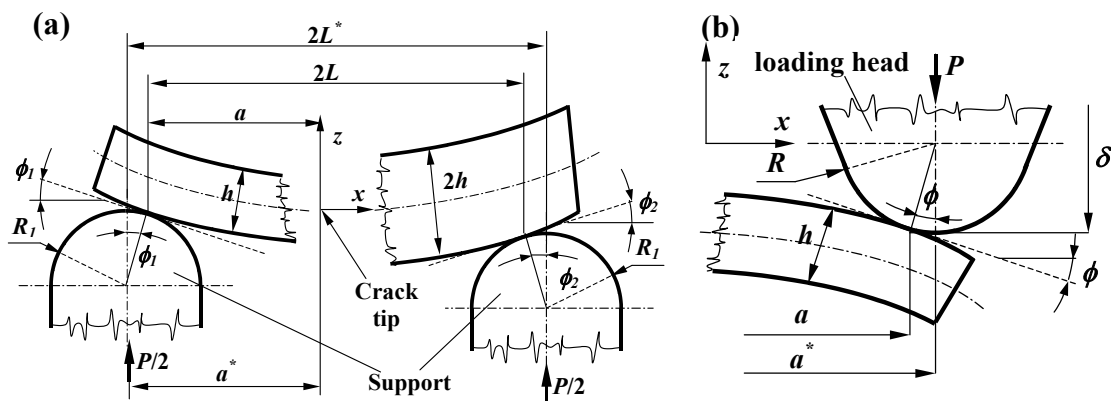


Fig. D2.
Correction of the SLB (a) and SCB (b) systems.

The same approximation in the case of the SCB configuration in Fig. D2b leads to the following equations:

$$a \cong a^* - R(g\delta - \frac{(g\delta)^3}{6}), \quad L \cong L^* - R(g\delta - \frac{(g\delta)^3}{6}), \quad (D.9)$$

where:

$$g = \frac{3(7a^{*2} + L^{*2})}{2(7a^{*3} + L^{*3})}. \quad (D.10)$$

This correction involves the correction of the full specimen length (L) of the SCB coupon since $L=a+c$. All in the equations a is the corrected, a^* is the measured crack length, δ is the experimentally measured specimen displacement at the point of load application. The radius of the supports is: $R=8$ mm.

APPENDIX E – Crack stability charts

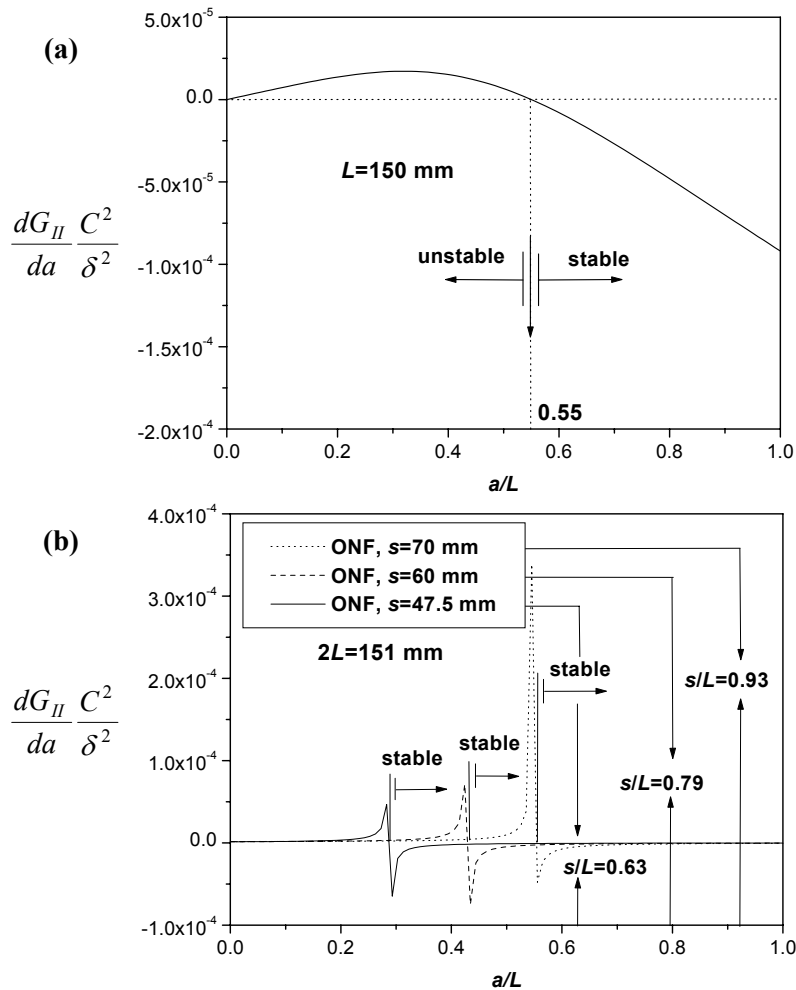


Fig. E1.

The crack stability charts of the ELS (a) and ONF (b) specimens.

APPENDIX F

F.1 The generalized *Krylov*-functions

The homogeneous, generalized *Krylov*-functions are (PONOMARJOV, 1968):

$$V_1(x) = \cosh(\lambda x) \cos(\lambda x), \quad (\text{F.1})$$

$$V_2(x) = \frac{1}{2} [\cosh(\lambda x) \sin(\lambda x) + \sinh(\lambda x) \cos(\lambda x)],$$

$$V_3(x) = \frac{1}{2} \sinh(\lambda x) \sin(\lambda x),$$

$$V_4(x) = \frac{1}{4} [\cosh(\lambda x) \sin(\lambda x) - \sinh(\lambda x) \cos(\lambda x)].$$

The deflection function of the uncracked region is:

$$w_{13}(x) = h_5 \cdot V_1(x) + h_6 \cdot V_2(x) + h_7 \cdot V_3(x) + h_8 \cdot V_4(x), \quad 0 \leq x \leq c, \quad (\text{F.2})$$

where according to OZDIL and CARLSSON (1999a) λ is equal to:

$$\lambda = \frac{6^{1/4}}{h} \left(\frac{E_{33}}{E_{11}} \right)^{1/4}, \quad (\text{F.3})$$

where E_{33} is the through-thickness modulus of the specimen.

F.2 Constant parameters

The constants in Eqs. (6.3), (6.4 and (F.2) are:

$$h_1 = \frac{1}{2} \frac{P(2a\lambda B + A) - P_1(L_1^2 \lambda^2 D + 2L_1 \lambda C + A)}{\lambda^2 I_y E_{11} D}, \quad (\text{F.4})$$

$$h_2 = -\frac{1}{6} \frac{P(3a\lambda A + 3C) + P_1(L_1^3 \lambda^3 D - 3L_1 \lambda A - 3C)}{\lambda^3 I_y E_{11} D},$$

$$h_3 = \frac{1}{2} \frac{P(2a\lambda B + A) - P_1(2L_1 \lambda B + A)}{\lambda^2 I_y E_{11} D},$$

$$h_4 = \frac{1}{2} \frac{P(a\lambda A + C) - P_1(L_1 \lambda A + B)}{\lambda^3 I_y E_{11} D},$$

$$h_5 = h_4, \quad h_6 = \frac{h_3}{\lambda}, \quad h_7 = -\frac{Pa - P_1 L_1}{\lambda^2 I_y E_{11}}, \quad h_8 = \frac{-P + P_1}{\lambda^3 I_y E_{11}},$$

where:

$$A = \cosh^2(\lambda c) - \cos^2(\lambda c), \quad (\text{F.5})$$

$$B = \cosh(\lambda c) \sinh(\lambda c) + \cos(\lambda c) \sin(\lambda c),$$

$$C = \cosh(\lambda c) \sinh(\lambda c) - \cos(\lambda c) \sin(\lambda c),$$

$$D = \cosh^2(\lambda c) + \cos^2(\lambda c) - 2.$$

F.3 Form of the system of equations

We express the forces P_j in an unabridged form. Combining Eqs. (6.17), (6.19) and (6.22), with Eq. (6.23) the ' j '-th force results in:

$$P_j = s_j \left(\sqrt{(w_u(-L_{2j}) - w_l(-L_{2j-1}))^2 + L_{0j}^2} - L_{0j} \right) \sin\left(\arctan\left[\frac{w_u(-L_{2j}) - w_l(-L_{2j-1})}{L_{0j}}\right]\right). \quad (\text{F.6})$$

Rearranging Eqs. (6.17) and (6.19) the lateral displacements can be rewritten in the following form:

$$w_u(L_{2j}) - w_l(L_{2j-1}) = \gamma^P + \sum_{i=1}^n \gamma_i P_i, \quad (\text{F.7})$$

where:

$$\gamma = \frac{\lambda^3 [L_{2j}^2(3a - L_{2j}) + L_{2j-1}^2(3a - L_{2j-1})] + 6\lambda^2 a(L_{2j} + L_{2j-1}) + 3\lambda(L_{2j} + L_{2j-1} + 2a) + 6}{6\lambda^3 I_y E_{11}}, \quad (\text{F.8})$$

$$\gamma_i = \frac{\lambda^3 [\phi_{2i} + \phi_{2j-1}] + 6\lambda^2 (L_{2j} L_{2i} + L_{2j-1} L_{2i-1}) + 3\lambda (L_{2i} + L_{2j} + L_{2i-1} + L_{2j-1}) + 6}{6\lambda^3 I_y E_{11}}. \quad (\text{F.9})$$

In order to simplify Eq. (F.6) we use the following trigonometric identity:

$$\sin(\arctan(x)) = \frac{x}{\sqrt{1+x^2}}. \quad (\text{F.10})$$

Thus, from Eq. (F.6) the simplest form of the equation for the ' j '-th force P_j becomes:

$$P_j = s_j \left[1 - \frac{1}{\sqrt{1 + \left[\frac{1}{L_{0j}^2} (\gamma^P - \sum_i^n \gamma_i P_i) \right]^2}} \right] (\gamma^P - \sum_i^n \gamma_i P_i), \quad (\text{F.11})$$

which has only a numerical solution. We have ' j ' number of equations, where the ' j '-th equation contains all the forces ($i=1\dots n$). Eqs. (F.6)-(F.11) are suitable to determine the unknown forces which arise in the bridgings.